Universitat Autònoma de Barcelona

Metallosurfactants and drug delivery systems for biomedical applications

Glòria Garcia Ortega

UAB
Universitat Autònoma
de Barcelona

METALLOSURFACTANTS AND DRUG DELIVERY SYSTEMS FOR BIOMEDICAL APPLICATIONS

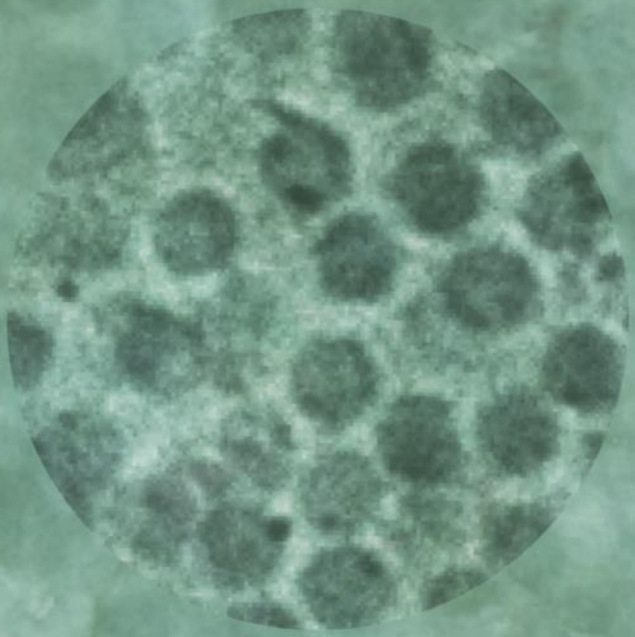

Glòria Garcia Ortega

PhD in Chemistry

2022

Supervised by

Dr. Òscar Palacios Bonilla

Dr. Pau Bayón Rueda

Universitat Autònoma de Barcelona

PhD Thesis

Metallosurfactants and drug delivery systems for biomedical applications

Glòria Garcia Ortega

Chemistry PhD program

Supervised by

Dr. Òscar Palacios Bonilla

Dr. Pau Bayón Rueda

Chemistry Department

Faculty of Science

2022

Manuscript presented to obtain de PhD Degree by Glòria Garcia Ortega

Glòria Garcia Ortega

With the approval of the supervisors of the Doctoral Thesis, Dr. Òscar Palacios Bonilla, and Dr. Pau Bayón Rueda associate professors at *Universitat Autònoma de Barcelona*.

Dr. Òscar Palacios Bonilla

Dr. Pau Bayón Rueda

FINANCIAL SUPPORT

The work described in this PhD Thesis has been possibble to perfomr thanks to the financial support of the following projects:

- "COMPRENSION DE LAS INTERACCIONES MOLECULARES ENTRE METALES Y SYSTEMAS BIOLOGICOS PARA EL DISEÑO DE APLICACIONES BIOMEDICAS Y BIOTECNOLOGICAS. SP2- APROXIMACION QUIMICA"; BIO2015-67358-C2-02-P; PI: Mercè Capdevila Vidal. Granted by Spanish Ministerio de Ciencia e Innovación and FEDER.
- PIF scholarship of 4 years granted by *Universitat Autònoma de Barcelona* to develop this PhD thesis in *Bioinorgànica* research group
- SAXS-WAXS experiments performed at NCD-Sweet beamline at ALBA Synchrotron, within the Project "Unveiling the structure of metallosurfactant aggregates and metallosomes".

ACKNOWLEDGMENTS

Vull donar les gràcies als meus directors per donar-me l'oportunitat de gaudir de la beca PIF, ja que m'ha permès desenvolupar aquest treball i sobretot, evolucionar com a científica. Gràcies, Òscar Palacios i Pau Bayón per permetre'm aquests anys afrontar tot allò que suposa una investigació. Vull també agrair molt especialment l'ajuda d'en Ramón Barnadas, de la Unitat de Biofísica, ja que sempre ha estat allà per atendre'm, recolzar-me i aconsellar-me, gràcies. I, aprofito per fer esmena especial a tots els companys i professors del departament de biofísica. D'igual forma també vull agrair a en Ramon Pons[2] per obrir-me el seu laboratori i donar-me tot el suport per esbrinar que passava amb aquestes molècules "que feien coses rares"; també voldria fer extensiu aquest agraïment al seu grup, l'Imma Carrera i en Jaume Caelles perquè em van rebre com un més. "Ramons", gràcies per creure en aquest treball i en mi, i per ajudar-me a proposar un projecte de sincrotró que m'ha permès posar la cirereta a tot l'esforç. A en Joan Suades vull agrair-li el suport que m'ha donat durant tota la tesi, estan a prop o lluny sempre m'ha fet palès que hi era. Mercè Capdevila, per mi ets un referent, tant com a científica com a dona, gràcies. ¡Fernando Novio, ha sido un placer poder contar con tu ayuda siempre que la he necesitado! També agrair a tots els altres professor de la planta, ja que sempre han tingut un somriure que oferir, i en molts cassos algun que altre consell. També al Servei d'Anàlisi Química, on hi ha grans professionals que m'han brindat el seu ajut sempre que ho he demanat; vull mencionar especialment a l' Òscar i l'Ignasi per les discussions prèvies a cada mostra. Gràcies també al grup Protein Engineering and Nanomedicine del IBB, molt especialment a la Dr. Julia Lorenzo i al Dr. David Montpeyó, pel seu suport i ajuda en les parts "bios" d'aquesta tesi.

Special acknowledgment to Prof. Paola Lucini and Dr. Simone Alenadri who welcomed me in their lab and taught me everything they could. Being there made me felt valuable, as well as, the luckiest researcher, thank you, most sincerely. Also, all the group who welcomed me as one more, Marianna, Gregor, Despo, Sara, Aymar, Miki, Cristina, Rosanne, and Adelina. Special thanks to the cell culture lab, Gina, and Ivo, who dedicated their time to help me out with this project! From my time in Switzerland, I must also mention my flatmates cause I couldn't have had a most perfect place to stay. Gaby, Päscu, and Mike, for the dinner cooking, the Disney and Netflix nights, the craziest game nights and a memorable road trip, thanks guys!

I gràcies a tots els bons companys i amics que ja venen des de l'inici d'etapa a la UAB, gràcies Esther, Lluís, Xavi, Raúl, Sergio, Adri, Ester, Loreto, Pau... i a tots aquells que no esmeno per no fer-ho infinit.

Agrair a tothom que estava per la planta d'inorgànica quan va començar aquesta tesi, va ser una etapa fantàstica! I sobretot amb tots els que acabo, ha sigut magnífic rebre els vostres consells i ajuda, però sense cap mena de dubte, el millor és saber que m'enduc amics. Gràcies, Fran, Dani E., Dani G., Miriam, Lavi, Mariona, Rosa, Solde, Jordi M., Sam, Marc, Abel, Héctor, Clara... Momo, Diana i Lucia, els riures i experiències amb vosaltres no els puc mesurar amb res! Gràcies!

Vull, però fer algunes esmentades especials. Quim, m'ho has ensenyat tot al laboratori, has dedicat tot el temps que no tenies, t'ho agraeixo de tot cor; et dec tant! Mario, no podria haver imaginat un millor company de laboratori i amic, fer aquest viatge amb tu ha sigut una de les millors coses que m'han passat mai. Quim i Mario, no canvieu perquè sou increïbles.Arnau, ànims que jo ho tens! Fatima keep going because your effort is gona be rewarded! També donar les gràcies a l'Anna i la Christina, perquè han estat de molta ajuda! I no m'oblido dels companys de Pt, moltes gràcies per tot orgànics. A tu Kevin per ensenyar-me que tot arriba! I, Marc el Pt es queda en bones mans, ànims amb la feina i gràcies per les xerrades i queixes compartides. D'allà dalt, a la quarta, no vull deixar d'anomenar i agrair al Marc V., en Sergio i l'Adri.

A les companyes de dansa i la Marta, a la que fa 4 anys que li prometo que no arribaré tard, gràcies maques!

I per tots els "amics de sempre" i per aquells que han arribat. Perquè sempre hi sou, d'una manera o un altre. Ana, Rocío, Javi, Jeni, Montse, i cia. Alba i Desireé, les meves arquitectes que em fan boles amb pals, us dec molt. Cristina, Jandro i Marc vau fer que el confinament, el qual ha marcat part d'aquesta feina, fos gairebé una festa constant. A tu també Martí, infinites gràcies pel teu suport constant.

No m'oblido de la família, tietes, tetes, cosinetes i Anabel, perquè sento sempre el vostre suport. Lalos i Joaquin, gràcies per creure sempre en mi i donar-m'ho tot. A les iaies Carme i Carmen perquè pensant en vosaltres se'm reflecteix la imatge de dones fortes, que m'han donat l'empenta des d'allà on sigueu. També al iaio Joaquin perquè no he conegut persona més treballadora al món. I, finalment gràcies als meus dos àngels que van en taxi, iaio Josep i tiet Fernando... perquè no puc negar que tot això és una mica per vosaltres.

“At the end of the day, we can endure much more than we think we can.”

— **Frida Khalo**

“We are not going in circles; we are going upwards. The path is a spiral; we have already climbed many steps.”

— **Hermann Hesse, Siddhartha**

ABSTRACT

Platinum drugs are widely used as antineoplastic agents in the treatment of several cancers. However, pernicious side effects related to the systemic toxicity of these types of therapies enforce the improvement of drug delivery systems. In this sense, the preparation of Pt(II) metallosomes -mixed vesicles of a Pt(II) surfactant complex and structural phospholipids- will gather the activity of the Pt(II) complex with the benefits of liposomes as drug delivery systems, such as the enhanced biocompatibility, or the improved therapeutic efficiency .

In the first part of this thesis, a new family of linear amino sulfonates {$NH_2(CH_2)_nSO_3Na$, L2 (n=2), L6 (n=6), and L10 (n=10)} is synthesised and characterised. Likewise, their respective *cis*-[PtI_2L_2] (L = L2, L6 and L10) complexes are obtained after the reaction between the amino sulfonate ligands and K_2PtCl_4 in water. All compounds are fully characterised by common analytical techniques {NMR, IR, ESI-MS and UV-Vis}. Furthermore, the choice of the chemical groups, the reaction mechanisms and the complexes interaction with biomolecules and its cytotoxic activity are thoroughly discussed. Additionally, the physical behaviour of the ligands and complexes are investigated. In some cases, they have shown unique physicochemical properties, such as pH dependant, solubilities or supramolecular organisation studied by small angle-X-ray scattering, and *cryo*-transmission electron microscopy. Moreover, the critical aggregation concentration of the *cis*-[PtI_2L_2] is estimated using fluorescence and dynamic light scattering.

Finally, due to its unique physicochemical characteristics, *cis*-[$PtI_2(L10)_2$] proved to be a suitable molecule to prepare metallosomes using traditional liposome preparation methods. The study of the resulting metallosomes has permitted to relate the size of the vesicles with the metallosurfactant/phospholipid ratio. Likewise, the preparation of metallosomes with various phospholipids indicates distinctive interaction between the surfactant complex and the lipidic bilayer, analysed by anisotropy, dynamic scanning calorimetry, and small-angle-X-ray scattering, among other techniques. The deep characterisation and analysis of crucial features of our metallosomes like size, Pt-internalisation, cytotoxicity and stability, evidence their promising activity as chemotherapeutic agents.

SYMBOLS AND ABBREVIATIONS

a.u.	Arbitrary units
Abs	Absorption
B.E.	Binding energy
CAC	Critical aggregation concentration
CD	Circular dichroism
CMC	Critical micellar concentration
COSY	Correlated spectroscopy
CPP or *p*	Critical packaging parameter
***Cryo*-TEM**	Cryogenic transmission electron microscope
***ct*-DNA**	Calf-thymus DNA
Cyt C	Cytochrome C
DDS	Drug delivery systems
DFT	Density-Functional theory
DLS	Dynamic light scattering
DMEM	Dulbecco's Modified Eagle Medium
DMF	*N,N*-Dimethylformamide
DMPC	1,2-dimyristoyl-*sn*-glycero-3-phosphocholine
DMSO	Dimethyl sulfoxide
DOPC	1,2-dioleoyl-*sn*-glycero-3-phosphocholine
DS	Disulfonate product
DSC	Differential scanning calorimetry
DSPC	1,2-diasteroyl-*sn*-glycero-3-phosphocholine
$E°_{red}$	Standard reduction potential
EA	Elemental analysis
EMA	European Medicines Agency
EPR	Enhanced Permeability Effect
ESI-MS	Electrospray ionisation mass spectrometry
EtOH	Ethanol

f	Oscillator strength
FBS	Fetal bovine serum
FDA	Food and Drug Administration
FTIR-ATR	Fourier transform infrared-attenuated total reflection
GUV	Giant unilamellar vesicles
HS	Halosulfonate product
HSA	Human serum albumin
I	Intensity
ICP	Inductively coupled plasma
IL	Intraligand
IM-MS	Ion mobility mass spectrometry
K_b	Binding constant
K_{obs}	Observed constant
K_{sv}	Stern-Volmer constant
LANL2DZ	Los Alamos National Laboratory 2 Double-Zeta basis set
LC	Ligand centred
LMCT	Ligand-to-metal charge transfer
Ls	Family of alkyl sulfonate ligands
LUV	Large unilamellar vesicles
m/z	Mass to charge ratio
Mb	Myoglobin
MEM-α	Minimum Essential Medium α
MeOH	Methanol
MLCT	Metal-to-ligand charge transfer
MLV	Multilamellar vesicles
MS	Mass spectrometry
MTL	Metallosomes
MTS	Metallosurfactant
MVV	Multi vesicular vesicles
MW	Molecular weight
NMR	Nuclear magnetic resonance
NTO	Natural transition orbital

OES	Optical electron spectroscopy
OLV	Oligo lamellar vesicles
PBE	Perdew-Burke-Ernzerhof functional
PBS	Phosphate buffered saline
PC	Phosphatidylcholine
PDI	Polydispersity Index
PEG	Polyethylene glycol
pI	Isoelectric point
RES	Reticuloendothelial system
ROS	Reactive oxygen species
RPMI	Roswell Park Memorial Institute Medium
SAXS	Small angle X-ray scattering
SEM	Scanning electron microscope
SPC	L-α-phosphatidylcholine from soybean

SUV	Small unilamellar vesicles
T	Temperature
TD-DFT	Time-dependent Density-functional theory
Tf	Transferrin
T_m	Main transition temperature of lipids
TS	Transition state
UV-Vis	Ultraviolet visible
WAXS	Wide-angle X-ray scattering
WST-8 (CCK8)	Water-soluble tetrazolium salt (Cell Counting Kit-8)
XPS	X-ray photoelectron spectroscopy
Zn_7-MT1	Zn7 isoform 1 metallothionein
ZP	Zeta potential

TABLE OF CONTENTS

1. INTRODUCTION

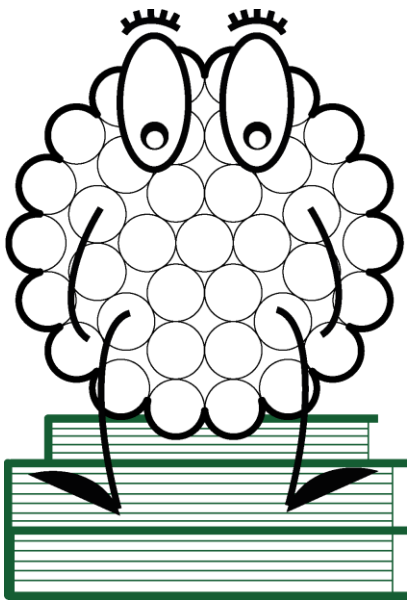

In this section the main features related to the subjects considered important during the development of this thesis are reviewed. From a state-of-the art of cancer diseases, including the main treatments and its side-effects, to drug delivery systems are discussed. Followed by a deep description of liposomes and their structural units, to finally introduce the surfactants and liposomes containing metals.

1.1 Cancer

Cancer is a group of diseases generated when abnormal cells grow uncontrollably. They can start in almost any organ or tissue of the body, spread to others, and invade distant parts. Oncology is the medical specialty that deals with the prevention, diagnosis and treatment of cancer.

In most countries, cancer leads the cause of death for population below 70 (**Figure 1.1**). In 2020, an estimated of 19.3 million new cases were diagnosed and 10 million deaths were accounted for cancer. And, the number of cases is expected to rise to 23.6 million by 2030.[1–3]

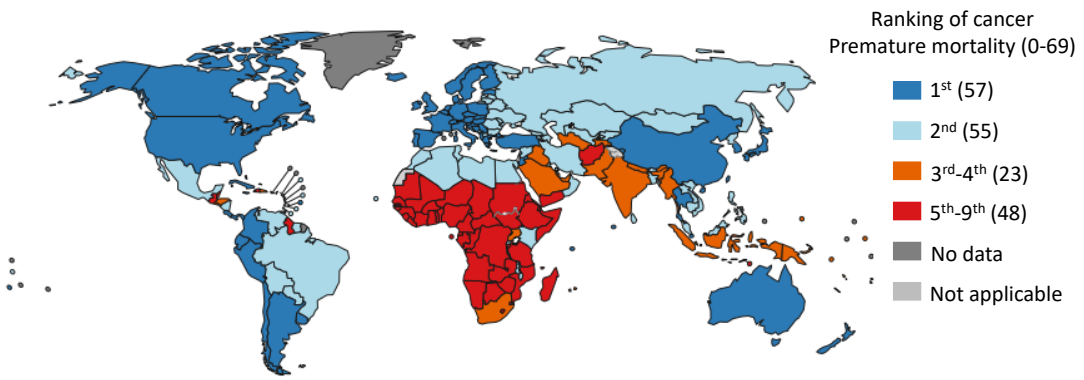

Figure 1.1 Global map showing the national ranking of cancer as a cause of death at ages below 70 years in 2019. Figure reproduced from literature.[1]

Lung, prostate, colorectal, stomach and liver cancer are the most common types of cancer in men, while breast, colorectal, lung, cervical and thyroid cancer are the most common among women.[1]

1.1.1 Involved metabolism

Cells, divide through a cell cycle, following a well-ordered set of events: the synthesis of DNA (S-phase), growth phase and mitosis preparation (G2-phase), mitosis (M-phase), and cell growth (G1-phase), ending into two descendant cells. Cancer occurs when the process

becomes abnormal, with cells dividing and forming more cells without control. Then, an abnormal cell that grows and divides uncontrollably will cause a tumour. The tumour is said to be benign if the cancer cells do not invade the surrounding tissue. If it does so, the tumour is recognised as cancer. Invasiveness, which is a fundamental characteristic of cancer cells, makes the cancer cells break, lose, enter the blood or lymphatic vessels, be transported at distant sides through the vasculature, and form secondary tumours; termed metastases.[45] Cancer cells alter or avoid cell control by which multicellular organisms are built and maintained, adapting their metabolism to support tumour initiation and progression.

1.1.2 Hallmarks of cancer

Cancer generation is described as a multistep process. During the last decades, transformations of normal cells into tumorigenic and their dissemination have been grouped in metabolic alterations. These biological capabilities were described in 2000 by Hanahan *et al*[6] and they are known as "Hallmarks of cancer".[6] Briefly listed below, they gather the main features committed by carcinogenic cells to the development and growth of cancer.[6,7]

- *Sustaining proliferative signalling*: cancer cells show better self-sustainability than normal cells. Neoplastic cells can outrun apoptosis and anti-proliferative extracellular signals.
- *Evading growth suppressors*: inactivation of tumour suppressors that limit cell growth and proliferation.
- *Resisting cell death*: bypass of the programmed cell death by apoptosis, which is an innate hindrance of healthy cells to cancer development. Similarly, cancer cells display defective intracellular mechanisms to stop cell division after DNA damage or in response to cellular stress (such as hypoxia).
- *Enabling replicative immortality*: overcome the limited number of successive cell growth-and-divisions cycles by overcoming a non-proliferative state, usually related to cell death. The overall sequence is also known as immortalisation.
- *Inducing angiogenesis:* vascularisation occurring around the tumour to fulfil its needs, such as nutrition, oxygen availability, and metabolic and CO_2 evacuation.

- *Reprogramming of energy metabolism*: alterations in the energy metabolism to support cell growth and division needs. The most remarkable is commonly named as The Warburg Effect, reviewed in section 1.1.3.
- *Activating invasion and metastasis*: described by the capability of invading other tissues by a multistep process named invasion-metastasis cascade, described in section 1.1.4.
- *Evading immune destruction*: cells and tissues are watched by the immune system, which recognises and defeats a great number of incipient cancer cells. Hence, the tumours that are finally bred, have avoided its detection by the immune system, or have exceeded the capacity of immunological eradication. Nonetheless, it is important to highlight that the immune system's role is not fully comprehended.

Generally, tumours display several of the ''Hallmarks'' but only a few shows all of them. This specific display has also contributed to better tumour classification and treatment.[8]

As reviewed by Hanahan *et al.*,[6] metabolic activities under oncogenic control are responsible for cancer. It is demonstrated that certain oncogenes can induce, or are involved, in multiple competencies and therefore in several Hallmarks. Joining these hallmarks there is genome instability and inflammation, which shelters multiple hallmark functions.[5,7,9]

1.1.3 The Warburg Effect

Innate evidence of metabolism change is the increased consumption of glucose and lactate generation (lactagenesis). Lactogenic cancer cells present enlarged aerobic glycolysis, and therefore, an excessive lactate production. It is one of the most characteristic malfunctions in cancer cells commonly known as the Warburg Effect that supports biosynthetic requirements of uncontrolled cell proliferation. The adapted mechanism was termed during the early 1970's by Efraim Racker, after Otto Warburg, its discoverer.[10]

Cells mainly metabolise glucose up to ATP and CO_2 in mitochondria, through the well-known tricarboxylic acid cycle (or Krebs Cycle). In the cycle, production of NAD^+ sustains oxidative phosphorylation to maximise ATP obtention with minimal production of lactate. In contrast, under anaerobic conditions cells produce a large amount of lactate. Whereas, in tumours and other proliferating cells, even in the presence of oxygen, glucose consumption is incremented. A high amount of lactate is produced because they rely on metabolic glycolysis for ATP obtention, hence also termed as aerobic glycolysis (**Scheme 1.1**).[11]

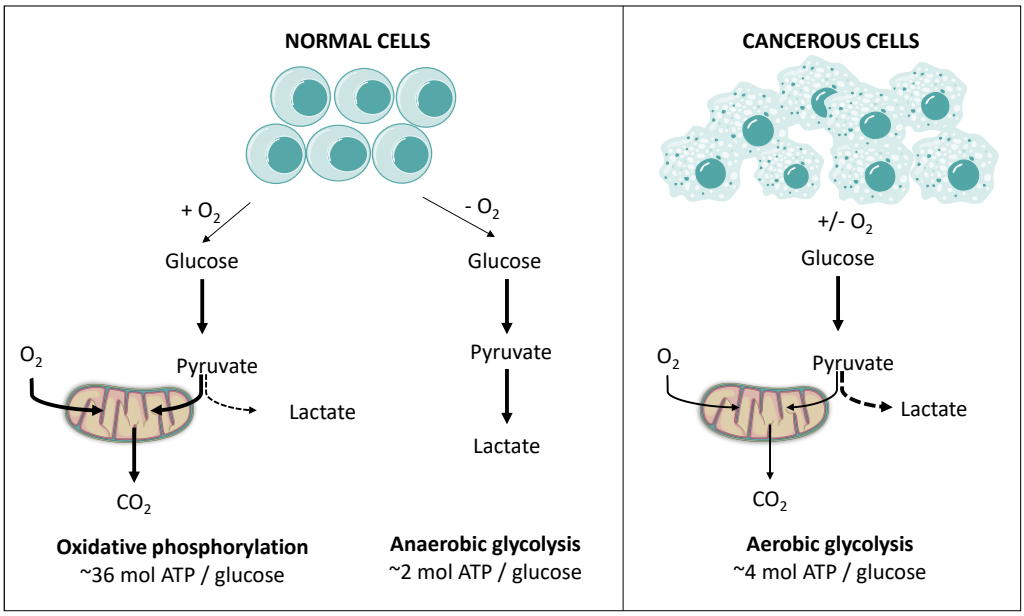

Scheme 1.1 Representation of aerobic respiration in normal cells (left) vs aerobic glycolysis (right) showing that cancer cells prefer aerobic glycolysis although in presence of oxygen and with a lower ATP production with respect to oxidative phosphorylation.

The augmented lactate production is hypothesised as a key element in carcinogenesis. As cancer cells "ferment" glucose into lactate, even in the presence of enough oxygen. The metabolism from glucose to lactate generates 2 ATPs for each glucose, while oxidative phosphorylation generates 36 ATPs per glucose molecule when completely oxidised to CO_2. Then, it is necessary to disclose why cancer cells employ aerobic glycolysis, a less efficient glucose metabolism for energy obtention.[11] One possible explanation relies on the metabolic needs of proliferating cells. The production of lactate from glucose is 10 to 100 times faster than the total oxidation of glucose in the mitochondria. This suggests that even with inefficient ATP production from aerobic glycolysis, its faster ATP production shows an advantage when competing for energy sources with mitochondrial respiration.[10]

Krebs Cycle is also crucial for the synthesis of other biochemical reactions involved in biomass replication in cells, for instance, the synthesis of amino acids precursors. This means that the cell spends resources from carbon surplus from lactate production for the biosynthetic requirements of uncontrolled growth and proliferation. Consequently, the bulk of glucose cannot be completely converted to CO_2 by oxidative phosphorylation to enlarge ATP yield, because it would wrangle the needs of the uncontrolled proliferating cells. This inquiry may disclose part of the selectivity upon aerobic glycolysis.[11,12]

Mammalian cells in organisms have a regular source of surrounding nutrients but cells do not consume nutrients from their environment unless growth factors coerce to do it. In uncontrolled cell proliferation, acquired genetic mutations in the growth factors alter this pathway. Moreover, for initial proliferating cells, nutrients are not restrained, and theoretically, they would not need to maximize ATP production. Inefficient ATP synthesis by aerobic glycolysis would become an obstacle only when the energy resources are scarce.[13] And, usually, this is not the situation in proliferating cancer cells with abnormal surrounding vasculature or angiogenesis.[14]

Hypoxia, oxygen deprivation in cancer cells, even being important for several cancer progression conditions (angiogenesis, metastasis, resistance to radio and chemotherapy, etc.) is pointed to be a late-occurring manifestation. So, it is not a dominant aspect of the shift from oxidative phosphorylation to aerobic glycolysis. In fact, it is known that cell proliferation can viably rely just on respiration.[11]

In general, the Warburg Effect provides an ambient that leads to cell proliferation. For instance, because the elevated amount of produced lactate tumour microenvironments has a decreased pH. Excreted H^+ diffuse into the tumour interface and so, increases the invasiveness.

Moreover, metabolic pathways bringing redox homeostasis are also dysregulated. Controlled reactive oxygen species (ROS) levels are needed to promote cancer cell growth and proliferation. For instance, ROS are involved in tumour invasiveness, metastasis, and angiogenesis, among many others. Their production in cancer cells is raised because of the increased metabolic activities. However, an excessive amount of ROS harms fundamental cells by means of oxidative damage. The Warburg Effect appears to be a mechanism by which the cell reduces ROS amounts and consequently oxidative stress: the production of NADH in the Warburg Effect leads to a survival mechanism for cancer cells, maintaining a proper redox status.[12]

It is also pointed out that the higher reliance on glycolysis limits the availability of glucose from immune cells implicated in killing tumour cells as, tumour-infiltrating lymphocytes.[15,16]

Some studies hint that the Warburg Effect is essential for the carcinogenic process.[17] Warburg proposed malfunctions in mitochondria as the origin of cancer, indicating that initial metabolism defect occurring in the respiratory chain coerces cancer cells to employ glycolysis for energy obtention. However, posterior works evidence that mitochondria are not defective

in most cancer cells.[11,17] Other studies suggest that even been an early event in oncogenesis, it is not entirely essential in the initial state, but a consequence of an oncogenic mutation found also in early benign states. Overall, it is not thoroughly clear if the Warburg Effect is a cause or a requirement in carcinogenesis. Nonetheless, a better understanding of cancer metabolism above and beyond the Warburg Effect may exploit improved treatments and therapeutic paths.[18,19]

1.1.4 The invasion-metastasis cascade, angiogenesis, and the tumour microenvironment

Metastasis is a multi-stepwise process in the invasion-metastasis cascade (**Figure 1.2**). Metastases occur when cancer cells from a primary tumour spread to a distant part of the body and is responsible for 90% of deaths in many types of cancer, rather than the primary tumours.[20,21] The biological bases of metastases remain poorly understood: its complexity relies on the intrinsic multifaceted aspects of the disease, such as genomics, metabolism, and microenvironment.[22,23] Both, modified cell division and inactivated apoptosis, support tumorigenesis, but then, cancer cells must migrate to metastasise, survive, and proliferate in a different environment.[7,24]

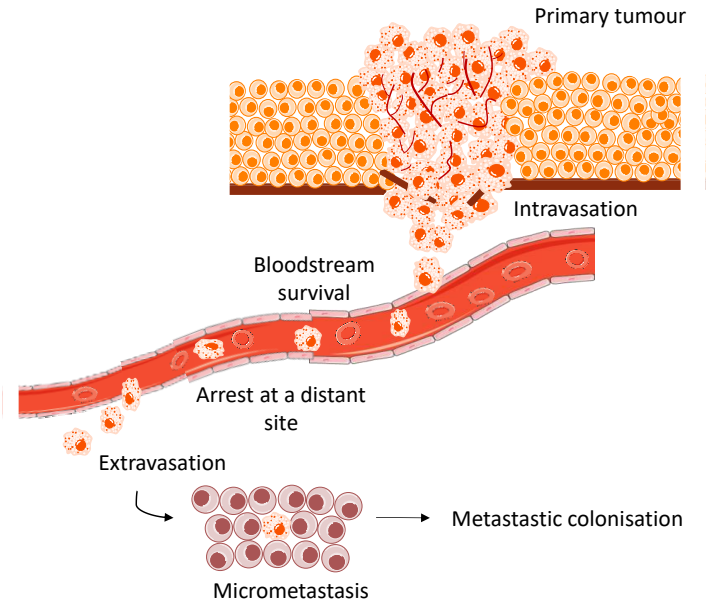

Figure 1.2 Representation of the Invasion-Metastasis Cascade from which a primary tumour ends generating a micrometastasis at a distant tissue in the body.

The general steps of metastases, similar in almost all tumour types, consist of (i) local invasion and dissociation of the bulk tumour -through surrounding extracellular matrix and stromal cell layers-, (ii) intravasation into the circulatory system, (iii) survival to transport through the

circulation vessels, (iv) arrest at distant organ sites, (v) extravasation from vessels, (vi) micrometastases formation in the foreign microenvironment, (vi) and metastatic colonisation by restarting proliferation at metastatic locations, generating clinically detectable metastatic lesions (secondary tumours).[4,22,25–28]

The main functions of the cardiovascular system are the transport and delivery of nutrients, oxygen, blood and immune cells to all organs and tissues. It also removes metabolic wastes (*i.e.*, CO_2 or nitrogen wastes). Usually, it develops and matures through two strict coordinated mechanisms: vasculogenesis and angiogenesis.

Reinforced in tumours, angiogenesis is the formation of new capillaries from previous vessels (**Figure 1.3**).[26]

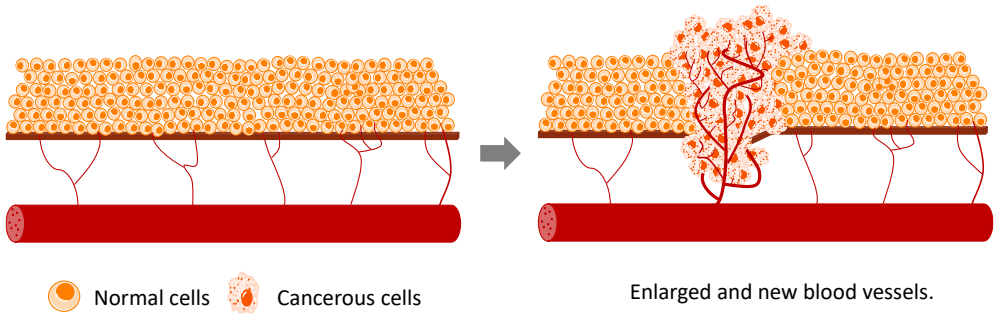

Figure 1.3 Representation of abnormal vascularity in angiogenesis

Physiologically, angiogenesis is necessary for several common processes such as the embryo-state, inflammation, or wound healing. But in tumours, it is associated with the secretion of excessive growth and angiogenic signals that attract blood supply.[29,30] Nonetheless, it is important to notice that tumours vessels are leaker, more disorganised and convoluted than normal vasculature, bringing associated clinic pathologies seen in cancer patients. [9,29]

Hypoxia is another conductor of angiogenesis. When the tumour demands of nutrients and oxygen are higher than the local supply, which occurs when the tumour has a diameter of 1-2 mm, the hypoxic microenvironment pledges the required oxygen levels by the expression of hypoxia-inducible factors.[31] Even though, angiogenesis is rather balanced by oxygen levels than by nutrients, delivery of both relies on the vasculature.[9]

Over and above, it is indisputable that tumours display an intrinsic complexity. The environment around the tumour, which includes the surrounding blood vessels, immune cells, fibroblasts, signalling molecules, the decreased pH, and the extracellular matrix, are in

constant interaction and are collectively designed as the tumour microenvironment.[31] It also alters the therapeutic responses and resistance to drugs. The development of new means to treat human cancer may arise from the understanding and targeting of components into the tumour microenvironment.[7]

1.2 Cancer treatments

1.2.1 A brief history of chemotherapy

Surgery is considered the first approach against cancer. In 1809 an ovarian tumour was removed by Ephraim McDowell and was the demonstration that tumours can be treated by surgery. In the mid and late 19th century, with the appearance of anaesthesia and antisepsis, surgery became the option to beat cancer in almost any organ. However, it was subsequently shown that radical *en bloc* removal of tissue was worse than removal of the tumor mass.[32]

The discovery of X-rays by Roentgen (1895) and radium by the Curies (1898) are considered the departure point of radiotherapy. A milestone in radiation therapy was the cure of head and neck cancer in 1928, and the modern era of radiotherapy started with the use of cobalt in external beam radiotherapy. Also, advances in technology have been improving the delivery of beam energy more accurately to the tumour.[33]

Surgery and radiotherapy dominated cancer therapy up to 1960s. However, at that time it was clear that local treatments' cure rates had flattened out, mainly because of the impossibility to treat micrometastases.[34,33]

The use of chemicals in the treatment of cancer can be found-back in ancient Egypt where the stomach and uterus cancer were treated using barely and other ingredients. Then, in the sixteen century Paracelsus, a pioneer in the use of chemicals in medicine address a current concern in oncology: *''How can I treat and hopefully cure a cancer patient with a drug at a nontoxic or acceptable dose without the risk of conversely overdosing and risking severe side effects or even the death of my patient?''.*[32]

In the early 1900s, the chemist Paul Ehrlich coined the term chemotherapy, defining it as the use of chemicals to treat diseases. He was also among the pioneers in the use of animal models to test and screen the potential activity of drugs. Ehrlich was interested in drugs to treat cancer and developed the first alkylating agents (*i.e.*, aniline dyes).[34]

During World War I, soldiers exposed to sulphur mustard ended up with minor white blood cell count because of the depletion of the bone narrow and lymph nodes, which motivated the potential therapeutic effects of these chemicals. The use of a less toxic chemical, nitrogen mustard, to treat patients with high blood cells counts related to lymphoid leukaemia and lymphomas was first tested in 1943. It fomented the synthesis and testing of several alkylating compounds. During the same time, folic acid was demonstrated to have an important role in bone narrow malfunction as it accelerated leukaemia cell growth. These observations lead to the synthesis of folic acid antagonists: antifolates such as aminopterin and amethopterin, which were tested for treating children leukaemia. Similarly, these advances provided a stimulus for the synthesis and study of other drugs bringing to the discovery of thiopurines, which have been also used to treat infections or immunosuppression necessities. Another program related to the World War II proved the use of some antibiotics for the treatment of cancer, which are still in common service as antitumour agents.[34]

After the 1960s the use of combinate treatments, surgery and/or radiotherapy along with chemotherapy became the chance to cure patients with advanced cancers and deal with micrometastases. The antitumour effect could be maximised with lower toxicity to normal tissues, yielding the field of adjuvant chemotherapy. The use of drugs combination after surgery showed a significant diminishing in mortality for breast and colorectal cancer, with Dr. Fisher as the pioneer in conducting an adjuvant study against breast cancer. Nevertheless, the field of oncology was not officially established until 1973.

Around 1965, the type of tumours responding in a better way to cytotoxic agents were those with fast doubling times, around a few days. Among them are lymphomas, leukaemia, some types of sarcomas and testicular cancer.[32]

One of the greatest successes in the field of bioinorganic chemistry is the discovery of cisplatin (*cis*-diamminedichloroplatinum(II)) for cancer treatment by Rosenberg in 1965. While conducting an experiment to study the effect of the electrical field in cell division, Rosenberg placed platinum electrodes into *E. choli* bacteria solution. When current started, bacterial cells stopped dividing and reassume its division when the current stopped. The first impression of Rosenberg and colleagues was that electricity was controlling cell growth. Nonetheless, after two years they finally pointed out that cell division was blocked by a platinum compound released by the electrodes, cisplatin.[35–37]

In preliminary studies, the use of cisplatin decreased the size of tumors in animals, which prompted its evaluation against human tumor systems. Cisplatin entered the clinic in 1972 and was approved by the FDA in 1978.[35] The use of drug combinations in which cisplatin was included increased the cure rate of metastatic testicular cancer from 10 to 60% by 1978 and, has increased nowadays up to 95%.[38,39]

Many new drugs against cancer have been introduced since the 1980s. Some of them even not being chemotherapeutic agents (*i.e.*, antibodies) work well in conjunction with chemotherapy. Chemotherapy has, in fact, transitioned to the age of ''targeted therapy'', thanks to the research and improved knowledge in molecular biology that has identified oncogenes, suppressors, signalling pathways or genome sequencing, among others. Besides, in the past 25 years, immunotherapy has become an important component in cancer treatments.[33,34]

1.2.2 A deeper view to platinum-based drugs

The human body needs about 10 essential metals to function properly. About 46 non-essential metals are used in drug therapies and as diagnostic agents, such as platinum (cancer treatment), lithium (bipolar disorders), silver (antimicrobials), bismuth (broad-spectrum antibiotics) or radionuclides such as technetium-99.[40–42]

The discovery of cisplatin activity highlighted the scope of metallodrugs. It is still considered the main architecture for the development of platinum-based and other metal-based systems. Even though they entered the market almost 40 years ago, platinum chemo-drugs still comprehend 50% of anticancer therapies. [39,43,44]

Cisplatin analogues have extended the scope of benefit, looking for fewer toxic drugs, with a broader activity spectrum and, the ability to overcome cell acquired resistance. Still, because these complexes are structurally derived from cisplatin and exhibit the same mechanism of action, the drawbacks of cisplatin are usually inherited.[44] The main examples, shown in **Figure 1.4**, are carboplatin and oxaliplatin, with worldwide approval and nedaplatin (approved in Japan), lobaplatin (approved in China) and heptaplatin (approved in Korea).[39,44,45]

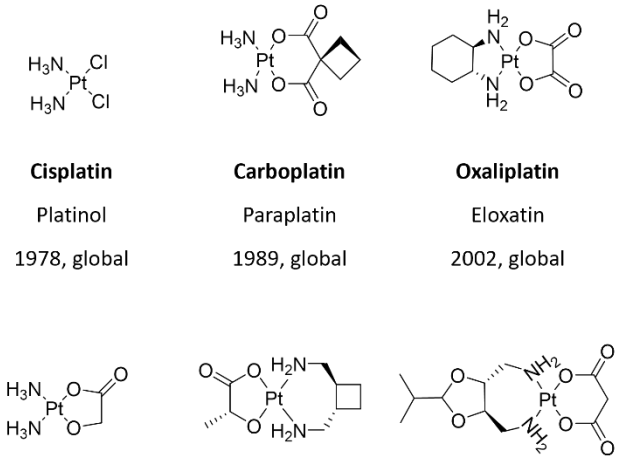

Generic Name	**Cisplatin**	**Carboplatin**	**Oxaliplatin**
Trade Name	Platinol	Paraplatin	Eloxatin
Approval	1978, global	1989, global	2002, global

Generic Name	**Nedaplatin**	**Lobaplatin**	**Heptaplatin**
Trade Name	Aqupla	-	SunPla
Approval	1995, Japan	2010, China	1999, Korea

Figure 1.4 Structures of the main used platinum drugs in cancer treatments, their generic and commercial name, and the year and approval area.

The mechanism of action of cisplatin and similar platinum drug is strongly related to its chemical structure. Cisplatin is a neutral square-planar Pt(II) compound with two ammine ligands in *cis* conformation, referred to as non-leaving groups, and two *cis* chlorine atoms as anionic ligands, termed as labile ligands. The soft Lewis acid nature of Pt(II) ion offers a suitable option to create thermodynamical stable bonds with N as donor atoms.

Cisplatin analogues usually bear two monodentate amino groups or one bidentate diamino ligand, with the other two square planar positions occupied by two labile ligands, constituting a neutral complex. The active molecule is formed when one or both labile ligands are replaced by water molecules. Thus, the anionic ligands must bind strong enough to avoid too fast water exchange and, consequently high reactivity with highly toxic effects. However, at the same time, these bonds must not be too strong to avoid inactive complexes.[44]

1.2.3 Mechanism of action of cisplatin

The mechanism of action of cisplatin is divided into four main steps: (i) cellular uptake, (ii) activation by aquation, (iii) DNA binding and, (iv) cell death caused after cellular progression of DNA lesions (**Scheme 1.2**).[39,46,47]

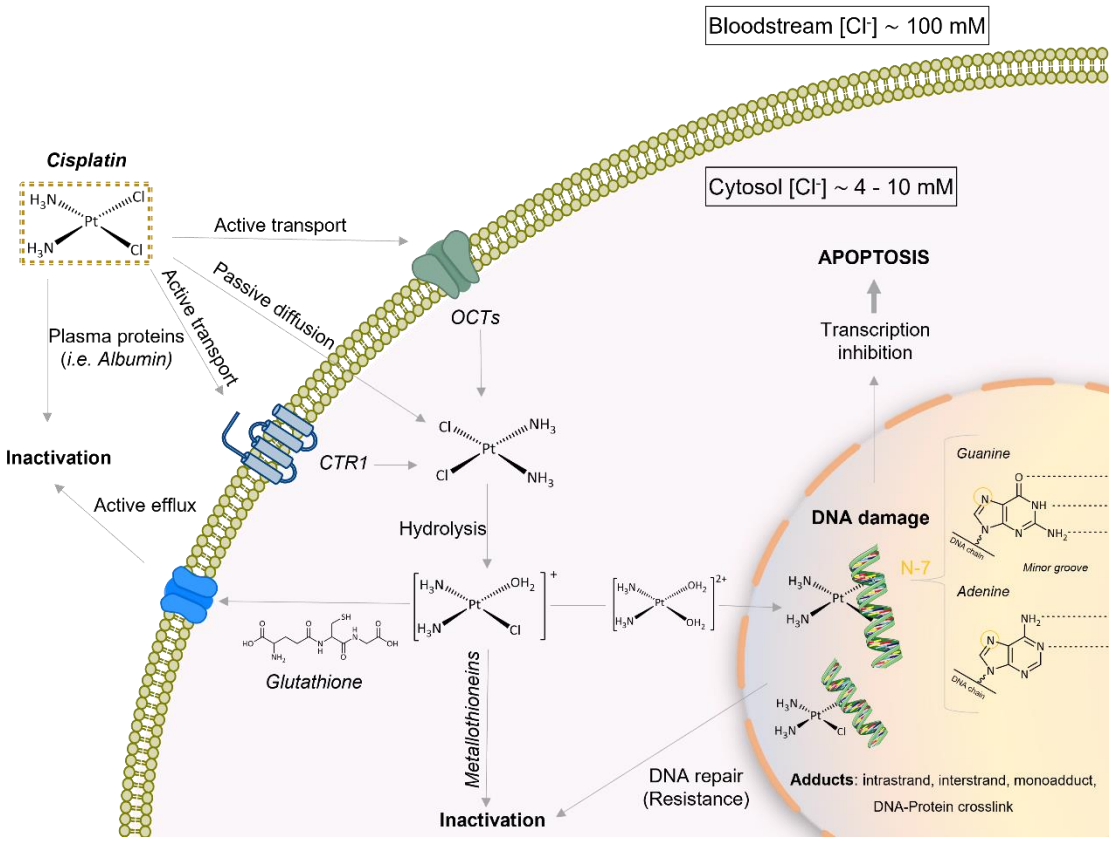

Scheme 1.2 Mechanism of action of cisplatin, showing intra- and extracellular events influencing cisplatin and leading to apoptosis or inactivation of the molecule.

Cells internalise cisplatin by two pathways: passive diffusion through the plasma membrane and by active transport by some membrane proteins.[48] Cisplatin uptake is proportional to the administrated concentration, which supports greater passive internalisation of cisplatin, related to its planar geometry and small size. Nonetheless, other studies pointed out that active transport by copper transporters is predominant. Even though cisplatin uptake must be explained by the combination of both, it is still unknown how these two pathways influence each other.[49–52]

Even before entering the cell, there exist pathways that can prevent platinum drugs to induce apoptosis. For instance, after intravenous administration, they may be kidnapped by bloodstream proteins. Among them, human serum albumin (HSA) is the most frequent and might interact with cisplatin after binding with cysteine and methionine residues, as well as with other thiols in the bloodstream.[53]

Once inside the cell, the square-planar geometry of cisplatin boosts its activation after the substitution of one or two chlorine ligands by water molecules, since in the cytoplasm the chlorine concentration is lower than in the bloodstream. The substitution of chlorines usually

takes up to 2 hours, what makes it different from other platinum-based drugs, *i.e.*, carboplatin or oxaliplatin, which possess more inert chelated ligands and the water exchange takes even up to months. Then, aquated species can enter the nucleus, and the negatively charged DNA attracts the positively charged species: *cis*-$[Pt(NH_3)_2Cl(H_2O)]^+$ or *cis*-$[PtCl_2(H_2O)_2]^{2+}$. Specially the monochlorido form, which is the most common, and is a potent electrophile. The coordinated water molecules are substituted by a heterocyclic DNA base. The binding takes place in the sites with more nucleophilic character in DNA, mainly in the N7 atoms residues of purine, but also in guanidine and adenine. The created adducts are moderately kinetical stable since the N ligands display a low *trans* effect. First, they are mainly monofunctional, but then the remaining chlorine ligand is substituted by a second residue and generates inter- or intrastrand cross-links.[38,39,44] Moreover, the presence in platinum drugs of NH_3, NH_2R or NHR_2 as non-leaving groups that can form hydrogen bonds with peripheral phosphates of DNA, contribute to the stabilisation of the drug-DNA adducts.[44]

The formation of adducts alters the DNA structure, inducing bending or unwinding of the double helix. The cell cycle of those with damaged DNA is detained in the G2 or M-phase. Then, the expression of pro-apoptotic proteins rises, motivating the release of cytochrome C and the activation of intracellular caspases, which are the proteases involved in the programmed cell death of cells or apoptosis. One of the main pathways that induce apoptosis after platinum lesions, is the inhibition of transcription by RNA polymerases.[38,39]

Nonetheless, cells attempt to repair the damage after cell cycle arrest by removing the platinated DNA. For instance, the homologous recombination pathway mediates the repair of double strands breaks. Or nucleotide excision repair, which excises the damaged section. When these mechanisms are enhanced resistance to cisplatin cells emerge.[54–56]

Inside the cell, metallothioneins are known to capture platinum complexes.[39,57] There, glutathione, an S-containing tripeptide involved in ROS homeostasis of cells, can deplete cisplatin by quenching the monofunctional DNA-adduct before a bifunctional adduct can be organised. Usually, cisplatin resistance cells show elevated glutathione concentrations. Moreover, the detoxification of cisplatin by glutathione increases the toxicity shown in kidney cells.[57–59]

The acquired mechanisms of resistance against drugs are usually due to mutations and epigenetic events that limit drugs' efficacy. Upon drug administration resistance may arise due

to several features, *i.e.* excess of a resistance factor, defective apoptotic pathways, reduced uptake, intracellular detoxification through the drug efflux pumps, decrease platinum-DNA binding, increased DNA damage repair, etc.[54,60–62] The tumour microenvironment is also involved in platinum-based drugs resistance: increased acidity and shear stress, the hypoxic conditions or the close organisation of the tumour nearby, cause decreased drug delivery.[60]

It has been proved that the accumulation of cisplatin in cells is strongly related to its high toxicity: the greater DNA adducts, the greater the cytotoxic effects. A cancer cell must be exposed to a toxic concentration of the drug during enough time to induce apoptosis, as anticancer drugs usually show steep dose-response curves. But tumour remission is mainly attained for fast-growing tumours where cytostatic agents alone or in combination therapy are most effective in killing the rapidly dividing tumour cells. Advanced tumours usually display multidrug resistance phenotypes, and their growing rates are lowered provoking poor response to chemotherapy.

For treating metastatic cancer, chemotherapy regimens are usually applied in combination with hormones or novel agents, which nowadays are considered the best option for hindering or reducing the size of the primary tumour and/or metastases. Whereas, it is basically palliative treatment and improvement in overall survival through the introduction of novel drugs has generally not been more than a few months.[32,63]

Pharmacology, more specifically pharmacokinetics, and pharmacodynamics are dedicated to the study of drugs upon administration and have become crucial for the determination of dosing, benefit, and side effects of any drug. Pharmacodynamics studies the biological activity of a dispensed drug, in other words, the effect and the body response towards it. Whereas, pharmacokinetics studies the fate of an administrated drug in the body after its administration, with special attention on their adsorption and distribution, until body excretion.[64,65]

Pharmacokinetics must be considered an important aspect for the development of new drugs that will end up in pre-clinical and clinical assays. Aside from low selectivity and specificity, the most critical limitation of chemotherapeutic agents is the poor cellular uptake as a result of the inability of most drugs to cross the cell membrane. In addition, the heterogeneity due to the vascularisation, and the necrotic and hypoxic areas of the tumours mean that they may have little response to anticancer drugs.[32]

1.2.4 Side effects of platinum-based drugs

All cancer treatments present side effects in patients primarily due to the toxicity of chemotherapeutic agents towards normal cells. Chemotherapeutic drugs cannot distinguish between cancer and normal cells, and this low selectivity is the main responsible for the undesirable side effects. To date, drugs used in conventional chemotherapy exhibit a minor selective uptake in tumour tissue, and generally, only a very small fraction of the administered dose reaches the tumour. Frequently, a low molecular weight of common agents is responsible for the rapid diffuse into healthy tissues and the fast clearance from the circulatory system.[66,67]

Drugs are taken by growing cells, which means that cancer cells (with abnormal growth), but also fast-growing tissues will have a high uptake, and consequently, will have to deal with off-site toxicity. Mucous membranes, stomach, intestines but also bone narrows or hair follicles are fast-growing tissues that are usually damaged in the treatments, with the resultant side effects (**Table 1.1**).[47,68,69]

Table 1.1 Platinum-based chemotherapy most relevant side effects and its clinical.

Damaged tissue	Related side-effect	Clinical profile
Mouth, throat, stomach, and intestines mucous membranes	Gastrointestinal toxicity	Weight loss, nausea, and vomiting
Bone narrow	Reduced white and red cells production	Depression of the immune system. Dizziness, tiredness, lethargy, prompt to infections and increase of body temperature
Hair follicles	Alopecia	Body hair loss
Ear follicles	Ototoxicity	Hearing loss and disequilibrium
Kidney (due to drug excretion)	Nephrotoxicity	Renal dysfunction up to failure
Liver (due to drug detoxication)	Hepatoxicity	Liver damage
Nervous system	Neurotoxicity	Weakness, loss of vision, memory, and intellect

The side effects of all platinum-based drugs are comparable. The administered dose depends on several factors such as the specific drug, the concentration of certain biomolecules or the patient body mass. The amount of drug administered before the side effects experienced by the patient are too severe to prevent dose increment is known as a dose-limiting toxicity and is different for each platinum drug. Generally, the most active is a drug, the most side effects it presents. This is linked to their chemical reactivity and translated into hydrolysis rates

because drugs with highly labile leaving groups increase the capacity of platinum to bind biomolecules in the body. To prevent side effects, the aquation process must be reduced during administration and penetration, and ideally before the targeting tissue is reached. For that purpose, each platinum drug is administrated in the corresponding formulation to avoid prompt aquation. For instance, cisplatin is formulated in a saline solution (0.9% NaCl), while carboplatin and oxaliplatin are administrated in a 5% glucose solution.[35,47,68]

Fortunately, the killing effect of chemotherapeutic agents has a definite selectivity for cancer cells over normal cells. Normal tissues can repair themselves and continue to grow, so the injury caused by chemotherapy is rarely permanent.[70]

To overcome limitations of conventional chemotherapeutic agents, advance in cancer treatment is a much-need. To minimise some of the side effects related to these therapies, and to defeat cells acquired resistance mechanisms over platinum-based treatments, improved administration and delivery are meaningfully investigated.[68] Likewise, a better understanding of the biochemical and physiological characteristics of cancer, as well as the advances in analytical and diagnosis tools, is a sweeping glance for oncology treatment. Several strategies, comprehending activatable platinum pro-drugs, targeted drugs or nano-delivery systems are pursued as the next generation of platinum drugs.[38,39,47,71–73]

1.3 Drug delivery systems

Due to their physicochemical properties, nanomaterials have become a breakthrough in the biomedical field with applications ranging from imaging to regenerative medicine.[74] Properties such as size, shape, chemo-physical and optoelectronics, along with their tailoring and tuneability, convert materials in the nano-scale in suitable vehicles for drug delivery. Thus, a wide range of nanoscale compounds based on synthetic polymers, proteins, lipids, and organic or inorganic particles have been employed as drug delivery systems (DDS) (**Scheme 1.3**).[75–77]

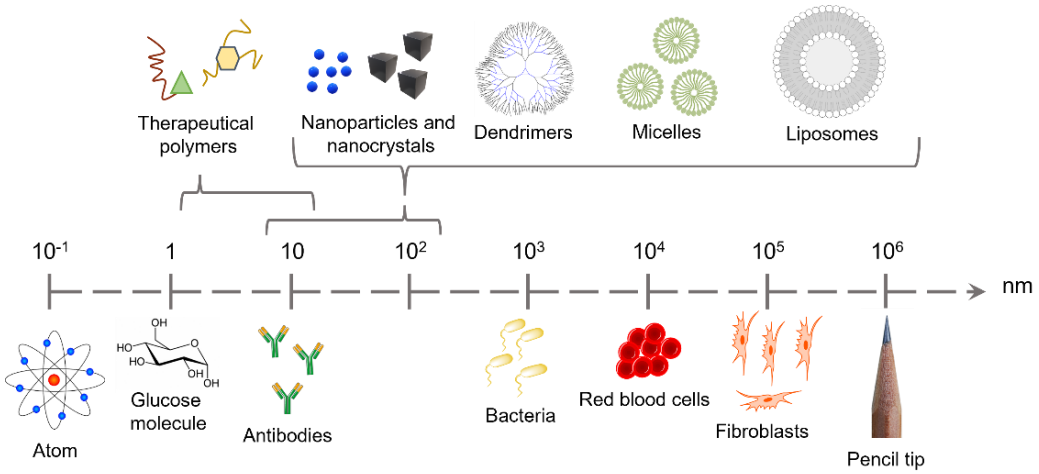

Scheme 1.3 Representation of some DDS (top) and their size comparison (down).

The small size is the major advantages of nano-carriers because allow them to circulate through the body without disrupting the bloodstream. Moreover, their characteristic surface area to volume ratio efficiently allows to carry drugs and biomolecules such as DNA, RNA, proteins, along with imaging agents.[74,78]

The use of DDS is a potential approach to significantly improve the pharmacokinetics of drugs, by enhancing solubilisation and protecting the drug from degradation and inactivation and thus, allowing longer circulation times.[66,77]

Likewise, drug encapsulation in targeted DDS facilitates the cell uptake of therapeutic agents at the desired site of action, particularly when the parent-free drug shows poor biodistribution or significant off-site toxicities. Two types of targeting are described in nano-carries: passive and active targeting.

The passive targeting mechanism is related to their small size and implies the accumulation at tumour sites by the so-called Enhanced Permeability and Retention (EPR) effect. In consequence of angiogenesis in cancer (section 1.1.4), tumours show vast and disorganised vascularity and defective lymphatic function. The abnormal vascularity favours drugs up to 200 nm to penetrate the tumour endothelia and the extravasation into the tumour, while penetration through healthy vasculature is limited to species smaller than 2 nm in size. Besides, the nano-sized drug is accumulated in the tumour interstitium, as the rediffusion to circulation is hindered for molecules bigger than 4 nm.[79–82]

On the other hand, active targeting (or ligand mediated-targeting) refers to the surface attachment of biomolecules that will bind to the overexpressed receptor on a diseased organ,

tissues, or cells.[79,83,84] For example, cancer cells excessively express a high number of receptors, *i.e.*, folate receptors are overexpressed in more than 93% of ovarian carcinomas.[85,86]

All the mentioned characteristics result in enhanced therapeutic in front of the raw drug. However, several concerns, such as the lack of specific guidance, hamper the regulation and approval of new DDS. Likewise, they are considered for some countries as medical devices, generating regulatory standard gaps regarding its classification.[87]

The distinctive pharmacodynamics and pharmacokinetic displayed for DDS is, as well, one of the most complicated steps into the drug regulation, since the available data of the bulk material does not represent the safety and efficacy of the analogue nanomedicine. What is more, the physicochemical characteristics of DDS are altered in physiological environments.[88] As an example, proteins corona are reported to cover nanomedicines right after injection in the bloodstream, and so the estimated size of the nano-system will differ in the physiological environment right after drug administration. Nano-drugs are typically administered intravenously or orally, and less frequently transdermally.[77,89]

Further, testing nanotoxicity and assessing the preclinical safety data is a challenge, as nanomaterial properties may disrupt results from *in vitro* and *in vivo* assays.[90] Besides, the translation of nanomedicines into clinical is sometimes obstructed by the complexity of manufacturing nanomedicines with high stability, reproducibility upon batches, and in sterile conditions.[91,92]

Even regulation and clinical translation impediments, in 2020, over 50 nanomedicines and nanotechnology-based medical products were approved by the FDA and EMA. Additionally, around 100 nano-based products are estimated to be in clinical trials.[91,93,89] Reported by M. Germain *et al.*, from the 409 clinical trials ongoing between 2008 and 2020, 65% of them were related to cancer applications (therapy and diagnosis). In May 2020, a part from cancer therapy, vaccines, pain treatment, infectious diseases, and imaging represent the current clinical indications in ongoing trials.[93]

Over the past decades, a vast number of nano-materials and devices have been under clinical development. However, the number of approved and yet commercial nano-medicines is still small when compared to traditional drugs.[94]

DDS devoted to cancer are considered the main use in nano-carriers, including encompassing diagnosis, therapy or theragnostic applications. The most notorious advantages of DDS in oncology coincide with the main benefits of DDS.[68,95] Altogether, compared with the direct administration of chemo-drugs, DDS lead to the reduction of side effects in cancer treatments, improving the quality of life of patients during the treatment.[93,96,97]

Related to platinum-based DDS, several strategies to delivery cisplatin or Pt(II) molecules have been developed over the years and are exemplified in numerous publications. [39,45] Some examples are cited hereunder.

The work undertaken by Sadler, published in 1998, based on albumin-based NPs took advantage of the natural binding affinity between albumin and cisplatin[98] Some cytostatic activity was maintained even the irreversible binding between the protein and cisplatin while the renal excretion was importantly reduced.

Chen *et al.* prepared poly-(lactic-co-glycolic acid) NPs containing Pt(II) and catalase, that delivered O_2 and drug as a response to H_2O_2 in cells avoiding hypoxia-induced resistance.[99]

Another strategy developed by Binaul *et al.* is based on the degradation of linkages between a polymer backbone and Pt(II) amine ligands based drugs.[100] Their pH-responsive micellar systems accelerate the drug release and targeting because of the acidic extracellular microenvironment of tumour cells.

In the period 2008 to 2020, among the DDS liposomal formulations stand out with more than 50% of ongoing trials linked to them. Interestingly, in May 2020 at least 3 trials started on vaccines for COVID-19 were based on lipidic nanomedicines.[93]

1.4 Liposomes

Liposomes were first described by Dr. Alec D. Bangham during the 1960s when demonstrated that phospholipids in the presence of water adopt a spherical shape.[101–103] When testing a new electronic microscope, the observation of ovolecitin showed the presence of self-closed ordered structures, like cell membranes. This observation enterprise the study of cells using liposomes as models.[104]

1.4.1 Structural units

Lipids are the structural units in liposomes. They are classified after several characteristics, but a subclassification based on their chemical structure categorises them into simple and complex

lipids. Simple lipids are composed of C, O and N. Triacylglycerols, commonly known as grease or oil, are an example of simple lipids. Complex lipids incorporate other elements in their structure. We can distinguish between phospholipids, sphingolipids, and glycolipids.[105]

Phospholipids are a key component of cell membranes. Structurally, phospholipids are constituted by a phosphate group, an alcohol residue, a glycerol group and saturated or unsaturated fatty acids. The phosphate group, a diester, binds the molecule to the fatty acid and at the other extreme is connected to other residues (**Scheme 1.4**). This organisation confers the characteristic amphiphilic nature, being lipids soluble in organic solvents, such as chloroform or methanol, but insoluble in water.[106]

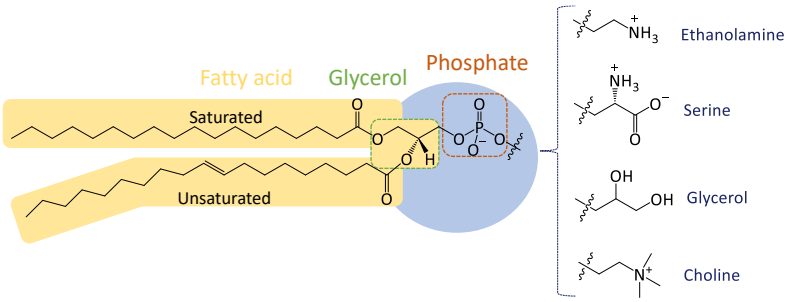

Scheme 1.4 General composition and chemical structure of naturally occurring phospholipids.

The addition of a group to the phosphate, with molecules like choline, ethanolamine, or serine, known as head groups, gives rise to the final phospholipid's structures. They are produced industrially by natural or synthetic methods. The most common sources of natural phospholipids are soybean, rapeseed and chicken egg yolk.[107]

The lipid head-groups of natural phospholipids can be either zwitterionic or negatively charged. Phosphatidylcholine (PC) and phosphatidylethanolamine (PE) are examples of zwitterionic lipids. As negative charged, phosphatidic acid, phosphatidylserine, and phosphatidylglycerol are the most common lipids. Positively charged phospholipids are synthetically produce and usually do not contain a glycerol backbone. Some examples of the later are *N*-(1-(2,3-dioleoyloxy)propyl)-*N*,*N*,*N*-trimethylammonium (DOTAP) and *N*-(1-(2,3-dioleyloxy) propyl)-*N*,*N*,*N*-trimethylammonium chloride (DOTMA).[107,108]

As amphiphilic molecules, in water, phospholipids self-organise in aggregates with their polar heads interacting with the aqueous phase and the hydrophobic tails pointing toward the centre, so minimising the non-polar tail contact with the solvent. They are also designed as

tensioactive or surfactant molecules because they decrease the surface tension between two interphases.

Other typical amphiphiles are classified after their structure, based on the number and kind of connection of polar heads to hydrophobic tails. There are amphiphiles with double chains and one polar head, gemini amphiphiles with two chains and two polar heads linked by a spacer, or bolaamphiphiles, which possess two polar heads connected to one alkyl chain, among others (**Figure 1.5**).[109–111]

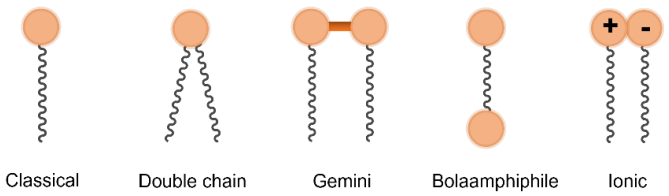

Figure 1.5 Illustration of types of amphiphiles.

1.4.2 Organisation

Amphiphilic molecules can form supramolecular assemblies, such as bilayered vesicles, micelles or reversed micelles, to keep thermodynamically or kinetically stable conditions.[112] Within them, when referring to lipids, liposomes are the most significant assembly.

Liposomes are closed spherical vesicles made up of an aqueous core encircled by one or more concentrical bilayers. The formation of liposomes requires the application of external energy to the system. The preferred packaging is dictated by the shape of the amphiphilic molecule, which acquires the best organisation for minimising repulsions in the given solvent. Still, they can be also influenced by the lipid concentration, pH and temperature.[113]

The geometrical shape is quantified by the 'critical packing parameter' (*p*) which is described by the formula in **Figure 1.6**.

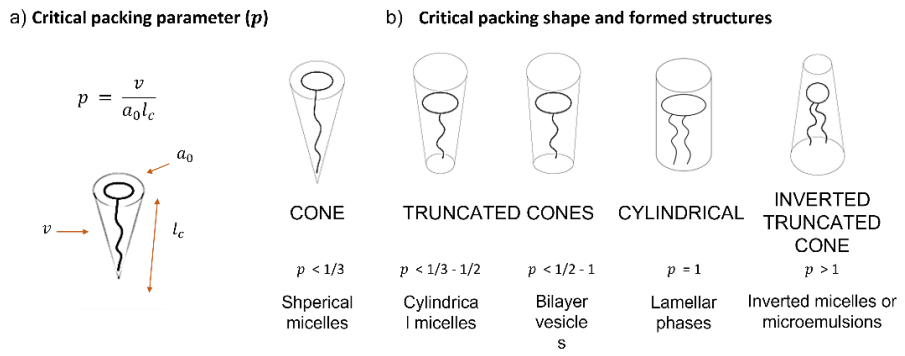

Figure 1.6 (a) The formula describing the critical packing parameter for lipids organisation in water. (b) Different shapes showed by phospholipids and the formed structure.

For *p* values below 1/3, amphiphilic molecules form spherical micelles; cylindrical micelles are formed when *p* values are between 1/3 and 1/2. Double-chain lipids with large head region, form bilayered vesicles. Whereas an increase in the ratio of polar area to tail region supports the formation of planar bilayers or inverted micelles.[114,115]

Virtually, all the lipids possess a truncated cone structure as their polar head groups are big respect to their hydrophilic tails. Hence, their preferred organisation in water is the formation of bilayered vesicles, known as liposomes.[112,113,116,117]

1.4.3 Energy in liposomes formation and size classification

About a certain concentration, referred to as critical micelle concentration (CMC) or critical aggregation concentration (CAC), amphiphilic molecules aggregate. Energetic contributions influence the entire vesicle formation process, as well as the final size distribution.

In liposomes' formation, when amphiphilic molecules start to rearrange, the vesiculation process begins. A disk-like bilayer is initially formed, and its energy increases with the perimeter of the disk (edge energy). Then, to minimise the energy, the planar bilayer tends to bend until the edges merge and form a self-close spherical vesicle. At the bending process, the total energy of the system increases until the vesicle is formed, when the total energy decreases. During this process, there are destabilising forces such as hydrodynamic forces that can lead to the breakdown of the bilayer and consequently to the production of smaller vesicles. On the contrary, the patch can also grow because of the addition of phospholipids or other patches.

The size of the liposomes is highly dependent on the kinetics of membrane size growth. Even though, there is a critical membrane size, distinct for each phospholipid, below which the liposomes formation is energetically unfavourable.[118–120] The self-closed structure organisation is enhanced by the formation of hydrogen bonding, Van de Waals forces and other electrostatic interactions.

Different types of lipid vesicles (liposomes), depending on the number of lamellae or size, can be generated. They are enumerated thereupon and illustrated in **Figure 1.7**.[121–123]

- Unilamellar vesicles (UV): a single lipid bilayer creating one inner aqueous centre.
    - Small unilamellar vesicles (SUV) for 20-100 nm vesicles' sizes.
    - Large unilamellar vesicles (LUV) when are larger than 100 nm.
    - Giant unilamellar vesicles (GUV) when overcoming 1000 nm dimensions.
- Multilamellar vesicles: concentric liposomes in their interior.
    - Multilamellar large vesicles (MLV) containing more than five lamellae.
    - Oligolamellar vesicles (OLV) for onion structured bilayers up to five concentric lamellae.
- Multivesicular vesicles (MVV): smaller liposomes enclosed in the internal aqueous phase of a large vesicle.

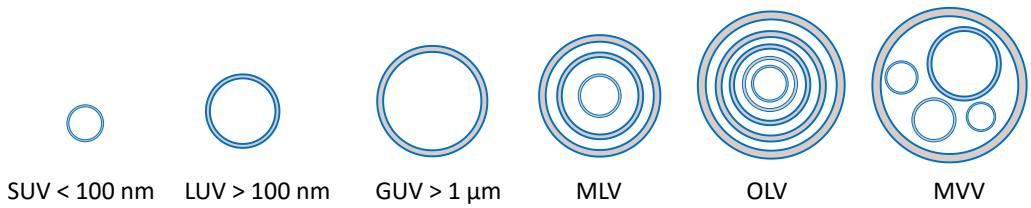

Figure 1.7 Graphical representation of liposomes classification after their lamellarity and size.

The preparation of liposomes presents several steps, starting from the phospholipids solubilised in an organic solvent. When the solvent is removed by evaporation, phospholipids rearrange to form a stack of bilayers. The stack of bilayers is hydrated and then the bilayers slowly separate. Depending on how fast this process occurs, mainly multilamellar vesicles (MLV) or unilamellar vesicles (UV) are formed. A high shear flow causes slow bilayers separation and, if the bilayers edges merge in a faster rate, MLVs are obtained. While, the absence of shear flow or the application of electric fields, causes fast bilayer separation obtaining UV.[124]

1.4.4 Main transition temperature of lipids

Another important characteristic of phospholipids is the phase transition. Lipids can ensue several phases depending on the temperature of the medium, being the most important the main transition temperature (T_m).[121] Below the T_m the lipid exhibits the so-called gel phase (or "solid" phase), which shows a well-packed and rigid bilayer. Above the T_m the liquid-crystalline phase (or "fluid" phase) is found, characterised by a disordered organisation of the acyl chains (**Figure 1.8**).[125]

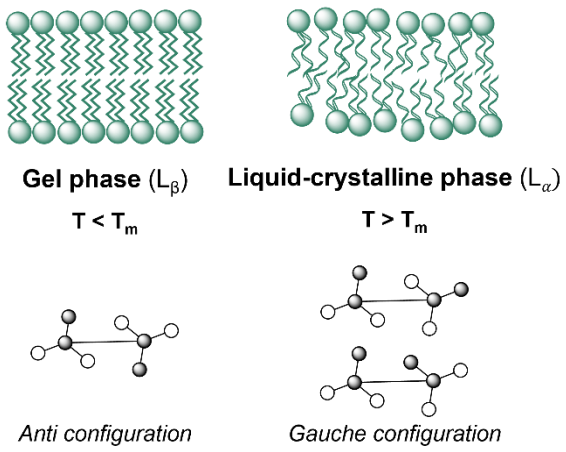

Figure 1.8 Representation of the lipid organisation below and above the phase transition temperature (T_m) in a two-dimensional lipid bilayer.

The order of both phases is related to the conformation taken by the hydrocarbon chains in the lipidic units. Below the T_m, the hydrophobic chains are in extended staggered configuration, while above the T_m, they display a high number of *gauche* configurations, resulting in the gel or liquid phase, respectively (**Figure 1.8**). In consequence, the bilayer thickness is maximal in the gel phase, where the surface area per lipid in contact with water is minimal. In the liquid phase, as the surface area per lipid is higher, the bilayer thickness is decreased. T_m values are higher for longer hydrocarbon linear chains and they decrease as a function of the extent of unsaturation.[113,126]

1.4.5 General procedures in the production of liposomes

1.4.5.1 Methods for liposomes preparation

There are multiple methods for the preparation of liposomes and the choice of the method will rely on the needed final properties of them. In general, methods for liposomes preparation involve four main simple steps: the solubilisation of the lipids in an organic solvent, the drying of the organic solvent, followed by the dispersion in aqueous media, and finally the purification

of the resulting preparation. The most common and oldest method is the Thin Lipid method, also known as Bangham method (**Scheme 1.5**). In this method, lipids are stacked on a flask wall after the evaporation of the organic solvent in which they were solved. Then, water or buffer solution is added and consequently, the lipids slough off and swell under vigorous stirring. Obtaining a quality thin film affects the final liposome size and size distribution: the organic solvent must be completely removed; however, it is important to avoid the boiling of the solvent, which would generate irregular lipid dry films. Other features, such as the stirring speed, the flask and the aqueous dispersion media will influence the final liposomes. With this methodology, mainly MLVs are formed but they can be reduced to LUVs or SUVs using mechanical forces such as sonication or extrusion. The limitations of the method include poor entrapment capability, non-scalability, heterogenous size and the need for a reduction size step.[122,127,128]

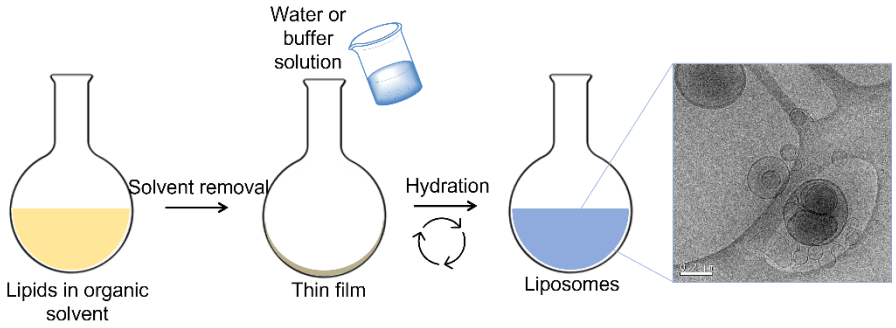

Scheme 1.5 Representation of the main steps for liposome preparation by the Thin Lipid method: addition of lipids solved in organic solution, evaporation of the organic solution to obtain a thin film and hydration and agitation to obtain liposomes.

Since small sized liposomes are indispensable for drug delivery purposes, two main protocols are used to transform them into homogenous SUV: extrusion or sonication. During extrusion process, the liposomal suspension is forced to go through polycarbonate membrane filters with predetermined pore sizes. Extrusion renders low size distribution, which depends on the lipid composition and is mandatory to be conducted above the T_m temperature of the lipid to facilitate the pass through and improve the encapsulation efficiency of drug, if present. Nonetheless, small hydrophilic drugs may show reduced drug loading efficiency because the resultant SUV have a minor aqueous core. When employing mild sonication, random fragmentations of the phospholipid bilayer arise, which tend to self-close to produce thermodynamically stable liposomes. Nevertheless, the reproducibility of sonication is

relatively low since it is dependent on several factors such as time, power, composition or concentration, impacting on the mean size.[129,130]

Other common techniques for liposome preparation are the ethanol injection[131], in which an ethanolic solution containing lipids and drug is injected into the aqueous phase, or the emulsion method that employs intermediates water in oil and double emulsions to subsequently evaporate the organic solvent and obtain the final liposomes. The heating method and reverse-phase evaporation are other significant methods of liposome preparation. Supercritical-assisted methods take advantage of supercritical fluids properties and are used at large scale productions.[128] Besides, more recent methodologies rely on the use of microfluidics that allows higher control over the process increasing reproducibility, homogeneity, and assets the fast preparation of liposomes. Examples of methodologies include pulsed jetting, emulsion templating, transient membrane ejection and ice droplet hydration, among others.[120,127,132,133]

1.4.5.2 Liposome's characterisation

It is noteworthy that the features of liposomes are deeply reliant on properties such as size, lamellarity or surface charge. Hence, a precise characterisation of the properties of the produced liposomes is crucial. In this section the most common techniques for this purpose are mentioned.

Dynamic Light Scattering (DLS) provides quick information about the mean size, the size distribution, and the homogeneity of the population (polydispersity index, PDI) by measuring the fluctuations of the light scattered by the vesicles. Besides, evidence about the stability of the liposomes can be also obtained from DLS measurements.[134,135] Size exclusion chromatography (SEC) separates liposomes by their hydrodynamic size, allowing the determination of the molecular mass. Besides, SEC is also used as purification step, since it allows the separation of salts or non-encapsulated drug.[136]

Information about the morphology of the liposomes, mainly shape and lamellarity, can be visually obtained by means of electron microscopy techniques: being transition electron microscopy (TEM) the most used. Nonetheless, to analyse liposomes in their native state, samples are usually cryogenised. It allows the observation of liposomes avoiding other processes such as chemical fixation, dehydration, or staining, which affect the liposomes' morphology of the liposomes. However, in the cryogenisation process, care must be taken in

case artefacts occur due to the generation of thin films of amorphous ice in the grid.[137] Lamellarity can be also determined by nuclear magnetic resonance (NMR), usually ^{31}P-NMR, and electron paramagnetic resonance (EPR), but they have not been intended in this thesis. Furthermore, small-angle X-ray scattering (SAXS) is a powerful technique to obtain information about bilayer characteristics such as the lamellarity.[120]

The main transition occurring between the liquid and crystalline phase of phospholipids, T_m, is typically measured by means of differential scanning calorimetry (DSC). The T_m is determined in the calorimetry when the sample shows the higher heat capacity at constant pressure, further, the enthalpy of the transition can be also calculated.[138] However, several limitations are faced with lipids that present a T_m below 0 °C. Hence, DSC allows to study the phase T_m when additives or drugs are included in the formulation, since they will modify the order of the lipidic structure.

The surface charge of liposomes will depend on the type of lipids used and will predict the stability of the colloidal solution. For instance, the surface of the liposomes surface will be neutral when zwitterionic phospholipids as lecithin are employed, however it may change when a drug is added. The surface charge can be determined by measuring a parameter call Zeta potential (ZP). It corresponds to the potential at the slipping plane of a particle moving under an electric field, which can be performed by microelectrophoresis in a modified DLS instrument.[128,134]

The bilayer fluidity impacts the permeability and stability of the liposomes, driven by the freedom of movement of the alkyl chains in the phospholipids. For example, the addition of cholesterol avoids crystallisation and influences the bilayer fluidity. Thus, it is extremely important to examine the addition of a constituent. Anisotropy fluorescence allows the determination of the rigidity of the lipidic bilayer: in this technique, a fluorescence probe is added, and its rotational mobility and orientation shift are measured when excited with polarised light. It provides information about the order in the hydrocarbon chain, which can be extended to the perturbation of the probe caused by drug molecules. The most common probe is 1,6-diphenyl-1,3,5-hexatriene (DPH) that locates in the bilayer region.[139,140]

1.4.6 Liposomes as drug delivery systems

Liposomes were first proposed as DDS in the 1970s. As bilayer structures, they can incorporate drugs in both, their inner aqueous phase and within the bilayer. This means that they can

contain hydrophobic molecules in the lipid layer, or/and hydrophilic molecules in the aqueous region. This capacity of internalising a vast type of molecules, along with several properties such as their high biocompatibility, biodegradability, non-immunogenicity or versatility, convert liposomes into ideal DDS.[95,122,141,142]

Liposomes are usually 90 to 150 nm in diameter, thus, are slightly larger than DDS counterparts such as NPs. Also, they overcome one of the main drawbacks of conventional DDS, which is the removal of non-biodegradable residues that can cause toxicity.[83]

Based on their composition, liposomes can be classified as conventional, long-circulating, cationic, stimuli-sensitive or immunoliposomes, among others. Their corresponding drug encapsulation, as well as vectorisation approaches, are depicted in **Figure 1.9**.

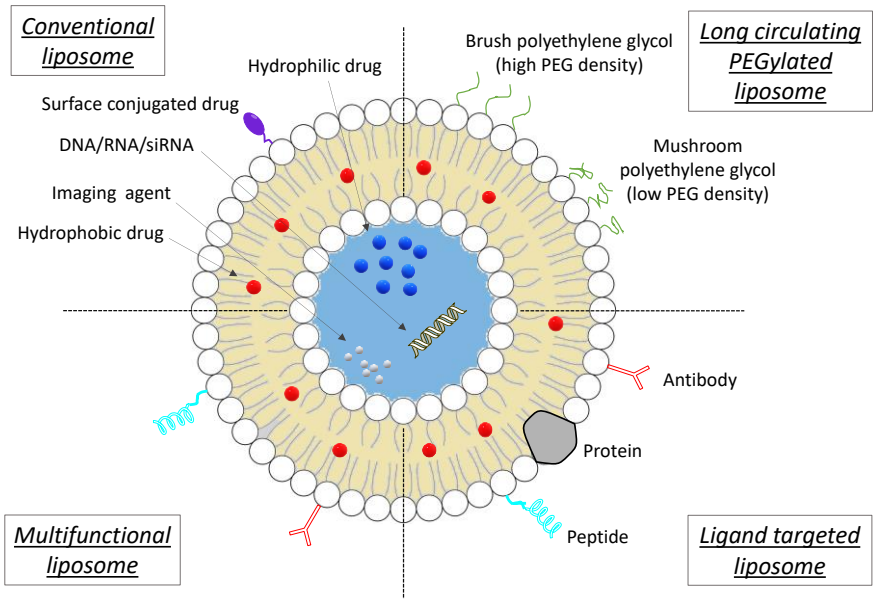

Figure 1.9 Graphical representation of liposome versatility as DDS, showing the encapsulation and incorporation of several molecules, and their possible surface modification.

Nonetheless, liposomes face several issues: they tend to have short half-life, some phospholipids can undergo oxidation and hydrolysis reactions, as well as, drug leakage or low stabilities.[122] To overcome some of these limitations, several strategies and approaches have been applied during the last decades, evidenced by the evolution from the so-called first-generation of nanovectors to the second and third-generation. The action of the first-generation type relies in their accumulation related to size, while the second-generation, with a high degree of complexity, is related to specific recognition of affected tissues. Among the second-generation, prime examples are immunoliposomes or thermosensitive liposomes.[108]

As previously indicated, the characteristic main transition of phospholipids, T_m is crucial for the final properties of the liposomes. The permeability of liposomes is higher when the bilayer is in the liquid-crystalline state than at the gel phase. Thus, the bilayer is more permeable to water, which may enhance the drug encapsulation. Nevertheless, in the liquid phase, liposomes are also leakier structures, which may prevent the drug to reach the site of action inside the body.[121,125] Besides, liposomes prepared with lipids showing a low degree of unsaturation generate a more rigid and less permeable bilayer due to the strong hydrophobic interactions between fatty acid tails.[143]

As reviewed, the choice of the phospholipid for liposomes fabrication stains the final characteristics of the system. However, physicochemical characteristics can be modulated by the addition of different molecules to the formulation, such as other lipids, non-ionic surfactants, etc.[144,145]

An important additive, extensively used in liposomes formulation, is cholesterol. Even though it does not form aggregates by itself, cholesterol helps to stabilise liposomes. Natural rotational freedom of lipids promotes leakiness of cargo molecules, but cholesterol enhances lipids organisation reducing the membrane permeability. Cholesterol fits between the alkyl chains of the lipids, generating packaging disorder, but the stabilisation effect of cholesterol on lipid membranes arise from the increase in the cohesion of lipids and the promotion of the liquid-ordered phase.[113] Cholesterol could be incorporated up to 50% in the membranes. [121,138,146,147]

The use of lipid mixtures is common in liposome formulation that may result in the formation of domains enriched with one of the lipids.

Regarding the liposome's surface charge, it may determine the final application of the liposome. Highly charged liposomes are more stable upon aggregation and coalescence in storage conditions because their surface exhibits electrostatic repulsion.[146]

Also, there is electrostatic attraction between cationic liposomes and negatively charged cell membranes, which may increase cell-liposomes interaction and internalisation after cell charge-sensitive binding and endocytosis by certain type of cells.[148] Nevertheless, the extent of cationic liposomes can be critical: liposomes with 5 - 10% of cationic lipid can reduce the interaction between plasma and liposomes, but higher proportions could induce macroscopic agglomerates and/or be toxic for cells. Interestingly, cationic liposomes are suitable for electrostatic RNA loading.[149–151]

To prolong their circulation time, the liposomal surfaces can be stabilised by the addition of a steric hindrance layer (Stealth liposomes). This is the case of polyethylene glycol (PEG) chains that prevent the rapid clearance of circulation by the reticuloendothelial system (RES) and has shown to greatly increase blood circulation times. Interestingly the addition of PEG is reported to inhibit the adhesion of liposomes to macrophages.[149,152] Though, during the last years, rapid clearance of PEGylated liposomes has been reported after repeated administration, because of the production of antibodies towards the components of the nanocarriers.[153,154]

The cargo release profile of liposomes is highly affected by their composition.[155,156] Reviewed by Cipolla *et al.* surfactants usually used to liposomes' solubilisation can be used to alter their encapsulation and release properties.[157]

1.4.7 Liposomes for cancer treatments and platinum-loaded liposomes

Various DDS have been developed to overcome the shortcomings of platinum-based chemotherapy and increase its efficacy developing novel structures and strategies. Thus far, liposome formulated drugs are documented to be one of the most successful commercial DDS. Liposomal formulations can be modified to match the pharmacokinetic profile of encapsulated drugs along with size and charge properties. Moreover, targeted delivery, as portrayed in section 1.3, can take advantage of liposomal formulation's sizes for passive targeting, and of surface decoration for active targeting.

Therefore, one of the crucial research areas in oncology is the development of novel platinum analogues drugs and engineer novel platinum drug formulations to enhance therapeutic efficiency. Such efforts have led to the development of platinum analogues. In fact, in 2016, six types of liposomal platinum anticancer drugs reached clinical trials. A few of them are cited hereunder.[158,159]

Doxorubicin encapsulation in PEGylated liposomes was the first liposomal drug carrier to reach cancer patients. Doxil®, the liposomal formulation of doxorubicin approved by the FDA in 1995, increases the circulating time up to 100 times and enhances drug availability with reduced adverse effects in comparison to the free drug.[32,83]

Lipoplatin™ contains cisplatin loaded liposomes with a size around 110 nm. The lipidic bilayer is constituted of a mixture of SPC, DPPG, cholesterol and PEG-DSPE. Its presence in tumour tissues improved *vs* the parent drug, solubility was enhanced, as well as the circulation time, which increased per three. In pre-clinical trials it was seen that the accumulation in solid

tumours was 200-fold higher than in adjacent normal tissues. Moreover, in combination with other drugs, *i.e.*, paclitaxel, the efficacy of treatment was comparable or even better than for cisplatin but with fewer systemic toxicities. The product has been launched as Lipoplatin™ for the treatment of pancreatic cancer and as Nanoplatin™ for the treatment of lung cancer. [160]

Similarly, SPI-077, with cisplatin entrapped in neutral liposomes sterically stabilized for long circulation, showed a huge half-life in mice (around 16 h *vs* 0.24 showed for cisplatin) and lower kidney accumulation. However, despite their improved pharmacokinetics, the cytotoxic activity did not show improvements with respect to cisplatin. In clinical trials, SPI-077 showed low therapy efficacy, related to the slow release of cisplatin, and was then halted from clinical trials. Comparably, a similar formulation named LiPlaCis was removed from clinical trials but also in this case cisplatin was almost unable to be released and cross the cellular membrane, leading to severe toxicity in Phase I trials.[161–163]

Other platinum-based drugs, such as Oxaliplatin has been encapsulated inside liposomes with the trade name Lipoxal. In this case, the cellular uptake of the complex was improved in this formulation. An Oxaliplatin derivative was also internalised in liposomes to form Aroplatin, which was the first liposomal formulation loading a cisplatin derivative reaching the clinic. Following the same trend, MBP-426 is a lipidic formulation of oxaliplatin that includes transferrin, as transferrin receptors are overexpressed in certain types of cancer cells. The formulation did not show prolonged retention times in the bloodstream but in tumours. It was more effective in suppression factor growth than their parental free drug and reached Phase II in clinical trials.[158,163,164]

In 2020, El-Shafie *et al.* reported the loading of nedaplatin (approved exclusively in Japan) in a PEGylated liposomal formulation. It resulted in higher activity against human non-small cell lung cancer cell line (A549) and human osteosarcoma cell line (U2OS) than the free drug, with more tolerable side effects profile.[165]

The progress of liposomes, from which drug release can be actively triggered, is therefore of key importance. Since, they can contribute to maximizing the potential of platinum-based formulations, guiding liposomal drug delivery technologies to wide clinical applications in the treatment against cancer.[166,167]

1.5 Metallosurfactants

As already mentioned, a tensioactive or surfactant is a molecule that lowers the surface tension between two interphases. The addition of d- or f-block metal ions in a surfactant emerges as a little explored area where both, the amphiphilic behaviour and the metal activity are gathered in a single molecule. Nonetheless, as reviewed by Polarz *et al*. the preparation of surfactants with inorganic constituents can be arduous due to the need of synthesising no symmetric molecules with pronounced distinct polarities.[168]

Structures of ordinary surfactants provide them sparse chemical reactivity; in fact, they are commonly known to exhibit certain inertness. But the synthesis of a metallic complex with surfactant properties, hereinafter referred to as metallosurfactant (MTS), provides a tool to include the singular metal properties in the interfaces, fostered by the surfactant moieties. These hybrid molecules have attracted researchers for at least the last three decades. Driven by their innate interdisciplinarity, the development of MTS has encompassed a vast number of examples and applications: magnetic resonance imaging,[169–173] optoelectronics components,[174–176] mesoporous materials,[177–179] homogeneous catalysis,[180–185] nanomaterials scaffolds or precursors,[186] to biomedical applications[187] such as antiparasitic treatments,[188–190] or antimicrobial.[191,192]

1.5.1 Metallosurfactants classification based on the type of ligand

1.5.1.1 Metallosurfactants constituted by non-tensioactive ligands

A great number of MTS described in the bibliography are constituted by non-tensioactive ligands, in which the polar head includes the metallic centre, while the amphiphilic behaviour is acquired after metal coordination. In **Figure 1.10** the different types of metal binding to non-surfactant ligands are illustrated.

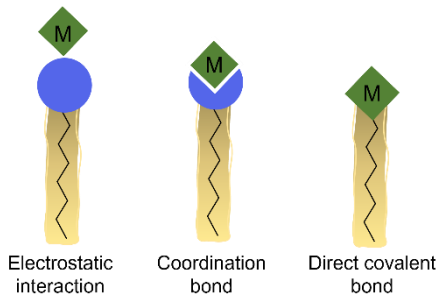

Figure 1.10 Different types of metal (M) interaction to surfactant ligands. Adapted from literature.[168]

An important family of non-tensioactive ligands are constituted by amines (mono-, di- and tetramines) or crown ethers as they include the metal cations in their interior. These macrocycles, prone to encapsulate alkalines and alkaline earth metals, were termed annelids and were first described in the 1980s by Le Moigne and Simon.[193] Then, the induction of mesophases was observed by the macrocycles coordination to other metal ions: Co(III), Cu(II), Ru(III), Cd(II), Zn(II), Mn(II), Ni(II), Fe(II), Cr(III) and Ag(I).[194–197]

Amine derivate ligands have been exhaustively studied, in terms of solution and aggregation behaviour, when complexed to several metals: Cr(III),[198] Co(III),[199,200] Ag(I),[201,202] Zn(II),[203–208] Cd(II),[203,206] Pd(II),[203,206,209] Ni(II),[210] and Cu(II).[211,212]

Co(II) and Cu(II) MTS with ethylenediamine and triethylenediamine are reported to be use in homogenous catalysis.[213–215] Other examples employ ligands such as bipyridine,[216,217] phenanotroline,[177] and terpyridine,[218] with one or more alkyl chains. Some of them form liquid crystals metallomesogens because are prompt to form discotic liquid crystals due to their planar and rigid structure.[211,212] The formation of metallomesogens and liquid crystals comprehend a significant research in the field of MTS with non-tensioactive ligands, however they are out of the scope of this work.[193,219–221]

A great number MTS of Ru(II) with bipyridines or terpyridines[216,217,222–224] and Rh(III) to terpyridine are found. They have been used as a template for the preparation of mesoporous silicates with controllable pores diameter.[177,218] Also, Ru(II) MTS with similar ligands, as phenanthrolines or benzimidazoles, have been used to produce *Langmuir-Blodgett* films. Among them, the Ru(II) – Eu(III) films were studied for optoelectronic applications by Gao *et al.*[225–227] Remarkably, the first MTS able to aggregate forming inverse micelles was a Ru(II) bipyridine MTS with the addition of alkyl chains in the work of Domínguez-Gutiérrez *et al.*[228,229]

Recently, porphyrin-based MTS were used to form columnar liquid crystals with a promising use as semiconductors.[230] Ir(II)-based porphyrin MTS have been also proved to be useful in the preparation of Langmuir-Schaefer films.[231]

The work by Garcia *et al.*, focused on Fe(II) MTS using bipyridines and cyanides as ligands, and showed the first solvatochromic complexes soluble in the whole solvent range.[232–234]

Au(I) and Ag(I) complexes based on alkylsulfides led to the formation of the complexes at the water-organic interphase importantly reducing the surface tension.[235]

In the field of medicine, Co(III) MTS prepared with cage-amine ligands were proposed to fight stomachal parasites in the work of Walker *et al*.[188] Cu(II) MTS were developed to treat some type of carcinomas by mimicking a type of antibiotic, and also studied as redox catalyst.[188,236] Ru(II) has been studied as an alternative for platinum anticancer medicine: of special interest is the work developed in Bonnet's group with Ru(II) MTS. They prepared an amphiphilic photoactivable complex that released the chemo active aquo species. The structure of the complex possesses a Ru(II) centre coordinated to bipyridine, terpyridine and, to a thioether-cholesterol ligand that provides the amphiphilicity to the molecule (**Scheme 1.6**). The complex, tested on six cell lines, demonstrated different cytotoxic activity upon irradiation and incubation times. They proposed two differentiated mechanisms depending on the concentration: below their CAC, the complex was able to enter the cell and to induce apoptosis, while above the CAC the supramolecular aggregates permeate the cell membrane and kill the cells by necrosis.[237]

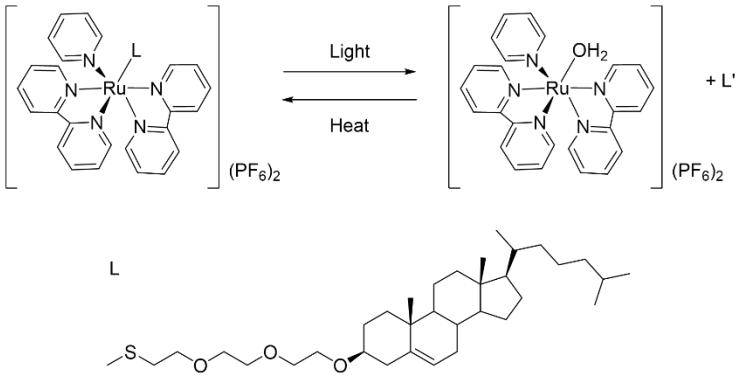

Scheme 1.6 Formation of the Ru MTS active compound through light expulsion of the thioether ligand L'.[237]

Another amphiphilic Ru(II) complex with a dodecyl chain pendant from a terpyridine moiety, able to aggregate showed high cytotoxicity: its red emission allowed the localisation of the complex in the perinuclear region by optical microscopy and to explain its cytotoxicity.[238]

Several Co(III) complexes with high amphiphilic character, mainly with amino chelated and aminoalkanes ligands, have shown cytotoxicity by increased hypoxia in tumour cells. This complexes were also applied in target-based cancer therapy and also, several others related complexes have been synthesised and tested.[239–243]

1.5.1.2 Metallosurfactants constituted by tensioactive ligands

Usually, in literature, the term MTS is exclusively used to denote tensioactive molecules with a metal as the polar head.[187] However, we differentiate a second type of MTS: those formed

by ligands, with already a surfactant structure, which binds to a metal maintaining amphiphilicity in the resulting unit. This type of ligand already poses a hydrophilic and a lipophilic segment as well as a donor atom able to coordinate the metal. A significant aspect of tensioactive ligands is the comparison of the physicochemical properties between them and their corresponding metal complexes. The MTS usually show a singular behaviour in solution which differs from standard tensioactives, based on the hydrophilic to hydrophobic ratio.

MTS prepared with tensioactive ligands have been widely used for catalytic processes. Among them, tensioactive phosphines have been the most used because of their capacity to coordinate metals strongly. However, in many cases, the MTS were not isolated and are not characterised nor studied as an entity.[244–248]

Several examples of MTS with tensioactive ligands are found in literature. To cite some, Rh(I) with tensioactive ligands showed catalytic activity for hydroformylation by assisting in the phase transfer of the substrate.[249] Other works in catalysis focused on the use of different media such as aqueous,[244,245] biphasic systems,[246,247,250] or at both.[248,251]

Cu(II) MTS with imidazole derivates, showed vesicles formation with the addition of the metal.[252] The effect of the MTS in the structure of the aggregates, has been extensively studied for a list of metals such as Co(II), Co(III) Mn(II) or Cu(II) [253–257] Remarkably, the permeability of this MTS, composed by Cu(II) and pyridine derivates as ligands, was studied in biologic membranes.[258] More recently, in 2020, the aggregation and interaction of albumin with tetradecyl pyridinium-based MTS with Mn(II), Co(II), Ni(II), Cu(II), and Zn(II) was reviewed.[259]

In previous works published in our group, the characteristics of sulfonated phosphines (**Scheme 1.7**) and their Pd(II) MTS were analysed.[260,261] The behaviour of both, the ligands and their respective complex were studied by tensiometry, which showed a decrease in the CMC values after the metal coordination.[260] This peculiarity was related to aggregation showed for gemini surfactants.[262]

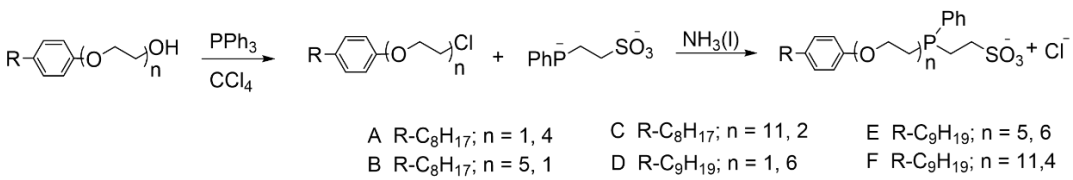

Scheme 1.7 Some of the sulfonated phosphines previously synthesised in our group and studied to coordinate Pd(II). Reproduced from literature.[260]

With the same sulfonated phosphines, the coordination to Rh(I) was also considered and used as catalyst for hydroformylation reactions in basic media.[263]

Kumar *et al*. prepared different Pt(II) MTS by the coordination of K_2PtCl_4 to several ionic surfactant such as N,N,N-trimethyl-1-ammonium bromide or cetylpyridinium chloride. In all the cases, they found decreased CMC values on increasing alkyl chains as well as lower CMC values with respect to the ligand counterpart. In their work, they studied thermodynamic parameters to support the occurring micellisation. The antimicrobial and cytotoxic activity of some of the MTS were also tested.[264,265]

Even so, in virtually all the MTS abovementioned, the metal is part of the polar head, which differs from the strategy exploited in this thesis: MTS bearing the metal in the hydrophobic region. The structure of a standard MTS and the approach used in this thesis is illustrated in **Figure 1.11**.

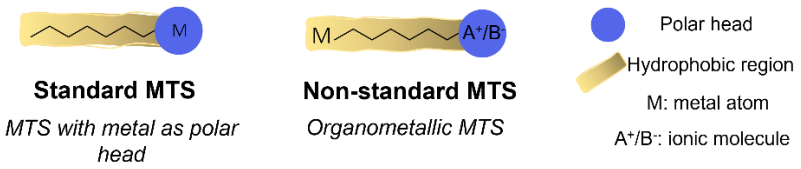

Figure 1.11 Representation of two types of MTS bearing tensioactive ligands.

In our group, the first Pt(II) MTS from a novel family of sulfonated phosphines were synthesised after their coordination to Pt(II) (**Scheme 1.8**). The *cis*-Pt(II) MTS showed lower CMC values than the parental free ligands, which at the same time increased with the alkyl chain length. More interestingly, they found that the conformation taken by the complex in the water/air interface was strongly dependent on the ligand length. It was determined that the complex with the longest chains acts as a bolaamphiphile surfactant, in which the fragment $\{PtCl_2\}$ acts as linker between the two hydrophobic chains (**Scheme 1.8**).[266]

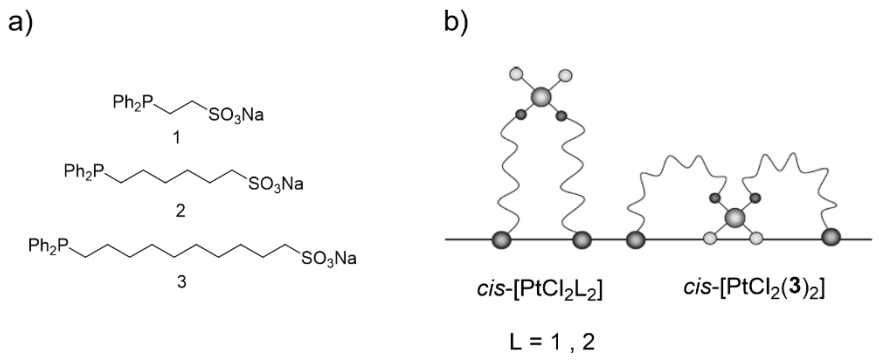

Scheme 1.8 (a) Structure of the sulfonated phosphines (with 2, 6 and 10 carbon atoms, respectively) and, (b) the illustration of the presumed different conformation of the MTS in the air/water interface. Adapted from literature.[266]

These non-standard MTS have been uncommonly synthesised and only a few examples can be found in the bibliography such as the Pt(II) sulfonated phosphines developed in our group, or the ferrocene-based redox-active surfactants. In this last case, cyclopentadiene was functionalised with an alkyl chain containing an ionic group in the opposite extreme, such as sodium sulfonate or trimethylamine bromide (**Scheme 1.9**).[267–269] In the reduced form, the ferrocenyl acts as a hydrophobic group, and in presence of sodium dodecylbenzenesulfate they can form or disrupt vesicles by potentiostatic electrolysis.

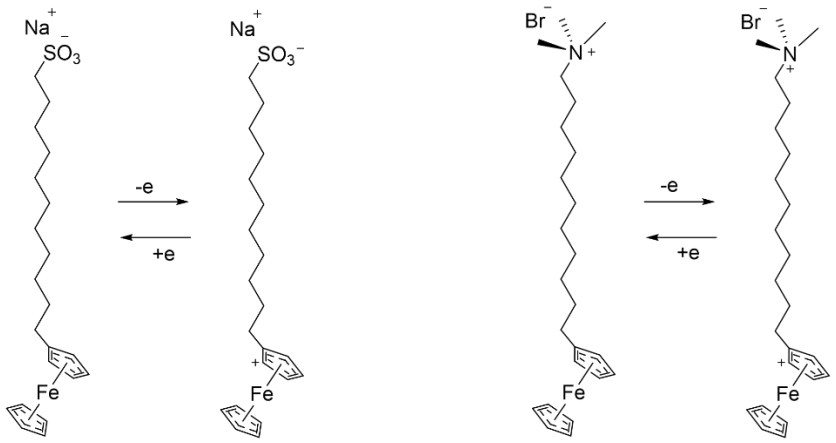

Scheme 1.9 Redox reaction of ferrocene: electrochemical oxidation of ferrocene to the ferrocenium, adapted from literature.[267,268]

In our group, the sulfonated phosphines shown in **Scheme 1.8** were also studied for the coordination to hexacarbonyl metal carbonyls. In the study, one or two sulfonated phosphine ligands coordinated to $[Mo(CO)_6]$ yielded two type of surfactants. The MTS with $M(CO)_5L$ stoichiometry are considered analogous to classical surfactants and, the $M(CO)_4L_2$ that were related to bolaamphiphiles surfactants (**Scheme 1.10**). Both types of MTS showed lower CMC values compared to their parent surfactant ligands. All the MTS formed supramolecular

aggregates in water, in form of polydisperse SUV, LUV, MLV and MVV. The formation of vesicles instead of micelles, like phosphine ligands do, was related to the metal coordination which favours that type of self-assembly.[270]

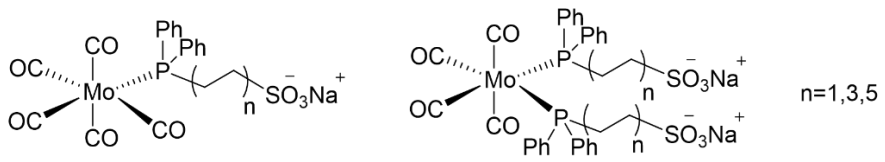

Scheme 1.10 Structures of Mo(II) carbonyl complexes based on surfactant sulfonated phosphine ligands.[270,271]

In a subsequent study of the Mo(II) MTS compounds, the presence of vesicles with principally one or a few membranes was reassured. This behaviour was explained by the electrostatic repulsion between sulfonated groups placed in the membrane. Besides, in the same study, small Angle X-ray scattering (SAXS) experiments fitted with a lamellar model, consistent with the formation of vesicles.[271]

1.6 Metallosomes

The molecular structure of a MTS determines the aggregation and dispersion properties. As for classical surfactants in solution, MTS orient and generate supramolecular aggregates to minimise the contact of hydrophobic moieties with the air or solvent. At low concentrations, MTS form highly soluble solutions, but at concentrations higher than their CAC, the molecules self-assemble into supramolecular aggregates. The preferred supramolecular assembly can vary from nanoaggregates such as metallomicelles or inversed metallomicelles up to vesicles.[187,228] In some works, when the vesicles formed by the MTS are bilayered, they are denoted as metallosomes (MTL).[257,272]

Back in 1999, phospholipids with Au NPs as polar head groups were synthesised and characterised. In the work, they defined metallosomes as a metal-containing liposome.[273]

Nevertheless, the term metallosomes (MTLs) is sometimes also used to denote mixed vesicles, between structural lipids and MTS, as in the work of our group conducted by Marín-García, *et al.* In related publications, Mo-based MTS with CO releasing properties render unilamellar vesicles, however, upon dilution the vesicles disaggregate. To avoid it, MTS were mixed with a structural phospholipid to form mixed vesicles. The resulted mixture results in the formation of stable MTL (**Scheme 1.11**).

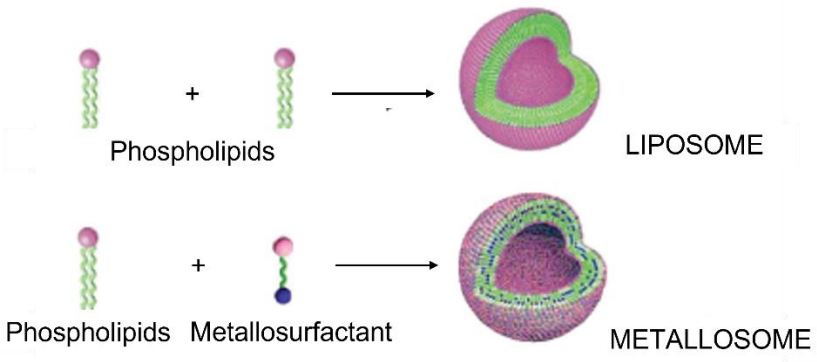

Scheme 1.11 Formation of liposomes with phospholipids or metallosomes by mixing metallosurfactants and phospholipids, adapted from literature.[274]

Marín-García, *et al.* demonstrated that depending on the Mo-MTS to lipid molar ratio, the type of aggregate formed differ (large vesicles, nanometric micelles, or micro-sized rods). Besides, the increase of the length of the hydrocarbon chain has a relevant influence on the aggregation properties of the mixed vesicles. So, mixed vesicles appeared to be good candidates for further biomedical applications as they can incorporate the metal into the cells with a lower cell toxicity than their MTS homologous.[274,275] A similar work is reported by mixing 1,2-diasteroyl-*sn*-glycero-3-phosphocholine (DSPC) and a manganese MTS to form mixed liposomes that were proven to release CO as potential photo-CO releasing molecule.[276]

Another example found in bibliography is vesicular Zn(II)-complexes prepared with Zn(II) tetraazacyclododecane amphiphilic complexes and DSPC, as structural lipid. In this work, micellar or vesicular catalyst systems for phosphodiester hydrolysis are presented and, as luminescent vesicular receptor for the recognition of phosphate species.[277,278]

Also, Aryal *et al* generated a phospholipid-like platinum compound that self-assembled showing, after extrusion circular aggregates of 100 nm, named as Ptsomes. The stability of these entities was reported too poor because of membrane fusion. This drawback was overcome with the DSPC-PEG mixture as it reduced the fusion and exceed their instability. [279]

The preparation of radio-labelled Tc-99m liposomes has been previously reported by our group. In this work, liposomes were labelled with an already assembled Te-99m MTS (**Scheme 1.12**). The radiolabelled or homologous Re MTS were prepared by 2 + 1 transmetallation between Zn and Re or Te-99m MTS, which were also reported to self-aggregate. The homologous Re compound showed how radio-labelled liposomes could be prepared under thermodynamic control, from Thin Film method, as well as under kinetic control by mixing the

Re compound to preformed (and non-radio-labelled) liposomes. Further, the methodology was proven to yield radiolabelled Tc-99m, in accordance with high-performance liquid chromatography data. Hence, providing a promising methodology for the preparation of radiopharmaceuticals simply, rapidly and at very low concentrations because the nature and short half-life of radio nucleus.[280]

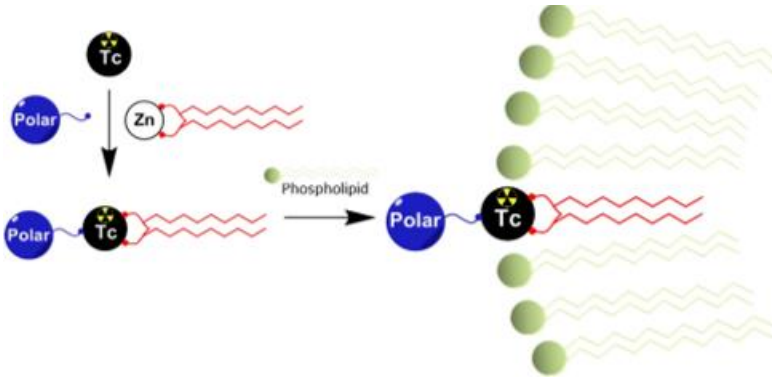

Scheme 1.12 Illustration of the ^{99}Tc MTL prepared by 2 + 1 transmetallation. Reproduced from literature.[280]

Photoactivatable anticancer therapy has been also combined with liposomes and amphiphilic complexes. The Ru(II) terpyridine complexes showed in **Scheme 1.6**, were included inside DMPC and DSPE-MPEG-2000. In the strategy there is radiative energy transfer (upconversion process) from a liposome containing a photosensitizer and an annihilator, to a second liposome including the Ru(II) complexes. Light-induced hydrolysis triggers the photodissociation of a Ru-S bond releasing the aquated complex to solution (**Scheme 1.13**).[281]

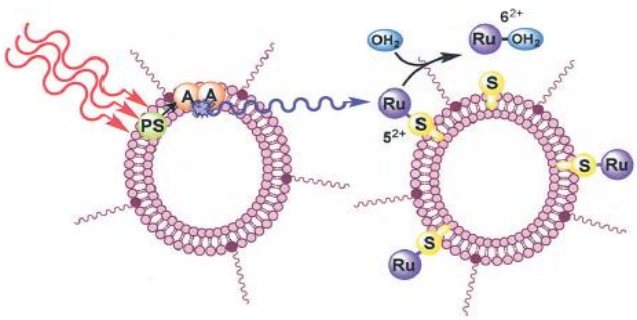

Scheme 1.13 Photoactivation of a Ru(II) complex by upconversion between liposomes. Reproduced from literature.[281]

2. OBJECTIVES

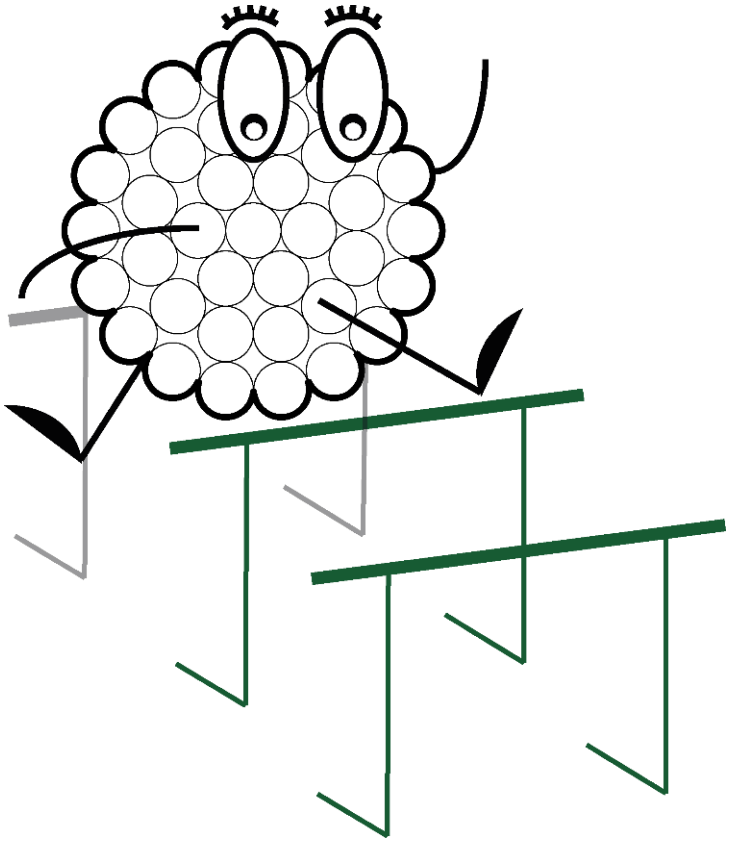

The main goal of this thesis is the preparation of platinum-containing liposomes, so called metallosomes, for their use as anticancer drugs. From this main motif, specific objectives arise:

- Synthesise and physicochemical characterisation of a family of alkyl amino sulfonate ligands with different carbon chain length.

- Synthesis and characterisation of a *cis*-Pt(II) complex family containing the alkyl amino sulfonate ligands in the coordination to Pt(II).
    - To evaluate their supramolecular behaviour.
    - To assess their interaction with biomolecules, and to study their cytotoxic properties against several cancer cell lines.

- Obtention and characterisation of metallosomes: mixed systems using structural phospholipids and Pt(II) complexes.
    - To use different phospholipids for metallosomes preparation and evaluating their outcome regarding to each lipid characteristics.
    - To assess the location of the complex and the bilayer perturbation in the metallosomes.
    - To study the toxicity of the metallosomes against cancer cell lines.

3. ALKYL AMINO SULFONATE LIGANDS

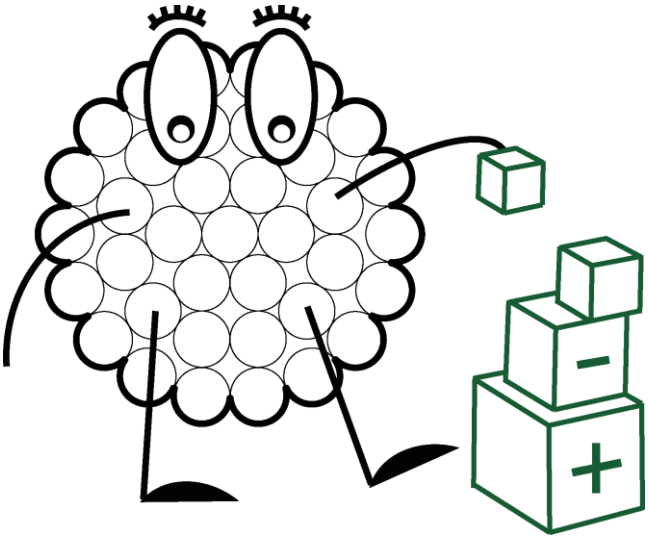

The starting point of this thesis is described on this chapter with the preparation of alkyl amino sulfonate ligands with three lengths of the hydrocarbon chains. The steps to optimise their synthesis, and more importantly their characterisation, are developed through the different sections of this chapter.

3.1 Synthesis of the ligands

3.1.1 Design

The rational design and synthesis of the proposed ligands was the first step in this work. Based on previous works in our group, in which surface-active sulfonated phosphines with different alkyl carbon chains were synthesised,[266,270] a new family of amino sulfonated ligands was designed (**Scheme 3.1**).

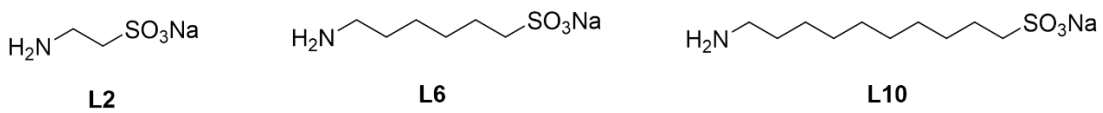

Scheme 3.1 Chosen ligands to be synthesised in this work: **L2**, **L6**, and **L10**.

Sulfonate group was chosen as hydrophilic head because it acquires a negative charge when solved in water. Sulfonates, display excellent stability at both acidic and alkaline pH. In contrast, the alkyl sulfate analogue would be completely hydrolysed. Moreover, in the majority of transition metal complexes, sulfonate anions are generally considered as weakly interacting or even as non-coordinating groups.[282] Concerning the chosen counterion, a biocompatible cation was essential, and at the same time, it must show extensible water solubility. Sodium, an approved counterion by the FDA for human studies, was selected for our products as it is the most common countercation in commercial drugs.[283]

On the opposite side of the alkyl chain, an amino group was chosen for the ligand's structures. The amino group acts as a good donor group, showing certain affinity to coordinate platinum. However, the intrinsic acid-base character of the group added synthetic difficulties which are further detailed.

Our family of amino sulfonated ligands, **Ls**, have a carbon chain between both groups that confers the final amphiphilic behaviour. The whole family of ligands differ in their hydrocarbon length. They were chosen based on previous studies[266,270] and below phospholipids average carbon chain lengths to not hinder the preparation of metallosomes. Hence, the maximum length considered was 10 C. The other two synthesised ligands were analogous ligands with 6 and 2 carbon atoms, respectively. The three ligand structures, sodium 2-

aminoethanesulfonate (**L2**), 6-aminohexanesulfonate (**L6**) and 10-aminodecanesulfonate (**L10**) are shown in**Scheme 3.1**.

In fact, **L2** structure at acidic conditions corresponds to 2-aminoethanesulfonic acid, already known as taurine. It is a β-amino acid usually referred to as a semi-essential amino acid since new-born mammals must rely on dietary intake. It has significant contributions to several cellular and physiological processes,[284] like cytoprotective activity, antioxidant activity, Ca^{2+} homeostasis or osmoregulation. Besides it gain importance in clinical applications as a therapeutic agent.[285] Taurine is reported to be chemically synthesised by two different synthetic pathways. The first involves the reaction between ethylene oxide and sodium bisulfite to form isethionic acid (2-hydroxyethanesulfonic acid), which after ammonolysis yield the synthetic form of taurine. The second reaction involves a direct reaction between aziridine and sulphurous acid.[286]

Nonetheless, it was decided to find a new route for the preparation of the alkyl amino sulfonate ligands that could be extrapolated for the preparation of the whole family.

3.1.2 Synthetic strategy

The preparation of the organic ligands with surfactant properties is an arduous and laborious task since as the syntheses proceed, the desired amphiphilic nature of the organic ligands hassles its manipulation, and standard procedures become complicated and require further steps and/or strategies. Besides, it is knotty to attach different groups to one alky chain. The synthesis of ligand **L10** was the first attempted following different approaches.

The first strategy followed was based on the synthesis of sulfonated phosphine ligands. Ideally, in the first step, a dihalogenated alkane chain must be sulfonated in one terminal position, and then an amino group must be attached in the opposite side of the chain as next step of the synthesis. The sulfonation step, based on an S_N2 reaction, was formerly reported in a previous thesis and the associated publications.[266] Following the same synthetic strategy, sodium sulphite in water is slowly added by means of a syringe and a perfursor at 0.3 mL/min, to a large excess of 1,10-dichlorodecane in a mixture of water/ethanol. After 4 h at reflux with vigorous stirring, a mixture of halosulfonated (**HS**), disulfonated (**DS**) and non-reacted 1,10-dichlorodecane products are obtained (**Scheme 3.2**).

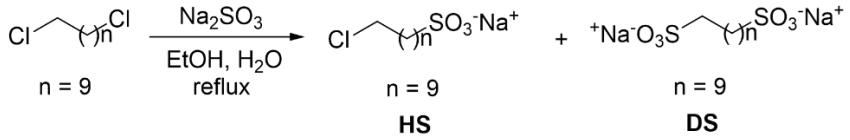

Scheme 3.2 Synthesis of the halosulfonated (**HS**) intermediate.

Liquid-liquid extraction with ethyl acetate is performed to separate the non-reacted precursor and then, the mixture of sulfonated derivatives is separated by recrystallisation in EtOH. However, the yield of the non-profitable disulfonated compound (**DS**) was elevated, being 72%. Additionally, the high amount of EtOH needed in the recrystallisation is about 250 mL/g of **HS** product, which is considerably time and resource consuming.

To sum up, the first step of the synthesis resulted in the obtention of **HS** product in a 28% yield. Nonetheless, the purification involved many recrystallisation steps with the corresponding decrease of the final yield.

Next step was amination. Ammonia is a great nucleophile and reacts with primary alkyl halides via an S_N2 reaction yielding alkyl amines. Hence, once the corresponding **HS** was obtained, several amination conditions were tried. Significant results are reviewed in **Table 3.1**.

Table 3.1 Attempts towards the synthesis of the aminodecanesulfonate product**.**

Entry	Reagent	Solvent	Conditions	Comments
1	NH_3 (30%)	H_2O	Reflux, 24h	High amount of non-reacted **HS** and sulfonated alcohol
2	NH_3 (30%)	H_2O	Autoclave 100 °C,4 h	Though separation of **HS** and aminosulfonate
3	HMTA	CH_2Cl_2	Addition at 0 °C, reflux, 20 h	Non-reacted **HS**
4	$NaNH_2$	NH_3(*l*)	-84 °C (cooling bath: ethyl acetate/liquid N_2)[287]	Non-reacted **HS**
5	Na	NH_3(*l*)	-84 °C (cooling bath: ethyl acetate/liquid N_2)[287]	Though separation of **HS** and aminosulfonate
6	Potassium phthalimide and hydrazine, NaOH or HCl	DMF	Reflux, 18 h Several conditions for cleavage	Though separation of **HS** and aminosulfonate

In entry **1**, **HS** was added to an excess of ammonia solution at 30% in water and let it react at reflux for 24 h. Then, pH was reduced to ~6 with diluted HCl and the solvent was evaporated under reduced pressure. The resulting ^{1}H-NMR spectra (**Figure A1**) showed predominantly non-reacted **HS**. The same reaction was performed in an autoclave reactor (entry **2**). In this case, in the ^{1}H-NMR, the amination was achieved, since chemical shifts for Hα-N from amino were appreciated. But non-reacted **HS** was also found, indicating that the reaction was not completed (**Figure A1**). Predictably, the conversion to the aminated species was higher in the reaction performed in the autoclave since reaction conditions are more extreme. Nonetheless, the separation of the species would have been difficult, and the fact that even at extreme conditions there was remaining starting **HS** product. Thus, this route was finally discarded.
Another strategy was to employ hexamethylenetetramine (HMTA) in excess to react with the **HS** product in DCM (entry **3**), as in *Delépine* reaction.[288] The reaction was set at reflux for 20 h. Nonetheless, as was seen by ^{1}H-NMR spectrum from the reaction crude (**Figure A2**), revealed the substitution of chlorine by HMTA did not occur.

In entry **4** and **5**, the chosen solvent was liquid NH_3.[289] In entry **4**, sodium amide was directly added to react with **HS**. In entry **5**, sodium amide was prepared *in situ* from liquid ammonia and sodium. Disappointingly, the chlorosulfonate **HS** product remained unreacted in both attempts. Again, the separation of the species turned out to be laborious, so this synthetic route was also discarded (**Figure A3**).

Gabriel synthesis for primary amines was considered in entry **6**, even the reaction would not be direct, because it requires at least two steps, it was considered a promising option. In Gabriel synthesis, potassium phthalimide serves as a $–NH_2$-synthon, which allows the preparation of primary amines by reaction with alkyl halides.[290] Therefore, **HS** and potassium phthalimide in DMF were refluxed for 18 h. The phthalic sulfonated intermediate was formed; however, unreacted **HS** was still in the mixture. Subsequently, the cleavage of the phthalimide moiety to obtain the amino group was attained by using hydrazine or by basic (NaOH) or acidic (HCl) hydrolyses (**Scheme 3.3**). Even though the cleavage was accomplished by hydrolysis, the resulting ^{1}H-NMR spectrum of the crudes showed again remaining **HS** precursor together with the corresponding phthalic derivative. Again, the purification of the alkyl amino sufonate resulted too though (**Figure A4**).

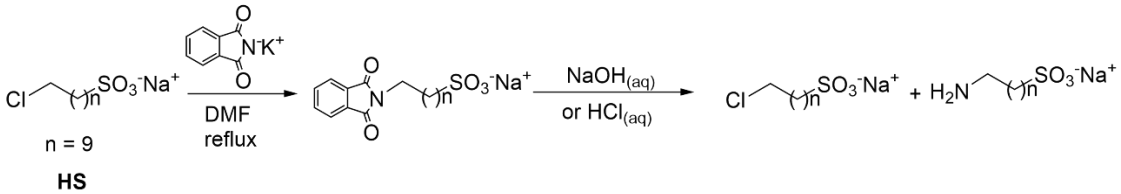

Scheme 3.3 Synthetic route for entry 6 starting from **HS**.

None of the approaches summarised in **Table 3.1** were considered to give synthetically interesting results, mostly because of the complicated separation and purification steps required for the isolation of the final compound from the different by-products and not reacted **HS**. The low of reactivity of the chlorinated group should explain the presence of non-reacted **HS**. This, together with the unfavourable electrostatic interactions between the chlorinated and the sulfonate group, hamper the obtention of the desired final compound.[291] Consequently, the full strategy was reevaluated.

First, to improve the reactivity of the precursor, 1,10-dicholordecane was substituted by their bromated analogue: 1,10-dibromodecane. But the most interesting modification was to perform the amination of one bromide group before the sulfonation reaction, as it was considered crucial to avoid the difficult separation of sulfonated species.

Following Gabriel's synthesis, 1,10-dibromodecane is treated with potassium phthalimide to yield the monobromated compound, in 63% (**Scheme 3.4**).[292] In this synthesis, the phthalimide intermediate was purified by column chromatography in hexane/AcOEt 10:1 v/v to isolate the intermediate from the dibromoalkane precursor, as well as, from the disubstitution product.

First, the synthesis of the substituted phthalimide position was assured by ^{1}H-NMR in $CDCl_3$, by comparing the spectrum with the corresponding di-bromated precursor. The spectra showed a shift in the proton α position to the bromide (Hα-Br), and the proton integrals agree with the mono-substitution. Besides, the methylene signals related to the linked phthalimide were also in accordance. After alkylation, phthalimide is no longer nucleophile and does not react, being a perfect option to protect the amino group when the sulfonation step proceed.

Then, the remaining bromo-position of the phthalic intermediate is sulfonated with sodium sulfite (Na_2SO_3) in water/ethanol. At this point, by liquid-liquid extraction in AcOEt/H_2O allowed to isolate the phthalimide sulfonated product is isolated from other organic by-products.

^{1}H-NMR of the sulphonation step crude showed how the peak corresponding to Hα-Br disappeared to give place to the Hα-sulfonate signal, however, the spectrum showed that phthalimide had already cleaved. Finally, after the acidic cleavage, the signals assigned to the phthalic moiety vanish in favour of the amino related signal, implying the complete deprotection of the amine.

Finally, the acidic hydrolysis gave the cationic form of the final ligand **L10** in a 77 to 88 % overall yield, before the purification. A second liquid-liquid extraction, as in the previous step, is conducted before the recrystallisation. Sometimes, if the product yields a yellow appearance, it is washed with acetone. Finally, recrystallisation is carried out in a mixture of H_2O/EtOH 50:50 v/v with a final yield of 28 %.

The success of this strategy encouraged us to follow the same procedure in the obtention of analogues **L2** and **L6** in their protonated forms (**Scheme 3.4**) with 57% and 46% overall yields, respectively.

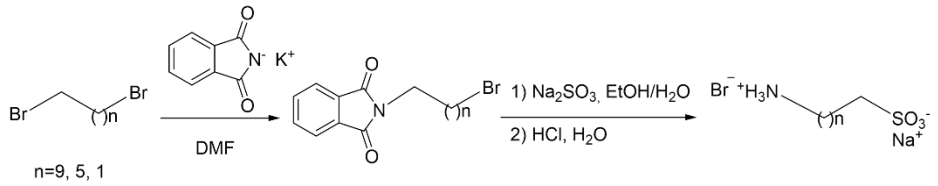

Scheme 3.4 Scheme of final ligands (**Ls**) synthetical route.

It is important to point out that impurities are seen along with the whole synthesis, which are present even after distillation of the dibromo alkylated precursors and are especially important in **L2** synthesis.

The reaction evolution is shown in **Figure A5** to **A7**. All three ligands were further purified by recrystallization in a mixture of a mixture of H_2O/EtOH 50:50 v/v. However, after the final recrystallisation unknown organic impurities remain

3.2 Chemical characterisation

The alkyl amino sulfonate ligands (**Ls**) were characterised by common techniques to ensure their chemical entity and purity in each step of the synthetic pathway.

Final characterisation of ligands was conducted at nearly neutral or basic pH (6 to 8) -or specified if different-, by several techniques: proton and carbon nuclear magnetic resonance (^{1}H-NMR -**Figure A8** to **A10**- and ^{13}C-NMR -**Figure A11** to **A13-**), and high-resolution electrospray ionisation mass spectrometry (HR ESI-MS) found in **Figure A14** to **A16**

To verify the assignation of N/S-H_β and H_γ signals in **L10** NMR spectra correlation spectra (COSY) experiment was undertaken. Cross peaks in COSY (**Figure A17**) indicate which atoms are connected (within a maximum of four bonds distance), so it was possible to determine that signals from H_α to respect the amine with chemical shifts 2.82 and 2.75 are related to chemical shifts 1.63 and 1.62, that correspond to H_β respect to the sulfonate group. While 2.50 and 2.43 chemical shifts from H_α to the amino group are related to 1.31 signal from the H_β to the amino group.

The preparation of ^{1}H-NMR tubes of **L10** demonstrated the sparse solubility of the compound even in D_2O and at low concentrations (< 10 µM), which in some cases resulted in the appearance of a precipitating white precipitate. Diffusion-ordered spectroscopy (DOSY) experiment was performed to discard the presence of several molecules or associations that could hinder the characterisation of the ligand when carrying out NMR experiments. In DOSY, the diffusion factor exposes the distribution of molecular sizes and allows diverse molecular species to be identified and assigned. The DOSY spectrum (**Figure A18**), revealed that all the proton signals shared a single diffusion constant, denoting the presence of only one specie in solution.

Noticeably, the final properties of the ligands are completely reliant on pH. In fact, as surfactants, they have to be considered amphoteric species because they simultaneously bear the anionic and cationic hydrophilic groups. As discrete molecules, they are considered zwitterions. This nature along with their amphiphilicity, significant for **L10,** substantially hindered the characterisation of these ligands.

When the synthesis of these ligands is completed, the final pH is given after the acidic cleavage and recrystallisation. To study the differences in front of pH variations ^{1}H-NMR of **L10**, was conducted at an increasing amount of NaOD (**Figure 3.1**).

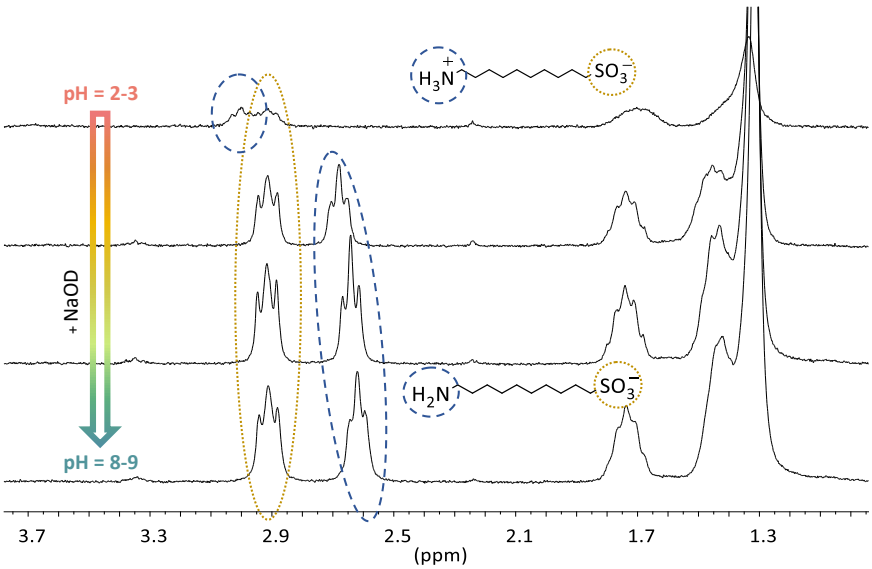

Figure 3.1 ^{1}H-NMR spectra of **L10** upon addition of NaOD in D_2O.

In the spectra, it is seen how chemical shifts of α-amino proton signals varies with pH. Most specifically, because shielding is increased, the α-amino proton signals are shifted to lower frequencies, while the signals corresponding to the α-sulfonate protons remain unaltered. In addition, the ^{1}H-NMR signals are noticeable sharper and more defined as the pH increases. Besides, the solubility was also greater at basic pH than at the acidic conditions. It suggests a correlation with variations in the intermolecular interactions of molecules of ligands due to charge changes.

The chemical entity of **Ls** was also confirmed by positive mode ESI-MS and negative HR ESI-MS, shown in **Figures A14** to **A16**, for which mass values fitted within the experimental error. In positive mode, ligands **L2** and **L6** ligands showed sodium and proton adducts, but no association of molecules was found. On the other hand, in the MS spectrum for **L10**, up to five molecules forming sodium and proton adducts were identified (**Figure 3.2**).

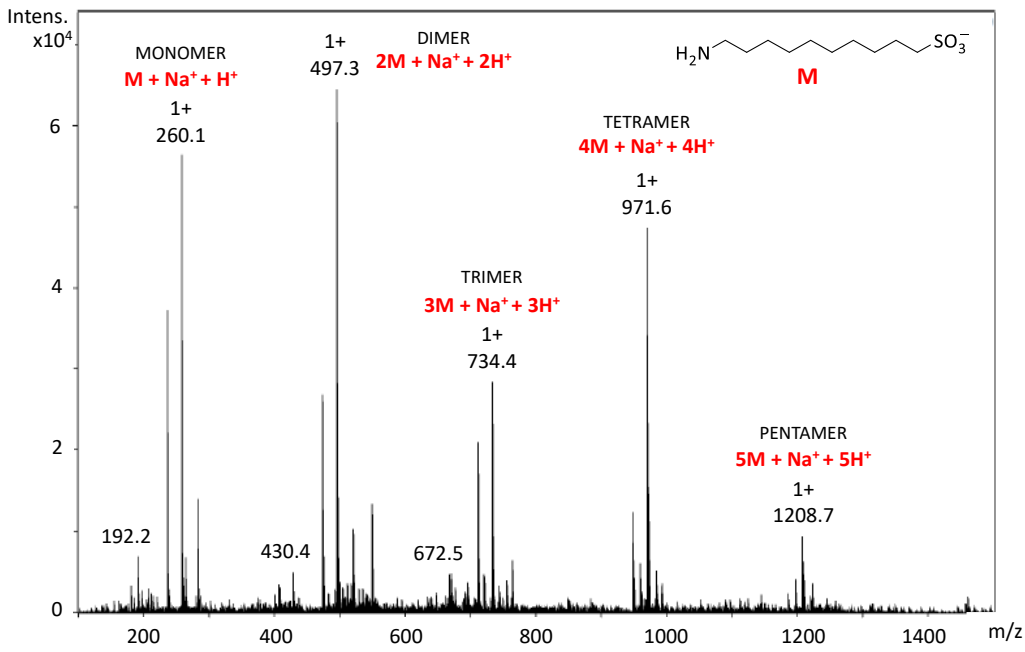

Figure 3.2 Positive ESI-MS showing **L10** association.

The formation of adducts is favoured in positive mode with respect to negative mode. [293] To discard that molecules' associations occurs as a consequence of the positive ionisation mode, MS was repeated in the negative mode, in which a lower number of sodium adducts are expected (**Figure A19**). It was found that regardless of the ionisation mode, associations up to six molecules of **L10** were detected by ESI-MS.

Several examples of molecules association in MS are reported in literature; for instance, back in the 1980s several studies reported up to 7 charged aggregates of alkyl sulfonates using FAB-MS/MS in positive mode.[294,295] Moreover, in the work of Siuzdak, *et al.* the study by ESI-MS of several surfactants such as sodium dodecyl sulfate (SDS), showed multi-charged aggregates with aggregation numbers up to 12.[296]

ESI is reported to be the most suitable technique for the generation of charged supramolecular aggregates, which mainly with polar solvents, can separate charges in solution, enriching the small droplets either in positive or in negative species and favouring the formation of the corresponding charged aggregates. More interestingly, ESI favours micelles' formation in the gas phase because of the progressively increased concentration after solvent evaporation, which is reported to be found even below the CMC. In this regard, charged supramolecular aggregates of surfactants can occur during the ionisation and they have a survival life long enough to be detected in several mass spectrometry experiments.[297] Besides, under typical ESI conditions, supramolecular organisations in polar or apolar solvents, or in the water/air

interphase, strongly impacts the fission of polar droplets as well as the ion emission and the solvent evaporation processes. Nonetheless, there is discussion in literature whether the aggregates observed in MS are due to the fragmentation process. However, several experiments agree that, as general trends, the aggregation processes observed in gas are similar to what could occur in solution.[298] In the case of study, the fact that pentamers and hexamers were only observed for the longest ligand (**L10**), in both positive and negative ESI mode, give the impression that a specific self-organisation exists and may occur due to the higher amphiphilicity of **L10** with respect to **L2** and **L6**. However, the work of Bongiorno *et al*. reports that ESI-MS spectra may not reflect the aggregation state present in the starting solution, as part of the molecules may self-assemble during the evaporation step of ESI.[297] Nonetheless, ESI-MS confirmed the surfactant behaviour of at least one of our ligands and led us to explore their nature for a better understanding of their interactions.

3.3 Physicochemical properties

3.3.1 Infrared spectroscopy and study of interactions

This section aims to assign and describe the Fourier transform infrared-attenuated total reflection (FTIR-ATR) bands yielded by our **Ls**. Several characteristics of the ligands are discussed by comparing molecules with analogue groups, and by defining the extension of the pH influences within the studied groups.

L2, **L6** and **L10** behold the same groups, a sulfonate, and an amine, separated by a hydrocarbon chain, which differs in the carbon chain length. Accordingly, it is expected rather similar signals between the three ligands. Due to the acid-basic properties of the **Ls**, FTIR-ATR analyses was performed at two distinct pH values, at pH 5.0-6.0 after the recrystallisation of **Ls**, hereinafter denoted as **acid-Ls**, and at pH 8.0-9.0 after the basification of the product, referred to as **basic-Ls**.

Theoretical bands rendered by the sulfonate group are two stretching modes, the asymmetric, in the interval 1250-1140 cm^{-1} that could be split in two. And the symmetric band is expected between 1070-1030 cm^{-1}. A less intense peak is associated with the bending of $-SO_3^-$ usually found under 800 cm^{-1}.[299,300]

Regarding **L10** sulfonate group (**Figure 3.3**), the most notable signals are two bands at 1161 and 1036 cm^{-1} due to the asymmetric and symmetric stretching of $-SO_3^-$, respectively. Also, a less intense signal at 795 cm^{-1} is identified as the bending of $-SO_3^-$. For **L6** asymmetric stretching

of SO_3^- are 1163 and 1129 cm^{-1}, and symmetric 1047 cm^{-1}. And **L2** display the asymmetrical signal at 1152 and 1100 cm^{-1} and the symmetric at 1033 cm^{-1}. It is important to remark that while the asymmetric bands are split in **L2** and **L6,** they yielded a single band in **L10**. Finally, bending signals are located at 788 and 740 cm^{-1} for **L6** and **L2**, respectively (**Figure 3.3**).

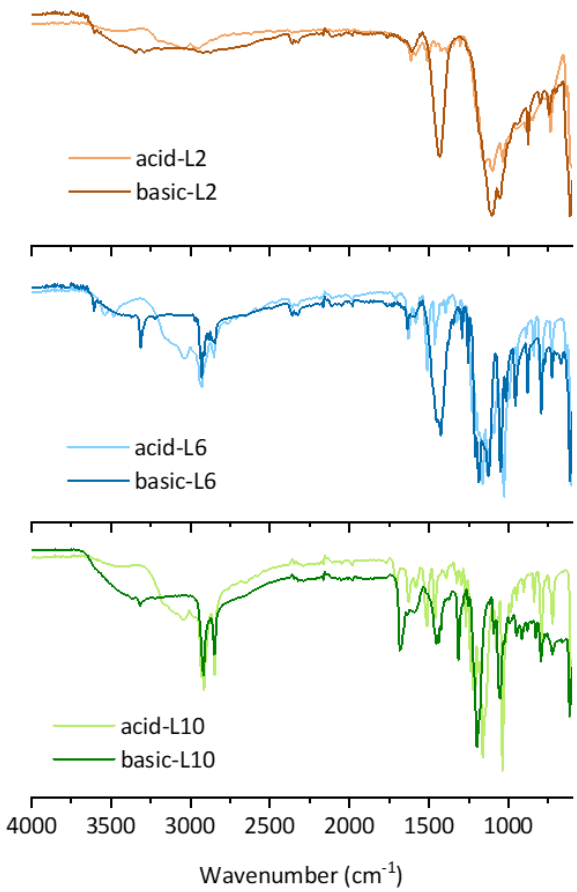

Figure 3.3 FTIR-ATR spectra of **Ls** species at acid pH (5.0 - 6.0) and basic pH (8.0 - 9.0).

Sulfonate groups are not protonated at any of the working pH values, since they have a predicted pKa ≤ 2.[301] Nonetheless, a shift in the sulfonate bands is observed when pH is increased. Probably, the shift occurs after the deprotonation of the amino group that may vary the interaction between both edges of the chain, slightly modifying the stretching signals. These modifications are observed in the asymmetric and symmetric stretching bands that in case of **L10** are shifted to higher wavenumbers, 1199 and 1054 cm^{-1}, respectively. In **L6** the asymmetrical band shifted to 1183 and 1126 cm^{-1}, while the symmetric moved to 1026 cm^{-1}. And in **L2**, the shifts converted the asymmetric peak in a broad band at 1103 cm^{-1}, while the symmetrical stayed almost unmodified at 1053 cm^{-1}.

The three **Ls** show characteristic stretching bands of methylene units between 2950-2850 cm^{-1}. Alkyl stretching modes are detailed in **Table 3.2** and are unmodified for acid or basic pH. The three ligands' alkyl stretching bands are perfectly coincident with the estimated wavenumber, though their intensities differ. As expected, more intense peaks are shown for longer carbon chains. Interestingly, methylene bending peaks (1400 cm^{-1}) are more intense in the basic form of the **Ls**.

Table 3.2 Alkyl stretching modes in **L10**, **L6** and **L2** FTIR-ATR spectra recorded with products isolated from solution at different pH values.

	L2	**L6**	**L10**
-CH_2- asymmetrical stretching (cm^{-1})	2982-2936	2929	2925
-CH_2- symmetrical stretching (cm^{-1})		2847	2846

Amino groups are reported in the literature to display several peaks in the IR related to their different vibrational modes. Primary amines present two stretching modes, the asymmetrical and the symmetrical between 3500 and 3300 cm^{-1}. Peaks due to stretching of the -N-H group are weaker and sharper than the -O-H stretching modes. The N-H bending for primary amines usually occurs between 1650 and 1590 cm^{-1} and wagging modes are also identified in a similar region. Moreover, it is of particular interest the peak located at around 1100 cm^{-1} will be characteristic for C-N stretching.[302] The fingerprint of the molecule may also show other peaks associated with twisting or rocking vibrations, but they do not concern this study.

When analysing the peaks related to the amine groups in our **Ls**, we must consider two pH-dependant species, the amino group (-NH_2) *vs* the ammonium group (-NH_3^+).

Ammonium salts of primary amines show vibration stretching peaks lower wavenumbers and with shorter intensities than their corresponding amino form. This differential behaviour will be a crucial point to determine the pH related state of the **Ls** in relation to pH. An indicative of -NH_3^+ group would be the appearance of one or two bands at the 1600-1500 cm^{-1} region, due to deformation vibrations of the protonated group. Nonetheless, N-H bending peaks are not expected to show significant displacement, and their less intense bands are usually difficult to observe.[302]

The peaks associated with amine signals for the three **Ls** are detailed in **Table 3.3**. The basification of the molecule was assured by treating the correspponding ligand with 1.5

equivalents of NaOH and drying completely the samples. For **basic-Ls**, stretching modes were located at higher wavenumbers with respect to their salts, as seen in **Figure 3.3** and **Table 3.3**.

Table 3.3 FTIR-ATR peaks associated with-NH_3^+ and -NH_2 for **L10**, **L6** and **L2**.

	L10 (cm^{-1})		**L6 (cm^{-1})**		**L2 (cm^{-1})**	
	Acid	**Basic**	**Acid**	**Basic**	**Acid**	**Basic**
-N-H asymmetrical and symmetrical stretching (-NH_3^+/ -NH_2)	3108 and 3048	3327	3045 and 3108	3314	3194 and 3139	2991 and 3345
-C-N stretching	1036	1053	1028	1049	1035	1049

Infrared spectra have also been an important tool to discern possible interactions occurring between our **Ls**, which may explain further solubility and associations of molecules. As reported, electrostatic interactions between sulfonates and aminated products are already known to be particularly strong and to influence other properties such as the pH, the isoelectric point or the solubility.[303–305] In the case of study, several possible inter, and intra-ligand interactions have been appraised. In particular, two electrostatic interactions may be present: hydrogen bonding, which can be found within amino groups and sulfonates from different ligands, and ionic interactions due to the charges of the existing functionalities. Accordingly, interactions among the amino group and the sulfonate group will be the most significant interaction to consider. Hydrogen bonding or dipole-dipole interactions may occur when the amino group is not protonated, whereas ionic interaction may arise when the amino group is protonated. So, we suggest that at low pH, when the ammonium group is present, ionic electrostatic interactions befalling may be greater than hydrogen bonding or dipole-dipole interactions. Moreover, attractive interactions, at high pH could be enhanced by the interaction between the alkyl chains of the attached groups. Such interactions made us portend their organisation with a head to tail arrangement. Moreover, for the longest ligand (**L10**), interactions may take place with the same molecule, generating unusual arrangements upon themselves. In fact, it is reported that flexible compounds with appropriate moieties can present hydrophobic collapse in polar solvents, and hydrophilic folding in non-polar solvents.[306]

Although interactions cannot be determined by the study of the FT-IR spectra of our **Ls**, a comparison to similar molecules was a supportive alternative to analyse the behaviour of the chemical groups. The study involved sulfonates or amino groups in the extremes of alkyl chains, which aided to predict the role and possible interactions of our molecules. It is reported

that broader bands are found when interactions take place, thus, peaks with major changes could indicate interactions.[307]

The chosen analogue molecules to determine the theoretical signals of the amino and the sulfonate groups of **Ls** were dodecylamine, sodium 1-chloro-10-decanesulfonate and sodium 1,10-decanedisulfonate (**DS**). In addition, a mixture between DS and dodecylamine was also analysed to compare bands shifts of the separated species and their mixture (**Figure 3.4**). All the spectra were compared to the longer ligand (**L10**) spectra. It is important to mention that all the samples analysed were previously dried under vacuum while slightly heated, to avoid the presence of water molecules, which could interfere in the spectrum generating hydrogen bonding.

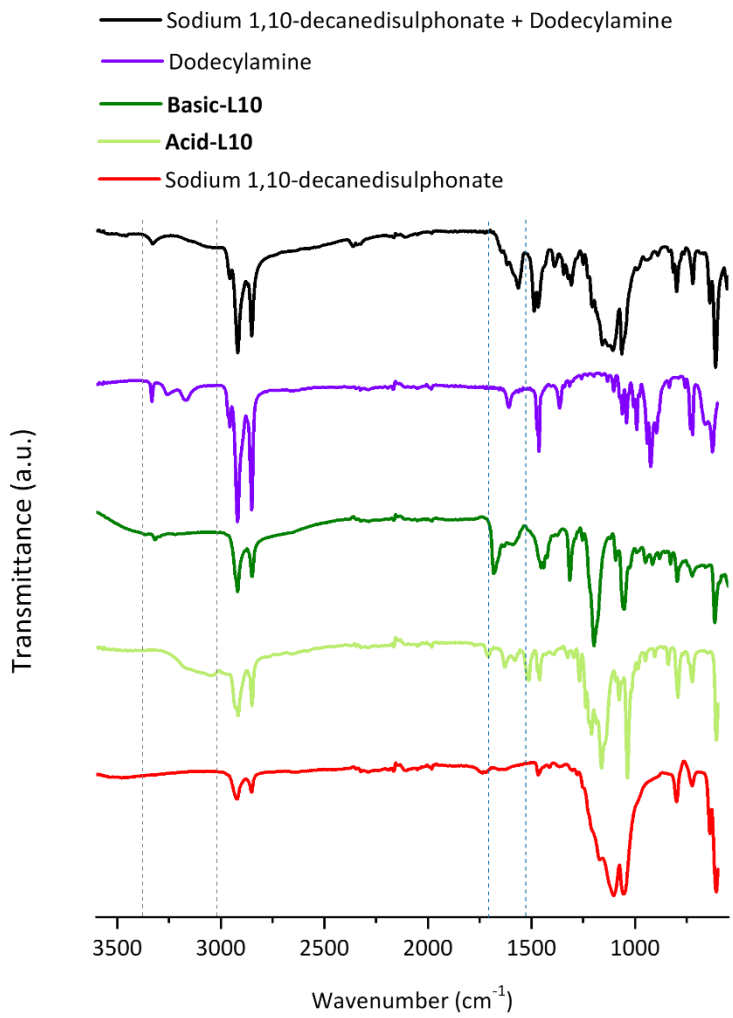

Figure 3.4 FTIR-ATR spectra of the mixture between DS and dodecylamine (1 eq.), dodecylamine, **Basic-L10**, **Acid-L10** and **DS** (top to bottom), the dotted grey lines denote the region for amino groups stretching and bending bands, and the dotted blue lines the most distinctive region between the spectra.

Focusing on the amino region (~3000 cm^{-1}) and comparing the peaks from dodecylamine and **L10**, it appears that the signals in **acid-L10** are shifted to lower wavenumbers and are broader than the ones in dodecylamine spectrum. While, when it is compared to the mixture of **DS** and dodecylamine, the peak position and shape are similar.

When comparing both the **acid** *vs* **basic-L10** with the mixture, wider -NH stretching modes signals are found for the **basic-L10**, while they are narrower for the **acid-L10** and the mixture, since hydrogen bonding seems more plausible in **basic-L10** (indicated with a grey dashed line in the figure). Unfortunately, as the sulfonate region is depicted near the fingerprint of the molecules, it is difficult to assign differences between the three spectra. Nonetheless, in the 1500-1700 cm^{-1} region (indicated with a blue dashed line in the figure), DS shows the absence of bands, and dodecylamine along with **acid-L10** show small and defined peaks. While, focusing on the mixture and the **basic-L10**, a sheerer signal is appreciated. Hence, we believe that the presence of non-protonated amino groups and sulfonates are the reason for this signal differentiation.

Considering the FTIR-ATR comparison of the different molecules and the already described interaction between sulfonates and amines, the presence of interactions and/or associations between **L10** molecules appears very plausible.
However, we must further study how the presence of electrostatic interactions affects the physicochemical properties of the **Ls**. Thus, it would be convenient to study the extent of this interaction with other physical properties.

3.3.2 Study on the pH dependence

As pointed above, pH is a crucial parameter for the characterisation of the three **Ls**. For concentrations between 10^{-3} - 10^{-4} M in water, the measured pH values after the recrystallisation, always range from 6.2 to 7.4. However, at higher concentrations of **Ls** pH is also measured. **Figure A20** is represented as an example.

As commented, at the working pH of this thesis, the sulfonate group (with a pKa lower than 2[301]), bears a negative charge. On the contrary, the higher pKa for the amino group will be responsible for the protonated species. In literature data, pKa for ethylamine, hexylamine and decylamine are 10.87, 10.69 and 10.64, respectively.[308–310] These values are estimated to be lower in the alkyl amino sulfonates ligands.[311,312]

Structurally, **L6** and **L10** can be compared to **L2** known as taurine. Interestingly, taurine is zwitterionic along in the whole physiological pH range. In contrast, amino acids that bear a carboxylic acid and an amino group, are unionised over the physiological range.[284]

The **Ls** species upon pH dependence are illustrated in **Scheme 3.5**. It is important to notice that the sulfonate group, with a very low pKa value, will be completely ionised. Hence the cationic species is not expected during this work. Generally, in amino-based surfactants with weak acidic character, the presence of the cationic species will strongly depend on the pH of the media.[313] Therefore, mainly the zwitterionic and the negative species are expected to be in equilibria around the studied pH values here, which should be displaced to the zwitterionic species around the physiological pH.

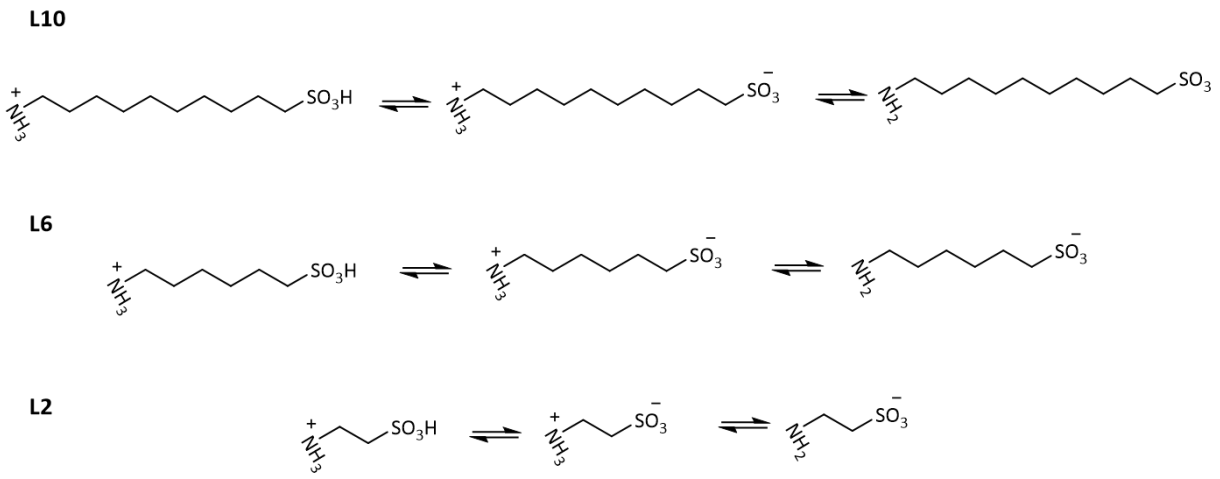

Scheme 3.5 Scheme of **Ls** species at distinct pH values: acid (left), zwitterionic (middle) and basic (right).

Moreover, it is described in literature that a zwitterionic molecule only achieves maximum mole fraction of neutral species when the separation of pKa units between the groups is 5 units.[314] It would be the case faced by our molecules as the pKa values of both groups are alike.

To further study the pH related behaviour of these ligands, a titration with NaOH was performed for the three ligands (**Figure 3.5**). For the titration, 0.5 mM of the corresponding ligand in a solution of $NaNO_3$ 0.1 M, was pre-acidified with HNO_3 and finally titrated with previously standardised NaOH solution at 0.998 M.

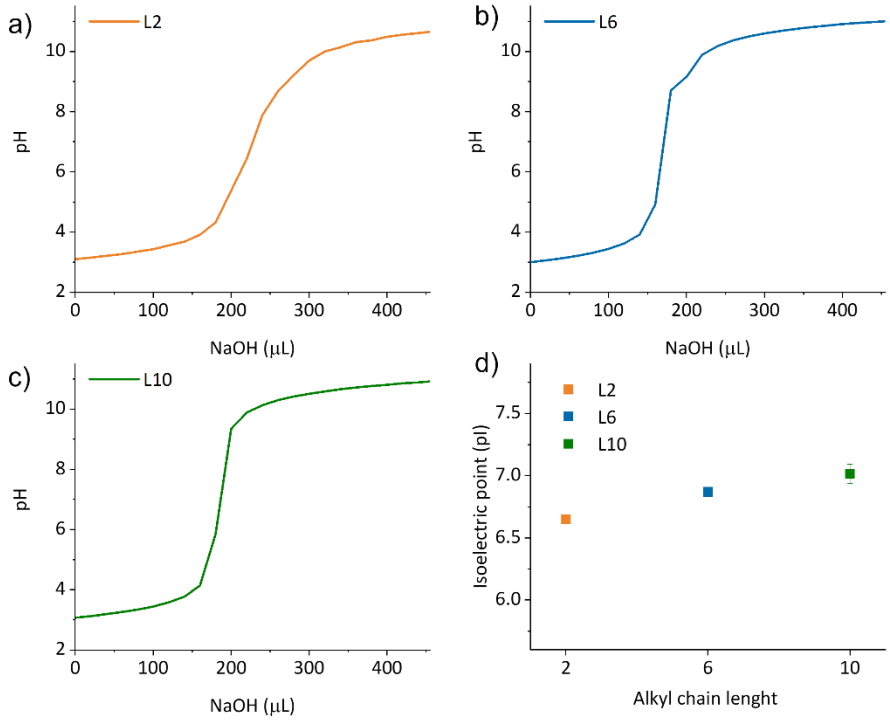

Figure 3.5 pH titration of **Ls** at 0.5 mM with NaOH 0.1 M., starting at pH = 3 after the addition of HNO_3: for (a) **L2** (b) **L6** and (c) **L10**. And (d) representation of the pI *vs* the carbon number in the corresponding alkyl chain.

In the titration plots, a single leap is observed. In fact, in the titration curve of diprotic amino acid, only one pH jump is predicted. The apparent pKa values can be determined from the titration curves, it will correspond to the pH value at the point of semi-equivalence, or what is the same, at the halfway before or after the inflexion point of the curve (related to pKa1 and pKa2 of the molecule).

The inflexion point of the sigmoidal corresponds to the isoelectric point (pI) in which the net charge of the molecule is zero. Mathematically, in a diprotic species, the pI can be calculated from the average of the pKa of both groups. And graphically, by calculating the equivalence volume, which is found at half point of the pH jump and can determined by the first and second derivate of the curve or by using a sigmoidal fit.

The pKa's determination was not performed in our case of study because the total positively charged species holding the protonated sulfonic acid exhibits a too low pKa value to be obtained in water. However, as the pH jump of the species was present in the titration, we could graphically calculate the pI.

We decided to fit the graph to the sigmoidal function and obtain the midpoint value, which corresponds to the sum of the obtained A1 and A2 divided by two. The pI of the **Ls** was 6.65,

6.87 and 7.01 for **L2**, **L6** and **L10**, respectively. This resulted in a higher acidic character in the sequence **L2** > **L6** > **L10**.

3.3.3 Solubility and counterions

We evaluated the solubility of the ligand in Milli-Q water at room temperature. Milli-Q water was added in small portions to each previously weighted ligand until total dissolution was observed. Before the next water addition, the samples were sonicated for several seconds and let rest for one minute to ensure no precipitation. Solubility was surprisingly high for **L2** and **L6**, with a value of 2.88 and 2.18 M, respectively. On the other hand, **L10** showed a low water solubility lower than 5 mM. At higher concentrations, **L10** was visually dispersed and after several hours visibly precipitated. In this case, we also studied the solubility when the temperature was increased, obtaining a solubility of 75 mM at 29.4 °C which rises to 200 mM at 60 °C. The low solubility of the longest ligand **L10** might be explained by the amphiphilicity character due to the C10 hydrophilic chain.

Already discussed interactions between molecules could be responsible for their peculiar behaviour. The interaction between an ion and a permanent dipole is higher than the interaction between two ions: 50-200 KJ/mol to 25 KJ/mol, respectively.[306] So, it is reasonable to think that solvation between sulfonate or amine group and water could be more intense than the intramolecular interaction of the two ions. Still, it is difficult to determine exactly because the interaction involving polar groups is high and directly influenced by ionisation.[306] In fact, it is reported that the self-association of zwitterions can even modify hydrophobic properties.[315] This, is usually driven by the charge density difference of the groups, which in **L10** are 10 C apart. And, although the interaction between charged groups is usually described to take place at short range, the flexibility in the long carbon chain could also play an important role.

Zwitterions can be classified into 4 types. Type 1 is an ampholyte while the other types correspond to zwitterionic ampholytes. Specifically, types 3 and 4 are strong acids and bases capable of forming zwitterions, both in water and octanol phases. However, the main difference between type 3 and 4 is that type 4 can compensate the two charges by resonance forms or by physically being in contact with other molecules. Besides, when charges can compensate, they show an intensely unlike lipophilicity profile.[306,315] These last rationalisation, may justify the minimal solubility of our longer ligand **L10**.

Concerning the **Ls**' counterion, sulfonate might attract up to 8 molecules of water per sulfonate group. However, in comparison to other groups from zwitterionic molecules, such as the carboxylate group, the attraction to water molecules is weaker. In the same line, studied by Shao *et al.*, the interaction of sulfonate groups and cations do not strongly depend on the type of cation; having the same sensitivity for the coordination of Li^+, Na^+, K^+ or Cs^+.[315] Thus, the expected counterion to accompany the sulfonate group in **L2**, **L6** and **L10** is sodium since sulfonation is carried out by the reaction with Na_2SO_3. In the case of ammonium cation, the expected counterion is Cl^- because HCl is used in the cleavage of phthalimide in the last step of ligands synthesis. Nonetheless, to some extent, Br^- should be considered as a possible counterion.

3.3.4 Aggregation studies

In this section, we consciously studied by several techniques the aggregation that may be occurring in our system. After the results reviewed above, no aggregation was suspected neither for **L2** or **L6**. Nonetheless, **L10** behaviour made us thoroughly study the aggregation process to discern if the actual interactions occurring between **L10** molecules were generating a highly ordered structure, for instance in form of micelles or bilayers.

3.3.4.1 Study of alkyl amino sulfonate ligands by pendant drop method

The pendant drop method allows the determination of the surface tension (γ) vs. the concentration of the analysed substance. Surface tension originates from the imbalance of the molecular attractive forces within a phase compared with those across the phase boundary (interface). In this method, the interfacial tension is determined by video image processing of a pendant drop of a solution of the studied compound after the analysis of the profiles of axisymmetric droplets. This method is based in Young-Laplace equation, further detailed in section 8.2.16.[316] In a collaboration with Dr. Ramon Pons from the *Institut de Quimica Avançada de Catalunya* (IQAC), we had the opportunity to study the surface tension of the solutions of the ligands at a vast range of concentrations.

The device (in **Figure A21**) enables the determination of eight concentrations in a unique experiment and so, they can be plotted in front of increasing concentration. Droplets are formed at the tip of straight cut Teflon tubes and are kept in a thermostatic water-saturated atmosphere. The stabilisation of the plot of surface tension as a function of the logarithm of

concentration is an indication of surface saturation that has been associated to the valued of critical aggregation concentration (CAC), although this association is subject to criticism.[316–320]

L10 solutions were prepared in three different media: Milli-Q water, phosphate buffer (PBS) pH and in a NaOH solution at 0.1 M. In Milli-Q water, **L10** was not entirely solubilised at concentrations above 1.5 mM whereas the use of PBS buffer allowed a better solubilisation.

The results for **L10** in water and PBS buffer solutions showed comparable γ values (**Figure A22**). The initial value in both media, at the lowest tested concentration, was lower than the γ for pure water (72 mN/m at 25 °C[321]). The surface tension was slightly reduced at higher concentrations of **L10**; from 64 to 50 mN/m in Milli-Q water, and 65 to 54 mM/m in PBS buffer, at ranging concentrations 0.075 to 10 mM.

However, **L10** in PBS showed a significant decrease with time and the surface tension was then measured for several hours and showed how the γ decreased over time (**Figure A23**). In the pendant drop method, the evaporation of droplets could lead to the reduction of γ values due to the increase in concentration, although there is a humid atmosphere, we verified that the size did not change significantly with time, therefore evaporation was not the cause. A plausible explanation is a slow organisation of molecules of the ligands in the surface of the droplets due to equilibrium between monomers in solution and other substructures that could be adopted. Also, near the surface, the monomer reorganisation at the interfase could be a rate-controlling process. In fact, it is reported that over a period of time, γ will decrease to an equilibrium value, and this period can range from milliseconds to days depending on the surfactant type and concentration.[322]

To avoid possible mixture of species due to the presence of the protonated and deprotonated species, we decided to measure the surface tension of our **Ls** solubilised in a standardised solution of NaOH 0.1 M. **L2**, **L6** and **L10** droplets of increasing concentrations solutions (8 µM to 10 mM) were hanged and measured over time at 25 °C (**Figure 3.6**).

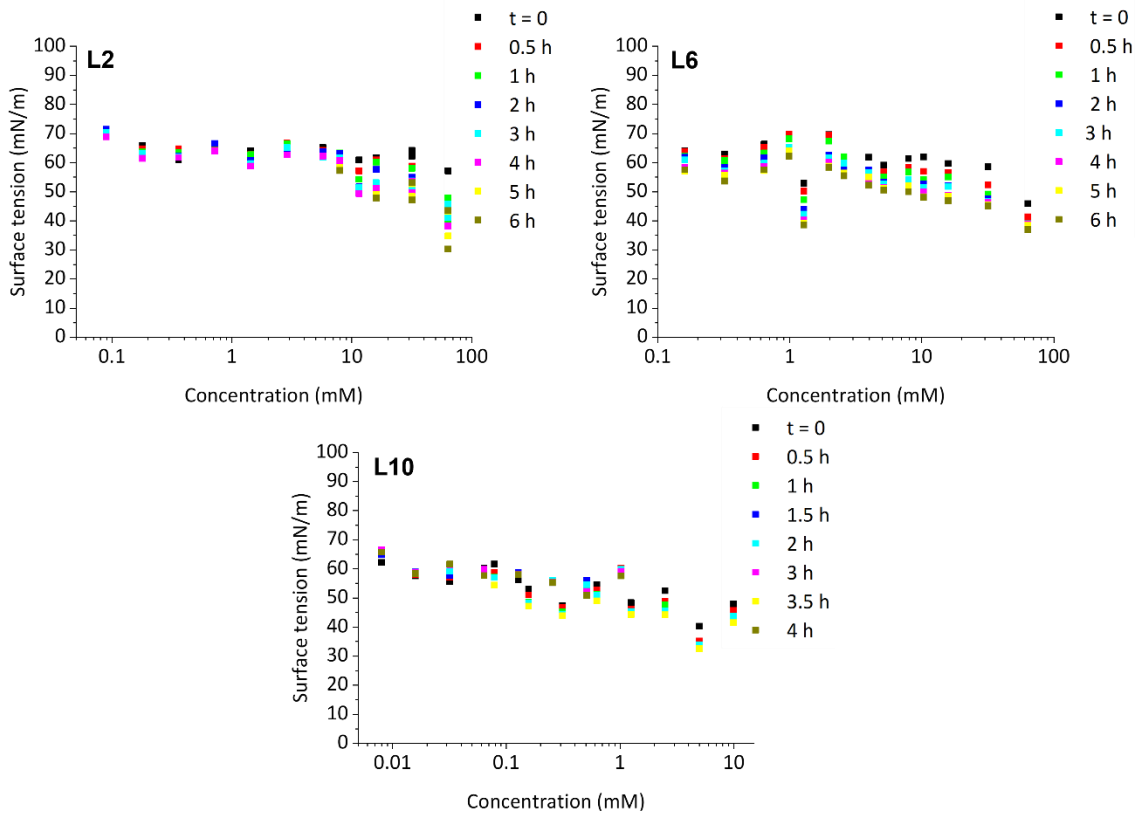

Figure 3.6 Surface tension *vs* concentration over time of **L2**, **L6** and **L10**, solved in NaOH (0.1M) measured by the pendant drop method at 25 °C.

A decrease in γ was noticed for the three ligands. Highly soluble ligands **L2** and **L6** studied from 0.08 to 100 mM, revealed lowering the γ from 70 to 50 mN/m for **L2**, and from 68 to 38 mN/m for **L6**, both measured at time six hours. Finally, **L10** dropped γ from 61 to 47 mM/m ranging from 0.008 to 10 mM. The γ decrease was noticed not only at high concentrations but along time in each concentration. The reduction along time was smaller than the one observed when PBS was used but still significant. Again, the values at the lowest concentration of **Ls** were already below pure water values in the three cases.

It is worth mentioning that none of the experiments showed a defined change in the surface tension at the studied concentrations. In the three ligands, two distinct tendencies in the plot might be observed; the tendency disruptions occur close to 3 mM, 1 mM and 0.1 mM for **L2**, **L6**, and **L10**, respectively. However, the slope change was not evident enough to resolve an accurate CAC value.

The intrinsic variability of the system, as well as the slow kinetics faced, hampered the determination of a precise CAC value. Also, we presume that because of the small size of the

Ls molecules, the associations and/or aggregates that they might form will be particularly small and difficult to determine.

3.3.4.2 Study of alkyl amino sulfonate ligands by conductimetry

Conductimetry is a technique that measures the specific conductivity (κ) of a compound in solution, and it is a quite precise technique for ionic surfactants that act as conventional electrolytes. The electrical conductivity of a solution is measured in front of increasing concentrations. It is extensively established that the conductivity of a solution is directly proportional to the concentration of ions in a straight line. However, if aggregates are formed, a breaking point in the measured conductivity is evidenced. Graphically, it will show as two straight lines with different slopes, whose intersection is correlated to the CAC value. When it is reached, the slope increases less abruptly, modifying the obtained line. This is supported by the fact that developed aggregates, such as micelles, are less mobile in an electric field than discrete surface-active ions because of their larger sizes.[323,324]

The determination of the conductivity of the **Ls** at increasing concentrations was performed by measuring each solution at 25 °C (**Figure 3.7**).

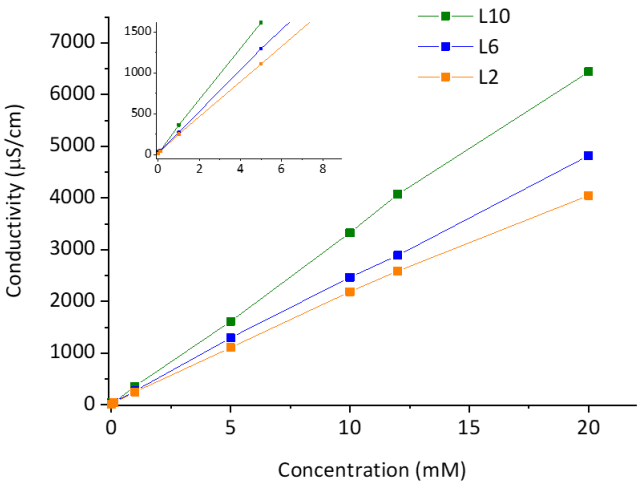

Figure 3.7 Specific conductivity vs concentration plot for **L2**, **L6** and **L10**.

In our study, the conductivity of each ligand linearly raised with increasing concentrations. Moreover, the measured conductivity increases in the following order **L10** > **L6** > **L2** (**Figure 3.13**). This behaviour was unforeseen because the number of ions should be equivalent for the three ligands since the groups conferring the charges are alike. Nonetheless, for some ionic

liquids it is reported that conductivity increases with alkyl chain lengths that was considered as a plausible explanation for the behaviour observed in the ligands.[325,326]

Although conductimetry has been historically used for the determination of CMC, it faces important limitations. Conductimetry is not sensitive enough for those surfactants with a low value of CMC or for solutions with a high amount of electrolyte, for which the sensitivity of the technique becomes too low at high ionic strength. Additionally, ionic surfactants micellisation is prevented by electrostatic repulsions between head groups and counterions highly affecting this process.[323,324,327] It is also reported that some surfactants lack a critical point, attributed to a stepwise aggregation.[328] It is believed, that in our case, the high ionic strength of the measured solutions could hindrance the observation of an aggregation process, if happening.

3.3.4.3 Study of alkyl amino sulfonate ligands by light scattering

Scattering of the **Ls** was studied by fluorescence. The excitation and emission wavelengths were set at 500 and 510 nm respectively. At such wavelengths, no absorption nor fluorescence were detected in none of the **Ls**, and so the recorded measure corresponds to the scattering occurring in solution. An abrupt change in the scattering of increasing concentration samples must be related to the appearance of aggregates, and so to a variance in the slope of the plot. Nonetheless, we obtained a flat signal *vs* concentration for the three ligands, as seen in **Figure 3.8**.

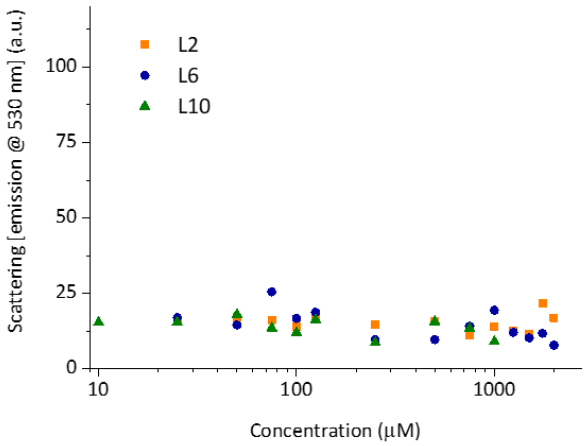

Figure 3.8 Ls scattering plot measured by fluorescence at increasing concentrations.

None of the three ligands showed variation in the scattering values at increasing concentrations. At the studied concentrations, all the samples scattered in the range of pure water, and in none of the ligands the tendency was disrupted as predicted when aggregates appear at a certain CAC.

3.3.4.4 Study of alkyl amino sulfonate ligands by fluorescence

Ligand **L10** was studied in more detail because its structure and the low solubility indicated that a particular organisation/aggregation of the molecules might be occurring. To achieve it, a specific probe suitable to detect the appearance of ordered structures at very low concentrations was used. We reproduce an experiment from Barnadas *et al.*,[307] in which the fluorescence changes of a water-soluble dye are measured. The used probe was 8-hydroxypyrene-1,3,6-trisulfonate (HPTS), known as pyranine, that has little influence on aggregation.[328] HPTS permits to evaluate the aggregation of a molecule by scanning the photophysical changes occurring to the dye since the excited states of the HPTS dye respond differently to distinct types of aggregates. HPTS exhibits two peaks in its emission spectrum corresponding to excited HPTS. One peak at 510 nm corresponds to the RO^{-}* form that bears four negative charges, and a second peak at 440 nm after the emission of ROH* species carrying three negative charges.

In our case, all the samples were prepared using a PBS buffer. **L10** concentrations ranged from 2 to 1050 µM and HPTS concentrations were 0.56, 5.6 and 88 µM for three independent experiments. All the samples were excited at 350 nm and the emission was registered from 360 to 650 nm (**Figure 3.9**).

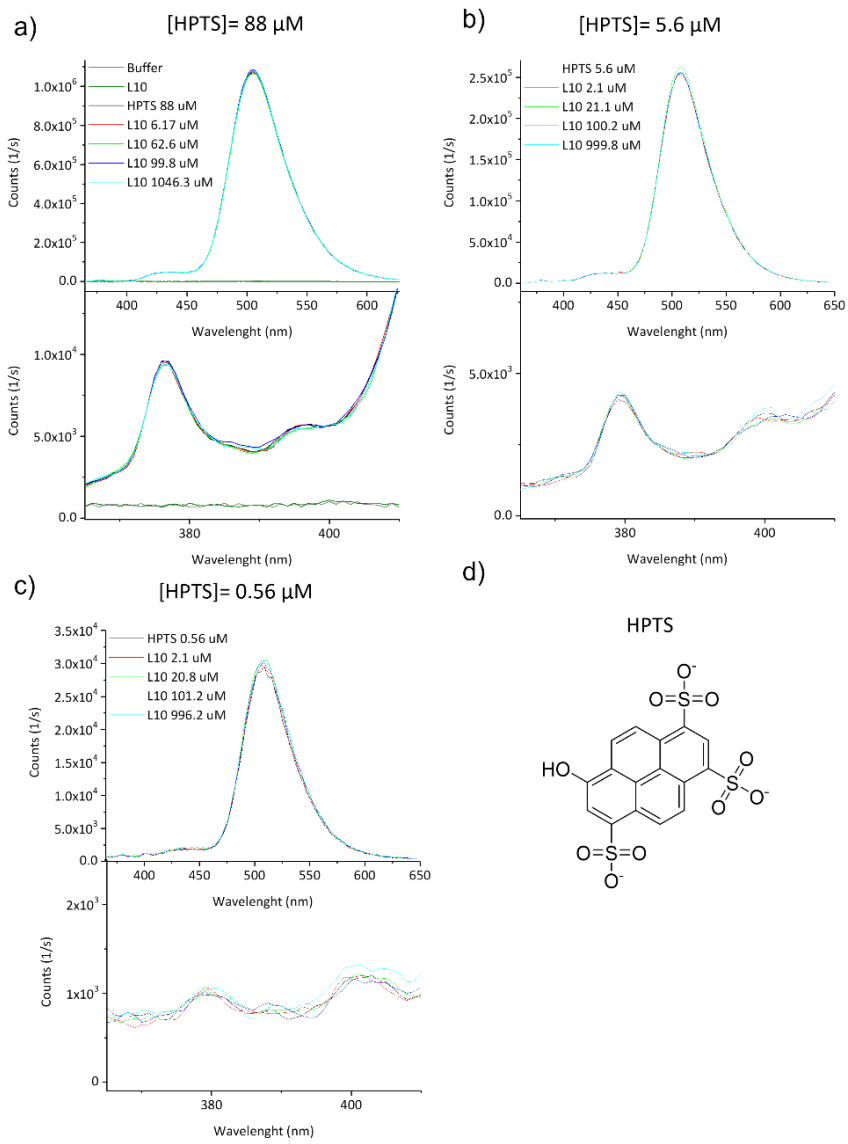

Figure 3.9 Fluorescence spectra of HPTS at (a) 88 µM, (b) 5.6 µM and (c) 0.56 µM and **L10** at specified concentrations. Bottom captions correspond to amplified 365-410 nm region, and (d) corresponds to the HPTS structure.

The results showed no significant variation in the spectra of HPTS* at any of the HPTS concentrations. Neither the intensities of the HPTS peaks were modified after the addition of **L10**. Thus, this behaviour was associated with no-appearance of aggregates.

Nevertheless, the invariance in the HPTS spectra could be justified by the presence of sulfonate groups in both molecules, **L10** and HPTS. The interaction between the amino group in **L10** and the sulfonates in the dye could be undermined by the interaction between the two groups of the ligands. If the sulfonate of the dye and the amino groups in the **L10** were interacting

between them, forming dimers or another kind of association, HPTS bands could remain unchanged.

3.3.4.5 X-ray scattering: small and wide angle

Finally small angle X-ray scattering was employed to gain insights into the organisation and behaviour of the prepared ligands. It is an analytical technique with which the structure of a system of particles (regarding their size and/or shapes) can be determined. In general, when a non-crystalline sample is irradiated with X-ray, scattering from differences in electronic density regions can be observed, which is related to domain form and/or domain correlation. The angle-dependent intensity of the scattered radiation is measured and from it, characteristic distances can be deduced. In SAXS experiments, the elastic scattering of X-rays through a sample is registered by a detector that records the scattering intensity at small angles (understood as those below the smallest angles usable in classical diffraction, that is below 5°), in front of the angle that is expressed as a function of the scattering vector called *q*.[329] Then, Wide angle X–ray scattering (WAXS) offers information about the scattered intensity at angles wider than SAXS. WAXS is employed for crystals or semi-crystalline compounds and provides insight below the micron range.

Simultaneous SAXS-WAXS experiments were conducted at the NCD-Sweet beamline at Synchrotron ALBA facilities, within the proposed project "Unveiling the structure of metallosurfactant aggregates and metallosomes". Due to time constraints only the preliminary analysis of the data has been performed. As general trend the data has been obtained after subtracting the background and averaging ten measurements.

Distinctive behaviour was observed for the three **Ls** when measured solubilised in water. **Figure 3.10** shows the obtained spectra for the three ligands.

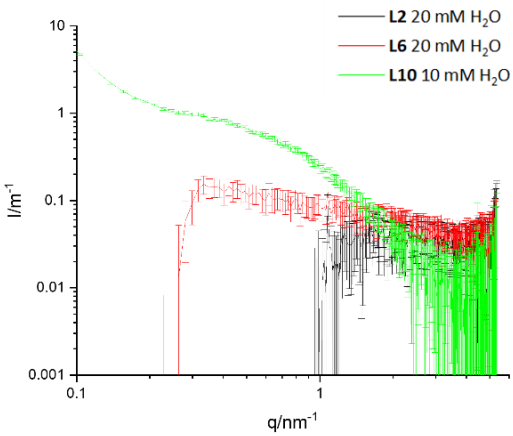

Figure 3.10 SAXS intensity as function of dispersion vector modulus q for **L2** and **L6** (20 mM), and **L10** (10 mM) in Milli-Q water.

A lack of signal has been observed for **L2** and **L6**. With regards to **L10** a peak, which seems to be related with the presence of organisation appears. At plain sight, the signal seems to be related with the presence of spheroidal micelles however random aggregation cannot be discarded. For that reason, **L10** plot will be fitted to a model to discern which type of organisation or aggregation acquires.

It should be noted that the maximum concentration in which **L10** could be measured corresponds to 10 mM due to solubility impediments. Nonetheless, as detailed previously in this chapter its solubility at basic pH is superior. This behaviour might be also related to the adoption of a different organisation by **L10**. Hence, the ligand solubilised in $NaOH_{(aq)}$ at three different concentrations has also been analysed (**Figure 3.11**).

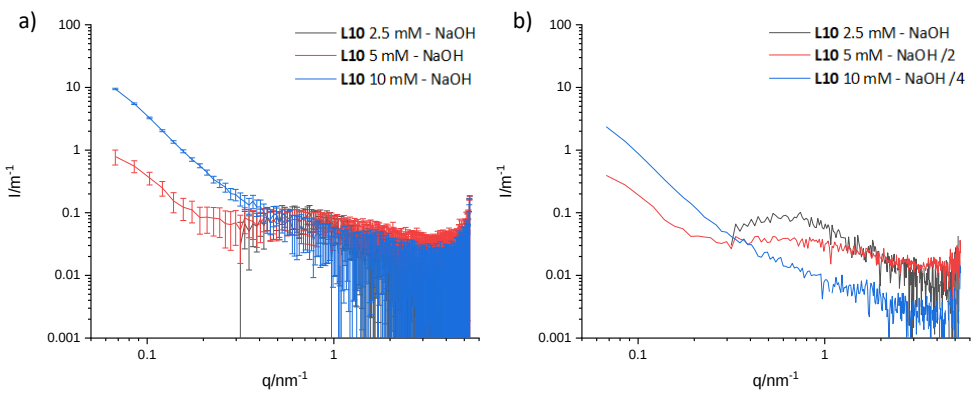

Figure 3.11 SAXS intensity as function of dispersion vector modulus q for **L10** solubilised with 0.1 M $NaOH_{(aq)}$ at (a) 2.5, 5 and 10 mM (b) escalated to 2.5 mM concentration to compare the obtained graphs.

Some variations in the spectra when **L10** ligand is solubilised at basic pH appear, which seem to be originated by an occurring phase transition. It has not been fully determined yet, but said

difference is likely related with a spherical to laminar transition. Nonetheless, the fitting to models must be conducted to confirm said theory.

Solid samples were also measured by SAXS-WAXS. To do so, solid containing sealed quartz capillaries were prepared. On **L2**, no SAXS signal was observed, only well-defined WAXS ones (**Figure A24**). This indicates that the ligand adopts a crystalline structure when in solid, but that the crystallites of the sample are exceedingly small, as they are not observable by SAXS. Contrarily, **L6** does show signals on SAXS in addition to the WAXS ones (**Figure A25**). Two different peaks can be observed, one at 2.21 nm^{-1} and its first harmonic at 4.41 nm^{-1} corresponding to distances of 2.84 nm. This suggest that, in this case, the crystalline structures formed by the ligand are larger than on **L2**. Likewise, on **L10** both SAXS and WAXS peaks are observed (**Figure A26**). However, the distances of the SAXS peak are almost half, since a peak of 4.44 nm^{-1} corresponding to distances of 1.41 nm is observed. If we assume that said SAXS distances correspond to the crystallite size, this will indicate that the crystals formed by **L10** are smaller than **L6.**

In conclusion, the obtained results suggest that **L2** does not present an organisation at large distance in neither solid nor solution while on solid it does shows some kind of structural arrangement. **L6**, which in solution does not present peaks in SAXS, when analysed as a solid it shows both long- and short-range ordering. Nonetheless, this large range ordering probably is derived from their crystallite size, not from supramolecular arrangements. Finally, **L10**, similar information as for **L6** is extracted.

3.4 General remarks

In this chapter, we have described the synthesis of a new family of alkyl amino sulfonated ligands accomplished from a straightforward synthetic route. Many attempts in the amination of a chloroalkyl position with a sulfonated moiety were undertaken. However, because of the low reactivity and the difficult by-products separation, the strategy was reconsidered. The precursor used was 1,10-dibromoalkane instead of its dichloro- analogue, and Gabriel synthesis for amine preparation followed by sulfonation was the final working strategy.

The three ligands, **L2**, **L6**, and **L10** were fully chemically characterised, and the features related to their structure and behaviour were further covered.

Interactions faced by them were seen by a great number of techniques such as MS and reproduced using analogue molecules by FTIR-ATR. It was seen that the nature of the groups plays an important role in the distribution of the molecules in solution.

Moreover, we demonstrated how the pH role is an extremely important parameter to control. Among the equilibrium species that could be faced by the molecules, the zwitterionic and the negative form were the two actual species to be found in solution at the working pH range. It was determined that at physiological pH the **Ls** will bear a totally ionised sulfonate group. On the other hand, the amino moiety would rather be ionised, yielding the zwitterion form at a slightly acidic pH. The determination of the isoelectric point, where the zwitterion form must be the predominant species, showed a similar value for the three ligands. This evidenced that the isoelectronic point, and so the pKa of the groups, was not notably affected by the carbon chain length.

The study of the solubility of the ligands revealed low values for the longest ligand **L10**, which is in fact sparingly soluble in water unless extreme pH values. Though, it was in contraposition to the great solubility in water of **L2** and **L6**. The solubility features were thought to be extremely dependant on the high amphiphilic character of **L10** and the interactions occurring between the sulfonate and the protonable amino group.

Finally, a deep study of the ligands' aggregation was performed to discern if the association of molecules was mainly directed by discrete interactions between the ionic and polar group of the **Ls**, or if aggregation generate supramolecular structures. In the case of **L2** and **L6**, they were theoretically discarded but it was interesting to compare the results with the longer ligand **L10**. In fact, in the case of **L10**, the slight solubility and the contained precipitation observed pointed to a more than plausible effect.

Several studies were performed to detect aggregation, thoroughly described in this chapter. Pendant drop, conductimetry, scattering and fluorescence were conducted willingly to find an alteration in the measured property along with growing concentrations that allows the intersection determination between two tangents. Nonetheless, the studies contradicted the presence of aggregates in none of the three ligands, even when using a fluorescence probe employed to detect pre-aggregation states.

However, the reduction on the surface tension (measured by the pendant drop method) indicated that all three **Ls** must be acting as standard surfactants. The surface tension

reduction, following the sequence **L10** > **L6** > **L2**, agreed with the expected higher amphiphilicity at increasing number of carbons. In addition, the following preparation of the corresponding complexes will benefit from the surfactant behaviour observed by the ligands.

4. PLATINUM(II) ALKYL AMINO SULFONATED COMPLEXES: METALLOSURFACTANTS

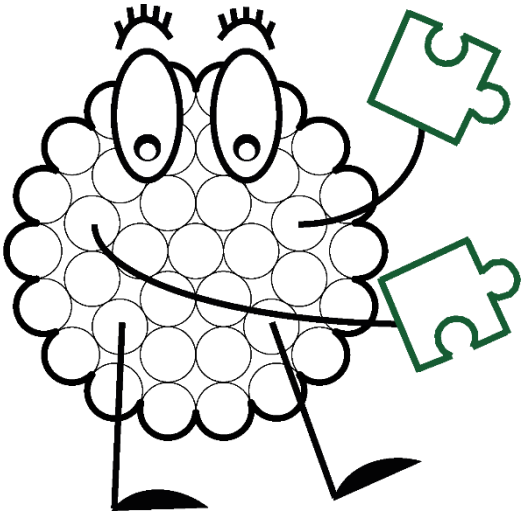

Platinum complexes bearing alkyl chains have been reported in several works, nonetheless in the present chapter we report the preparation of the first alkyl amino sulfonate Pt(II) complexes. Along this chapter, the developed research is accurately portrayed and several features, from the synthesis to the surfactant capacity of this novel complexes, are disclosed.

4.1 Preparation of Pt(II) alkyl amino sulfonated complexes

The synthesis, characterisation, and behaviour of the *cis*-Pt(II) complexes prepared with the alkyl amino sulfonate ligand family (**Ls**) are detailed in this chapter. Hereinafter, the *cis*-Pt(II) family will be shortened as **Pt-Ls**, being **Pt-L2**, **Pt-L6**, and **Pt-L10** when referring to the metallic complex composed by **L2**, **L6**, or **L10**, respectively.

The aim was to prepare a family of Pt(II) complexes with potential surfactant and cytotoxic properties that could boost one of the biggest challenges facing conventional medicine and DDS, the poor drug solubility.[83]

The followed steps to obtain the final **Pt-Ls**, the mechanism by which they are obtained, and finally, the study of their likely aggregation is described.

4.1.1 Disclosing the structure choice

For the final structure of the **Pt-Ls**, the general form *cis*-[PtX_2N_2] was taken as the reference molecule. This general form was already encompassed into the structure-activity rules conceived by Cleare and Hoeschele in 1973, in which neutral complexes containing *cis*-leaving groups and inert N-H donors exhibited high anticancer activity.[330]

The final structure of the **Pt-Ls** family bears two alkyl amino sulfonate ligands for each Pt(II) atom, and two iodo ligands located in *cis* position, **Scheme 4.1**.

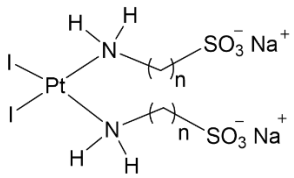

Pt-L2: n = 2
Pt-L6: n = 6
Pt-L10: n = 10

Scheme 4.1 Structure of expected **Pt-Ls** with general formula *cis*-[PtI_2L_2], where ligands are the ligands **L2**, **L6**, and **L10**, previously synthesised.

The so-called first generation of platinum chemotherapeutics holds two non-leaving groups that influence the nature of the platinum-DNA adducts, and two leaving group ligands, which contribute to the reaction kinetics and the lipophilicity of the molecule. In our case, the non-leaving group will be anchored to Pt(II) by the lone pair electrons from the nitrogen atoms as

ammonia in cisplatin. The ligand will also provide water solubility to the whole molecule through the sulfonated group. Differentially from cisplatin, the leaving groups will be iodide units. The substitution of iodo by chloro ligands, which would have only added one step to the final reaction was discarded: the presence of iodine atoms gives it a greater lipophilic character and, as it is known, a slower aquation kinetics, issues that are further detailed in this chapter. As explained in section 1.2.2, the nature of the leaving group has a crucial role in the mechanism of action of cisplatin. For the final structure of the **Pt-Ls**, the two halides were considered: chlorine and iodine. The use of chloride would have given us a more straightforward comparison to cisplatin. However, for our final purpose, iodide, a less labile group compared to chloride, will confer a higher lipophilic nature for the final complex and will help the internalisation of the **Pt-L10** in the preparation of mixed vesicles.[44]

The electronic configuration of Pt(II), [Xe] $4f^{14}$ $5d^{8}$ drives the final geometry in our complexes, with square-planar coordination, preferred for d^{8} transition metals. The amino group of **Ls** will be coordinated to Pt(II), and the reaction will be conducted at basic pH to assure the complete deprotonation of the primary amine. Likewise, sulfonate group was considered as non-coordinating, since it is rarely found directly coordinated to a metal ion.[282,331]

4.1.2 Synthesis of Pt(II) alkyl amino sulfonated

The synthesis of the **Pt-Ls** family started with the preparation of the complex with the longest chain ligand, **L10** to finally obtain complex **Pt-L10**. Once, its synthesis and purification were optimised, the same synthetic strategy was extrapolated to the preparation of the analogue complexes **Pt-L2** and **Pt-L6**.

Two different platinum precursors, K_2PtCl_4 and $PtCl_2$, were initially assessed in the preparation of **Pt-Ls**. During the optimisation process of the complexes preparation 2 equivalents (eq.) of ligands per 1 eq. of Pt atom were maintained as a general trend. In all cases, the alkyl amino sulfonate ligands were basified previous to the addition of the Pt(II) precursor to ensure the formation of the amine.

The first synthesis strategy attempted was performed with K_2PtCl_4 as Pt(II) precursor, with 2 eq. of ligand per platinum atom, and 2.5 eq. of NaOH per ligand. The solvent used to solubilise the Pt(II) precursor was water, while water/MeOH was employed for the mixture of **L10** and NaOH, since MeOH is known to avoid aggregation. The complexation reaction was conducted at 50 °C for 18 h, leading to a final yellow solution with a dispersed dark solid. Filtration was

attempted but the precipitate contained very small particles and it was not possible to isolate them. Also, the use of the centrifuge gave similar results. So, we decided to lyophilise the solution to dryness, thus obtaining two different solids in powder form. They were separated by gently adding a small portion of MeOH, in which the yellowish powder was solubilised, but the dark powder was sparsely dispersed. The yellow solid was characterised and the coordination of the primary amine from **L10** to Pt(II) was confirmed by positive ESI-MS (**Figure A27**). However, we could not control the isomer synthesised, most probable obtaining a mixture between *cis* and *trans* isomers, whose separation would have been extremely challenging. Moreover, the fact that we used a high number of equivalents of **L10** rendered the presence of uncoordinated water-soluble ligand, also difficult to separate from the complex.

Another attempt was conducted using $PtCl_2$ as the metal precursor. The reaction was based on the synthetic procedure described in a previous work of our group where the synthesis of Pt(II) sulfonated phosphines was reported to yield the pure *cis* geometry product.[266] However, because of solubility issues, we used water as the solvent, instead of DMSO. In this case, the **L10** solution was basified with 1.7 eq. of NaOH to reduce the excess of base, which could undesirably react with the platinum precursor. To this solution, a $PtCl_2$ solution (1 eq. respect **L10** solution) in water was slowly added at room temperature. Then, the resulting mixture was heated under stirring at 80 °C for 12 h and allowed to cool at room temperature. Nonetheless, distinctly from the reported reaction with the sulfonated alkyl phosphines ligands, no precipitation was distinguished even with the addition of ethyl acetate or acetone. Finally, the obtained yellowish solution was lyophilised, and ESI-MS showed mainly uncoordinated free ligand (**Figure A28**). Since the strategy was not successful, a new methodology had to be proposed.

Besides, finding a method to yield the *cis* isomer in our complexes was considered crucial. So, a modified *Dhara's method* was applied for the purpose. Dhara's method (**Scheme 4.2**), described by *Dhara* in 1970, is the most common method for preparing cisplatin. It is a multistep method, in which chlorine atoms in $[PtCl_4]^{2-}$ are substituted by iodides after the reaction of K_2PtCl_4 with KI. Then, in the reported method, ammonia or ammonium hydroxide is added to $[PtI_4]^{2-}$, which by the *trans*-effect drives to *cis*-$[Pt(NH_3)_2I_2]$ that is finally treated with $AgNO_3$ and KCl to yield *cis*-$[Pt(NH_3)_2Cl_2]$, as seen in **Scheme 4.2**. In the procedure, the

conversion from $[PtCl_4]^{2-}$ to $[PtI_4]^{2-}$ is the directing step because the higher *trans*-effect showed by iodine with respect to chlorine.[332,333]

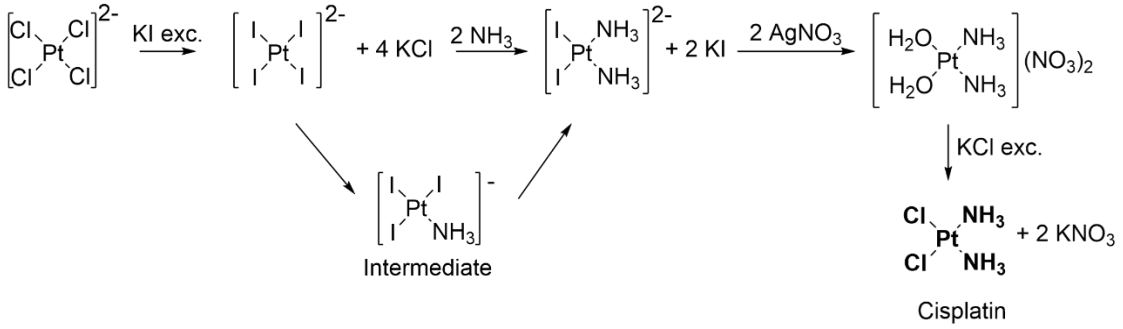

Scheme 4.2 Synthetic scheme of Dhara's method for the preparation of cisplatin.

Following Dhara's method, K_2PtI_4 was prepared *in situ* by treating K_2PtCl_4 with KI in water. An excess of KI is needed to promote the ligand exchange, however, there is controversy in the equivalents added, which in the literature ranges from 5 to 10.[333–336] It is reported that a stoichiometric amount of KI yield a brown impurity, but an excess stabilises $[PtI_4]^-$ specie.[337] In our case, an excess of KI (5 eq.) was added to a solution of K_2PtCl_4 in water because we observed that when the quantity of KI is higher, the colour change, from orange to brownish, experienced by the solution went back to the starting colour. Moreover, it has to be remarked that the reaction time must not exceed half an hour. Thus, the reaction was usually finished after 15 min, noticed by the colour change. Then, *in situ* formed K_2PtI_4 was added dropwise to a solution with the basified **L10** (2 eq. of ligand for 1 eq. of platinum atom and 2.05 eq. of NaOH for each **L10**, pH ~10-11). The reaction was first conducted in a mixture of MeOH and Milli-Q water. MeOH is a well-known solvent preventing vesicle aggregation, and for this reason, was used in a small percentage (less than 20%) during the reaction.[338] However, after optimising the reaction conditions it was proved that the reaction occurs equally in the absence of MeOH, so finally it was carried out without adding it. Afterwards, we discovered that the reaction was always taking place below the CAC of **Pt-L10**, which agreed with the no need for MeOH/water mixture. The mixture was let 6 h to react under stirring, when a colour change was observed: from yellow to a darker yellow/green solution. Longer and shorter reaction times were also tested but they resulted in unfinished reactions or yielded a total dark dispersion. The reaction (**Scheme 4.3**) was carried under N_2 atmosphere, and all the solvents were previously degassed. Moreover, the solutions were kept in dark while the reaction was performed.

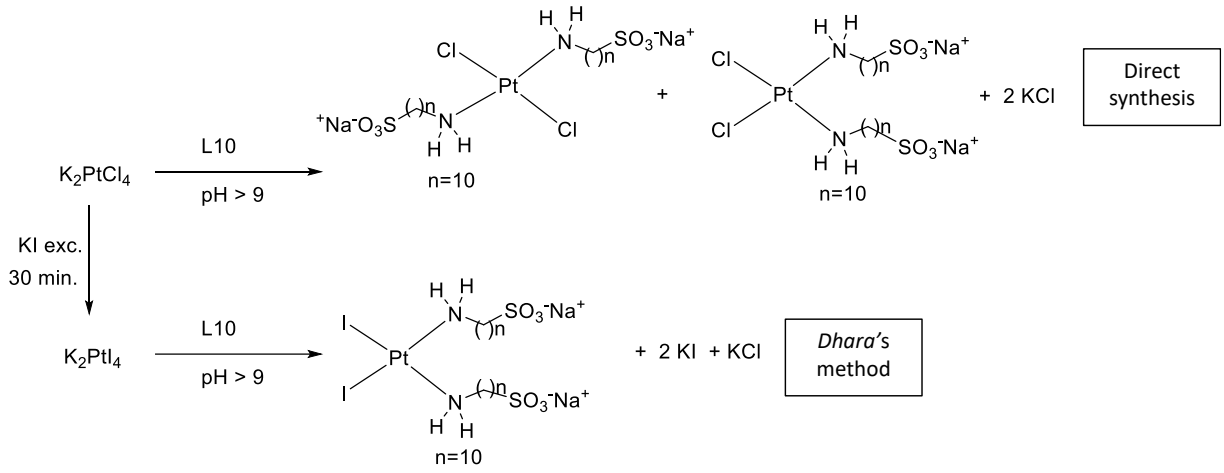

Scheme 4.3 Synthesis and stereoselectivity in the disubstitution reaction between tretrachloro and tetraiodo potassium platinates and amino sulfonate ligand **L10**.

Once the reaction finished, both, lyophilisation and drying off the solution under vacuum were attempted. In both cases, even when no air was introduced in the reaction vessel, a dark black solid appeared. By solubilising the mixture in hot MeOH and gravity filtration, it was possible to separate the dark residue from the yellow solution (**Scheme 4.4**). This step was necessary because it was also observed that if the reaction crude is left in water, the presence of the black solid progressed. However, if the sample was frozen in liquid N_2 to lyophilise it, and then further separate the black precipitate by solubilisation in hot MeOH, the appearance of the residue was reduced. As well, the separation of the dark residue with MeOH was more efficient, rather than filtrating the mother liquors prior to lyophilisation.

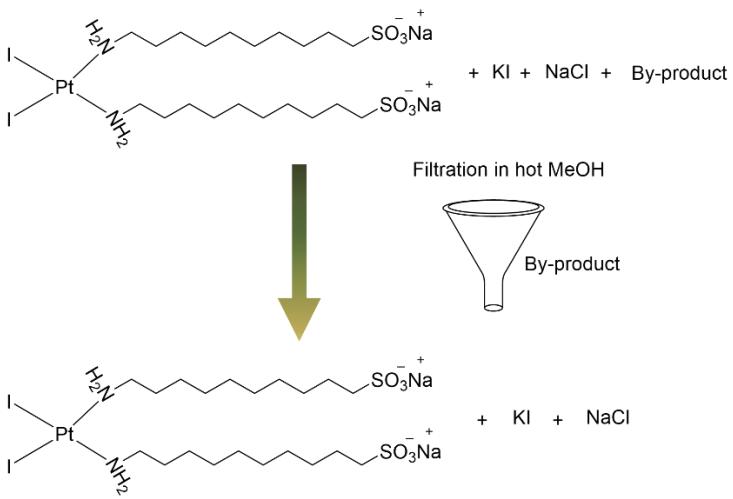

Scheme 4.4 Procedure for the separation of the black by-product from the final **Pt-L10** complex.

Pt-L2 and **Pt-L6** were prepared correspondingly: the same reaction conditions were favourable for their obtention as a yellowish fine solid. The appearance and removal of the residue after lyophilisation of the reaction mixture was performed alike.

Pt-Ls are obtained as yellow solids together with other salts deriving from the synthetic route. The purification of our complexes from remaining salts was difficult to accomplish since **Pt-Ls** present also ionic character. Several strived strategies are discussed hereunder.

4.1.3 Purification process

One of the main goals of our project was to prepare a water-soluble Pt(II) complexes, that can be used for the preparation of mixed vesicles. However, one of the biggest challenges was the separation of a metal complex bearing ionic units from ionic by-products, since salts such as KI, NaCl, or KCl.

Purification of cisplatin is reported to be performed by recrystallisation in 0.1 M HCl or 0.9% NaCl hot water.[332] In our case, this procedure did not end in the precipitation of **Pt-Ls**, most likely because of their high solubility in water. The addition of other solvents to induce precipitation by a change in the polarity, such as acetone or ethyl acetate, also failed. Alternatively, several options to separate the complex from salts were evaluated. First, the use of Sephadex™ was considered. Sephadex is the abbreviation for Separation Pharmacia Dextran, which is a reticular cross-linked dextran gel used to separate molecules by its size at mild conditions. The filtration is based on size exclusion chromatography: bigger molecules travel out the packed media before the small ones, which are more retained in the column. Hence, the separation of molecules in a sample is given by molecular weight distribution. Specially, it is used to quickly desalt and efficiently remove contaminants, which depending on the cross-linking degree of the resin, could be used for the separation from small molecules to very large biomolecules (G-10 for small ones to G-100 for big ones). Particle size also determines the flow rates and the maximum sample volumes that can be applied. In our case, G25 degree was employed, which is used for protein desalting as the main application and presents a cut off ≤ 1,500 Da, since the molecular weight of our **Pt-Ls** ranges from 743 to 967 Da. Nonetheless, this technique is not recommended to work with solutions higher than 30 % of the total volume of the column, which for us became a huge limitation in terms of obtaining purified complex in an operative quantity.

In the procedure, **Pt-L10** in water ([**Pt-L10**] < 1.5 mM) was added to the column after it was equilibrated, and the effluent is collected in approximately 1 mL aliquots. The first two fractions were taken as void volume, then fractions 3 to 12 were taken separately and lyophilised. In this type of columns, salts are expected to go through after fraction 8, that would be approximately 8 mL. Certain improvement in the ^{1}H-NMR spectra was seen since an enhancement in the resolution of the peaks was observed. In any case, to ensure the reduction of salts elemental analysis (EA) or quantitative NMR using an internal standard, are the analyses of choice. Though, both techniques were unfeasible because the amount of solid obtained was too scarce. It is worth noting that the separation of fractions also has an important visual component as a yellowish solution was seen when the complex was going through. However, because of limitations related to the volume and the sample concentration that could be loaded in the column, this purification method was discarded.

Therefore, the next method attempted to get rid of salts was purification by a reverse phase column, by means of a C18 silica columns. In this type of silica, the apolar molecules are more retained than the polar ones, unlike in common silica chromatography columns. Even with the high polarity of the sulfonate groups in **Pt-L10**, it was thought that the large hydrophobic chain may favour the retention of the complex and allow a good separation from salts. Besides, the solubility of the **Pt-L10** in water and MeOH permitted the employment of both solvents as eluent. Our procedure started with the solubilisation of the complex in water which was introduced into the C18 column, around 1 mL (not high volumes or complex concentrations can be introduced at once). Then, at least 5 mL of water went through to drag all the salts, while the complex got retained in the upper part of the column (distinguished by yellow coloured C18-silica). Finally, when MeOH went through, **Pt-L10** was released from the reversed phase silica, and it was collected as a second fraction. Then, the column was rinsed several times with water and the procedure could be repeated. Finally, both fractions were evaporated using a rotavapor or lyophilising. The whole process is depicted in the next **Figure 4.1**. It is worth noting that usually, a gradient of H_2O/MeOH is used until reaching 100% MeOH, although for our purpose was not effective. In fact, similar procedures to separate big molecules, desalting peptides or traces of organic solvents can be found in literature.[339–342] Several techniques (^{1}H-NMR spectroscopy, ESI-MS, and EA) allowed us to determine that purification was significantly successful, as described hereinafter.

The following ^{1}H-NMR spectrum (**Figure 4.1.**) shows the **basic-L10**, and the coordinated **Pt-L10** before and after C18 silica column purification.

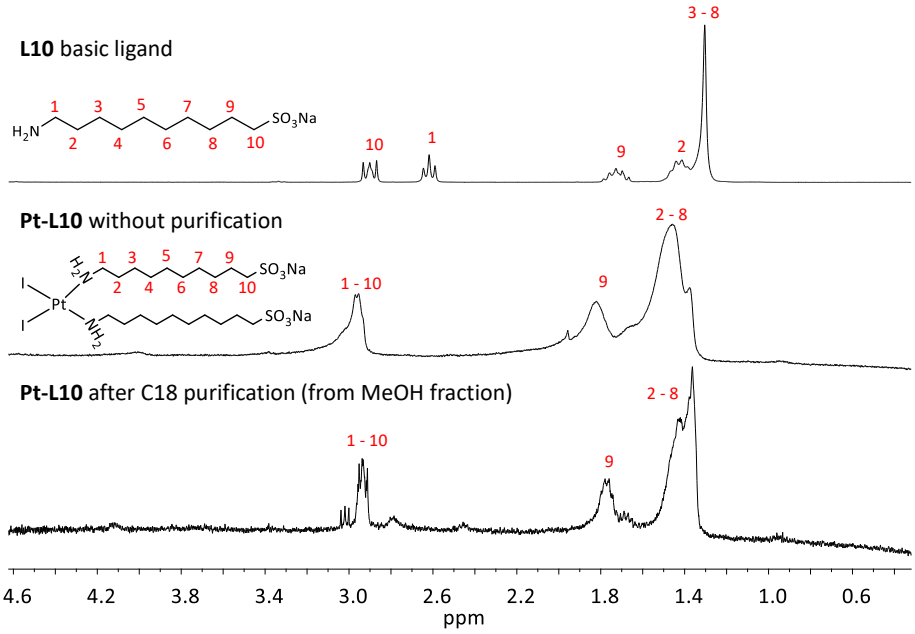

Figure 4.1 ^{1}H-NMR spectra showing the evolution of the coordination reaction: **L10** spectrum (top, 250 MHz), **Pt-L10** spectrum before C18 purification (middle, 400 MHz), and **Pt-L10** spectrum coming from the lyophilised MeOH fraction of C18 chromatography (bottom, 400 MHz); all the spectra were performed in water-d_2.

Moreover, if the water and MeOH fraction spectra from the C18 purification were compared, no organic moiety was found in the ^{1}H-NMR (**Figure A29**). Hence, we concluded that mainly salts were found in the water fraction, which was the main objective of the purification. Moreover, by means of quantitative analysis with ^{1}H-NMR spectroscopy using maleic acid as standard, we concluded that after the first purification through the column the apparent molecular weight lowered from 1629 to 1333 g/mol and after a second pass through the solid is obtained pure, showed by the structural characterisation of the molecules.

Similarly, negative mode ESI-MS of the water and MeOH fraction of C18 were compiled. The fraction coming from MeOH showed clear peaks assigned to **Pt-L10**. Whereas the aqueous fraction has usually shown signals below the detection limit of the technique (at background level), or a low amount of complex without iodide. Accordingly, the major peaks differed before and after purification, showing the decrease of K^{+} and Na^{+} adducts after purification (**Figure A30**).

Purification through reversed silica was performed over the other two complexes: **Pt-L2** and **Pt-L6**. However, the retention of the shorter complexes in the reversed column was not as

efficient as for **Pt-L10**. Even their C18 purification was effective, filtration with MeOH through celite was also employed in the separation of impurities. It is noteworthy, that both shorter complexes showed high water solubility, but still displayed good solubility in MeOH.

4.2 Characterisation of Pt(II) alkyl amino sulfonated complexes

4.2.1 Structural analysis

Significant changes for the α-nitrogen proton signals were observed in all ^{1}H-NMR spectra of the three Pt(II) complexes (**Figure A31** to **A33**). Intending to assign some of the characteristic signals, coordination of **L10** to K_2PtI_4 was performed *in situ* (**Figure A34**). To do so, consecutive additions of $[Pt(I_4)]^-$ solution in D_2O to an NMR tube with basified **L10** were performed. It was possible to observe how the corresponding peak slightly displaced to higher frequencies up to ~ 3.2 ppm almost overlapping the signal assigned to α-sulfonate protons that remains unaffected since it is too far from the coordination centre. However, when the ligand is totally coordinated to the metal the initial signal widens and totally overlaps the α-sulfonate signal. The deshielding of the α-nitrogen protons was attributed to the removal of electron density after coordination. At this point, it was clear that after the coordination of **L2**, **L6**, or **L10** to the Pt(II) core, the corresponding peaks of the ligands showed deshielding (to higher chemical shifts) due to the transference of electron density from the amino group of the ligands to the platinum ions. This fact was taken as a complexation confirmation. Moreover, it was also revealed an attenuated deshielding in the H_β and H_γ, most probably associated with the amino group coordination. However, in the chase of **Pt-L6** and **Pt-L10** was not possible to discriminate between H_β and H_γ signals for the amino or the sulfonate group.

Nonetheless, the spectra of the complexes resulted in wide and smudged signals which could be explained by the presence of ionic molecules; it is reported that salts have an inherent "shielding effect" on the environment of molecules and increase the sample conductivity. Salts may introduce additional noise because they can modify probe performance and sensitivity, reduce the efficiency of the rf pulses (so tuning and matching are modified), as well as high ionic strength affects T1 relaxation.[343]

The ^{13}C-NMR spectrum was recorded for the three complexes. The α-amino positions were shifted downfield to higher frequencies with respect to the corresponding parent ligands. The chemical shift of α-sulfonate positions was unmodified in all the cases, even for **Pt-L2** (**Figure A35** to **A37**).

The entity of the complexes was confirmed by negative mode ESI-MS and HR ESI-MS, for which mass values fitted within the experimental error. The m/z ratio and the isotopic pattern demonstrated the stoichiometry of the complexes: two **Ls**, two iodo ligands, and a counterion per platinum atom (**Figure A38 to A40**). The isotopic patterns completely agree with the presence of two **Ls** because the absence or presence of one of them alters importantly the pattern. Also, even though iodide anions do not strongly modify the isotopic pattern, chlorides, which would be the other possible coordinated halide, would render modified different patterns. The charges of the fragments, which had to be anionic to be identified in negative mode ESI-MS, were compensated by one sodium cation in one of the sulfonates while the other born a negative charge. Other peaks with the net charges compensated with a K^+ or H^+ counterion were also noticed in the MS spectra of the complexes. Nevertheless, the presence of several counterions in MS spectra is the expected behaviour when dealing with sulfonate groups and a mixture of cations in the sample and the mobile phase employed.

Ion-mobility mass spectrometry (IM-MS) is a technique that can separate mixtures in gas phase to resolve ions that are identical by a standard MS. In IM-MS ions in the gas phase are separated accordingly to their interaction with a collision gas and their masse. First, ions are separated based on their mobility through a buffer gas. Then, the ions are introduced to the mass analyser that determines their m/z ratios.[344,345] The ion mobility for **Pt-L10** was measured. The ion mobility spectra for the 922.047 m/z mean peak, corresponding to the loss of two sodium counterions and the addition of one H^+ were studied, showing two differentiated signals (**Figure A41**). This was related to the presence of two isomers, *cis* and *trans*. It was possible to correlate the signal to each isomer because compact ionic structures travel faster than elongated or extended ones. Hence, the first signal corresponds to the majority (approximately 83%) *cis* isomer, while the second corresponds to the *trans* isomer (approximately 17%). Unfortunately, since the instrument was not still available in the university installations, the measurement of the rest of the complexes were precluded However, we considered as a proof in the production of the *cis* isomer as the majority peak employing the modified Dhara's method corresponds to this isomer.

The infrared spectra (FTIR-ATR) of complexes (**Figure 4.2**) showed comparable peaks with those of the **Ls**.

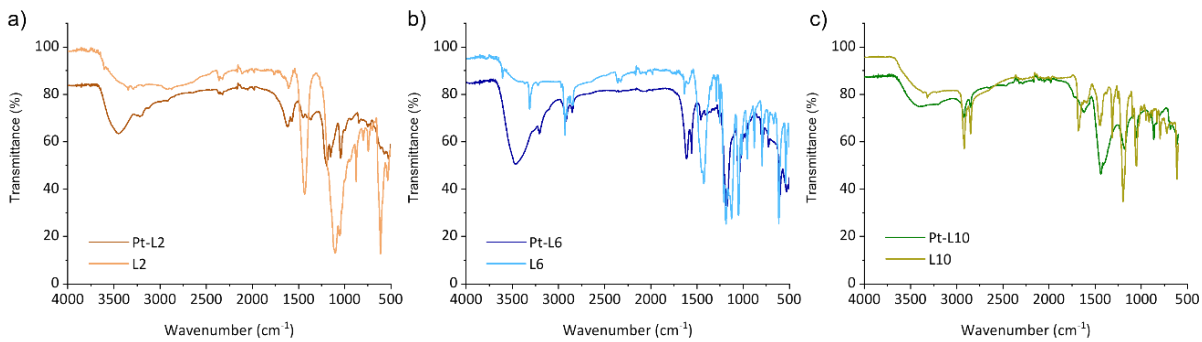

Figure 4.2 FTIR-ATR spectra of **Pt-Ls** *vs* **Ls**: **Pt-L2** *vs* **L2** (a), **Pt-L6** *vs* **L6** (b) and **Pt-L10** *vs* **L10** (c).

The main shift was found in the coordinated amino group peaks, as expected. Upon metal coordination, it is known that peaks get narrower because of higher constraints in the system compared to the free ligand band. In our case, the primary amino peaks were slightly narrower and sharper regarding the **Ls**, suggesting the coordination of the group to the metal ion. Additionally, a slight displacement towards higher wavenumbers was observed in the whole range (500-4000 cm^{-1}), but more specifically in the 3500 cm^{-1} region, in accordance with other Pt(II) complexes reported.[346] The Pt-N or Pt-I stretching bands would be present around 300-480 cm^{-1} region but, unfortunately, the region could not be reached in our FTIR-ATR instrument.[347,348]

4.2.2 Photophysical characterisation

Examination of the performance of the complexes in solution was deemed necessary considering their potential function as chemo-active species. For that purpose, the absorptions of **Pt-Ls** in solution were recorded by UV-Vis spectroscopy. Several concentrations of each complex were analysed to be able to examine all the transitions occurring in the complexes.

It is expected that **L2**, **L6**, and **L10** ligands, as aliphatic organic molecules, may mainly show absorptions in the UV region. Their corresponding complexes could involve charge transfer transitions (CT) such as ligand to metal charge transfer (LMCT) and metal to ligand charge transfer (MLCT). The electronic configuration of Pt(II) is $[Xe]4f^{14}\ 5d^{8}$ in a square-planar configuration and suggests that absorption bands due to d-d transitions must be expected when appropriate concentrations are used.

Alkanes undergo $\sigma \rightarrow \sigma^*$ transitions, in which an electron in a bonding σ orbital is excited to the corresponding antibonding orbital (σ^*). However, these transitions are not seen in typical UV-Vis spectrum as the required energy for them is too high. Other organic compounds

containing nitrogen, oxygen, or sulfur, which is the case for the **Ls** family, frequently contain non-bonding electrons (n), which absorb UV-Vis radiation. This means that the most probable occurring electronic transitions for **Ls** and **Pt-Ls** are $n \rightarrow \sigma^*$. These transition absorptions are not very intense (typical range of 150-200 nm). In our case, they may be related to the unshared lone pair of electrons in nitrogen or oxygens atoms in sulfonate group.

The recorded UV-Vis spectra of **Pt-L2**, **Pt-L6,** and **Pt-L10** (**Figure 4.3**) show 3 to 4 absorption bands for each complex.

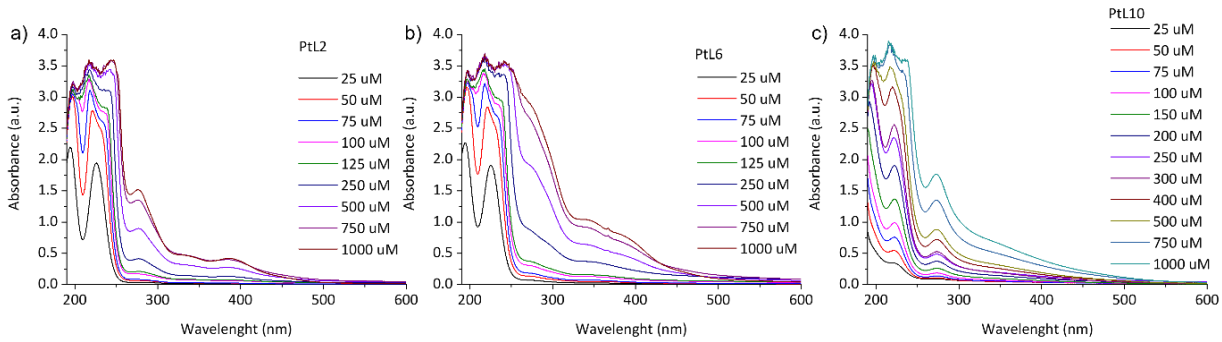

Figure 4.3 Absorption spectra of **Pt-L2** (a), **Pt-L6** (b), and **Pt-L10** (c); concentrations ranging from 25 to 1000 µM.

The absorption spectra of **Pt-L2** and **Pt-L6** are very similar at low concentrations. A first absorption band is seen at 194 nm, a second one at 224-225 nm, and the third one at 275-276 nm. A last one is identified at 389 nm for **Pt-L2** and at 360-370 nm for **Pt-L6**. Additionally, a shoulder about 235 nm in both spectra is perceivable. However, it is not further discussed as it is only seen at high concentrations where the signal is saturated. The spectrum of **Pt-L10** slightly diverges from the others; a first band is found at 195 nm, a second one at 221 nm, the third one at 273 nm, and a last one around 350 nm. An increasing tendency in the location of the bands is noticed as greater are the alkyl moieties: the bands shift to higher wavelengths following the order **Pt-L2** > **Pt-L6** > **Pt-L10**.

Interestingly, in the three complexes, a slender bathochromic shift (red shift) at increasing concentrations is observed. Bathochromic shifts are usually related to the stabilisation of the involved transition orbitals. Actually, it must be the reason behind the observation of the first band of **Pt-L10** just at the higher concentrations. Another plausible explanation for this wavelength deviation is the aliphatic nature of **Ls**. As previously discussed, the saturated carbon chain does not contribute to an absorption band due to the absence of non-bonding electrons nor conjugated double bonds. But the coordinating amine shows the $n \rightarrow \sigma^*$

absorption band, which is in the UV range, as well as the characteristic sulfonate signals generating the detailed shift.

Nevertheless, it is tough to establish the exact occurring transition in the spectra because several transitions, depending on the nature of the ligands and metals can occur. The high intensity bands of the three spectra might be showing MLCT or LMCT, associated with the coordination of iodide anion and primary amines, which are acting as strong π–donor ligand and σ–donor ligand, respectively. In the MLCT, the electrons are promoted from a metal orbital into an empty ligand orbital whereas, in the LMCT, the electrons are promoted from a molecular orbital with ligand character into an empty molecular orbital with a metal character. We believe that in our case LMCT is more probable because of the ligands' nature. Besides, the high intensity bands on the spectra of the complexes might be associated with a ligand-centred transition, which is sometimes reported to be found when the contact with the metal centre is hindered by the structure of the complexes.[349,350] Nonetheless, without more information, is not possible to ascertain which transition is happening in each band, because even both types of transitions could be occurring at the same time having different contributions.

The d-d transitions of Pt(II) are emerging with complex concentrations above 200 µM. These transitions are undoubtedly related to the band at 389 nm for **Pt-L2** and 360-370 nm for **Pt-L6**. Not as sharper, but still perceivable, is the band around 350 nm in **Pt-L10** spectrum. However, the band corresponding to d-d transitions is probably blurred by the intensity of the previous absorptions.[351] Moreover, when comparing the d-d bands recorded for *cis*-$[PtI_2(NH_3)_2]$ (350 nm)[335], *cis*-$[PtBr_2(NH_3)_2]$ (330 nm)[352] and other analogues like c*is*-$[PtI_2(amine)_2]$ (350-400 nm)[350] it is observed that the bands' location are in concordance with the values reported in the literature.

4.2.2.1 Density-functional theory calculations to identify the electronic transitions

Pursuing the identification of the transitions occurring in each absorption band, a preliminary DFT computational study for **Pt-L10** has been developed. Ground-state geometry optimisation for **Pt-L10** solvated in water was conducted using PBE functional with LanL2DZ basis set, for all the atoms, and was followed by harmonic frequency calculations to confirm the existence of a local minimum-energy structure.[353,354] The optimised structure shows the folding of one sulfonated alkyl chain around a sodium atom (**Figure A42**), in agreement with reported structures for other sulfonate-containing molecules.[353]

Then, excited states were calculated as vertical transitions through time-dependent DFT (TD-DFT). To cover the spectral range, from 600 to 200 nm, and to obtain a better match between the calculated and the experimental spectra, a total of 180 transition states were computed. Each transition was evaluated employing an associated oscillator strength (*f*) that represents the probability of the transition to occur, and with it, a simulated spectrum was generated. The superimposition of the experimental and simulated spectrum of **Pt-L10** (**Figure A43**) show three main comparable bands. The shift in the theoretical absorption spectra with respect to the experimental is within the range of typical TD-DFT calculations and is attributable to compute absorptions as vertical transitions.[355]

To elucidate the main electronic transition states (TS) occurring, the TS with the most representative *f* values were chosen for the molecular orbital analysis, in **Figure A44**. The description of an excitation state might involve several sets of highest occupied molecular orbital (HOMO) and lowest unoccupied molecular orbital (LUMO) and hence a set of molecular orbital pairs for each transition. In our case, several transitions involved two HOMO and their corresponding LUMO, one of them including three pairs of orbitals, hindered their interpretation. However, natural transition orbitals (NTOs), which are representations of the orbitals transformations during an electronic transition, allow the interpretation of the transition in a comparatively smaller set of basis pairs, giving a simpler image of the involved molecular orbitals.[356] Thus, the analysis of the transitions was conducted after the simpler representation of the NTOs, displayed in the annex of this thesis (**Figure A45**).

The molecular orbitals involved in the first absorption band (~210 nm) were mainly associated with ligand centred (LC), LMCT, and MLCT involving Pt(II) and iodide ions. The NTOs associated with the second (~250 nm) and third (~275 nm) band of the spectrum suggest that the most important transitions are LMCT and LC transitions, the latest also involving the sulfonate and the alkyl chains. Additionally, an intra-ligand charge transfer (ILCT) transition between sulfonates is proposed for TS 64. To sum up, the most energetic bands arise from LMCT and MLCT transitions, with the highest energetic band associated mainly with iodo ligand and **L10**, respectively. Finally, the absorption band around 410 nm has been related to one computed transition state which seems to exhibit a d-d transition as well as MLCT and LMCT involving Pt(II) and iodide ions.

Overall, there is no doubt that ligand **L10** has a significant role in the main transitions occurring within the complex. Moreover, the molecular orbitals in the alkyl chain are observed to be involved in some of the represented transitions. This fact would explain the hysprochromic effect observed for the whole **Pt-L10** spectrum is to some extent displaced towards the UV region.

4.2.3 Unravelling the reaction mechanism

In the previous section 4.1.2, where the synthesis of **Pt-Ls** is reported, we have described the appearance of a black solid that is isolated from the complex by recrystallisation with MeOH. Initially, the appearance of the dark solid seemed to be favoured when vacuum was employed to evaporate the reaction solvent. In order to elucidate the nature of the black solid it was decided to perform an X-ray photoelectron spectrometry (XPS) analysis of both, the yellow solid and the black solid separated by recrystallisation.

Briefly, in XPS the material surface is analysed under vacuum after the irradiation with a monoenergetic soft X-ray, evaluating the kinetic energy of the emitted electrons. Every element yields a unique spectrum that is represented as the number of detected electrons per energy interval *vs* the kinetic energy. The identification of chemical states is made from the measurement of the peak positions, which can be compared to plots and tabulated energy shifts. The obtained peaks in a spectrum can be disclosed after tables of binding energies that identify the shell and spin-orbit of a peak produced by an element. Additionally, from the determination of the present elements, information about bonded elements can be obtained, and more importantly their speciation.[357–359]

The two analysed samples were obtained from one **Pt-L10** reaction from which the black solid was separated from the yellow solid with hot MeOH and gravity filtration, as previously described. For both samples, the analysed regions corresponded to the binding energies associated to N, I, and Pt. The raw data was set to a baseline and the peaks deconvoluted in their constituent peaks. Deconvolution was sorted out keeping the ratio intensities, distances between peaks, and the full width at half maximum depending on the constraints of each element. Finally, data extracted from the plots was compared with the online XPS database and literature.[357,358,360]

For N 1s, two coincident peaks for each sample were detected after deconvolution (**Figure 4.4**).

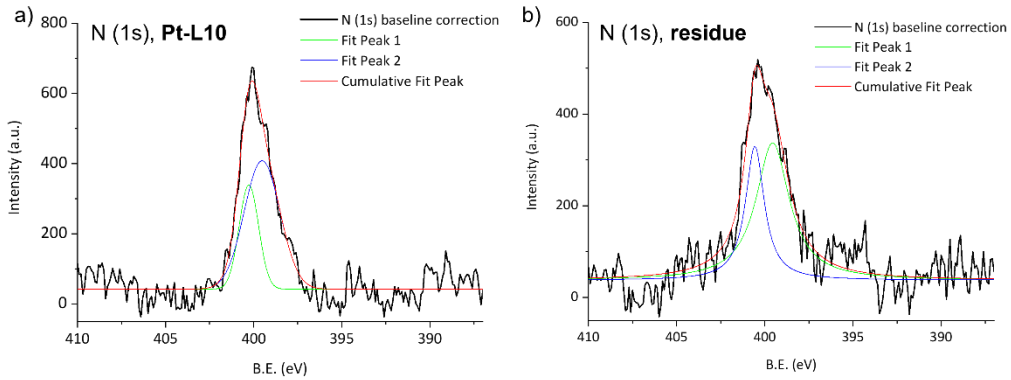

Figure 4.4 XPS spectra of N (1s) for **Pt-L10** (a) and the black solid residue of the synthesis (b).

In literature, amino-aliphatic species range between 399.1 and 399.6 eV.[361–363] Since, the signal localised at 399.5 eV was related to the R-NH_2 group of **L10** ligands. The second deconvoluted peak at 400.4 eV for the **Pt-L10** sample, and at 400.6 eV for the residue sample may be associated with the presence of coordinating amino group, as seen in the literature. More specifically, some articles show primary amines coordinated to Pt(II) and halides.[364–367] This means that, to some extent N from the ligand was also identified in the residue sample. Besides, it can be assumed that no oxidation nor protonation occurred to the amino group in any of the samples.

Iodine is studied in the region of 3d, and every iodine species renders to peaks: the $3d_{3/2}$ and $3d_{5/2}$ due to the spin-orbit components. The experimental spectra of the analysed samples revealed two peaks: $3d_{3/2}$ (630.9 eV) and $3d_{5/2}$ (619.3 eV), with a split of 11.5 eV in both samples (**Figure 4.5**).

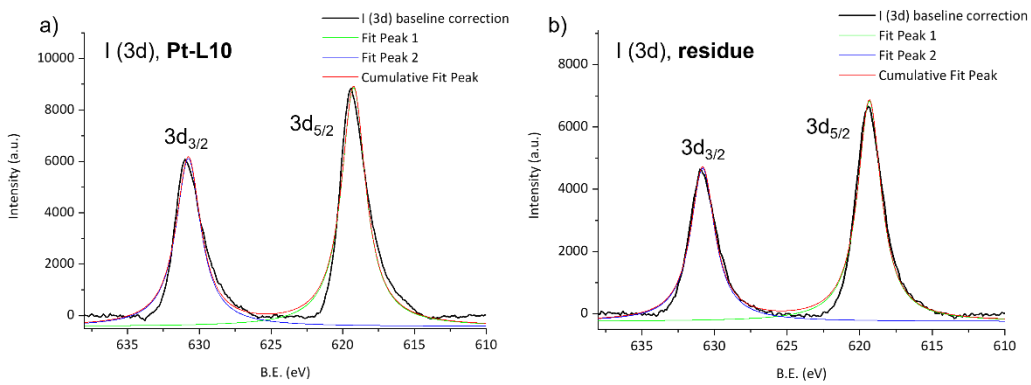

Figure 4.5 XPS spectra of I (3d) for **Pt-L10** (a) and the black solid residue of the synthesis (b).

The peaks position and the split comply with the literature and were associated with iodide presence.[357] Reported values for $3d_{5/2}$ are in the same range for Pt(II) species with two

coordinated iodides, nonetheless, the other type of ligand in the complexes are too distinct from literature to be categorically correlated.[368] In other references, the average binding energy for all metal iodides is specified at 619.3±0.6 eV, completely according to our experimental data.[360,369] Hence, only one iodine species was present in the samples. The presence of I_2 in the XPS spectra was discarded since would render smaller peaks at slightly higher binding energies.[360]

The greater difference between both samples was found analysing their Pt XPS spectra (**Figure 4.6**).

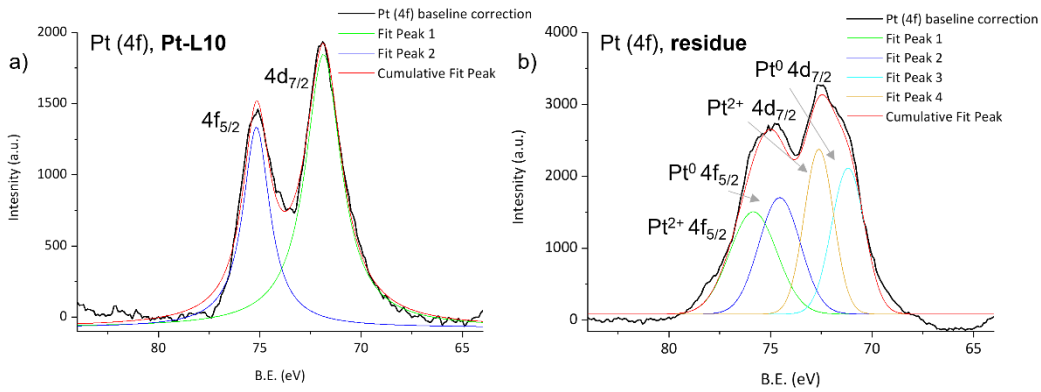

Figure 4.6 XPS spectra of Pt (4f) for **Pt-L10** (a) and the black solid residue of the synthesis (b).

Theoretically, the Pt 4f region has to present well split spin-orbit components with a separation of 3.3 eV and show symmetrical peaks for Pt(II) and Pt(IV) compounds and slightly asymmetrical for Pt(0) compounds, if existed in the sample. The range of 4f in **Pt-L10** showed a pair of peaks related to the $4f_{5/2}$ (75.9 eV) and $4f_{7/2}$ (72.6 eV) with a split of 3.3 eV, both confirming the presence of an single Pt species, which corresponded to Pt(II) (**Figure 4.6**, a).[370–373] For the residue sample, two broader peaks were successfully deconvoluted in two pairs of doublets corresponding to $4f_{5/2}$ and $4f_{7/2}$ for two Pt species: Pt(II) and Pt(0) (**Figure 4.10**, b). The $4f_{5/2}$ peak at 75.9 eV and $4f_{7/2}$ at 72.6 eV confirmed the presence of Pt(II), and the 74.5 eV ($4f_{5/2}$) and 71.1 eV ($4f_{7/2}$) determined the presence of Pt(0).[359,370–373]

It is worth mentioning that the fit peak is not perfect, but it must be attributed to the high charge in the samples, which generates asymmetry mainly appreciated at low B.E.[359] Besides, as predicted, no Pt(IV) was identified in none of the samples.

Thus, we corroborated the reduction of Pt(II) during the synthesis of the whole **Pt-L** family. We also determined that the separation method was not ideal, since most probably a certain

amount of the complex remained in the separated portion since N, I, and Pt(II) have been also determined by XPS in the Pt residue sample.

Once the identity of the black residue was confirmed, potential mechanisms responsible for the Pt(II) reduction were considered. A plausible explanation would be the elimination of a proton in β position with respect to the nitrogen, which after a reductive elimination could yield Pt(0). Even so, the reaction would advance generating acid as a by-product, which in basic media it is unlikely to happen unless the acid would be removed under vacuum. Though, we decided to reproduce the same reaction using a ligand without available β protons. Sulfanilic acid was chosen to coordinate, and the rest of the reaction conditions were maintained. The diiodo disulfanilic Pt(II) complex was characterised by NMR and negative modes ESI-MS, but during the synthesis, black dispersed solid was also noticed, which indicated that our proposed mechanism of β elimination was not taking place. In fact, the presence of acid was hard to ponder in basic media.

Then, the presence of these species was assessed in the reaction mixture and their standard reduction potential (E^0red).was also searched. Iodide (potassium iodide) has a E^0red of 0.54 V.[374–376] While Pt(II) reduction to Pt(0) could derive from two species present in solution, the Pt^{2+} cation or the $PtCl_4^{2+}$ specie, with E^0red of 1.2 and 0.73 V, respectively. Nonetheless, $PtCl_4^{2+}$ is particularly prompt to be found in water.[375,376] By calculating the standard potential of the reaction, in which iodide would be oxidised to iodine and either of the Pt(II) species will be reduced to Pt(0), the total standard potential of the reaction is 0.66 V for the Pt(II) species, and 0.19 V in the case of $PtCl_4^{2+}$ specie to be occurring. Either way, the final potential is positive meaning that the reaction is spontaneous, and the most plausible reason for the presence of Pt(0).

The I_2 formed by iodide oxidation must remain soluble by the combination with iodide giving triiodide ion, I_3^-, that is totally water-soluble. It may help the continuous Pt(II) reduction when it is still in solution and should be the explanation for greater reduction when direct evaporation was tried. When lyophilising, the sample is instantly frozen in liquid nitrogen, thus, the sublimation of water hinders the reduction to continue.

Overall, we determined the nature of the black residue generated during the coordination reaction to be reduced Pt, which is deeply described in many platinum complexes preparation.

4.3 Aggregation of Pt(II) alkyl amino sulfonated complexes

The prepared **Pt-Ls** were designed and thought to lead to supramolecular arrangements, at least in the case of the complex containing the longest ligands. As portrayed during this thesis, previous works in the group have shown the supramolecular aggregation of Pt(II) and Mo(II) alkyl sulfonated phosphines.[266,271] Still, it is worth noting the distinct lipophilicity of the ligands used in precedent works in contrast to the ligands employed in the current thesis. The coordinating group used to be a phosphine with a larger number of C atoms, which would confer higher lipophilicity with respect to the amino group of our **Pt-Ls**. Hence, to study the behaviour of our **Pt-Ls** molecules in water was crucial to examine their potentiality as metallosurfactants (**MTS**).

Further, solubility was an issue in the synthesis of the ligands, as described in the previous chapter. Nevertheless, once coordinated to platinum the whole family of **Pt-Ls** is completely soluble at working ranges in water and other polar solvents such as MeOH. One of the final targets of the complexes is to be tested as cytotoxic compounds, and the high solubility is a great advantage in front of regular platinum compounds. Moreover, if they behave as **MTS,** their performance against cancer cell lines might be influenced. Several experiments and studies to ascertain the organisation and determine the CAC in the solution of the **Pt-Ls** compounds are hereinafter described.

4.3.1 Analysis by conductimetry

The conductivity of increasing concentration of our **Pt-Ls** was measured to detect the concentration at which the appearance of supramolecular organisations occurred. All the samples were prepared individually from a stock solution in Milli-Q water and submitted to a rotatory shaker overnight to reach equilibria and measured the next morning (**Figure 4.7**).

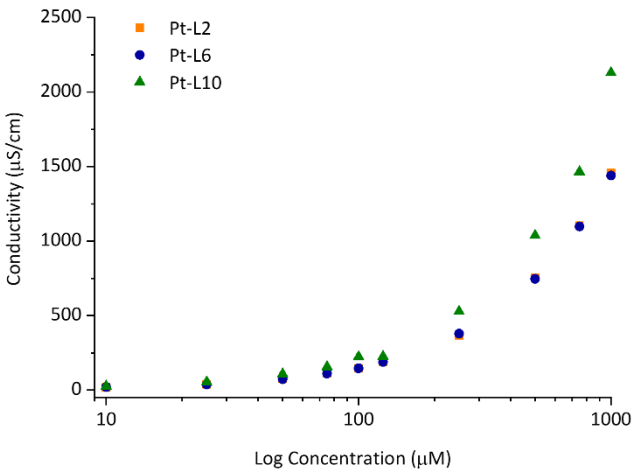

Figure 4.7 Conductimetry of **Pt-L2** (orange squares), **Pt-L6** (blue circles), and **Pt-L10** (green triangles) at different concentrations. The horizontal axis is represented as the logarithm of the concentration.

Interestingly, **Pt-L2** and **Pt-L6** show almost superimposable data while **Pt-L10** had lightly higher values (**Figure 4.7**). Nonetheless, the trend of conductivity for the three complexes was unambiguously equivalent and increases linearly, without showing any disruption in the tendency that could be associated with a reorganisation of the species in solution.

Limitations on the technique, already described in the previous chapter, could have hindered the determination of the CAC. Besides, the conductivity values obtained at the lower concentrations studied were almost in the limit detection of the technique, so reducing the concentrations to analyse then the behaviour was not an option. Hence, other techniques were required.

4.3.2 Measuring light scattering

4.3.2.1 Using fluorescence spectrometer

Scattering of the **Pt-Ls** was studied using a fluorescence spectrometer[271], measuring fresh solutions of a wide range of concentrations of **Pt-L2**, **Pt-L6,** and **Pt-L10**. The excitation and emission wavelength were set at 500 nm for excitation and 510 - 700 nm for emission, and the split was fixed at 15 nm. At such wavelength, no absorption nor fluorescence were detected in none of the **Pt-Ls**, and so the recorded measurement corresponds to the scattering occurring in solution. A sudden variation in the scattering when increasing concentrations samples would be associated with the rearrangement of species in solution (**Figure 4.8**).

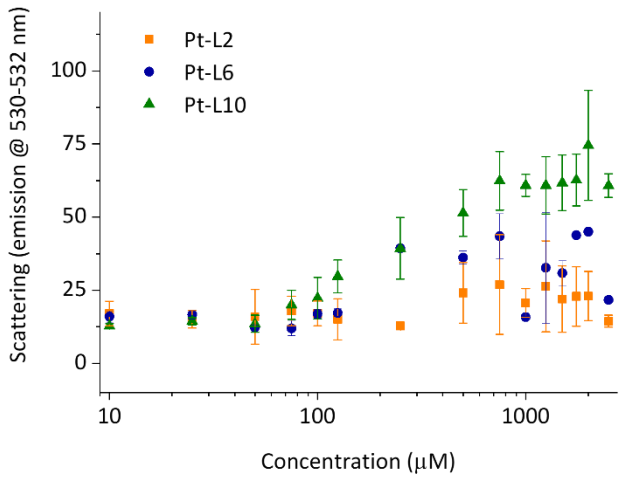

Figure 4.8 Scattering of **Pt-L2** (orange squares), **Pt-L6** (blue circles) and **Pt-L10** (green triangles) measured by fluorescence excitation at 500 nm an emission at 510 - 570 nm (n = 3), with the slits set at 15 nm. The horizontal axis is represented as the logarithm of the concentration and values are the mean of two independent experiments with the associated standard error of the measurements.

The graph shows the average and the standard deviation of three independent series of samples for each complex. The represented values are taken in the maximum emission: 531 nm (**Pt-L2** and **Pt-L6**) and 530 nm (**Pt-L10**).

For **Pt-L2**, we did not observe a disruption in the tendency. In contrast, a shift in the tendency is observed from 100-125 µM for **Pt-L6** and around 75 µM for **Pt-L10**. This alteration might be related to a reorganisation of the discrete molecules. However, other scattering-based measurements were perused to assure this behaviour.

4.3.2.2 Using Dynamic Light Scattering

Dynamic Light Scattering (DLS) is a technique employed to determine the size of aggregates, also called photon correlation spectroscopy, in which random changes in position due to the Brownian motion of particles are recorded as a function of time. The technique relies on the principle that small particles move faster than the large ones. The continuously mobile particles within a dispersion scatter the incident laser and cause constructive and destructive interferences. Hence, the intensity of scattered light fluctuates over time, which is detected in DLS as a frequency distribution along time. Then, this scattering intensity pattern is processed in real-time by the software into a power spectrum, generating an auto-correlation function (with itself). It provides the translational diffusion coefficient that is used to estimate the hydrodynamic radius applying the *Stokes-Einstein* equation. It should be highlighted that the

results in this technique are dependent on the viscosity and temperature, which must be maintained constant.[134,377]

Even if the main objective of the technique, DLS is not to determine the CAC of a molecule, this application has been reported in several works.[378,379] For this purpose, the absolute intensity given in the lecture of samples is plotted against the sample concentration. Below the CAC, the intensity of scattered light detected from each concentration should be similar to that obtained from the solvent.

The tested experiment was performed twice using two different DLS instruments. The first instrument used was a *Litesizer 500* (Anton Paar GmbH) from Luciani Research group in Bern University (Switzerland). Initially, the instrument was calibrated with 100 nm polystyrene NPs.

The absolute intensity (Kcounts/s) was recorded for each sample, and the value was corrected by taking out the absolute intensity shown by the blank solvent, Milli-Q water. In this case, the samples were diluted *in situ* and measured after 2-3 min of preparation (**Figure 4.9**).

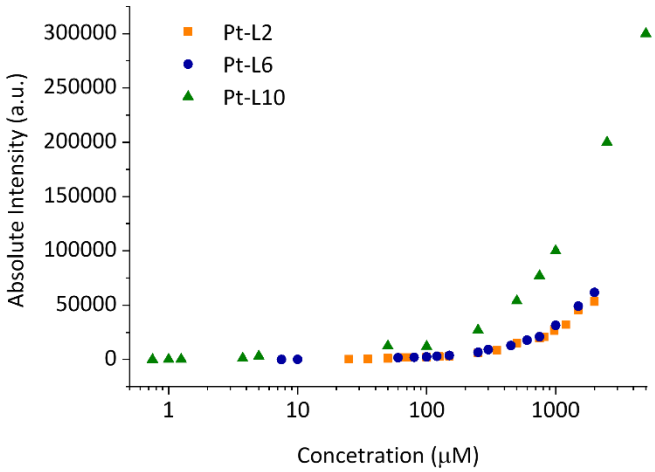

Figure 4.9 Plot showing absolute intensity vs concentration of **Pt-L2** (orange squares), **Pt-L6** (blue circles), and **Pt-L10** (green triangles), recorded in *Litesizer 500*. The horizontal axis is represented as the logarithm of the concentration.

Graphically, it is seen how from around 97 µM **Pt-L10** the trend is disrupted and increases more abruptly. In **Pt-L2** and **Pt-L6** the trend variation is seen above 260 µM and 150 µM, respectively. Unexpectedly, the value and the tendency for both shorter complexes (**Pt-L2** and **Pt-L6**) were pretty similar.

Moreover, before reaching the abovementioned value, we realised that the obtained auto-correlation functions showed very poor signal-to-noise ratios and no size distribution could be obtained. However, the auto-correlation functions obtained after the mentioned concentrations showed an improvement and it should mean that signal is detected nearby the mentioned CAC range.

The second instrument employed was a nanoparticle size analyser, with Microtrax Ultrafine Particle Analyser from the department of Biophysics at UAB. The main difference between both instruments is that, unlike common DLS instruments, Microtrax uses frequency power spectrum, which works with the distribution of energy over distinct frequencies. It has been demonstrated that the auto-correlation function is the Fourier transform of the power spectrum and therefore, DLS can be also performed in the spectral domain.[380] Frequency power spectrum does not require a curve fitting into the auto-correlation function, as in photon correlation spectroscopy, and since enables higher resolution. In this case, the linear frequency power spectrum recorded the Loading Index is calculated. The Loading Index is the sum of all amplitudes of each frequency channel, which is proportional to the particle concentration and provides a single number for total scattering. Hence, in this instrument, the intensity along time is not measured, but we took the loading index as a value representing the total scattering in the sample (**Figure 4.10**).

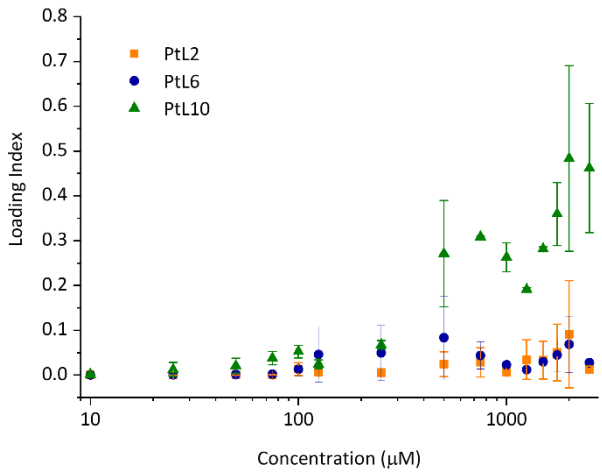

Figure 4.10 Loading index *vs* concentration of **Pt-L2** (orange squares), **Pt-L6** (blue circles), and **Pt-L10** (green triangles) recorded in Microtrax Ultrafine Particle Analyser. The horizontal axis is represented as the logarithm of the concentration and values are the mean of two independent experiments with the associated standard deviation.

Interestingly, the trend for the three complexes (**Figure 4.10**) was comparable to the graphs obtained with the *Litesizer 500* (**Figure 4.9**). A slight disruption in the measure is observed at 125 µM for **Pt-L6** and about 100 µM for **Pt-L10**. By contrast, in this case, we considered that **Pt-L2** did not reveal a disruption near 260 µM, as we pictured in the previous measurement.

Remarkably, at 1257 µM the three **Pt-Ls** showed a noticeable decrease in the measurement, (**Figure 4.10**) which yet has not been understood. The fact that happens at the same concentration for the three complexes hampers its correlation to a reorganisation of the molecules. We advocate the reason for an artifact given by the instrument or the measure itself. However, we were unable to underpin this fact in the literature.

We conclude that the three based scattering methods show an equal trend. They seem to indicate certain reorganisation of **Pt-L10** molecules outlined between 60 - 100 µM. In the case of **Pt-L6**, reorganisation might occur after 125 µM, however it is not as clear as in the case of the longest complex. Trend variations in the scattering *vs* concentration for **Pt-L2** are fairly seen. Finally, the presence of a decrease at 1257 µM, seen in the three **Pt-Ls**, is still not understood.

4.3.3 *Cryo*-transmission electron microscopy

At this juncture, we contemplated that a morphological analysis of **Pt-Ls** solutions at distinct concentrations might help to discriminate if the changes observed by scattering techniques were related to the formation of supramolecular reorganisations. *Cryo*-transmission electron microscopy (*cryo*-TEM) was believed to be the most appropriate technique because allows for the specimen of interest to be seen without disturbing their assembly, as would be in solution due to cryogenisation.[381] The sample under observation is frozen-hydrated by plunge-freezing a thin layer of the sample.[382]

Samples were prepared in Milli-Q water and let to reach equilibrium overnight. The chosen concentration was 5 mM (**Figure 4.11**), to be above the estimated CAC determined for **Pt-L6** and **Pt-L10** by scattering.

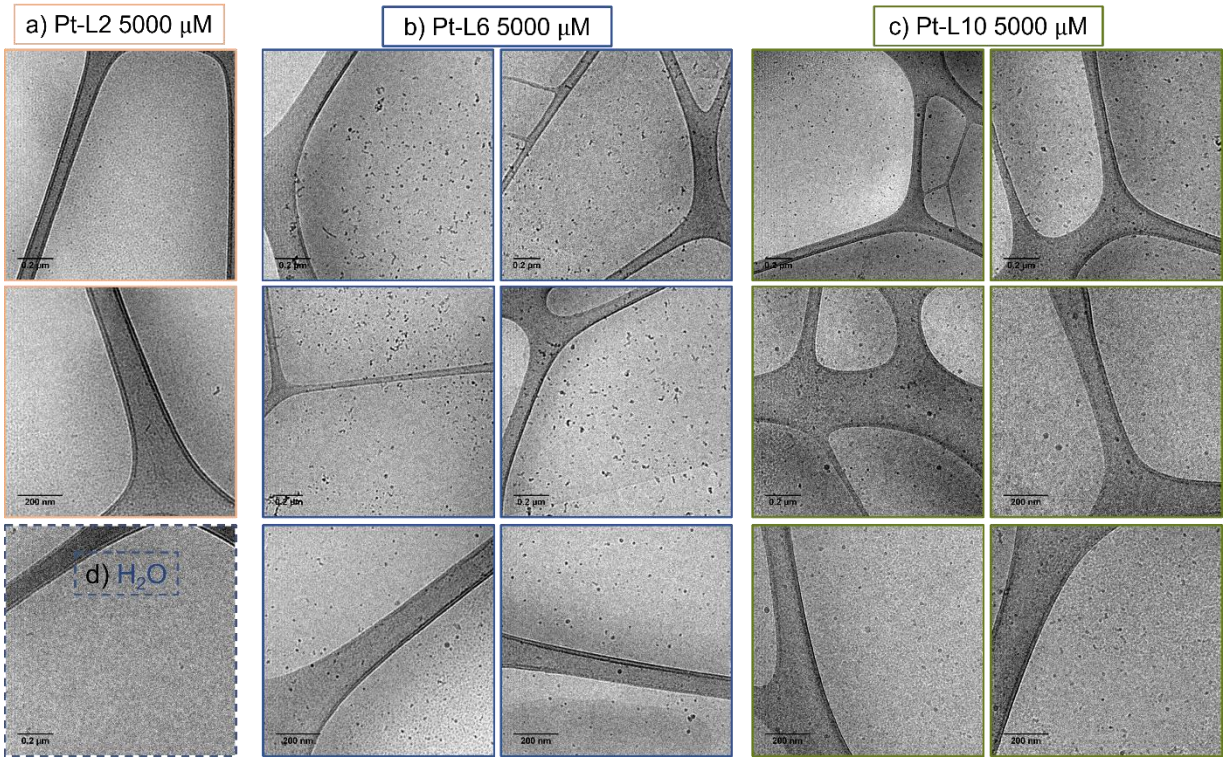

Figure 4.11 *Cryo*-TEM micrographs of **Pt-L2** (a), **Pt-L6** (b), and **Pt-L10** (c) at 5 mM in Milli-Q water. For comparison, Milli-Q water was also recorded (d).

The micrographs of **Pt-L6** and **Pt-L10** showed the presence of aggregates, seen as small dark spots. Whereas, **Pt-L2** micrographs, show the absence of them. The size of the identified aggregates of **Pt-L6** and **Pt-L10** exhibit sizes between 10 and 14 nm. However, the number of aggregates in the micrographs are insufficient to generate an accurate histogram.

Finally, it was decided to significantly increase the concentration to examine if the type of aggregates changes. We chose to study a 15 mM **Pt-L10** solution, shown in **Figure 4.12**.

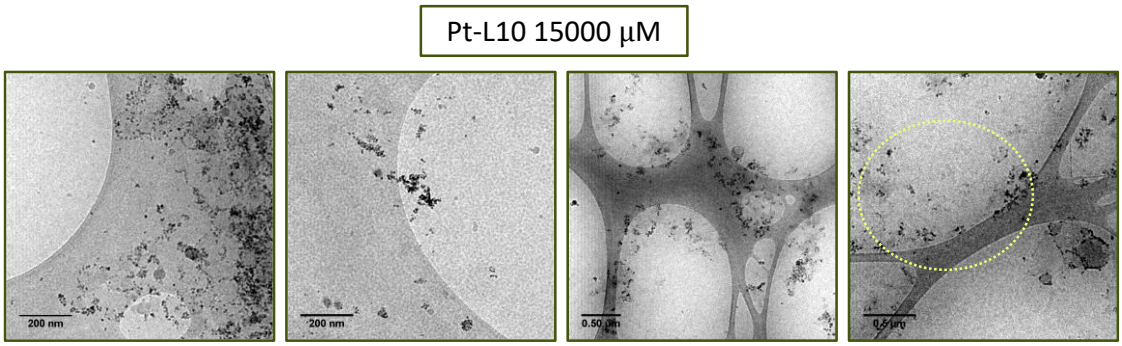

Figure 4.12 *Cryo*-TEM micrographs of **Pt-L10** at 15 mM in Milli-Q water. The dotted yellow circle shows the section where EDS has been used.

The increased concentration of **Pt-L10** showed similar aggregates but showing higher agglomerates of them. Moreover, energy dispersive X-ray spectroscopy (EDS) was performed on the sample, indicated in the fourth micrograph of **Figure 4.12** with a yellow dotted circle.

Using the EDS results (**Table A1**) it was possible to compare the ratio between Pt and I atomic percentages and theoretical percentages. The results are summarised in the next **Table 4.1**.

Table 4.1 Comparison between the theoretical and the EDS Pt to I ratios for **Pt-L10** obtained from the *cryo*-TEM micrograph.

	Pt vs I	
Compounds	Theoretical relation	EDS relation
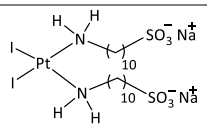	0.77	0.81
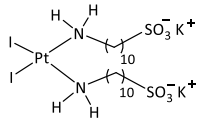	0.83	

The theoretical ratios are calculated using the theoretical elemental percentage of each element. Both cations that could be acting as counterions are considered and compared to the EDS ratio with the given atomic percentage. EDS is frequently referred to as a "semi-quantitative" technique, where its quantification accuracy is usually within ± 2 - 5% but can be higher depending on the sample nature and the standards used.[383,384] In our case, other elements in the complex were not considered to calculate the ratio for several reasons. For instance, elements present in the grid, such as carbon, were not even included in the EDS measure, or nitrogen which produces a weak response because of detectors' design.[385] Moreover, the technique is not usually accurate for the determination of light elements such as sodium or sulphur. In fact, it is reported how generally sulphur content determined from EDS analysis is slightly lower than the real sulphur content due to the unavoidable sublimation of it at high vacuum environment during the measurement.[386] Nonetheless, we consider that the similarity in the ratio Pt/I may indicate that the observed aggregates can be attributed to **Pt-L10**.

It is significant to note that in some micrographs the presence of arrangements reassembling to vesicles was observed (**Figure 4.13**). They appear to be larger than the other aggregates but just noticed for **Pt-L6** and **Pt-L10** in the micrographs shown below.

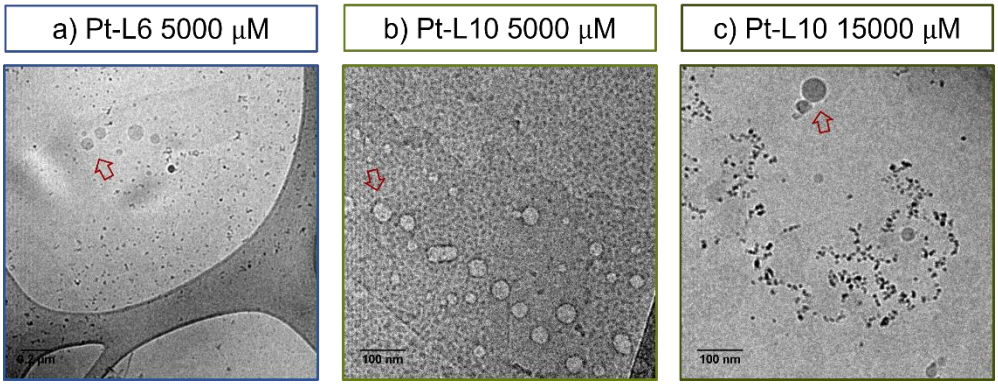

Figure 4.13 *Cryo*-TEM micrographs of **Pt-L6** (a), **Pt-L10** (b) at 5 mM, and **Pt-L10** (c) at 15 mM in Milli-Q water, in which vesicular arrangements are observed (red arrows).

However, it was not possible to discern if they were related to the darker spots associated with **Pt-L10** aggregates, or if they should be considered artefacts.

4.3.4 Dynamic light scattering and zeta potential

The fact that **Pt-L6** and **Pt-L10** have portrayed a probable organisation of their molecules in solution, encouraged us to study their behaviour in Milli-Q water. The size and potential in the slipping plane of the aggregates were measured by DLS and zeta potential (ZP).

All the **Pt-Ls** were measured at 1 mM concentration, to assure the performance above the estimated CAC value if aggregation was effectively occurring. The DLS plots by intensity and correlation functions plots can be found in **Figure A46**. In the next **Table 4.2**, we have summarised the size, polydispersity index (PDI), and ZP.

Table 4.2 Presumed CAC for **Pt-Ls**, and its measured hydrodynamic diameter (d. nm), PDI, and ZP value.

	Pt-L2	**Pt-L6**	**Pt-L10**
Estimated CAC, mM	n.d.	~ 0.1 – 0.125	0.06 - 0.10
Hydrodynamic diameter (nm)	250	202	258
PDI	0.28	0.24	0.24
ZP values, mV	-39.67 ± 0.49	-39.46 ± 0.50	-45.73 ± 2.06

DLS graphs for the three **Pt-Ls** showed a main peak rendering size between 200 and 260 nm at a concentration of 1 mM. Although the correlation function fits (**Figure A46**), we could not discard the presence of artefacts mostly because **Pt-L2** has not revealed self-rearrangement or aggregation.

The plot for **Pt-L10** showed a unique family with a size of 258 nm. Then, **Pt-L6** and **Pt-L2** also showed heterogeneity, with bigger and smaller families, significantly present in the last one. The DLS size values are extremely bigger than those seen in the *cryo*-TEM micrographs. The reason should be related to the techniques themselves. DLS is based on the intensity and prominence of larger particle sizes since intensity is proportional to r^6 and assumes that the particles are spherical. Furthermore, the scattered light from larger particles could drown in the scattered light from the smaller ones, being their contribution to the total scattered light particularly low. On the contrary, TEM is a number-based particle size measurement that emphasises the smaller particles. Moreover, in DLS, the measure corresponds to the hydration sphere and considers the stabilising layer, while electron microscopy techniques show the electron-dense part of the particles. Finally, a highly monodisperse size distribution would yield similar results in both techniques, but polydispersity would difficult the results.[387–389]

Then, we decided to measure by DLS the **Pt-L6** and **Pt-L10** samples studied by *cryo*-TEM and represent the obtained graphs by number. This would render a representation closer to that of the electron microscopy micrographs. Expectedly, the sizes measured by DLS expressed in number (**Figure 4.14**) are smaller than the ones previously reported, but still greater than the measure by the microscope technique.

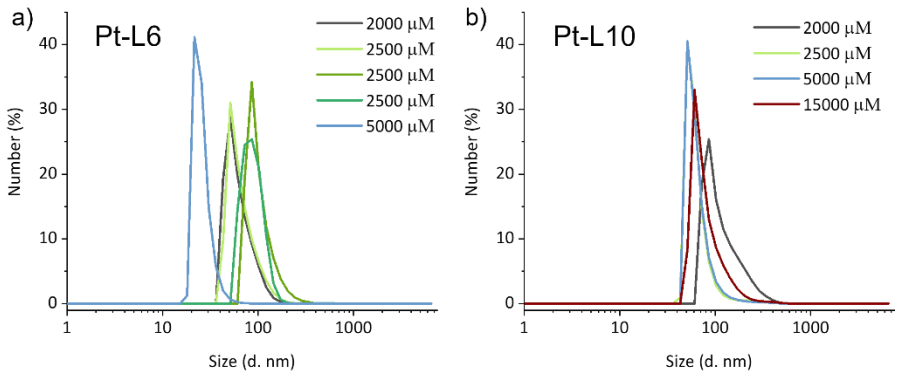

Figure 4.14 DLS plot expressed by number of **Pt-L6** (a) and **Pt-L10** (b) at concentrations ranging from2000 to 15000 µM.

The potential at the slipping plane of a colloid particle moving under an electric field is the ZP. A dispersion, to be considered as stable should display ZP values differing significantly from zero: usually below -30 mV or above +30 mV. Nonetheless, in ZP attractive van der Waals forces are not considered, and neither is steric interaction. Therefore, it cannot be unequivocal considered.[134]

The ZP at the slipping plane of the presumed aggregates (**Table 4.2**) showed negative values, slightly higher for **Pt-L10**. For the three cases, the values were below -30 mV and so could hint its stability. The negative values indicate that the predominant ion in the slipping plane weightily carries negative charges. Therefore, it is probable that the **Pt-Ls** aggregates bear the negatively charged sulfonates pointing outside if a supramolecular aggregation is assumed. The conformation rendering the sulfonate group-oriented to the water could fit with micelles or vesicle-like organisation. This type of organization for surfactants containing transition metals has been also reviewed in the bibliography by several authors.[390] Whereas, the bibliography differs from our study because in virtually all the cases, the metal ion is the polar group and since facing the aqueous phase.

Moreover, the negative ZP value would fit with a double-loop conformation behaving as bolaamphiphiles. In fact, this arrangement has been previously described in our group for Mo and Pt sulfonated phosphines MTS.[266,271] This could have been ascertained with surface tension data interface to obtain the surface excess concentration and estimate the area per molecule in the air/water interface. However, we were not able to measure such data, which eventually is questioned by some authors.[391]

In conclusion, even a CAC value has not been conclusively determined for the **Pt-Ls**, there is enough evidence to point out a CAC for **Pt-L6** around 0.1 – 0.125 mM and for **Pt-L10** between 0.06 and 0.1 mM. The discrepancies between sizes measured by TEM and DLS indicate polydisperse samples and probably not spherical shaped organisations. In addition, the ZP data, and the previous knowledge on MTS, give rise to think about a preferential conformation of double-loop.

4.3.5 Small angle X-ray scattering

To further investigate and characterise the intricacies of the formed organisations, in a collaboration with Dr. Ramon Pons, from *Institut de Química Avançada de Catalunya* (IQAC), we had the opportunity of performing small-angle X-ray scattering (SAXS) to **Pt-L10**.

A preliminary study of **Pt-L10** was conducted at two concentrations: 5 mM and 10 mM samples of **Pt-L10** in Milli-Q water were measured rendering the SAXS spectra shown in **Figure 4.15**.

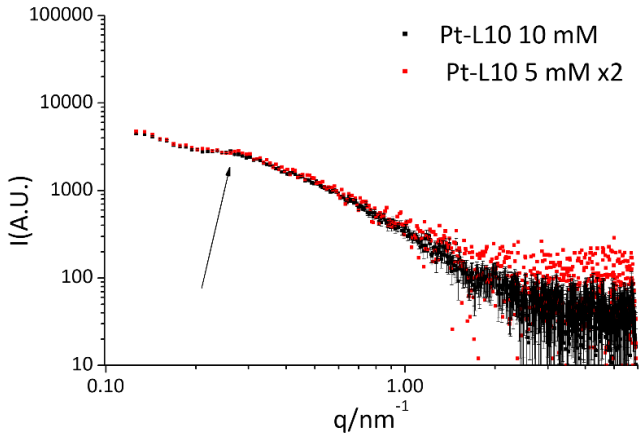

Figure 4.15 SAXS profiles, representing intensity recorded as a function of dispersion vector modulus q for samples of 5 mM (red) and 10 mM (black) in Milli-Q water of **Pt-L10**. The arrow shows the detected inflection point.

The small inflection around 0.25 nm^{-1} implies distances around 25 nm. Moreover, the fact that the spectra of both samples, 5 and 10 mM, double intensity means that the inflection is not due to concentration but related to a characteristic of the particle. Moreover, the profile seems to indicate a maximum length of the particles of 3 nm. Thus, another characteristic of the particles must contribute to the distances between particles. Micelles cannot endure such a big radius; the most suitable option would be that **Pt-L10** forms cylinders, vesicles, or another lamellar compatible organisation.

Nonetheless, the measurements were a preliminary study employed to proof the possibility of conducting these experiments using synchrotron radiation since it will allow to measure samples diluted up to 100 times: signal at small q will get reduced, but the uncertainty at big q would be also reduced in more than a magnitude order. Hence, synchrotron beamtime was requested for the project entitled "Unveiling the structure of metallosurfactants aggregates and metallosomes" and preliminary results are detailed hereinafter. The obtained plots are the result of the average of ten scans after subtracting the corresponding background.

The three complexes were measured at distinct concentrations (5, 10 and 20 mM) and solubilised in either water or PBS. The plots obtained for both solvents at 10 and 20 mM render comparable plots, as can be observed in **Figure A47**. Nonetheless, the differences between

both solvents seem to increase with the alkyl chain length, being higher for **Pt-L10** than **Pt-L6**, and in turn than **Pt-L2**.

A deeper analysis for the three complexes has been performed in water, shown in the next **Figure 4.16**.

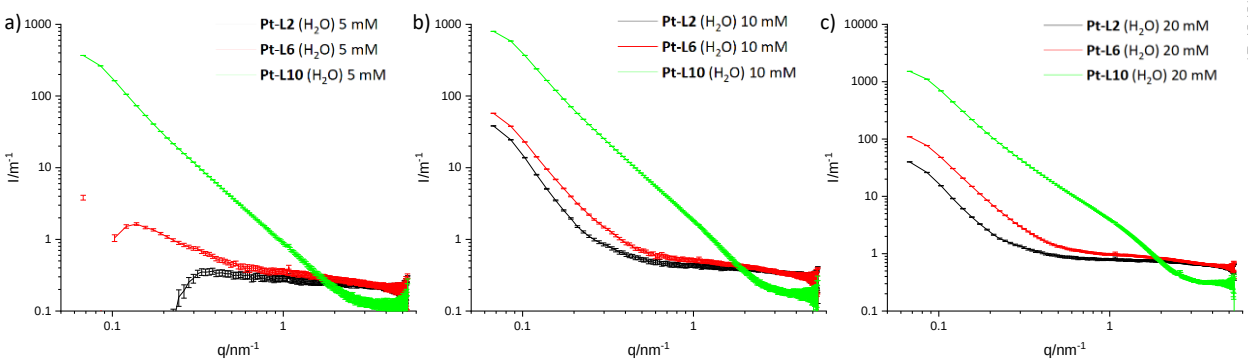

Figure 4.16 SAXS intensity as function of dispersion vector modulus q for **Pt-Ls** in water at (a) 5 mM, (b) 10 mM, and (c) 20 mM.

The obtained intensities for the three complexes at the studied concentrations suggest that they could be displaying long distance organisations. Nonetheless, the corresponding organisation must be discerned by the fitting of the plots to simulated patterns.

It is worth to mention that the slight bump at q = 0.25 nm^{-1} previously seen in **Figure 4.15** is not observed in the spectra recorded at the synchrotron (**Figure 4.16**). Because of that, and previous to the model fitting, the most plausible structure to be adopted by the complexes in solution seems to be a lamellar phase.

Furthermore, when the signals for each complex are escalated to the lowest concentration (**Figure A48**), they show differentiated responses. On **Pt-L10**, the intensity increases with concentration, whereas in **Pt-L2** and **Pt-L6** the trend changes from 5 mM to 10 and 20 mM. It suggests that for **Pt-L2** and **Pt-L6** a structural transformation may be occuring between the 5 and 10 mM concentrations. Moreover, the plots suggest that the thickness of the presumed lamellar structure are not equal and seem to not increase with the alkyl chain length, however it could be due to the high electronic density of platinum and iodine atoms that would stifle the density of the rest of the molecule. Again, fitting to simulated structures must be conducted to understand the occurring organisation.

When analysing the **Pt-Ls** as solids distinct behaviours arose. **Pt-L2** and **Pt-L6** show no peak at the SAXS range while both show a first peak in WAXS at 10.75 and 10.85 nm^{-1}, respectively (**Figure 4.17**), both corresponding to distances of 0.58 nm.

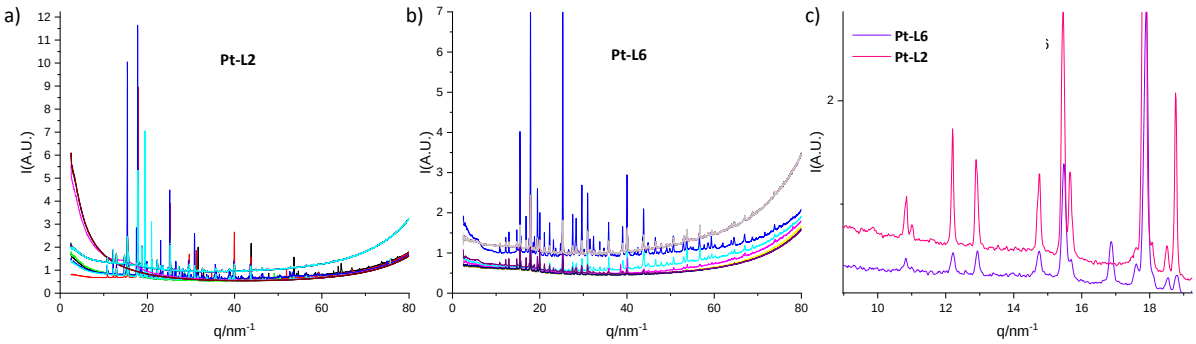

Figure 4.17 WAXS intensity as function of the dispersion vector modulus q of solid **Pt-L2** (a), and solid **Pt-L6** (b), and the comparison between both (c).

In addition, Pt-L2 and Pt-L6 share the first seven peaks found in their WAXS spectra, as seen in **Figure 4.17**, (c).

Concerning **Pt-L10**, peaks were obtained for both spectra, SAXS and WAXS (**Figure 4.18**).

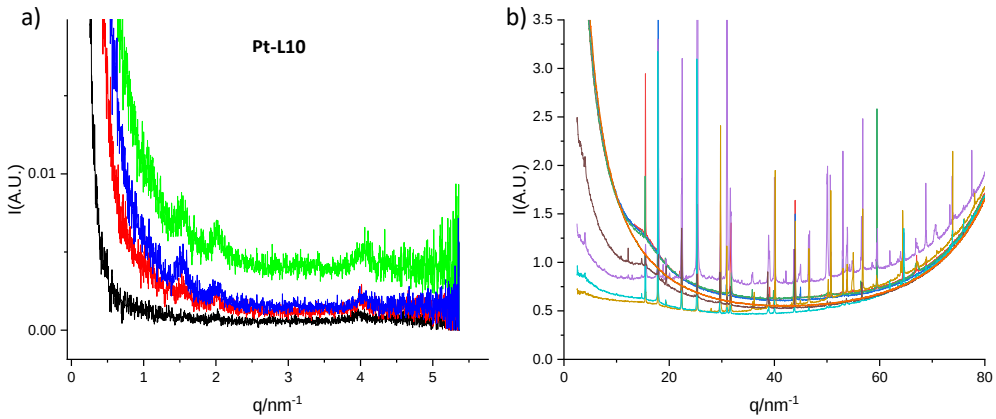

Figure 4.18 SAXS (a) and WAXS (b) SAXS intensity as function of the dispersion vector modulus q for solid **Pt-L10**.

At small q, two peaks at q values of 1.5 and 2 nm^{-1}, which correspond to distances of 4.19 and 3.14 nm, are related with a square root of two between them. A third peak is observed for q = 4 nm^{-1} which being present at q values of 2 and 4 may be related to a laminar phase (prior to their fitting to the simulated pattern).

To sum up, the preliminary data treatment disclosed the presence of complexes organisation in solution that could be related to lamellar phases, occurring below 5 mM concnetration for **Pt-L10**, and above 5 mM for the shorter complexes.

4.4 Stability of *cis*-[Pt(L10)$_2$I$_2$]

The longest complex, **Pt-L10** will be used in the formation of mixed vesicles. Because of that, the stability of the complex in solution was considered an important aspect to evaluate.

Firstly, ESI-MS was performed to determine the entity of complex species along time. Two distinct samples were studied: a 0.5 mM **Pt-L10** solution in Milli-Q water and a 2 mM solution in MeOH. As will be specified in the next Chapter 5.1.2, MeOH solutions are crucial in the metallosomes preparation.

The samples were measured two days after their preparation and after two months; meanwhile, they were stored at 4 °C. Negative mode ESI-MS spectra for both samples are shown in **Figure 4.19**.

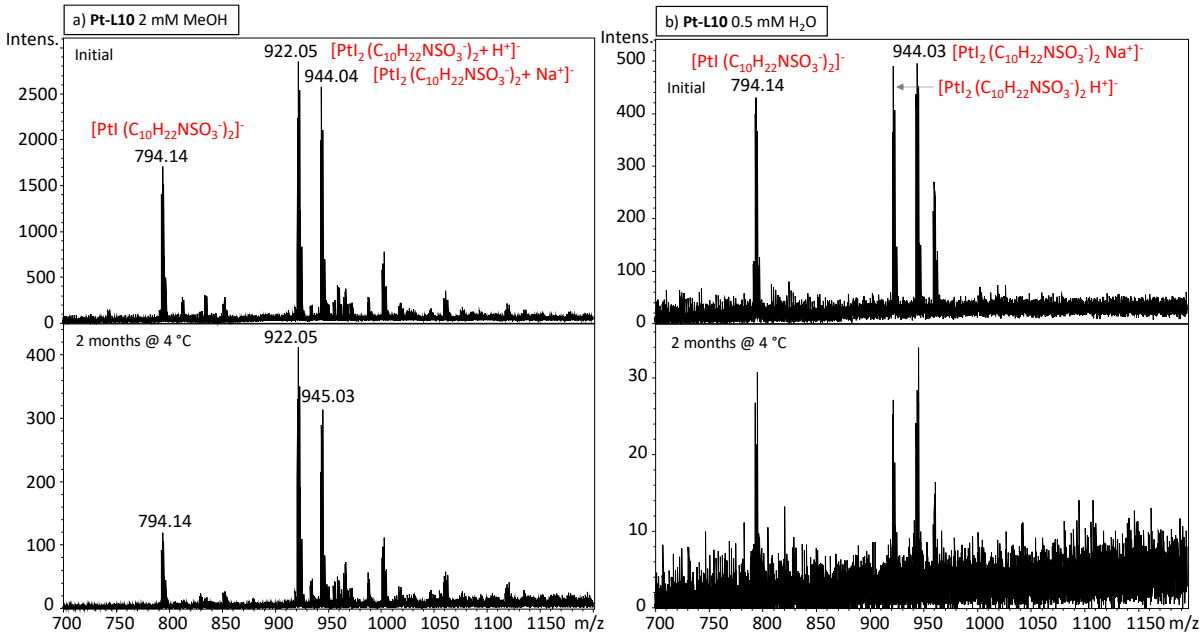

Figure 4.19 Negative ESI-MS spectra of **Pt-L10** in MeOH (a) and water (b) 2 days after preparation (top) and after 2 months of storing at 4 °C (bottom).

When comparing the spectra of the samples (**Figure 4.19**), it is confirmed that in MeOH the chemical entity of **Pt-L10** is maintained. Though, in water, the related molecule peaks decrease in intensity, probably because degradation process occurs. However, degradation products

could not be observed because the spectra were performed at higher m/z ratios and small moieties were not recorded.

Nonetheless, a remarkable feature related to **Pt-L10** stability was observed at certain conditions. During the purification of the complex using a C18 column, as detailed in section 4.1.3, when water was poured through the column to get rid of salts, some remaining complex was noticeable since the solution was slightly yellow. But then, this water-diluted solution became red throughout a couple of minutes. Besides, when they were let at room temperature over time (~48-72 h), the pale-yellow coloration was recovered, and more interestingly, if a spatula tip of KI was added to the solution, the colour reversion was quicker. This behaviour did not occur in the MeOH fraction when purifying, which remained yellow.

The most plausible justification, since it happens in a diluted solution, is the substitution of iodide molecules by water molecules in an aquation process. Actually, the substitution has been reported to occur in the cisplatin diiodo analog.[335]

During a **Pt-L10** purification, the MeOH fraction and the reddish water fraction were analysed by negative mode ESI-MS (**Figure 4.20**). The same species were observed in the spectra of both samples, yet the ratio between peaks was distinct in the two samples.

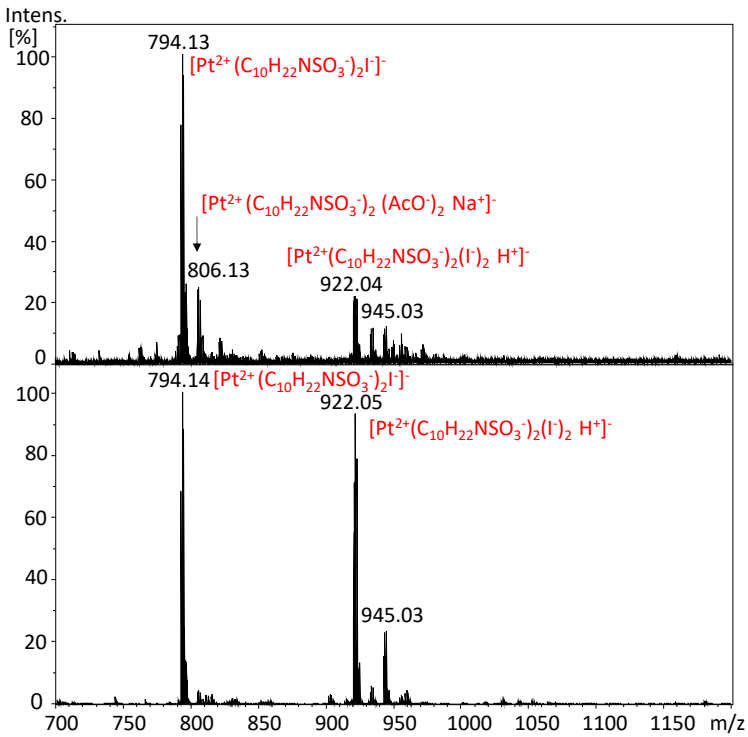

Figure 4.20 Negative ESI-MS spectra of **Pt-L10** species coming from the MeOH fraction (top) and the water fraction (bottom) after purification through the C18 column.

The red water solution showed the complex without one or two iodine atoms as the major peak, and the relative intensity with respect to the peak showing **Pt-L10** bearing both **L10** ligands and two iodides was 100 to 21% (charges were compensated by the presence or absence of sodium ions from the sulfonate groups). In contrast, the spectra for the MeOH fraction revealed that relative intensities of the complex without iodide and the peak of the complex with two iodide atoms were similar, 100 to 93%.

This experiment may corroborate our concept, showing less coordinated iodide presence in the water fraction. Nonetheless, it is noteworthy that the comparison between both samples was not conclusive, since the water solution was far less concentrated in **Pt-L10** than the MeOH fraction. Also, some differences could be attributed to the ionisation of the samples in two different solvents.

4.4.1 *cis*-[Pt(L10)$_2$I$_2$] in water throughout the time

Since the change in coloration was suspected to reveal a ligand exchange, a deeper study of **Pt-L10** behaviour in solution was conducted. A solution of **Pt-L10** at 77.5 µM was analysed by UV-Vis throughout 18 h at room temperature to ascertain sample evolution in water. The recorded spectra and amplified bands are shown in **Figure 4.21**.

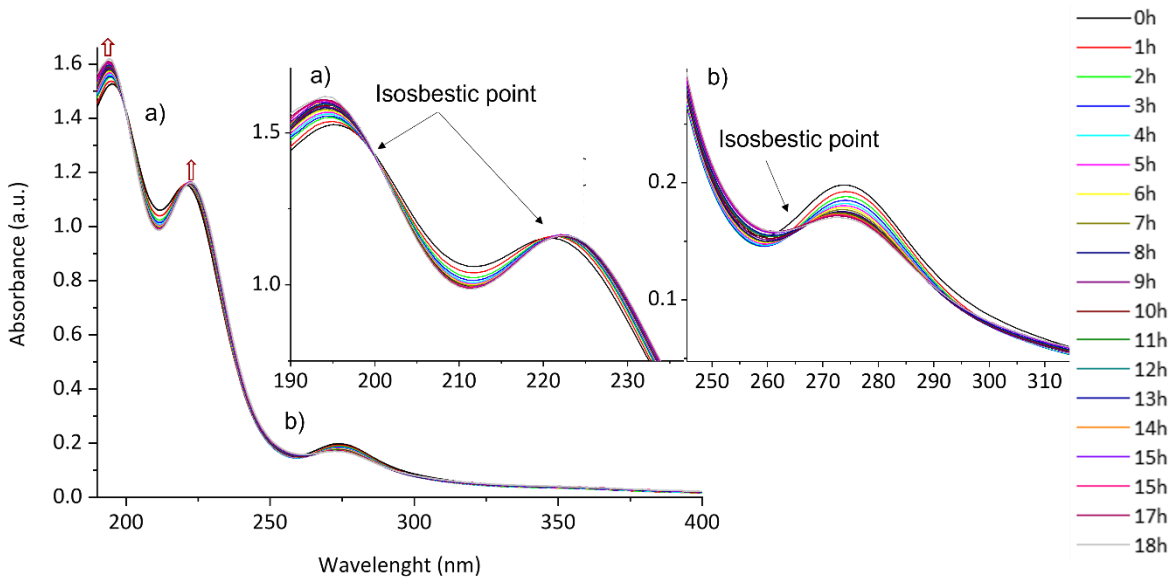

Figure 4.21 Absorption spectra of **Pt-L10** in Milli-Q water at 77.5 µM, recorded during 18 h, where (a) and (b) inserts correspond to indicated regions and the red arrows indicate the absorption evolution.

The UV-Vis bands displayed by **Pt-L10** are already discussed in section 4.2.2, but spectral changes were detected recording the solution over time.

It is reported that when halide ligands are substituted by water the d-d bands are displaced toward the UV, in a hypsochromic shift. However, this shift is usually determined to be very low with respect to the shift of higher intensity bands.[351] So, we decided to focus on the higher absorption bands, at µM range concentrations, not suitable for the study of the d-d bands, which even intuited in the spectra have not been further commented.

Regarding the high intensity bands, centred at the 195 nm and 221 nm, show hyperchromic shifts, being the latter very subtle, 0.1 a.u and 0.01 a.u., respectively. In contrast, a hypochromic shift is observed for the 273 nm band, which decreases 0.03 a.u. Moreover, the 221 and 273 bands show a slender bathochromic shift of 2 and 1 nm, respectively, while the first band at 195 nm endures a hypsochromic shift of 2 nm. Finally, we can highlight, three isosbestic points detected around 199, 222, and 260-267 nm and the arise of a new band around 211 nm.

The general spectral performance suggests that the gradual aquation of some of the Pt(II) ligands must be occurring. The hydrolysis of *cis*-$PtI_2(NH_3)_2$ has been reported to be close to that of cisplatin, where the ammonia ligands are retained while both halide ligands are substituted by water. However, the hydrolysis of *cis*-$PtI_2(NH_3)_2$ has been also reported to be slower, because of the higher Pt-I bond strength and the higher inertness due to the greater soft character of iodide with respect to chloride.

According to the bibliography, bathochromic shifts are displayed when hydrolysis of the amino groups occurs, while hypsochromic shifts are noticed when halides are substituted. Likewise, the bathochromic shifts are usually described to occur at moderate acid conditions, while the hypsochromic shifts are reported at physiological and basic pH.[335,351,392] As described above, the first band suffers a slight hypsochromic shift, while the second and third one a slender bathochromic shift. However, in reference articles, the computed shifts are greater than those shown here. For that reason, with the data obtained, we could not certainly assure which ligand is hydrolysed after the mentioned displacements. However, Messori *et al.* described the hydrolysis of the isopropylamine (C_3H_9N) groups taking place before the hydrolysis of the halides in the corresponding *cis*-$PtI_2(C_3H_9N)_2$ complex. When recording the UV-Vis of the complex, they reported a hyperchromic shift in the band at 300 nm, over 24 h, and sample incubation at 37 °C. Moreover, they supported the measurement following an appropriate concentration solution by ^{1}H-NMR, where they found free isopropyl amine signals.[336]

Overall, the hyperchromic shift of the 300 nm band recorded by Messori *et al.* is in contraposition with our related band (273 nm) in the **Pt-L10** UV-Vis spectra, which shows a hypochromic variation. This comparison made us rather consider the hydrolysis of halides instead of the amino group in the case of **Pt-L10**. Nonetheless, the platinum coordination of the isopropylamine might be more labile than the coordination of **L10**, because in our ligand the amine is bonded to a $-CH_2$ group instead of to more bulky $-CH_2(CH_3)_2$, as in isopropylamine. Therefore, with the gathered evidence the hydrolysis of the halides previous to the alkyl amine seems to be more plausible. In addition, focusing on the results obtained for the DFT calculations previously presented in this chapter, the NTO associated to the UV signals suggests that iodine is the ligand more involved in the hydrolysis process. Thus, it is consistent to think that the hydrolysis of iodine ligands is the main responsible for the observed UV-Vis spectra evolution.

Furthermore, several studies report a biphasic hydrolysis reaction for cisplatin and *cis*-$PtI_2(NH_3)_2$, which associate comparable evolution of the UV-Vis spectrum to the progressive release of two halides and their substitution by water molecules.[335,392] In literature, the displacement of the isosbestic point, at 285 and 274 nm for cisplatin and *cis*-$PtI_2(NH_3)_2$, is related to a biphasic hydrolysis reaction. The isosbestic point of **Pt-L10** shown in **Figure 4.21** (b), at 260 – 267 nm seems to reveal a biphasic hydrolysis reaction with similar rate constants to the ones reported for cisplatin and *cis*-$PtI_2(NH_3)_2$. In the proposed reaction mechanism, water acts as nucleophile at both acidic and basic pH by an associative mechanism.[335,392]

In the work of Miller *et al.,* the rate constant (K_{obs}) and the half-time ($t_{½}$) were determined treating the hydrolysis reaction as a pseudo-first-order reaction and fitting the absorbance at a maxima wavelength in front of time to a single exponential function (**Figure A49**). The K_{obs} and $t_{½}$ for **Pt-L10** are $5.77 \cdot 10^{-5}$ s^{-1} and 200.05 min, respectively. Meaning that the hydrolysis reaction of **Pt-L10** should occur faster than the hydrolysis of cisplatin or *cis*-$PtI_2(NH_3)_2$, with values reported in the literature, with K_{obs} and $t_{½}$ values of $4.45 \cdot 10^{-5}$ s^{-1} and 259.4 min for cisplatin, and $2.08 \cdot 10^{-5}$ s^{-1} and 555.58 min for *cis*-$PtI_2(NH_3)_2$.[335]

Finally, to reassure the spectral changes, we repeated the experiment incubating the solution at 37 °C and recording it several times for a week (**Figure 4.22**).

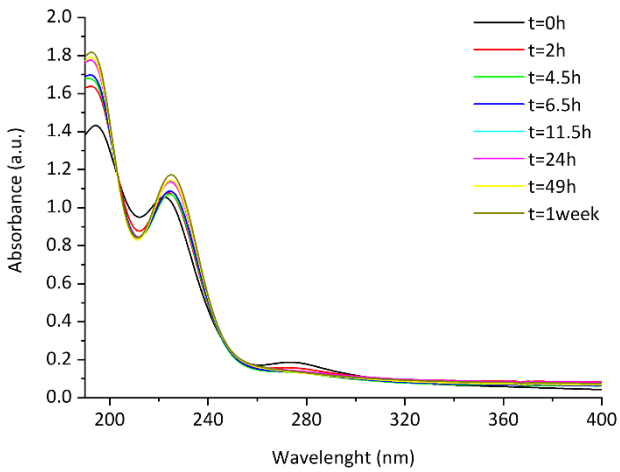

Figure 4.22 Absorption spectra of **Pt-L10** in Milli-Q water at 70 µM, incubated at 37 °C recorded for a week.

The main features in the evolution spectra are maintained: the 195 nm band progresses showing a more intense hyperchromic shift (0.38 a.u.), as well as the band at 220 nm (0.12 a.u). The band at 273 nm shows, again, a hypochromic shift that ripens to almost its disappearance. Similarly, the shifts to longer or shorter wavelengths are fairly unnoticed, except for the hypsochromic shift of the first band at 195 to 192 nm and the bathochromic shift of the 220 nm band to 223 nm. Interestingly, we see how the spectrum recorded after 49 h is almost equivalent to the one recorded after a week.

Nonetheless, the change in the 273 nm band is concordant with the behaviour reported in the literature, that, along with the previous evidence and experiments we propose the aquation of the iodide ligands in a biphasic mechanism when **Pt-L10** is solubilised in water.

In summary, the hydrolysis of **Pt-L10** was initially observed during the purification process, which seems to be favoured at high dilutions in the water fraction. Besides, **Pt-L10** showed compromised stability storage after two months in water, but a significant improvement when dissolved in MeOH. The mechanism of the hydrolysis seems to follow the same mechanism reported for *cis*-$PtI_2(NH_3)_2$ and cisplatin, releasing progressively the two halide ligands. The K_{obs} calculated for **Pt-L10** are in the same order of magnitude as that for cisplatin and *cis*-$PtI_2(NH_3)_2$.

4.4.2 General remarks

Three complexes with the general formula *cis*-$[PtI_2(L)_2]$ have been synthesised (**Pt-L2**, **Pt-L6**, and **Pt-L10**) bearing the amino alkyl sulfonate ligand family **L2**, **L6**, and **L10**, respectively. The complexes with ionic character have been isolated from common salts, or at least their quantity has been importantly reduced. To do it, several purification strategies have been

implemented, but finally, apolar silica column chromatography was considered the best option.

The complexes have been characterised by various techniques confirming their structure. Similarly, they have shown excellent water and low molecular weight alcohols solubility. Furthermore, the characterisation enabled the determination of the reaction by-products and endeavoured to propose a reaction mechanism.

The study of the supramolecular reorganisation of the complexes in water has portrayed the possible organisation of at least the longest carbon chains, **L6** and **L10**, complexes, and aimed their potential as MTS. A CAC value has not been accurately determined but an estimation has been obtained. Finally, the preliminary data obtained from SAXS experiments suggest the presence of a lamellar phases, however it is expected that the fitting of the obtained spectra will unveil the occurring organisation.

The stability of **Pt-L10** in solution seems to be hindered by the exchanges of iodides ligands by water. Yet, the complex has shown remarkable stability dissolved in MeOH.

5. TUNING UP METALLOSOMES: PREPARATION AND CHARACTERISATION

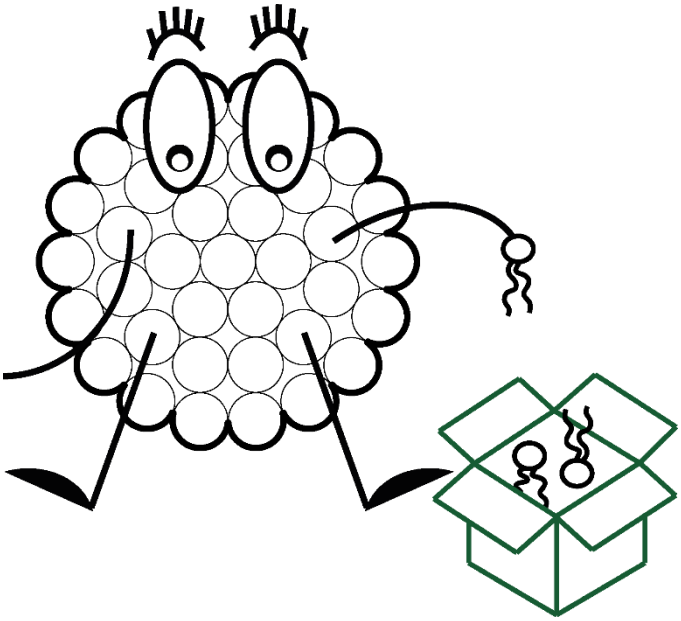

The present chapter is dedicated to the preparation of metallosomes (**MTL**), metal-containing liposomes. More concrete, based on the incorporation of the higher amphiphilic Pt(II) complex, **Pt-L10**, into structural phospholipids. This chapter is divided into two main sections: the first one is committed to evaluate if the encapsulation of the complex in liposomes was successful, and which was the optimum way to produce the liposomes. The second part of this chapter is devoted to the optimisation and extensive characterisation of the **MTL**, mostly conducted in Luciani Research Group, in Bern University, under the supervision of Prof. Paola Luciani and Dr. Simone Aleandri.

5.1 Initial study of platinum metallosomes

5.1.1 Why metallosomes?

The main advantages of liposomes as DDS have been considered in the introduction section of the thesis. In brief, the preparation of **MTL** was an already employed strategy for biomedical purposes in our group, when molybdenum sulfonate phosphines were employed in the production of **MTL** as CO releasing systems.[274,275] Following these precedents, the preparation of our **MTL** were conducted considering the potential chemotherapeutic interest of Pt(II). In **Scheme 5.1**, a schematic representation shows the general concept in **MTL** preparation.

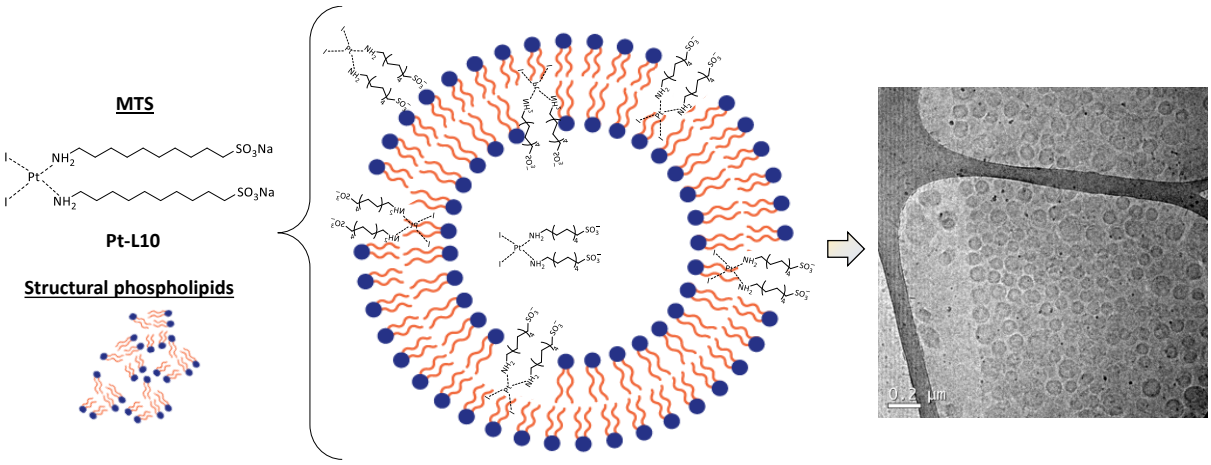

Scheme 5.1 Representation of the structural units of the prepared **MTL** and a *cryo*-TEM image of them.

The **MTS** or **Pt-Ls** were designed to bear a charge in one extreme of the complex that should function as a hydrophilic group. Nonetheless, due to the limited amphiphilic behaviour of **Pt-L2** and **Pt-L6**, and time constrictions, the preparation of **MTL** was restricted to the most amphiphilic complex, **Pt-L10**. One of the main reasons for this specific design was to produce metal-containing liposomes, that forces the internalised platinum complexes to be added to

the bilayer membrane of the vesicles. Nonetheless, the localisation of the complex in the **MTL** will be discoursed during this chapter.

5.1.2 Initial metallosomes preparation

Seizing the solubility of **Pt-L10**, two strategies for the preparation of **MTL** were investigated. In the introduction section, the most common preparation methods have been portrayed. Among them, the thin film hydration method was chosen as the appropriate methodology due to its simplicity and the lack of requirements for specific instrumentation. Employing this method, the drug can be internalised in the aqueous cavity, for hydrophilic drugs, or in the apolar region of the bilayer for lipophilic drugs.

During the film hydration, water-soluble drugs are usually added solubilised in the aqueous medium. In this way the compounds are encapsulated into the vesicular aqueous cavity. However, the encapsulation efficiency of water-soluble drugs is certainly low. The large volume required for hydration, in comparison to the entrapped volume in the aqueous interior lowers the encapsulation efficiencies that are also dependent on the sizes of the liposomes since larger and unilamellar liposomes can entrap higher amounts of drugs with respect to smaller ones.[393] On the other hand, free lipophilic drugs have limited therapeutical use that can be resolved by incorporating the hydrophobic drug into the phospholipidic bilayer. In this case, the lipophilic drugs are incorporated in the lipid film when prepared and end up in the lipophilic compartment of the bilayer. In these cases, the encapsulation efficiency is usually greater due to the internalisation is not correlated to the size of liposomes.[394,395]

The lipid chosen for the preparation of **MTL** was soy phosphatidylcholine (SPC), which is an easy to work natural zwitterionic phospholipid that has shown great results in previous work in our group. The **MTL** have been prepared at SPC concentration of 3 mM, and at a **Pt-L10** concentration ranging from 0.05 to 1.4 mM, which corresponds from 300/5 to 300/140 SPC:**Pt-L10** molar ratios.

The next main steps in film hydration method were followed. Considering that **Pt-L10** is highly soluble in MeOH and water, it can be included in the formulation as a lipophilic or hydrophilic drug. Hence, it could be added in two distinct steps of the preparation: in the hydration step, if the film is hydrated with an aqueous solution containing **Pt-L10**, or when producing the film, if **Pt-L10** is solved in MeOH and added before the film production. Both strategies are represented in **Scheme 5.2**.

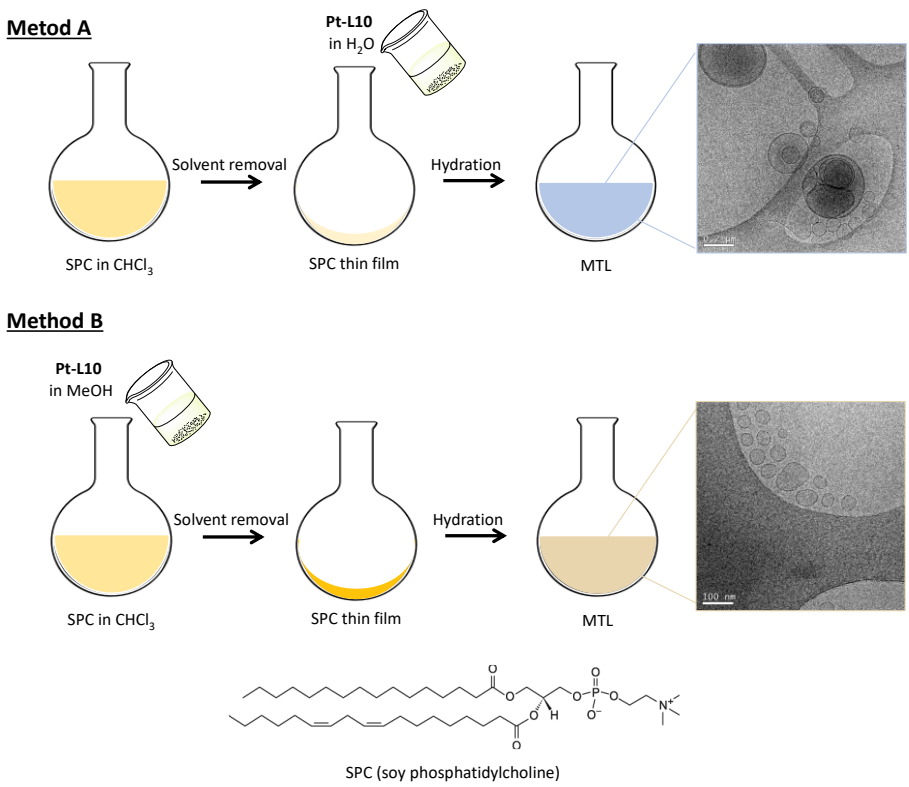

Scheme 5.2 Schematic representation of MTL preparation adding **Pt-L10** during water hydration (method A) and adding **Pt-L10** before the film preparation to obtain a mixed film after solvent evaporation (method B).

In method A, the lipid film is hydrated with **Pt-L10** solubilised in water that, in principle, should enhance the internalisation of the **Pt-L10** in the inner aqueous core. In method B, by adding the **MTS** in MeOH to the phospholipid solution in $CHCl_3$/MeOH 2:1 v/v and the following solvent removal, we obtain a homogeneous film that already contains the **Pt-L10**, which might favour the subsequent retention of the drug into the bilayer. After the hydration step, no further size tuneability nor purification steps were undertaken since the initial goal was to understand the performance and internalisation of **Pt-L10**.

The platinum encapsulation efficiency was calculated to compare the internalisation of both strategies. The internalised amount of **Pt-L10** is measured as the encapsulation efficiency, calculated with the general **Equation 5.1**.

$$\text{Encapsulation efficiency (\%)} = \frac{\text{Amount of drug entrapped in metallosomes}}{\text{Initial amount of drug in the suspension}} \cdot 100 \qquad \textbf{Equation 5.1}$$

Nonetheless, it is important to note that we were not able to directly determine the amount of drug entrapped in the liposomes. The metallosomes had to be separated from the aqueous media, in which the non-encapsulated drug will remain. This aqueous media or supernatant was separated by centrifugation and measured by ICP-OES. Then, the amount of entrapped

platinum in the metallosomes was obtained by the difference between the supernatant platinum concentration and the initial platinum amount on the stock solution (also measured by the ICP-OES), which gives the amount of drug retained by the pellet, or what is the same, entrapped into the **MTL**. Previous to this, for the sedimentation of the liposomes, centrifugation parameters were optimised to 15 min at 16800 rcf, what produced full sedimentation of the liposomes (**Figure A50**). **MTL** centrifugation was undertaken and then the supernatant was collected by decantation. The obtained encapsulation efficiency (%) is reviewed in **Table 5.1** as method A (**Pt-L10** addition while hydration) and method B (**Pt-L10** addition during film preparation).

Table 5.1 Results for the encapsulation efficiency (%) of platinum (mean ± standard deviation) in the prepared **MTL** using method A, in which **Pt-L10** in water was added during hydration step; and method B, in which **Pt-L10** in MeOH was used to prepare a homogenous mix film between de complex (from 0.15 to 1.4 mM) and SPC ([SPC = 3mM]). The platinum concentration was measured by ICP-OES for the obtained supernatant after liposomes sedimentation and the initial **Pt-L10** solution.

Method	Encapsulation efficiency (%)	Number of samples
A	20.6 ± 6.2	4
B	22.2 ± 5.9	10
Mean A + B	22.0 ± 6.0	14

The table, shows the mean of the encapsulation efficiencies percentages for the prepared **MTL** at the distinct molar ratios, suggesting comparable values for method A or B.

The sizes and morphology of the **MTL** were further examined. The size distribution of vesicles was determined by DLS, expressed by number, while microscope techniques allowed the visual evaluation of them: around 1 µm with optical microscopy and in the nm range for the electron microscopy. Nonetheless, the limitations of DLS and microscopy techniques had already been commented in the previous section. Hereinafter, these data for two distinct formulations are reviewed in **Figure 5.1** and **5.2**.

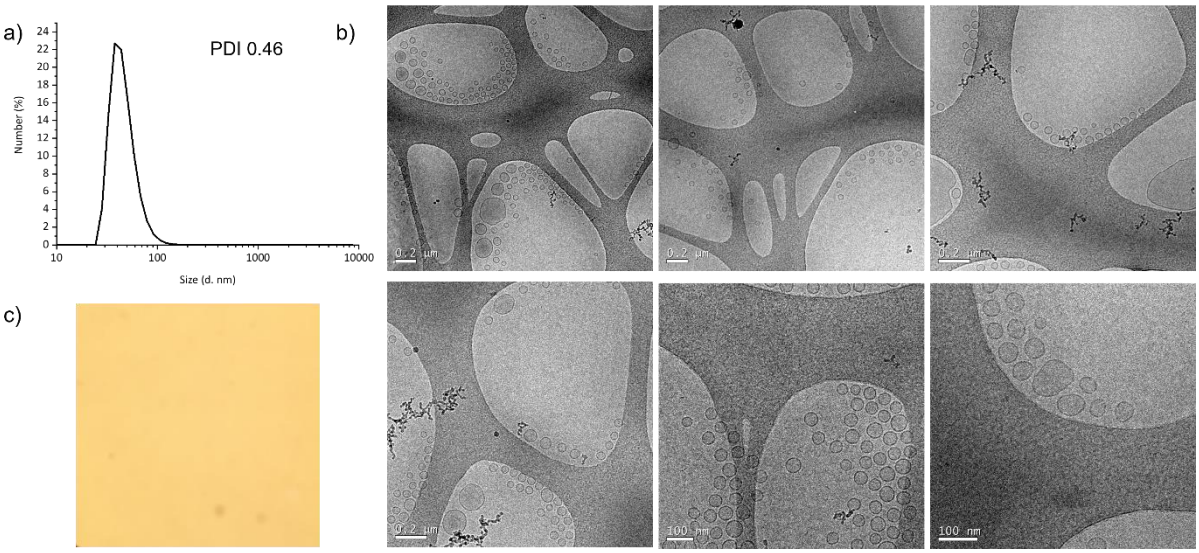

Figure 5.1 DLS plot (a), *cryo*-TEM micrographs (b), and optical microscopy image (c) for SPC:**Pt-L10** at 300/50 molar ratio.

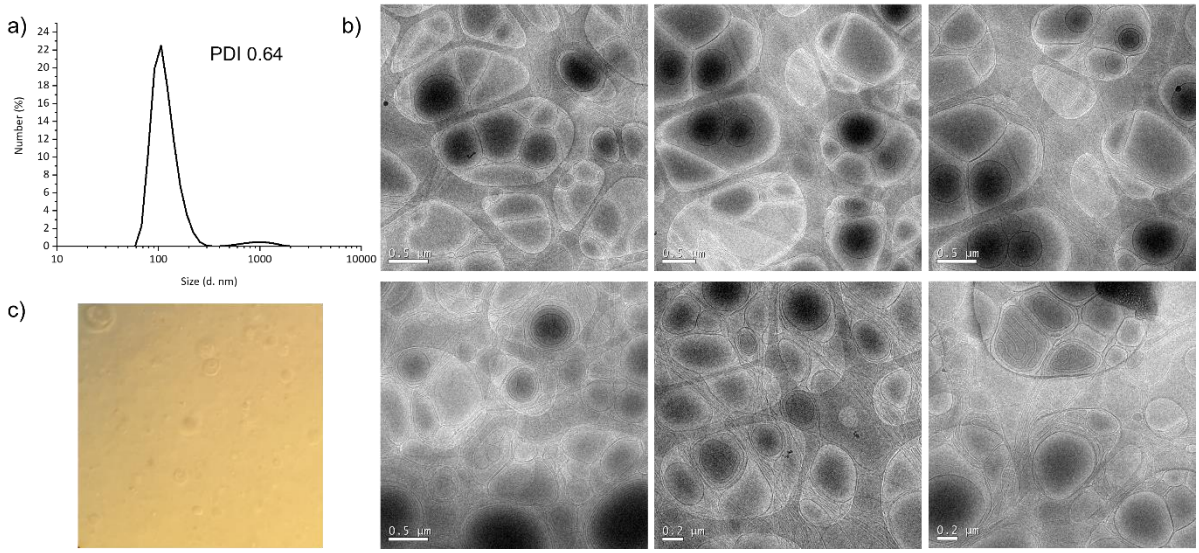

Figure 5.2 DLS plot (a), *cryo*-TEM micrographs (b), and optical microscopy image (c) for SPC:**Pt-L10** at 300/100 molar ratio.

Slightly smaller vesicles and lower PDI values were found in the formulation with less amount of **Pt-L10**. Specifically, 300/50 molar ratio presented vesicles around 50 nm measured by DLS, in accordance with the optical microscopy image, in which no big vesicles are observed, and with *cryo*-TEM micrographs, in which small vesicles are displayed. Whereas 300/100 molar ratio displayed larger vesicles with DLS sizes of 100 nm and 1000 nm since two families are observed. Nonetheless, it is evident that for both concentrations, a mixture between small and large vesicles is found. In both samples the morphology of the vesicles, **Figure 5.1**, b, and **5.2**, b, showed SUV and LUV, with the presence of few MLV and MVV in the 300/100 molar ratio.

Besides, in **Figure A51** a summary with several *cryo*-TEM micrographs is shown. Interestingly, the obtained morphologies did not differ significantly between methodology A and B.

Regarding the size of the **MTL** determined by DLS and expressed by intensity, distinct populations were measured, as expected for non-extruded SPC **MTL**. In all the cases, the size ranges from 100 to 5000 nm, the latter located over the detection limit of DLS. The supernatant and resuspended pellet were also analysed by DLS. Surprisingly, the supernatant showed the same populations but with higher intensities for the smallest population with respect to the initial **MTL** sample. Whereas the resuspended pellet indicated higher amounts of the bigger population of vesicles. Plots exemplifying this behaviour can be found in the annex section of this thesis (**Figure A52**). Even though the optimisation of the centrifugation parameters for plain SPC liposomes pointed to total sedimentation of vesicles (**Figure A50**), undoubtedly the centrifugation was not settling all the **MTL** since a fraction of them was observed in the DLS of the supernatant. Such a different behaviour could be attributed to a modification of the lipid bilayer with the addition of **Pt-L10**. Moreover, posterior studies conducted at *Unitat de Biofísica*, confirmed the optimal parameter set on this thesis for liposomes sedimentation. For the case of centrifugation of plain SPC MLV obtained in the same conditions as in the present work, previous results (Elodia Serrano, *Unitat de Biofísica* at UAB) show that for any centrifugation time higher than 8 minutes, and carried out at 16873 rcf, there is a massive sedimentation of big liposomes, and only 6.7 ± 2.7% (n = 3) of the initial SPC remains in the supernatants determined by colorimetric quantification by the Stewart method hereinafter presented.[396] Likewise, DLS measurements and optical microscopy images show that these supernatants are only constituted by liposomes smaller than about 2.5-3 µm. On the other hand, and due to their intense light scattering, MLV sedimentation could be also monitored by changes in the absorbance (visible range) of the supernatants, and the final absorbance was 7.3 ± 1.2% (n = 3) of the non-centrifuged samples, that is, a similar value than that obtained by colorimetric quantification. Thus, for this type of samples (SPC MLV) the measurement of the supernatant absorbance is a good reference of the amount of lipid that it contains after the centrifugation, shown in **Figure A50**.

This led us to question an important feature: if there were liposomes on the supernatant, it would imply that they are not fully sedimented, and that the encapsulation efficiency must be higher than the analysed by ICP-OES, since not all the **MTL** would be precipitated in the pellet.

To attain this question, the remaining phospholipid quantity on the supernatant was measured by means of the well-known Stewart method, based on the formation of a complex between phospholipids and ammonium ferrothiocyanate that can be extracted in $CHCl_3$ to be measured by UV-Vis.[396] Previously, the interaction between **Pt-L10** and the Stewart reagent was discarded by measuring the absorbance at 470 nm and a calibration pattern for each molar ratio was also performed (**Figure A53**). Then, the phospholipid concentration was measured at each sample. The next graph shows the measured concentrations (**Figure 5.3**).

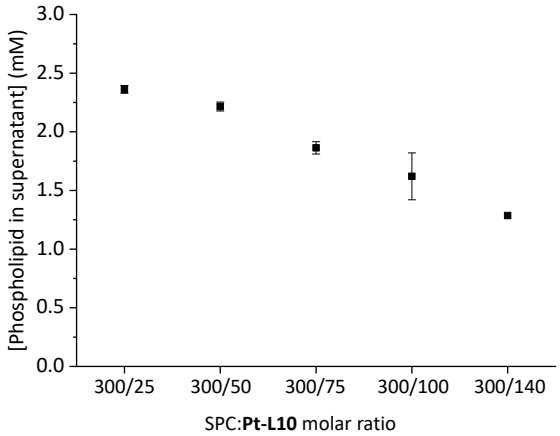

Figure 5.3 SPC concentration (mM) in the supernatant measured by Stewart method *vs* SPC/**Pt-L10** molar ratio.

The lipid concentration in the supernatant decreases whit higher **Pt-L10** concentration (**Figure 5.3**). This fact must be related with the presence of a high number of **MTL** that sediment after centrifugation, contrary to the previous results reported at *Unitat de Biofísica* for plain SPC MLV, where around a 92% were sedimented after centrifugation. Despite that the higher sedimentation of the **MTL** could be driven by an increase in size and/or aggregation, no significant differences between either the DLS size distribution of the **MTL**, their supernatant or the pellet were observed (**Figure A52**). Therefore, the higher sedimentation could be ascribed to a modification in the density of the solution arising from the increasing amount of platinum. To sum up, it is evident that the small size population of **MTL** increases with the presence of **Pt-L10**, which must be altering the liposome membrane.

5.1.2.1 Metallosomes stability

To examine the **MTL** stability, we studied the evolution of two samples by DLS over time. The two samples had 300/50 SPC:**Pt-L10** molar ratio and were prepared by methods A and B. These results are shown in **Figure 5.4**.

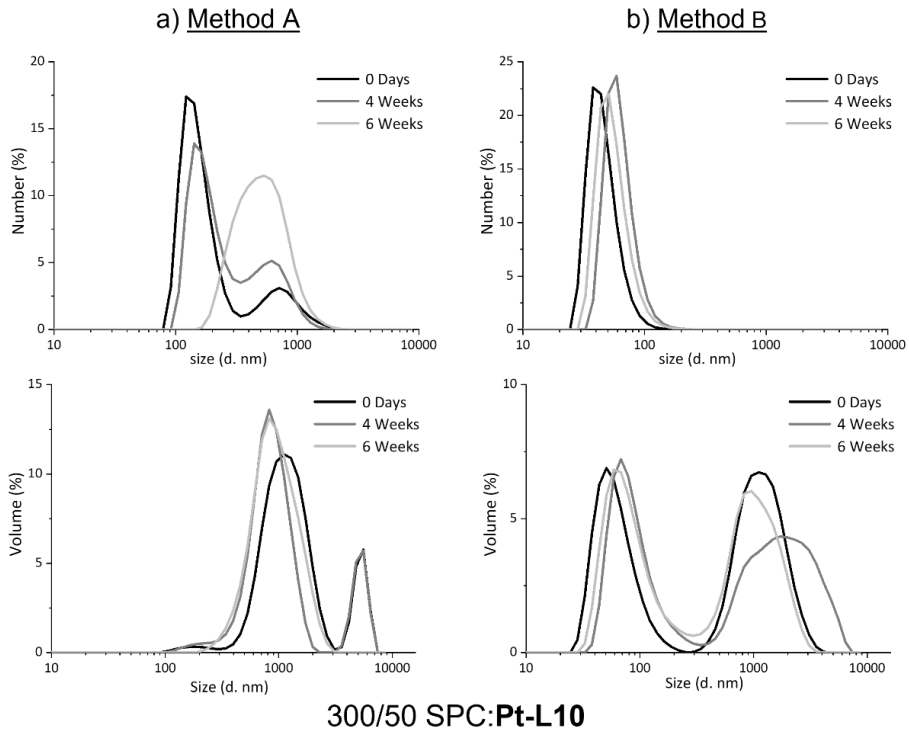

Figure 5.4 DLS graphs of 300/50 SPC:**Pt-L10 MTL** by method A (a) and method B (b), represented as percentage by number (top) and volume (down).

In both cases, **MTL** showed to be stable when stored at 4 °C for at least 4 weeks. However, the experiment only assures that the **MTL** are not considerably aggregating upon storing but is not considering the platinum concentration. Discrepancies between percentage of number and volume are normal and related to the technique, as already commented in section 4.3.4.[134]

Subsequently, we intended to study how the **MTL** behaved upon dilution to determine if the amount of **Pt-L10** encapsulated diminished. For that, a sample was diluted in water 1:1. The supernatants were collected after sedimentation over 1 hour and the samples were measured by ICP-OES. The experiment resulted in slight reduction of platinum after the first dilution that remained unchanged for 1 hour, as seen in **Figure A54**.

5.1.2.2 Size-exclusion chromatography purification

Typically, liposomes purification is done employing size exclusion chromatography, Sephadex™, which has already been outlined in the previous chapter 4. In that case, the main intention was removed of impurifying salts from **Pt-L10**. However, the most common utility of Sephadex™ is to separate the free drug from liposomes, especially crucial when the drug to be internalised is water-soluble. Hence, we considered it could be an optimal procedure to separate the free complex from the **MTL**.

To verify the procedure as a purification option, both plain SPC liposomes and a solution of **Pt-L10** in water were run through the column separately and measured. For that, 800 nm SPC liposomes at 1.5 mM were passed through Sephadex G-25 (PD-10 column) and collected in 1 mL fractions. By UV-vis it was seen that 800 nm liposomes went out in fractions 3 to 6, with a maximum absorption found at fraction 4. Then, using the same column, a solution of **Pt-L10** (1.3 mM) was inserted in the column and collected. Some of the 1 mL collected fractions were analysed by ICP-OES to determine where **Pt-L10** elutes. It was found that most of the complex flows out between the fractions 7 to 12 (**Figure 5.5**).

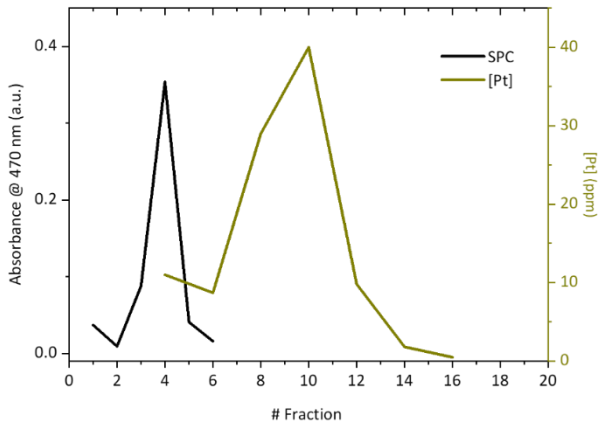

Figure 5.5 Plot showing the fraction were SPC liposomes (1.5 mM) and **Pt-L10** went out from Sephadex column, measured by UV-vis and ICP-OES, respectively.

These preliminary results indicate that the purification method could be employed for our **MTL** purification. However, we decided to repeat the experiment with a higher **Pt-L10** concentration to verify its dependence on the purification process. **Pt-L10** concentration was increased up to 3 mM since this concentration allowed to visually follow the complex through the column. When the complex went through the column, it was noticeable that a high amount of the coloured solution went out in fraction number 4, coeluting with the fractions where the liposomes go out. The inconsistency in the elution fraction of **Pt-L10** must be related to the solution concentration, doubled up between experiments. This suggests that at the highest concentration, the complex will flow out with the 800 nm liposomes, pointing that probably larger aggregates are arranged at greater **Pt-L10** concentrations. Thus, we deemed that this purification methodology would be impractical for our purpose due to its reliance on **Pt-L10** concentration.

5.2 Redefining the metallosomes formulation and characterisation

The optimal liposomal formulation can be attained by selecting the convenient phospholipids and components, functionalisation and even including a targeting strategy. The selected lipid is critical and determines the stability of the liposomes or efficiency, among others. These liposomes features are related to the head group and alkyl chain of the lipids, in addition to the ratio between lipids and other components. Nonetheless, the capacity of liposomes as DDS is affected by the addition of drugs that could affect its lamellarity, rigidity, surface charge or lipid organisation, etc. Due to this, liposomes must be exceptionally characterised.[397] In view of the importance of liposomes formulation, the current section describes the preparation of **MTL** employing distinct lipids with divergent characteristics and extensive characterisation of the obtained **MTL**. The study was conducted during an internship at Luciani Research Group, under the supervision of Prof. Paola Luciani and Dr. Simone Alenadri, at the Department of Chemistry, Biochemistry and Pharmaceutical Sciences at Bern University.

5.2.1 The choice of lipids

The evaluation of distinct phospholipids in the formulation will tune the final properties of our **MTL**. The lipid composition will shepherd the manufacturing method and the drug incorporation, affecting the physicochemical properties of the **MTL** formulations, including the drug release.

The chosen lipids varied in the degree of saturation and chain length but shared the choline moiety (in the headgroup) and thus the neutral charge, as zwitterionic lipids. The main characteristics of each structural lipid used are specified in the next **Table 5.2**.[126,143]

Table 5.2 Specific structural and physicochemical characteristics of the structural lipids employed as structural components in the preparation of **MTL**.

	Lipid	Carbon alkyl length	Unsaturations / chain	T_m (°C)
SPC	L-α-phosphatidylcholine from soybean	16 to 18 [a]	0 to 3[b]	-20 - -30
DOPC	1,2-dioleoyl-*sn*-glycero-3-phosphocholine	18	1	-20
DSPC	1,2-diasteroyl-*sn*-glycero-3-phosphocholine	18	None (fully saturated)	55
DMPC	1,2-dimyristoyl-*sn*-glycero-3-phosphocholine	14	None (fully saturated)	23

[a] Natural lipid with a fatty acid distribution of 16 C length (14.9%), 18 C length (83.8%).
[b] Natural lipid with a fatty acid distribution 0 unsaturations (18.6 %), 1 unsaturation (11.4%), 2 unsaturations (63%) and 3 unsaturations (5.7%).

Neutral liposomes have been reported to show encapsulation efficiencies up to 2.5-fold higher respect charged liposomes.[398] Regarding the saturation degree, fully saturated lipids present higher T_m than unsaturated ones and usually show increased liposome stability.[113,398–400]

Therefore, the **MTL** preparation with the four structural lipids may alter several features in their outcome. For instance, to efficiently encapsulate a drug in the bilayer, some flexibility is required, which is not a major asset of SPC. Moreover, the 14 C chain in DMPC will reduce the mismatch between the alkyl chain of the lipid and **Pt-L10**. Actually, the use of a shorter structural lipid is in concordance with the observations of McMullen *et al*., who showed that added molecules have a preference for lipids holding hydrophobic chains lengths approximately the same as the length of the lipids chain in the bilayer.[401]

Regarding the T_m, two of the lipids, SPC and DOPC display a low T_m and are at liquid-crystalline phase at room temperature. On the contrary, DSPC is at the gel phase at room temperature, while DMPC, which presents the phase transition near room temperature, is in between, hassling its manipulation. This is an important characteristic, since as mentioned in the introduction chapter, above the T_m the bilayers are fluid, and the bilayer thickness is lower than that of the gel phase. Next, in **Figure 5.6**, the phospholipids employed are represented along with the molar ratio tested for each formulation, which ranged from 10/1 to 1000/1 lipid:**Pt-L10**, at a lipid concentration of 5 mM.

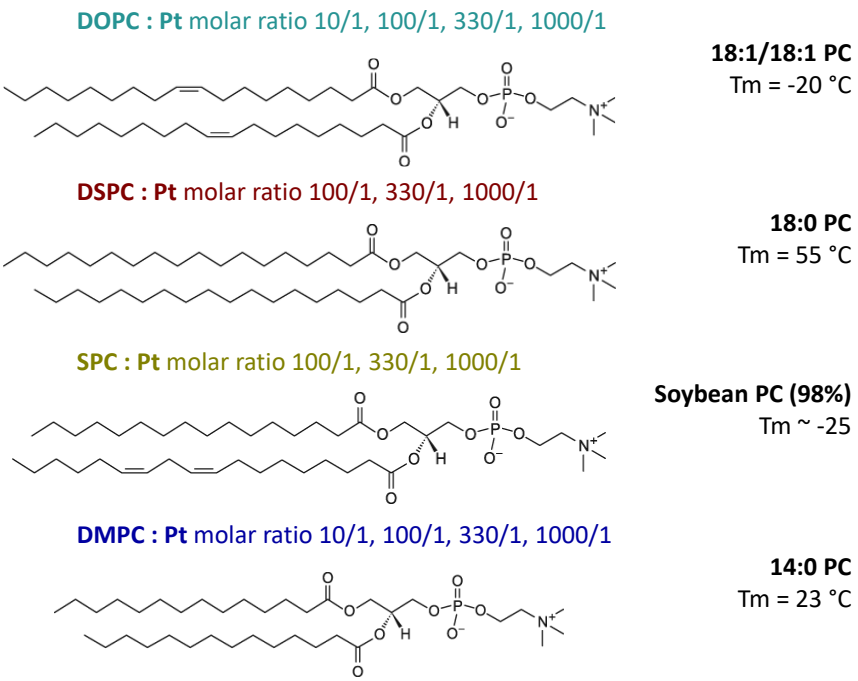

Figure 5.6 Main structures of the employed phospholipids with its average main transition temperature and the formulations used for the preparation of **MTL**.

Furthermore, the selected [**Pt-L10**] correspond to concentrations above 0.15 mM and below 0.05 mM the estimated CAC (0.10 – 0.12 mM).

5.2.2 Preparation of metallosomes

The preparation of liposomes followed the general procedure as the **MTL** prepared at UAB, however, an additional step, freeze-thaw cycles and a subsequent extrusion were included.[402] The preparation of liposomes is fully described in the experimental section of this thesis, section 8.3.3.2, and represented in **Scheme 8.1**. In summary, the lipid in $CHCl_3$ is added into a flask to subsequently add the **Pt-L10** in MeOH. The mixture is slightly stirred, and the solvent removed to obtain a homogenous film, let under vacuum overnight to assure complete dryness. The film is hydrated with PBS and the solution is twice vortexed and soaked in water bath at a temperature above the T_m. Afterwards, the liposomes are freeze-thawed six times. With the objective of inducing the formed MLV to mainly LUV. Besides, freeze-thaw cycles are reported to enhance the encapsulation of a drug.[403] Finally, the extrusion process through polycarbonate filters of 200 nm pore size is performed at 5 °C, again above the T_m of each lipid since they are required to be at the fluid phase during the process.

It is noteworthy, that the use of an automatic extruder, in which a pressure up to 50 bar can be employed, assists in the preparation of liposomes, providing a much faster and more convenient production than manual methods. Besides, the lipids with higher T_m, DMPC, and DSPC, especially the latter, it would have been hard to handle and extremely time-consuming with the use of a manual extruder.

During the preparation of the formulations, employing the four lipids at the previously specified molar ratios, some of the formulations were not successfully obtained. It happened for SPC and DSPC at the higher **Pt-L10** amount (10/1 molar ratio) which showed poor stability along extrusion process, and so they were not always considered during the characterisation. Most probably the rigidity of SPC and DSPC hindered the location of high **Pt-L10** concentrations.

5.2.3 Characterisation of metallosomes

5.2.3.1 Platinum encapsulation

The encapsulation efficiency for **Pt-L10** was a crucial point to be evaluated: the protocol for **MTL** preparation and the distinct type of lipids could lead to modified entrapment efficiencies.

Platinum was measured by ICP at two different points along the production process. The initial measurements were conducted before and after the extrusion process because it was essential to study if the process was affecting the **Pt-L10** encapsulation. For that reason, four liposome formulations were prepared. Per each formulation, solutions before and after the extrusion process were mixed with a 10% of Triton X-100 solution at 1:1 v/v to break the liposomes and the platinum percentage was analysed by ICP-MS. The results gathered in **Table 5.3** show the platinum percentage determined after extrusion.

Table 5.3 Percentage of total platinum after extrusion to evaluate how the process affected **Pt-L10** incorporation in **MTL**. The results were obtained after one experiment.

Formulation	Pt after extrusion (%)
DOPC:Pt 1/1	97
DOPC:Pt 10/1	70
DSPC:Pt 10/1	80
SPC:Pt 10/1	86

In general trend, a small amount of platinum seems to be lost during the extrusion process. However, the loss was not considered to compromise samples preparation.

The encapsulation efficiency was also determined after the **MTL** preparation, calculated using **Equation 5.1**. In this case, the supernatant was collected after ultracentrifugation of the final **MTL** solution. The resultant supernatant and the initial **Pt-L10** MeOH solution were measured by ICP-OES. With it, the encapsulation efficiency for the four structural lipids used in the formulation at 100/1 molar ratio were calculated. The results are shown in **Table 5.4**.

Table 5.4 Platinum encapsulation efficiency of **MTL**. The results were obtained after one experiment measured by duplicate, except for DMPC formulation.

Formulation	Pt after encapsulation (%)
DOPC:Pt 100/1	85 ± 8
SPC:Pt 100/1	93 ± 2
DSPC:Pt 100/1	80 ± 0.7
DMPC:Pt 100/1	73

The final encapsulation efficiency showed great internalisation values, in the range of other platinum-loaded liposomes.[404–408] The values for encapsulation t efficiency compared with the initial **Pt-L10** solution and before extrusion showed a similar tendency. Liposomes losses could take place through the polycarbonate membrane, and in fact, reduced encapsulation after extrusion is reported in several works.[403] Nonetheless, the extrusion technique provides excellent homogeneity on the samples and the final platinum internalisation was extensive.

Overall, even drug internalisation deeply depends on a lot of factors, such as the lipid to drug ratio or the lipid nature, the encapsulation efficiency in the four tested formulations state our **MTL** as a promising DDS.

5.2.3.2 Metallosomes size, homogeneity, and morphology

Particle size and PDI are crucial physicochemical factors due to the impact in the cellular uptake and internalisation, mainly occurring by endocytosis, an ATP consuming process that will take particles with a maximum size of 0.5 µm. Besides, particles sizes also influence the effectiveness of their clearance by the RES, which is increased for large particles. Likewise, carriers smaller than 150 nm are effectively extravasate from circulation by the tumour vascularity via EPR effect.[135]

The **MTL** sizes and PDIs were measured by DLS after the extrusion through a membrane of 200 nm pore size ten times. The results, gathered in **Figure 5.7**, show **MTL** with sizes ranging 70 to 160 nm (in intensity) with low PDI values.

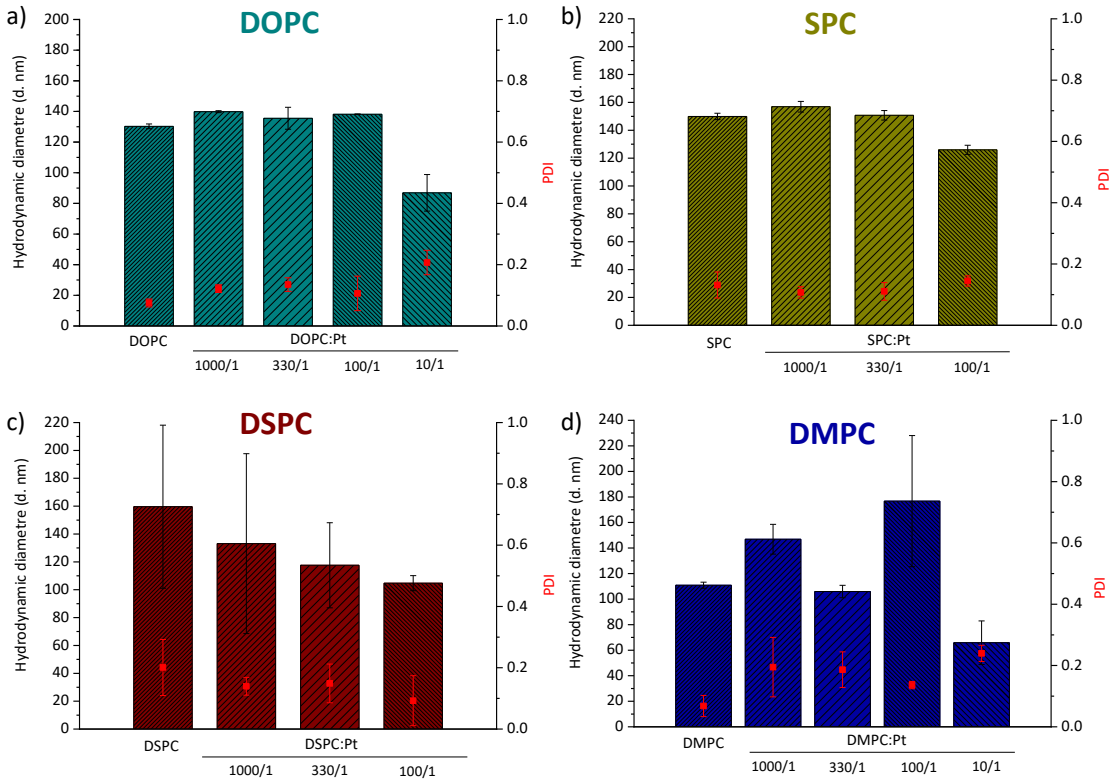

Figure 5.7 Size (expressed in intensity, column bars) and PDI (red squares), with the corresponding standard deviation, of the prepared **MTL** using DOPC (a), SPC (b), DSCP (c) and DMPC (d) as a structural phospholipids, at several lipid to **Pt-L10** molar ratio compared with the corresponding plain liposomes. Data are mean of three to five independent experiments.

An interesting tendency is observed, in which higher amounts of **Pt-L10** result in smaller **MTL**. This fact is particularly pronounced for DSPC formulations and should be related to the high rigidity of the bilayers formed by the mentioned phospholipid, or due to the introduction of charges to the membrane.

PDI represents the distribution size of the population in a sample. PDI's in liposomal formulation values are considered appropriate below 0.4,[134,135] hence indicating a homogenous population in our **MTL** formulations. Furthermore, PDI seems not to be affected by the increasing amounts of **Pt-L10**. Though, it must be considered that the use of a smaller pore membrane in the extrusion, or a greater number of extrusions will result in tinier liposomes with lower PDI.

The morphology of the samples was screened by *cryo*-TEM. Micrographs were taken for **MTL** suspensions at 100/1 molar to lipid ratio and shown in **Figure 5.8**.

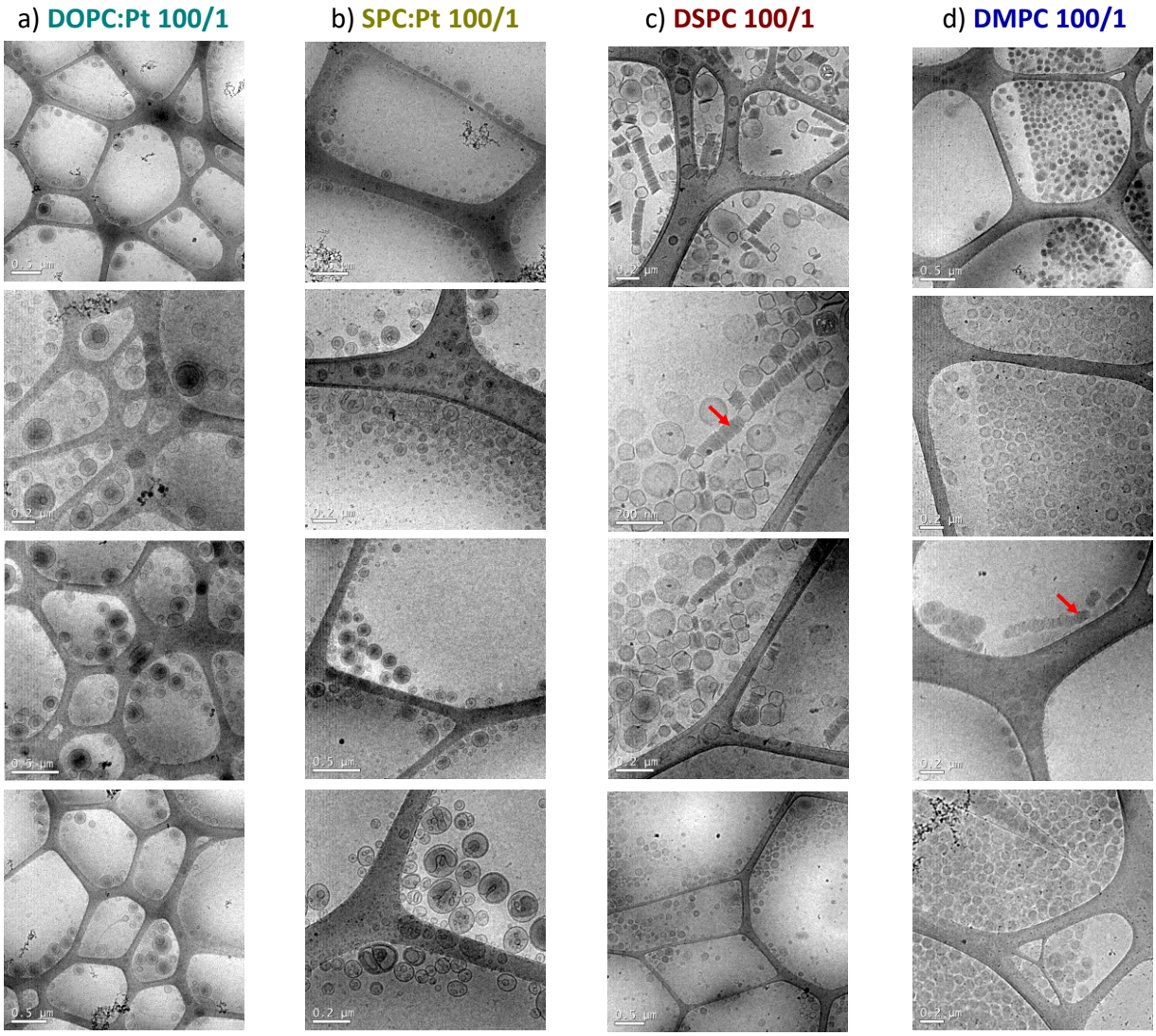

Figure 5.8 *Cryo*-TEM micrographs for DOPC:Pt (a), SPC:Pt (b), DSPC:Pt (c), and DMPC:Pt (d) at 100/1 molar ratio in PBS. Samples were extruded ten times through a 200 nm pore size membrane. Lipid concentration is 5 mM. Red arrows indicate **MTL** stacking.

Several features referring to the lamellarity and morphology of the obtained **MTL** must be highlighted. SPC and DOPC showed the presence SUV and LUV, however, there is also a noticeable amount of OLV and a few MVV, particularly found in SPC **MTL**. On the other hand, DMPC and DSPC formulations show the presence SUVs and LUVs with the absence of MLVs and OLV. Further, DSPC revealed the presence of square shaped **MTL**. Saturated lipids tend to generate liposomes with irregular shapes; usually explained by the high rigidity shown by saturated phospholipids, as is the case of DSPC.[409–412] However, the shape could be modulated after the incorporation of a molecules or additive, as reported in literature.[413,414]

In the micrographs, red arrows in DSPC and DMPC formulations indicate the presence of stacking of **MTLs**. Interestingly, this is observed in the two saturated phospholipids, though no

much understanding about this behaviour is described in literature, where aggregates structures were observed in DMPC liposomes incubated with an anionic boron cluster reported to be used to trigger the release of liposome content.[415,416]

5.2.3.3 Fluorescence anisotropy

Lipidic bilayers are dynamic structures, in which their elements can rotate or move laterally in the membrane plane, and the magnitude of these movements are identified as membrane fluidity. To further study the disturbances generated by **Pt-L10** in the lipidic bilayer, the fluidity of the membrane was attained by fluorescence anisotropy measurements. For this purpose, a membrane interacting fluorescence probe provides insights into the rigidity/flexibility of the bilayer, as well as the viscosity in the bilayer interior. When additional components are added to a given formulation, as **Pt-L10**, the differences in fluorescence anisotropy values compared to plain liposomes indicate the disturbances in the membrane. In our case, the apolar probe employed was 1,6-diphenylhexatriene (DPH), which is one of most used membrane interacting probe.

Fluorescence anisotropy (*r*) indirectly indicates variations in the order of the lipidic alkyl chains: when the order in hydrocarbon chains is decreased because of the rotation of the C-C bonds and then the membrane fluidity increases, which is translated to a *r* decrease.[139,140] To study how the addition of **Pt-L10** modify the rigidity of the lipidic membranes, anisotropy was measured after 30 min of incubation at 37 °C with DPH (DPH:lipid molar ratio 1/330). The results for the prepared formulations at several concentrations are shown in the next **Figure 5.9**.

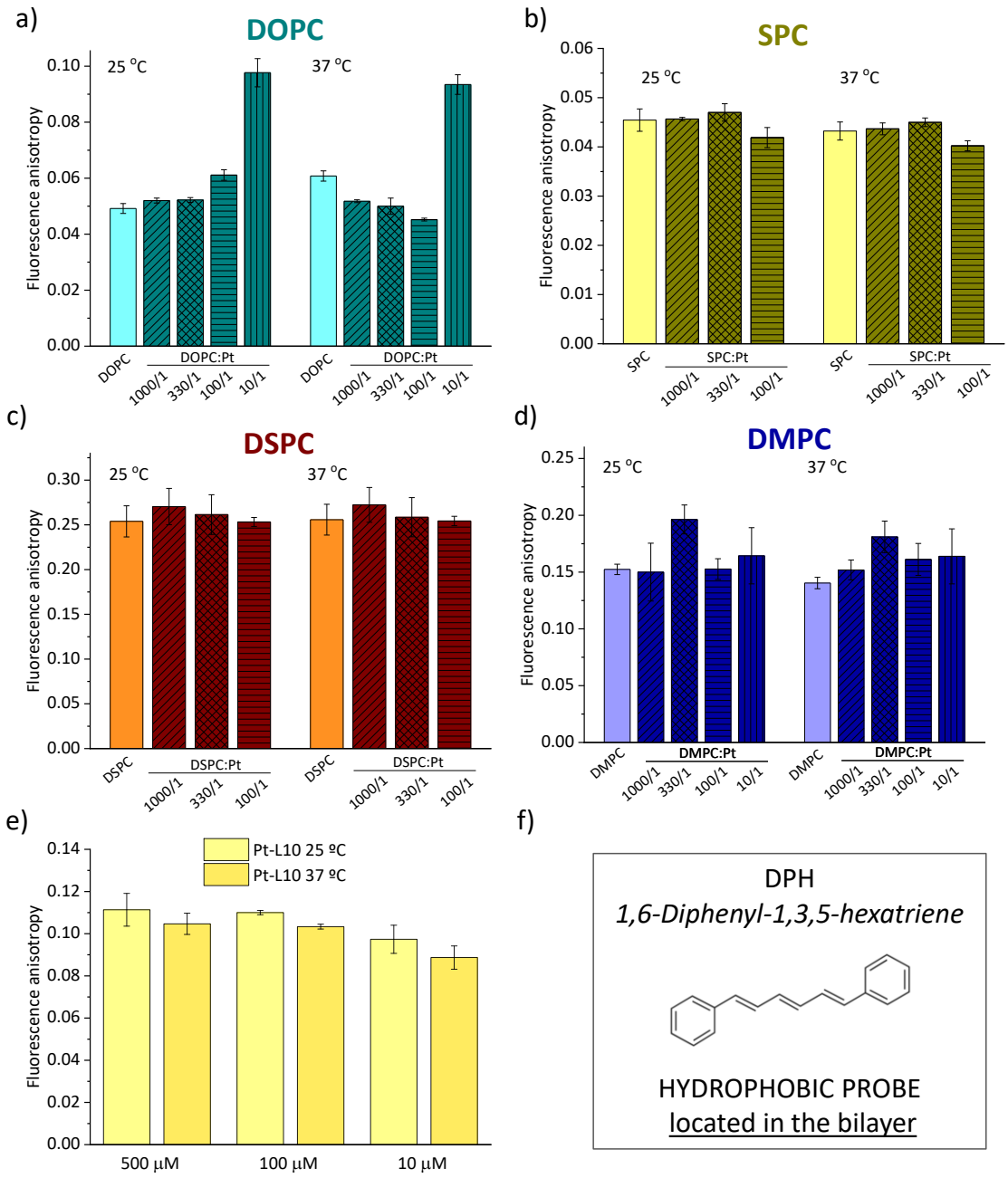

Figure 5.9 Fluorescence anisotropy of the **MTL** formulations (a) DOPC, (b) SPC, (c) DSPC, (d) DMPC, and (e) **Pt-L10** at several concentrations as control; (f) shows DPH molecule. The values are the mean of 3 to 5 independent experiments, with each sample conducted in triplicate (N = 3-5 and n = 9-15) and the associated standard deviations.

Fluorescence anisotropy was measured at two temperatures, 25 and 37 °C. The plain liposomes show higher *r* for the lipids generating a more rigid bilayer, in the sequence DSPC > DMPC > DOPC > SPC, corresponding to the higher *r* values with the saturated lipids. The *r* values should be compared with the same structural lipid upon the addition of **Pt-L10** to study the modification caused in the bilayer. Focusing on the **MTL** formulations, the *r* values show that

the prepared **MTL** are mostly unaffected by the addition of **Pt-L10**. The **MTL** formulations using DSPC and SPC suffer a slight increase at 1000/1 lipid:Pt molar ratio that diminishes for the more **Pt-L10** concentrated formulations. On the contrary, DMPC and DOPC formulations present higher *r* values with greater platinum amounts, so higher rigidity on the bilayer. Though, in this case, it is worth noting that the *r* increase at 10/1 lipid:Pt molar ratio in DMPC is negligible but is significative for DOPC formulations. We relate this behaviour in DOPC to membrane disturbances when fitting large concentrations of **Pt-L10**.

Interestingly, the two saturated lipids, DSPC and DMPC, show contrary tendencies: it could be explained after the different carbon chain length, which being shorter for DMPC might induce an increase in the rigidity due to the minor mismatch between the alkyl chain length of the lipid and the **Pt-L10**.

As a control, the fluorescence anisotropy was also measured for **Pt-L10** at several concentrations, 500, 100, and 10 µM. For **Pt-L10** the *r* values diminished with complex concentration. Assuming that the probe will locate in the membrane of the **Pt-L10** supramolecular organisations, which shows how increasing amount of **Pt-L10** cause the probe to have more degrees of freedom. Nonetheless, further studies on this topic would be worthwhile.

Variations on the organisation in the alkyl chains of the lipids impact the viscosity of the membrane. The apparent microviscosity ($\bar{\eta}$), abbreviated as microviscosity, was calculated using **Equation 5.2**, and the results are gathered in **Table 5.5**.[139,417,418]

$$\bar{\eta} = \frac{240\ mPa\ s \cdot r}{0.362 - r} \qquad \textbf{Equation 5.2}$$

Table 5.5 Calculated apparent microviscosity values at 25 °C. Formulations are expressed as lipid to **Pt-L10** molar ratio.

	$\bar{\eta}$ (cP)		$\bar{\eta}$ (cP)		$\bar{\eta}$ (cP)		$\bar{\eta}$ (cP)
DOPC	37.7 ± 1.36	**DSPC**	563.6 ± 38.6	**SPC**	34.4 ± 1.72	**DMPC**	174.5 ± 5.23
1000/1	40.2 ± 0.68	**1000/1**	708.9 ± 53.18	**1000/1**	34.6 ± 0.25	**1000/1**	169.8 ± 28..85
330/1	40.4 ± 0.65	**330/1**	624.0 ± 53.05	**330/1**	35.8 ± 1.34	**330/1**	284.4 ± 18.46
100/1	48.7 ± 1.52	**100/1**	558.7 ± 11.14	**100/1**	31.4 ± 1.53	**100/1**	175.0 ± 10.47
10/1	88.7 ± 4.57					**10/1**	199.5 ± 30.04

Typically, the microviscosity values for non-cholesterol containing phospholipid membranes ranges from, approximately, from 50 to 1000 cP at 0 – 40 °C; where unsaturated lipids fall in the lowest range of values. as our results show for plain liposomes.

As a summary, the fluorescence anisotropy values (*r*) and calculated apparent microviscosity ($\bar{\eta}$), suggest that the addition of **Pt-L10** leads to a slight modification on the membrane organisation, which is prominent for DOPC:**Pt-L10** 10/1 and noticeable in DSPC formulations. Finally, it is convenient to note how some authors have related the increase in bilayer disorder with an increase in cytotoxicity, which would correspond to the decrease of *r and* $\bar{\eta}$ values.[418]

5.2.3.4 Dynamic Scanning Calorimetry

Described during this chapter, the internalisation of **Pt-L10** in liposomes might alter the structure of the membrane, modifying features such as permeability and fluidity, which have been already analysed through fluorescence anisotropy. But until the current section, how the T_m of the lipids is altered remains undisclosed. Dynamic Scanning Calorimetry (DSC) is a convenient technique for this purpose since significant knowledge from the bilayer organisation and regarding the behaviour of the gel-to-liquid-crystal transition of the lipids is attainable from the shape and sharpness of the peak. The obtained thermograms will show the T_m as the maximum of the heat capacity at constant pressure, and the enthalpy variations associated with the area under the peak. The enthalpy variations will be associated with the thermal energy added when the lipid phase transition takes place because of the decrease of the hydrophobic Van der Waals interactions between alkyl chains.[138,419]

DSC analyses were conducted for the four lipid formulations at several molar ratios to examine the phase transition upon the addition of **Pt-L10** and compared to the corresponding plain liposomes. Non-freeze-thawed nor extruded liposomes were prepared. Lipid concentration was 50 mM for the following lipid:**Pt-L10** molar ratios 33/1, 10/1 and 1/1, and 20 mM lipid for 1/1 molar ratio. Vesicles formulated with only the structural lipid were also recorded at the same lipid concentrations.

The acquired thermograms are shown in **Figure A55** to **A59**, and the summary of the obtained results is shown below in **Table 5.6**.

Table 5.6 Thermodynamic parameters of the main phase transition undergone by the formulated **MTL**. Data obtained for DSC measurements (ramp of 2 °C/min). Enthalpies have been normalised to the lipid concentration for each formulation, considering PBS density.

Formulation	[Lipid] (mM)	Lipid:Pt-L10 molar ratio	Enthalpy (KJ/mol)	Onset T. (°C)	Peak T. (°C)
DSPC	50	-	35.2	53.66	53.94
DSPC:Pt	50	330/1	37.5	53.68	53.99
DSPC:Pt	50	100/1	45.8	52.60	54.11
DSPC	20	-	31.8	53.73	53.95
DSPC:Pt	20	10/1	37.8	51.18	52.30
DOPC	50	-	94.5	-23.30	-22.42
DOPC:Pt	50	330/1	94.8	-23.31	-22.43
DOPC:Pt	50	100/1	15.53	-23.77	-22.67
DOPC	20	-	266.4	-23.31	-22.40
DOPC:Pt	20	10/1	n.d.	-23.56	-22.18
DMPC	50	-	24.9	22.65	22.89
DMPC:Pt	50	330/1	23.5	22.46	22.77
DMPC:Pt	50	100/1	23.5	21.87	22.73
DMPC	20	-	26.8	22.62	22.86
DMPC:Pt	20	10/1	17.9	12.11	13.52
SPC	50	-	35.5	-22.5	-22.13
SPC:Pt	50	330/1	11.9	-22.43	-22.01
SPC	20	-	104.2	-23.38	-22.35
SPC:Pt	20	10/1	n.d.	n.d.	n.d.

As shown in the table and corresponding thermograms, DSPC formulations (**Figure A55**) show a single endotherm peak, which is affected by the presence of **Pt-L10**. The peak modification shows how the addition of **Pt-L10** in the formulation produces a slight decrease of the T_m, which is noticeable from 100/1 molar ratio. The peak decreases in height and becomes broader, thus indicating that the insertion of the **Pt-L10** on DSPC lipid bilayer affects lipid organisation. Interestingly, the pretransition observed on DSPC formulation at low complex concentrations vanishes and the main transitions is shifted to lower temperatures (~ 52 °C).

In the thermograms of DMPC formulations (**Figure A56**) a marked effect is observed, still following the same trend noted for DSPC formulations. The phase transition peak broadens and shortens with the addition of **Pt-L10**, while the pretransition peak initially fades. Lastly, at

the highest **Pt-L10** concentrations (10/1 lipid to complex molar ratio), the main transition peak is shifted to lower temperatures.

As regards DOPC formulations, an abrupt behaviour at the highest **Pt-L10** molar ratio is observed (**Figure A57**). DOPC:**Pt-10** molar ratios 330/1 and 100/1 ensued the trend observed for DSPC and DMPC formulations that is a decrease in height of the T_m peak for the lowest molar ratio, followed by a slight shift of the T_m and broadening of the peak for the 100/1 molar ratio. But, when the molar ratio increased to 10/1, the observed tendency was altered, and an exothermic peak arose. Thus, we decided to assess the DSC thermogram for **Pt-L10** and a 20 mM sample of **Pt-L10** in PBS was scanned from -80 to 70 °C (**Figure A58**). Interestingly, **Pt-L10** showed an exothermic peak at -22.16 °C. The appearance of an exothermic peak, where energy is released, suggests the increase of order because exothermic peaks are usually related to crystallisation processes.[138]

The presence of the exothermic peak for DOPC formulation at 10/1 molar ratio might be explained after the obtention of an exothermic peak for **Pt-L10** since both peaks, DOPC main transition and **Pt-L10** peak, fall in the same range. The shift and even the surpass of the main phase transition by the drug peak upon the incorporation of them is reported in several studies.[420–423] Nonetheless, the behaviour of **Pt-L10** is still poorly understood since comparable thermograms for metal complexes were not found in literature.

Finally, SPC formulations were analysed (**Figure A59**). SPC:**Pt-L10** molar ratio 100/1 shows a decrease in height of the T_m peak. When the molar ratio increases to 10/1 the peak related to the T_m vanishes. It seems that the endothermic peak of SPC bilayer is overshadowed by an exothermic peak at the same temperature through the addition of **Pt-L10**. Similar performance is reported for SPC liposomes upon the addition of drugs and it is explained by drug aggregation on the vesicle surface.[420]

Besides, the fact that DOPC:**Pt-L10** and SPC:**Pt-L10** had shown such a distinct behaviour at 10/1 molar ratio, becoming exothermic for DOPC and vanishing for SPC, suggest that the location of **Pt-L10** in each lipidic membrane may be different. It could even indicate the presence of phase separation. Nonetheless, it is a hypothesis that should be further investigated.

Altogether, focusing on the lowest **Pt-L10** ratios, we observe that 100/1 and 330/1 lipid to **Pt-L10** molar ratios for the four lipids, show a shortening and widening of the corresponding T_m

peak, along with a slight enthalpy decrease. In addition, DSPC and DMPC loss their pretransition. These observations should indicate non-homogenous mixing of the structural phospholipid and **Pt-L10**. In fact, studies have demonstrated that the addition of drugs with long chains shows the gel-to-liquid-crystalline phase transition shifted to lower temperatures and broadened the peak as the drug content increased.[424] It is evident that the incorporation of **Pt-L10** affects the thermotropic behaviour of the mixed formulations, however, the effect is minimal until formulations reach 100/1 molar ratio.

5.2.3.5 Measuring the zeta potential of metallosomes

Zeta potential (ZP) provides information concerning the nature and magnitude of surface charge, which is another valuable marker to evaluate the physical stability of the nano-formulation. High ZP is related to highly charged particles that prevent aggregation because of the electric repulsion between them: values below -30 mV or above 30 mV are considered to offer stable nanodispersions.[134] In general, nanostructures with positive ZP values have a long circulating half-life because of the absorption of protein components in the blood. In contrast, nanostructures with negative ZP values can be more easily cleared by the RES.

The ZP values for the prepared formulations are compilated in **Figure 5.10**. To compare the results, ZP for **Pt-L10** at 1 mM was recorded, obtaining a negative values of - 45.73 ± 2.06 mV.

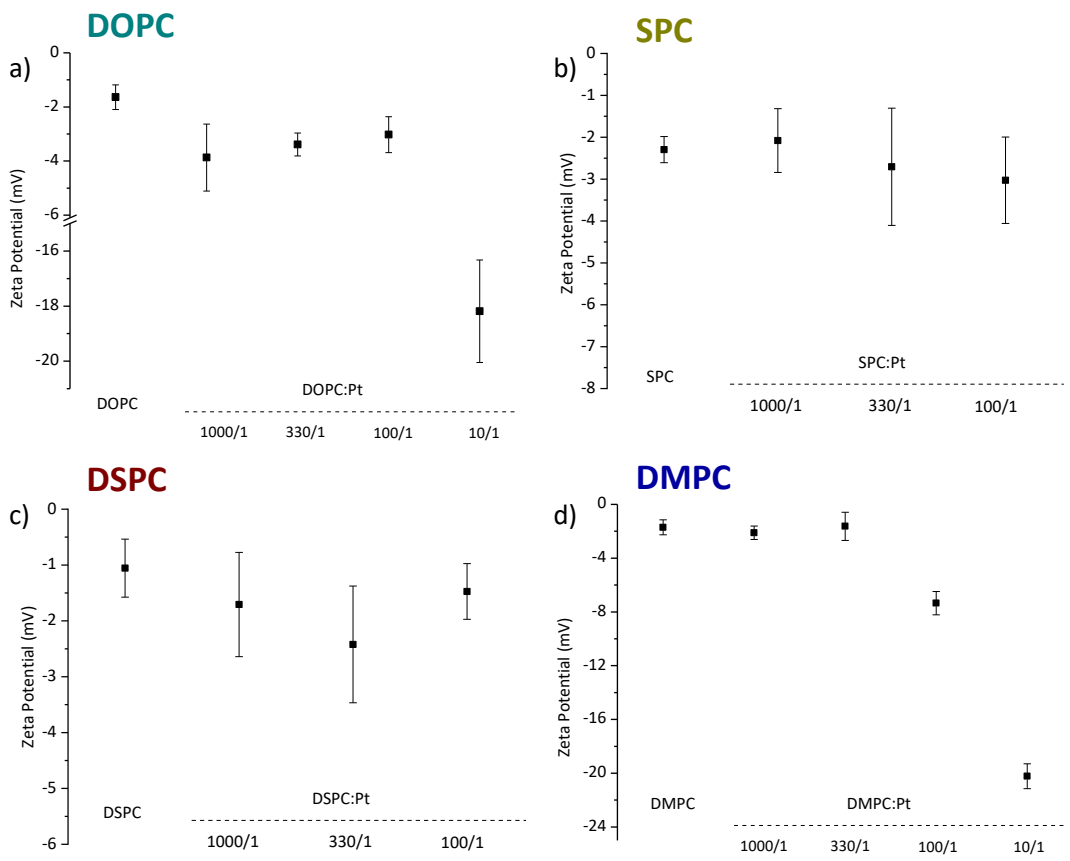

Figure 5.10 ZP values for DOPC, SPC, DSPC, and DMPC **MTL** formulations. The values are the mean of 3 to 5 independent experiments with the associated standard deviations.

Moderate negative ZP values for the plain liposomes are in the typical range for phosphatidylcholines.[147,425]

The **MTL** formulation showed that, in general, upon the addition of **Pt-L10**, the resulted ZP values have greater negative values. DOPC formulations present a small decrease of the ZP until the highest **Pt-L10** molar ratio when decreases to -18 mV. DMPC formulations show negligible ZP decrease for the formulations with the lowest **Pt-L10** amount, but from 100/1 molar ratio ZP values diminish, reaching the value of – 19 mV at 10/1 molar ratio. SPC formulations show a humble but constant decrease when compared to their plain liposomes. With regards to DSPC, initially a ZP reduction is observed but at the highest **Pt-L10** concentration added the values are similar to plain DSPC liposomes.

Increased negative ZP values indicate further negative filed in the slipping plane of the liposomes. Hence, this fact can be considered as evidence for the **Pt-L10** location, which provides a more negatively charged surface due to the sulfonate groups embedded in the

aqueous medium that surrounds the vesicles. Because of that, conceivably **Pt-L10** will located within the lipidic bilayer. This would also explain the elevated encapsulation efficiency: it is generally higher if the drug is internalised in the membrane because then, the entrapped amount of drug is independent of the liposomes' sizes.

ZP values between -30 and 30 mV may indicate that the suspended particles are prompt to aggregate or increase their size.[134] In the case of the MTLs prepared either using DOPC, DSPC, or SPC, the obtained ZP values are slightly negative but out of the acceptable ZP range in terms of stability. On one hand, regarding the ZP value measured in **Pt-L10**, the stability of the liposomes might be reduced. Nonetheless, ZP results should not be taken as an absolute measurement of liposomes stability.

5.2.3.6 Refinement of the stability of metallosomes

The stability of liposomes should be considered from two perspectives: chemical and physical degradation. The chemical degradation involves oxidation and hydrolysis processes occurring on the lipids, but they have not been assessed in this thesis.

Physical degradation is usually related to structural changes, such as aggregation or the fusion of membrane bilayers, which can be examined by DLS. Previously in this chapter, the SPC:**Pt-L10 MTL** showed their stability when followed by DLS for 6 weeks (stored at 4 °C). However, the measured ZP values for the rest of the developed formulations may indicate poor colloidal stability. Hence, to reassess the prepared formulations, they were monitored by DLS over seven or eight weeks, stored again at 4 °C. The results for the 100/1 lipid:**Pt-L10** molar ratio formulations are shown in **Figure 5.11**, while the full range of formulations can be found in the Annex section (**Figure A60** to **A63**).

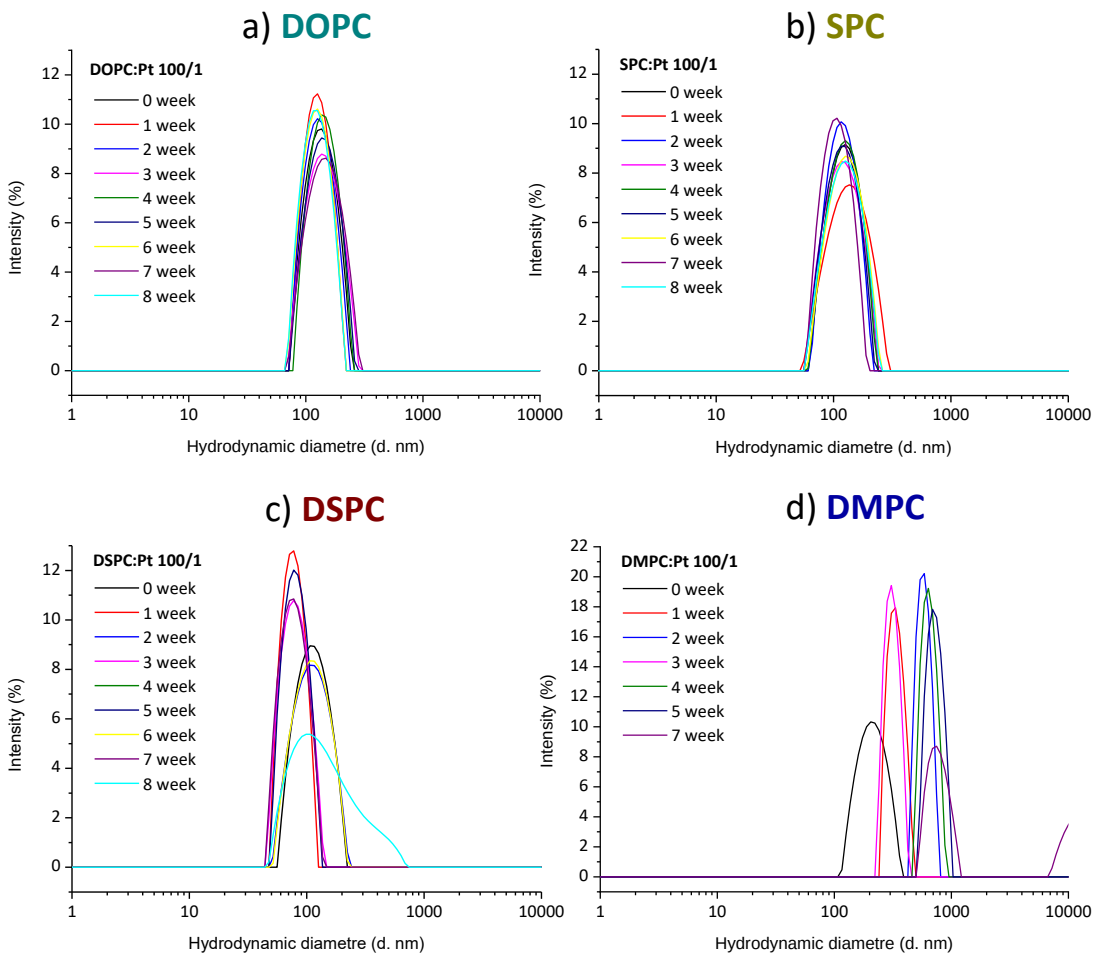

Figure 5.11 DLS graphs showing the hydrodynamic diameter of the MTL for 100/1 lipid:**Pt-L10** molar ratio to disclose the formulations' stability using DOPC (a), SPC (b), DSPC (c), and DMPC (d) as structural lipid.

Analysing the DLS graphs, it is possible to ponder the outcomes of the formulations over time: the maintenance of the vesicles' stability and the occurrence of agglomeration.

The formulations prepared with unsaturated lipids display higher stability: SPC and DOPC. They show practically no size difference when followed by DLS along time. Even though the **MTL** ZP values were lower than the considered for optimum colloidal stability (+/-30 mV), they demonstrated remarkable stability over time. The **MTL** size was maintained at least during 56 days for DOPC and SPC formulations. On the contrary, the saturated lipids, DSPC and DMPC, show moderate stability of three to four weeks.

Nonetheless, despite it is out of the scope of this thesis, it is important to note that there exist several strategies to improve liposomes the stability and storage of liposomes. For instance, the addition of pegylated chains, which could also benefit the long-term circulation of the liposomes.[426]

5.2.3.7 Platinum release study

The ideal liposome formulation consolidates the equilibrium between several factors such as the entrapped drug concentration, stability, and the optimal drug release at the targeted organ or tissue, etc. Among them, the *in vitro* drug release profile is a critical consideration since it could apprise the behaviour of the encapsulated drug before *in vivo* studies. Nonetheless, it must be noted that several authors are aware that the obtained release *in vitro* may be hindered by membrane transports effects in the drug passage *in vivo*.[427–429]

The *in vitro* release profile of the prepared **MTL** was assessed in a preliminary study upon dilution in PBS at physiological temperature. The chosen methodology involves sac dialysis, widely used in literature for the measurement of release kinetics. The sac dialysis allows sampling over time from the acceptor chamber, which due to the semi-permeable membrane allows the separation of the released drug. On this basis, the released molecules cross the membrane while the still encapsulate drug is unable to penetrate the membrane. To evaluate the amount of platinum released upon the chamber we relied on ICP measurements. The four formulations assessed (DOPC:**Pt-L10**, DMPC:**Pt-L10**, DSPC:**Pt-L10** and SPC:**Pt-L10** at 100/1 molar ratio), which corresponded to 0.05 mM **Pt-L10** concentration, were placed in a dialysis bag with a 25 kDa cut-off and immersed in the corresponding preheated PBS bath (37 °C, pH 7.4), which was sealed to avoid medium losses. Samples were withdrawn from the dialysate at convenient time intervals and measured by ICP-MS.

Below, in **Figure 5.12,** the obtained *in vitro* profile revealed moderate on-average drug release for the four tested lipid formulations.[406,430,431]

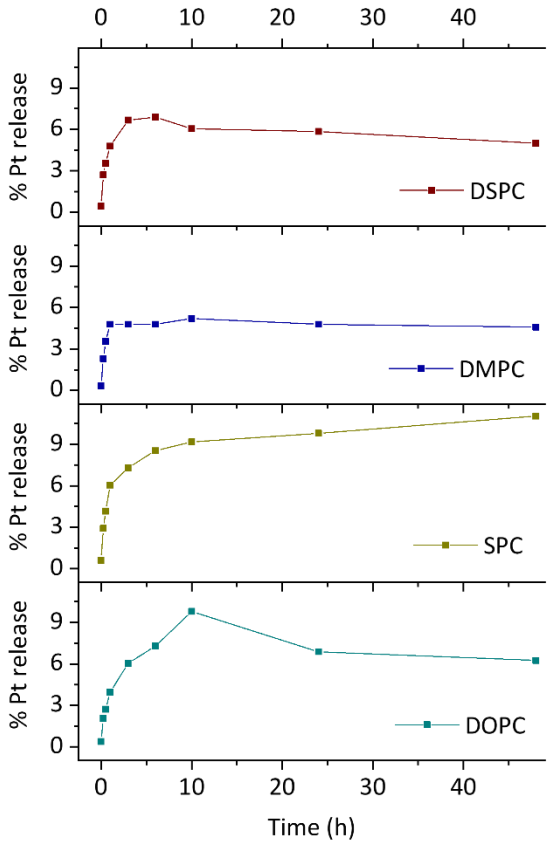

Figure 5.12 Release profile of **MTL**, formulated with DSCP, DMPC, SPC or DOPC, and **Pt-L10**, at 100/1 lipid to Pt molar ratio. The release experiments were conducted in PBS at 37 °C in a sealed container, sampling from the dialysate at the convenient time over 48 h.

In increasing order, the percentage of platinum release at 25 h was 4.8% for DMPC, 5.9% for DSPC, 6.8% for DOPC, and 9.8% for SPC. At 48 h the values were 4.5%, 5.0%, 6.2% and 11.0%, respectively. Except for SPC, it is observed that a maximum release is achieved.

As attained during this chapter, lipid characteristics such as the alkyl chain length and the unsaturation modify the membrane properties, which should explain the obtained platinum release results The unsaturation degree of the alkyl chains and the unsaturation position are responsible for local perturbation in the lipidic membrane packaging, usually accountable for Van der Waals interactions between alkyl chains, and so, decreasing also the permeability of the bilayer.[113,398,400]

As can be observed in **Figure 5.12**, the unsaturated lipids, DOPC and SPC, showed a higher release. On the contrary, the fully saturated lipids, DMPC and DSPC, presented the smaller drug percentage release. Among them, DMPC, owing to the shorter alkyl chain revealed the lowest release, most probably associated with a better accommodation of **Pt-L10** into the bilayer.

Therefore, the characteristic of the lipids is in accordance with the abovementioned release order found for each liposome formulation.

Besides, due to the fact that the T_m of DOPC and SPC are below 37 °C, they will be in the liquid-crystalline phase. Consequently, in this phase, the membrane packing is lessened generating leakier systems with increased bioavailability, which along with the alkyl chain unsaturations explains the higher platinum release.[121,125,432] Whereas, DSPC, with a lower release, has a much high T_m, meaning that at physiological temperature, it is in the gel phase. More interestingly, DMPC, with a T_m of 23 °C, could undergo the transition from gel to liquid-crystalline phase once the release experiment begins, affecting the drug release.

Furthermore, is it meaningful to mention that a future perspective of this project would be the modification of our liposomes to acquire a controlled or triggered platinum release. Actually, current liposomal cisplatin analogues had shown improved pharmacokinetics in comparison with cisplatin. However, the therapeutic efficiency has also been limited since the delivery to tumours is enhanced but they show too slow or ineffective release kinetics.[159] Thus, several studies are focused on triggering of the encapsulated drug by applying a physical input, such as light or ultrasounds, to control the drug release.[77,99,433,434]

5.2.4 Study of metallosomes by small angle X-ray scattering

SAXS-WAXS experiments in ALBA synchrotron were also applied to obtain information about the nature of the produced **MTL**.

In the study of liposomes by SAXS-WAXS, evidence of the bilayers thickness can be obtained. Moreover, insights into the lamellarity of the liposomes can be extracted. Usually a broad symmetric peak can be related to unilamellar liposomes, while the spectra for multilamellar liposomes show two order of diffraction peaks at regular distances.[435,436]

For these experiments, since the phospholipids concentrations must be adequate to be analysed by SAXS, two concentrations were tested: 5 mM and 20 mM. Nevertheless, in the case of the 20 mM samples, due to the concentration of phospholipid they could not be manually extruded. Hence, the reduction in size and lamellarity was conducted by sonication. In addition, 5 mM phospholipids concentrations were both, sonicated and extruded to compare both procedures. The chosen **Pt-L10**:phospholipid molar ratio was 100/1. As detailed in the experimental section, all the samples were thermostated at 25 °C, assuring DOPC, SSPC

and DMPC to be at the liquid-crystalline phase, and DSPC at the gel phase. It is important to mention that WAXS spectra showed no information in the measured conditions.

When comparing the spectra with and without **Pt-L10** at 20 mM of phospholipids (**Figure 5.13**), we can assume that in all the cases a reduction in the bilayer thickness occurs due to a shift in the maximum peak. The magnitude of thickness reduction is different for each type of lipid.

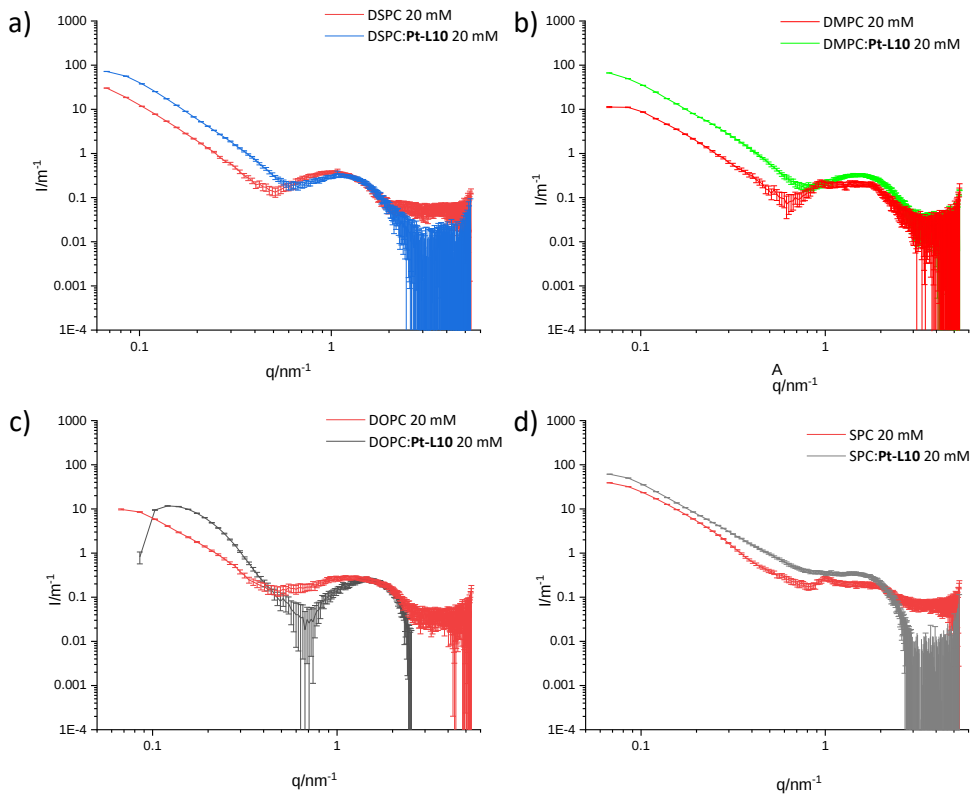

Figure 5.13 SAXS intensity as function of dispersion vector modulus q for 20 mM plain liposomes and **MTL** (phospholipid:**Pt-L10** molar ratio 100/1) prepared in PBS and after sonication for DSPC (a), DMPC (b), DOPC (c), and SPC (d).

Regarding the reduction on the bilayer thickness of the samples for the 20 mM phospholipids concentration the decrease is about a 5 % for SPC, a 15 % for DMPC, a 20 % for DSPC, and 30 % for DOPC.

When focusing on plain DMPC a small peak is observed for q = 0.936, which correspond to distances of 6.71 nm and might indicate multilamellarity. Similarly, on SPC a small peak indicating multilamellarity it is observed at q = 1.01, related to a repetition at 6.22 nm. The greatest modification is observed for DOPC, in terms of thickness reduction as well as behaviour at low q, which is consistent with the observations on DSC and fluorescence anisotropy experiments.

Considering the sonicated 5 mM phospholipid, the spectra for both, the plain liposomes and the ones containing metal are similar, which could be related to an absence of bilayer reduction since no shift of the maxima is observed (**Figure A64**). In the case of DMPC, the disappearance of the peak related to 6.54 nm distances (q = 0.96 nm^{-1}) in the **MTL** with respect to the plain DMPC has been associated to multilamellarity loss. On the SPC formulation, the sample containing platinum shows a smaller intensity and marked curvature with respect to the plain SPC sample. In DOPC formulations the highest differences between the platinum containing **MTL** and the plain liposomes are encountered: even the DOPC **MTL** shows a negative curve at small q, which is also present in the 20 mM sample.

The extruded liposomes and **MTL** at 5 mM phospholipid concentration are also considered (**Figure A65**). In the case of the extruded samples, the intensity of the q modulus is higher for the platinum containing vesicles. The greater differenced are found in DMPC and DOPC formulations. Extruded DMPC formulations present less multilamellar vesicles than the sonicated sample, which can be expected from the extrusion procedure with respect to sonication. Also, extruded DOPC samples show a high curvature as the sonicated one but, in this case, negative values are not observed.

In general, a decrease on the bilayer thickness was observed when adding the platinum metallosurfactant in the 20 mM liposomes. The 5 mM formulations show comparable results when extruded or sonicated. However, due to time limitations, only preliminary results after the data treatment have been include. To delve deeply into the role of **Pt-L10** in the **MTL** SAXS spectra must be fitted to models. As well, to gain additional understanding into the interaction between platinum **MTS** and the bilayer membranes the deduction of the electron density profiles as function of the distance to the centre of a bilayer will be conducted.

5.3 General remarks and future perspectives

The initial preparation of **MTL** proved the internalisation of **Pt-L10** into SPC liposomes, assuring the feasibility of its obtention using the thin film method. Moreover, the amphiphilic nature of **Pt-L10** allowed its addition in two distinct steps of the method, named in this thesis as method A, and B, when the complex was added in the hydration step or during the lipid film preparation, respectively. Both methods resulted in a similar platinum encapsulation efficiency, however, method B was preferred because of the advantages in the preparation of a mixed film between the lipid and the complex.

The encapsulation efficiency, with an average value of 22.0 ± 6.0%, was calculated by sedimenting the **MTL** and measuring the amount of platinum in the corresponding supernatant. Nonetheless, it was clear that precipitation of **MTL** was uncompleted and so the obtained entrapment efficiencies are the minimum value that would be internalised. Actually, the measurement of the supernatant by DLS indicated the presence of remaining **MTL**. Consequently, it was noticed that the initial of **Pt-L10** decreased the size of the obtained **MTL** and explained the incapacity of sediment them using a bench centrifuge. Finally, a preliminary study indicated the stability of the **MTL** over at least 6 weeks stored in refrigerated conditions, as well in front of dilution. Nonetheless, the separation of the complex and the **MTL** through Sephadex™ was not possible since the method relying on size was dependent on the **Pt-L10** concentration.

An optimisation of the **MTL** formulation is described in the second part of this chapter. Four structural lipids with distinct characteristics were tested and fully characterised. The obtained vesicles after extrusion showed sizes in the range from 65 to 160 nm with a PDI below 0.3 in all the cases. The encapsulation efficiency was significant and compatible with the presence of **Pt-L10** in the lipidic bilayer. Moreover, the ZP measurements were consistent with the presence of **Pt-L10** in the bilayer. Regarding the study of the bilayer by DSC and fluorescence anisotropy, we were able to point out several physicochemical features. Formulations prepared with DOPC show a higher modification of the bilayer backed up by DSC thermograms and fluorescence anisotropy. Whereas DSPC, DMPC, and SPC formulations showed noticeable decrease of T_m, which is usually related to non-homogenous mixing of the components and the loss of interaction between them. Furthermore, the stability exerted by all the formulations was analysed by DLS, resulting in extensive stability up to 28 days for DMPC and DSPC formulations and over 56 days for DOPC and SPC formulations. Next, the release study showed modest platinum release, with lower release values found in the saturated lipids, DSPC and DMPC followed by the unsaturated ones, DOPC and SPC.

The characterisation of the physicochemical properties of the **MTL** unveil that the disturbances caused by **Pt-L10** in the prepared mixed vesicles compared to plain liposomes are minimal up to 100/1 lipid:**Pt-L10** molar ratios. Then, from 10/1 lipid:**Pt-L10** several features, such as the characteristic T_m or the rigidity of the **MTL** bilayer are compromised. However, two formulations at 10/1 were not stable enough upon extrusion and could not be fully characterised. Therefore, in the next chapter, cell viability assays will be conducted for 100/1

lipid:**Pt-L10** molar ratio **MTL** since gathered the maximum **Pt-L10** addition and modest disturbances on the liposomes.

Preliminary analysis of the SAXS experiments conducted at Alba Synchrotron show thickness decrease bilayer at the highest measured phospholipid concentration. Nonetheless, they do not suggest great modifications to the bilayer, in accordance what had been observed employing other analytical techniques.

In conclusion, we highlight the successful preparation and characterisation of Pt(II) containing **MTL** to be explored as DDS with promising chemotherapeutic activity.

6. ASSESSING THE BIOCHEMICAL BEHAVIOUR OF LIGANDS, COMPLEXES AND METALLOSOMES

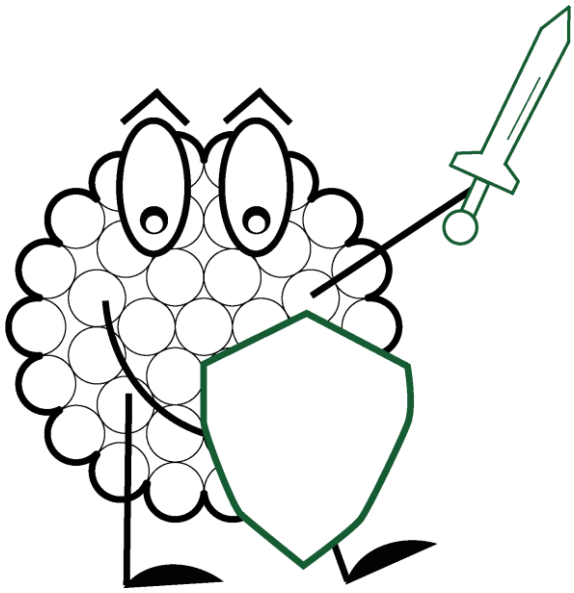

In this chapter features related to the biological and biochemical performance are approached. The interaction with proteins and DNA of the **Ls** and **Pt-Ls** are studied to understand the potentiality of the Pt(II) alkyl amino sulfonated complexes as chemotherapeutic drugs. The evaluation of the biological activity in several cell lines has been also assessed, testing **Ls** and **Pt-Ls**, and the formulated **MTL**. The evaluation of DNA and proteins interaction has been conducted at UAB. While the antiproliferative assays detailed on the last section of the chapter were conducted in two laboratories studying distinct cell lines; during a stay in Luciani Research Group, and also carried out in the IBB.

6.1 Protein binding studies

The primary mechanism by which platinum drugs bind to DNA as the main via to induce cellular apoptosis is depicted in the introduction of this thesis.[53] Bloodstream plays a crucial role in the biodistribution and uptake of most of the actual chemotherapeutic drugs and the binding to plasma proteins directly impacts the biological effects. For instance, the drug concentration is influenced when the binding to biomolecules is high, generating short lifetimes or poor biodistribution.[437] In addition, the interaction between a drug and the tumour microenvironment is a complex event. Cells have natural strategies to prevent toxicity, for instance, the inactivation of the active species, normally led by the interaction with proteins.[59–61,63,438,439] Inside the cells, aquated Pt(II) species are prompt to react with sulphur-rich proteins, such as metallothioneins and glutathione.[58,59,440–444] The strong reactivity of platinum compounds towards sulphur donor molecules generates stable bonds that end in the inactivation of the drug and is accounted to be related to drug resistance generation. Actually, cisplatin and analogue drugs are reported to be deactivated and cleared from tumours and induce severe side effects.[68]

Hence, insights into plasma proteins-drugs binding is a key investigation in the pharmacokinetics and pharmacological fate of the drugs.[439] Therefore, studying the potential interactions between proteins and the **Pt-Ls** complexes was necessary. In the current investigation, the chosen proteins intend to represent those that are predominant in the human body and could interact with platinum complexes. The selected proteins were human serum albumin (HSA), bovine transferrin (Tf), myoglobin (Mb), isoform 1 of Zn_7-metallothionein (Zn_7-MT1) and cytochrome C (Cyt C).

HSA and Tf are both the majority proteins in the bloodstream. Mb was tested as a haemoglobin model in red blood cells. Zn_7-MT1, a mammal isoform 1 of metallothionein associated with 7 ions of Zn^{2+}, which is highly present in the intracellular media. Finally, Cyt C is a small heme-protein found in association with the inner membrane of mitochondria and used as a model for globular proteins.

The interaction of the five proteins with **Pt-L2**, **Pt-L6** and **Pt-L10** was analysed by ESI-MS. Moreover, the interaction of HSA with the complexes and the corresponding ligands was also studied by fluorescence. The next sections are devoted to the results obtained using the above-mentioned techniques.

6.1.1 Interaction with proteins by electrospray ionisation mass spectroscopy

ESI-MS has been demonstrated as a particularly significant technique in the screening of protein-complexes interactions. In our group, numerous studies concerning this type of experiment have been reported, underlining the necessary working conditions to ionise and observe proteins.[440,443]

HSA, Tf, Mb, Cyt C and Zn_7-MT1 were incubated with **Pt-L2**, **Pt-L6** and **Pt-L10** at 37 °C for 24h. Two complex:protein molar ratios were chosen for the experiment: 1:1 and 1:2. Protein concentrations were 100 µm for HSA, Tf, Cyt C and Zn_7-MT1, and 75 µm in the case of Mb. A spectrum was also recorded for each free protein for comparison. Analysing the proteins spectra, we assured they yielded the mass peak under ESI-MS conditions, verifying the presence of several ionisation states in the m/z working range chosen and the absence of interfering species, as detailed in **Table 6.1**.

Table 6.1 Experimental molecular weight (MW) of the proteins used in this work determined by ESI-TOF MS: human serum albumin (HSA), transferrin (Tf), myoglobin (Mb), cytochrome C (Cyt C) and isoform 1 mammal metallothionein with 7 Zn(II) ions (Zn_7-MT1). The experimental error associated with the mass determination was always lower than 0.5%.

Proteins	HSA	Tf	Mb	Cyt C	Zn_7-MT1
Theoretical MW (Da)[443]	66478	77000-80000	17565	12361	6606
Average experimental MW (Da)	66564	78376	17575	12366	6609

The characterisation of the proteins showed that the experimental MW agreed with the theoretical. Mb showed a value 624 Da higher with respect to the corresponding apomyoglobin, implying the presence of the haem group (616.45 Da) in the protein.[443]

The results obtained for HSA, Tf, Mb, Cyt C and Zn_7-MT1 can be found in the annex section of this thesis in **Figure A66** to **A70**, respectively. From the study of the interaction of each complex with the selected proteins at the two tested ratios, no appreciable changes in none of the proteins considered were detected. These results were extremely surprising since the interaction between platinum complexes and proteins is fully reported[336] and a huge drawback in the use and development of chemo drugs. Several explanations may arise from this result. Whether the ratios we chose for conduct the experiment were not high enough to promote the presence of binding between the proteins and the complexes, because in some cases, ratios up to 1:10 protein to complex molar ratio are reported to be tested. Or, the structural peculiarity of our **Pt-Ls**, mainly related to the presence of a highly polar group and bulky alkyl chains (mainly for **Pt-L10**) hinder the interaction with the examined proteins. In literature, it is suggested that binding between metal complexes and biomolecules such as albumin is enhanced when coordinated ligands are planar, which would support our statement.[445]

Added to the special structure, the zwitterionic nature of **Ls**, and to some extent of the complexes, could be responsible for the low interaction. In fact, Chen *et al*. demonstrated that some zwitterionic materials resist non-specific protein adsorption. The non-fouling behaviour of some zwitterions is reported to be influenced by their electrostatic induced hydration, balanced charge, and minimised dipole.[446] In the case of our **Pt-Ls** we consider that the hydration should be the factor showing higher significance.

To summarise, we conclude that fortunately no covalent interactions are shown between **Pt-Ls** and the five tested proteins (HSA, Tf, Mb, Cyt C and Zn_7-MT1) after recording ESI-MS.

6.1.2 Assessment of human serum albumin binding by fluorescence

Albumin is a globular non-glycosylated protein with a high number of ionic amino acids, with a total charge of 185 ions per molecule. Hence it tends to bind complexes non-covalently but with ionic interactions. Drugs usually show an effect on their biological performance when bonded weakly to albumin, such as short lifetime or poor biodistribution. While strong binding to plasma proteins directly influences the drug concentration.[445]

Fluorescence spectroscopy allows the determination of the interactions likely to occur. The fluorescence emission of albumin upon excitation is produced by three amino acids residue: tryptophan, tyrosine, and phenylalanine. Nonetheless, tryptophan being in a higher relative ratio arises as the main responsible. The interaction with metal complexes generates perturbation on the secondary structure of the protein, or polarity variations alters its environment. This, results in spectrum modification due to several processes, like molecular rearrangements, energy transfer, excited-state reaction, or collision quenching.[445,447]

Recording the albumin fluorescence quenching, HSA in our case, with the addition of increasing concentration of **Ls** or **Pt-Ls** allows us to investigate the befalling interaction in more detail. Upon higher concentrations of quencher, the intensity is expected to regularly decrease, indicating coordination to the biomolecule. On the other hand, hypsochromic or bathochromic shifts are expected if the microenvironment of HSA is altered.[445] Fluorescence was measured to 1, 5 and 10 equivalents of **Ls** or **Pt-Ls** *vs* HSA (r_i = [quencher]/[HSA]). Additionally, HSA (0.5 µM) fluorescence quenching occurring after the addition of $CuCl_2{\cdot}H_2O$ (5 µM) was measured as a positive control (**Figure 6.1**).

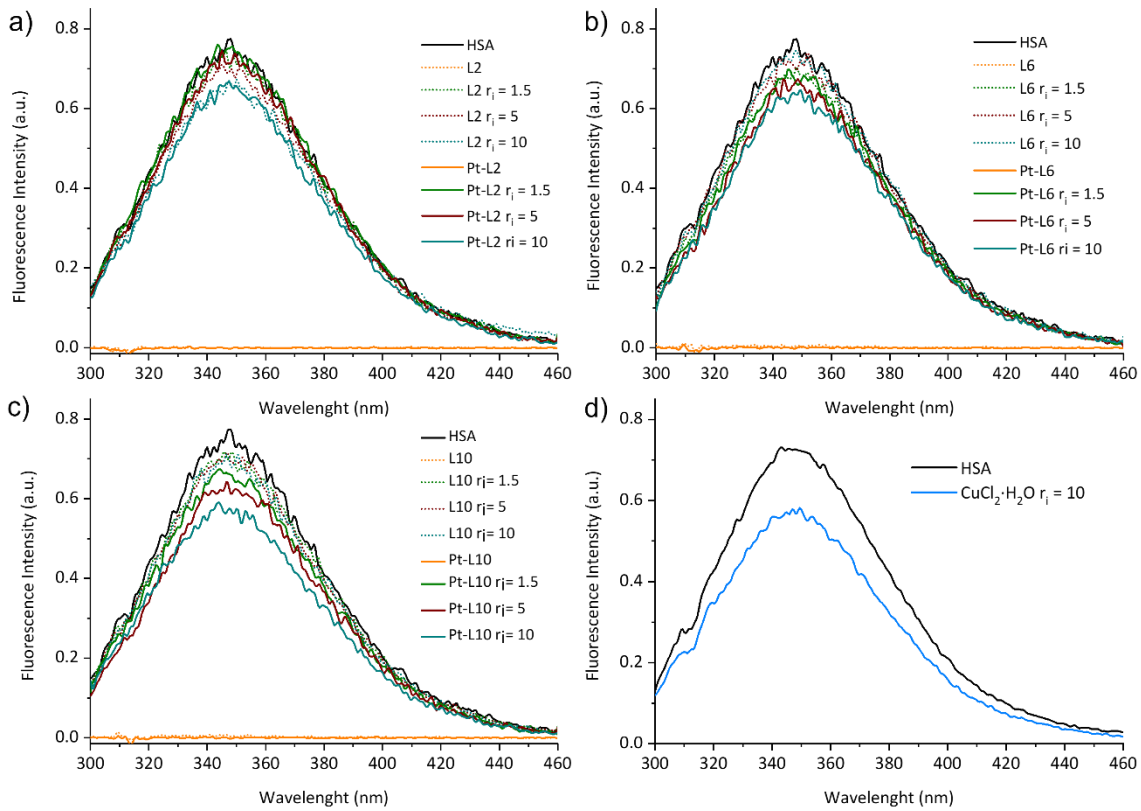

Figure 6.1 Fluorescence emission spectra of HSA upon increasing addition of **Ls** or **Pt-Ls**, at r_i from 1 to 10. Spectra (a) shows **L2** (dotted lines) and **Pt-L2** (full line); (b) shows **L6** (dotted lines) and **Pt-L6** (full line); (c)

shows **L10** (dotted lines) and **Pt-L10** (full line); and (c) shows $CuCl_2$ positive control. In spectra (a), (b) and (c), the flat line responds to a control of the corresponding ligand and complex, showing no fluorescence emission at the studied range. All the solutions were prepared in 10 mM PBS, pH 7.4.

Distinct behaviour arises in the study of HSA interactions with the **Ls** and **Pt-Ls** families. In the case of **L2** and **Pt-L2**, the observed quenching is perceptible but modest, just being significant at r_i = 10. And, more interestingly, the recorded spectra alterations are similar for the ligand and the corresponding complex in the three analysed r_i. On the other hand, **Pt-L6** and **Pt-L10** complexes showed higher quenching than their corresponding ligands, **L6** and **L10**. In **Pt-L6** the observed quenching at increasing concentrations of complex (r_i = 1 to 10) was slight. **Pt-L10** showed higher quenching observed for the complexes than their parental ligand, with a maximum quenching for r_i = 10. The differential quench seen between **Pt-L6** and **Pt-L10** is most probably explained by the distinct size and charge of both complexes regarding their corresponding ligands.

In summary, the quench observed for the ligand and complex family is moderate, and we associate it to the great ionic strength after the presence of the sulfonate moiety. Moreover, the presence of the metal, displays increased interactions in comparison to the corresponding ligands. Simple cases of fluorescence quenching are described by the Stern-Volmer equation (**Equation 6.1**), and applying it is possible to calculate the binding efficiency or binding constant of the given interaction.[445,448]

$$\frac{F}{F_0} = 1 + K_{sv}[Q] \qquad \textbf{Equation 6.1}$$

Where F is the fluorescence intensity in the absence of quencher [Q], and F_0 in the presence of it. And K_{sv} is the Stern-Volmer quenching constant. Based on the data, the graph F_0/F *vs* quencher concentration are represented (**Figure A71**), and the calculated K_{sv} found in **Table 6.2**.

Table 6.2 Quenching percentage at r_i = 10 and the corresponding calculated K_{sv}.

Sample	% quenching (r_i = 10) (@ 480 nm)	K_{sv} (M^{-1})
Pt-L2	14	$8.6 \cdot 10^3$
Pt-L6	19	$3.3 \cdot 10^3$
Pt-L10	21	$1.2 \cdot 10^4$
$CuCl_2 \cdot H_2O$	27	n.d.

Usually, the obtention of a straight line in the Stern-Volmer plot is related to one type of quenching occurring, either static or dynamic. While linearity deviation indicates a mixed mechanism. However, we did not go further in discovering the type of quenching arising since was out of the scope of this analysis.

The quenching percentage is slightly increased with higher with longer carbon chains in the **Pt-Ls** family. The K_{sv} values obtained for the three complexes were below 10^5 M^{-1}, which is the value taken as indicative of a relatively strong interaction between albumin and metal complexes.[445,449,450]

In summary, the environment of HSA seems to not be impacted by none of the three complexes since no bathochromic or hypsochromic shifts are detected. In addition, the quenching on the fluorescence spectra indicates that just low ionic interactions are rendered.

6.2 Pt(II) alkyl amino sulfonated interaction with DNA

In the mechanism of action of conventional metallodrugs, DNA is considered one of the main targets. Hence, understanding the interaction between metal complexes and nucleic acid is an indispensable step to predict the biological response of these types of drugs in chemotherapy. Diverse interactions between metal complexes and DNA can take place, features, such as geometry, charge, or the type of metal and ligands, are crucial factors driving the interactions.[451]

Interactions between a metallodrug and the DNA are divided into two main types: covalent and non-covalent interactions. The covalent mode of binding usually implies the formation of adducts, which are irreversible because of their high biding strength. Generally, covalent binding induces the DNA inhibition process causing cell death. Moreover, if the adduct is bulky, the DNA backbone is distorted, affecting transcription, and inducing replication inhibition or failure. The most frequent covalent binding mode is the replacement of labile groups in a metal complex with nitrogenated bases of DNA, which leads to intra and inter-strand cross-linking; as it is the main mechanism in cisplatin, detailed in the introduction chapter. The second relevant type of covalent interaction are the DNA alkylating agents, which are the oldest class of anticancer drugs. Alkyl groups are added to molecules or DNA binding sites, causing mispairing or DNA fragmentation, inhibition of replication and transcription and so, cell death.

Among non-covalent, intercalation, groove binding, external binding, and electrostatic interactions are the most typical interactions. They usually affect DNA conformation, prompting structural perturbations, interference in DNA-proteins interactions or generating mitochondrial DNA malfunction. In comparison to covalent binding, they are less cytotoxic, mainly because their interactions are reversible, and present lower associated side-effects.[451–453]

Therefore, in the present work, several methods to assess the conceivable interactions between **Pt-Ls** and DNA have been conducted. The study has focused on the determination of non-covalent binding since the highly hydrophilic moieties of the ligands in complexes would most probably hinder the formation of covalent binding.

Circular dichroism (CD) spectroscopy is extremely sensitive to changes in the secondary structure of DNA and is typically intended to determine the favoured binding mode. Nitrogen base pairs do not show chirality by themselves, but it is given by the bonding of the bases to sugars in the DNA backbone. And, this chirality induces a CD signal, valuable to determine asymmetry and detect minor conformational changes upon drug interaction (**Scheme 6.1**).

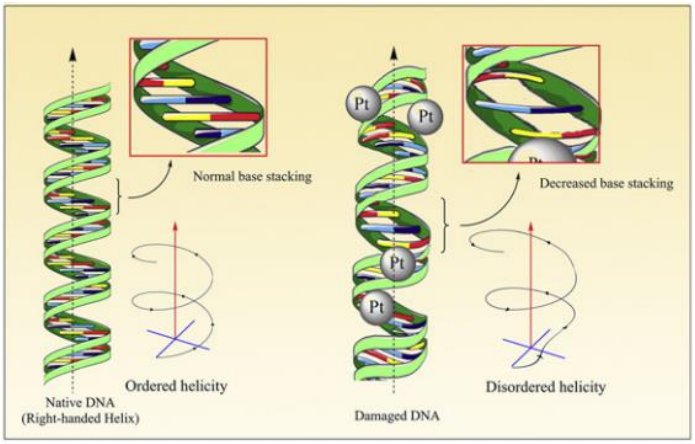

Scheme 6.1 Base-stacking destabilisation and loss of right-handed helicity upon interaction with Pt. Extracted from literature.[399]

In solution, CD spectra of *ct*-DNA, whose pairs are perpendicular to the helix, shows three bands: two positive bands at 220 and 275 nm, and a negative band at 245 nm. Purine and pyrimidine bases are the main ones responsible for the CD spectra, as the sugar and the phosphate group does not absorb significantly in the region. The peak near 275 nm is related to base stacking while the peak around 245 nm is associated with polynucleotide helicity. Generally, both bands crossover around 260 nm in B-DNA.[453,454] For simplicity our study is focused on these two bands, the 245 nm negative band and the 275 nm positive band, referred to as positive and negative band, respectively.

Variations in the CD spectra for increasing amounts of **Pt-L2**, **Pt-L6** and **Pt-L10** were monitored. The *ct*-DNA analysed samples were incubated at 37 °C for 20 h with increasing complex concentration, from 0 to 1.5 equivalents, indicated as r_i = [Pt]/[DNA] (**Figure 6.2**).

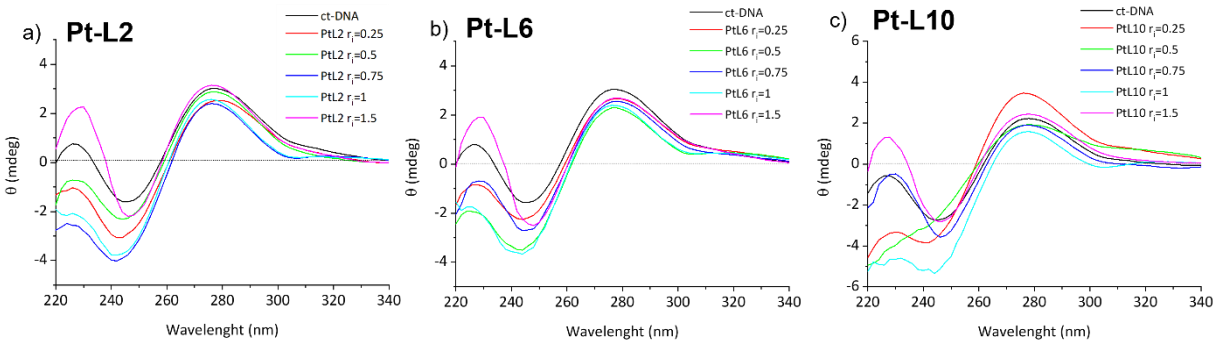

Figure 6.2 DNA-binding studies showing CD spectra at 50 µM *ct*-DNA at r_i = 0.25, 005, 0.75, 1 and 1.5 in Tris·HCl 5 mM at pH 7.2, incubated at 37 °C for 24 h for **Pt-L2** (a), **Pt-L6** (b), and **Pt-L10** (c).

For the three complexes, the CD spectra show deflections in DNA signals, still without causing significant structural alterations on the helicity of the *ct*-DNA.

The elliptical signals of both, negative and positive bands in **Pt-L2** spectra, show hypochromicity upon increasing equivalents. Though, the highest distortion is seen in the negative band that significative decreases and shows a slight hypsochromic shift. The CD spectra of *ct*-DNA upon **Pt-L6** addition keeps the same trend as its shorter analogue, however, the distortion of the bands are less significant than for **Pt-L2**. The decrease in the positive band has been associated with instability of the base stacking, however even present for **Pt-L2** and **Pt-L6**, it is modest.[455] The behaviours of the negative bands are not conclusive since their correlation to a specific trend revealed awkward.

For **Pt-L10** a slight erratic behaviour is observed, an initial increase of the positive band but a decrease of the negative band is beheld. Then, upon increasing **Pt-L10** eq., the negative band amplitude still lowered but the positive band decreases and subsequently increases for the highest r_i. A similar spectral modification was reported by Serebryanskaya *et al*. for a Pt(II) tetrazole based chlorido complex, which gradually increased the positive band and showed subsequent hypochromicity upon drug concentration. The changes were attributed to the characteristic mode of binding of cisplatin and further related to *cis*-bidentate platinum drugs that induce an initial stabilisation of the base stacking and a following destruction with increasing platinum content.[404,455,456] Besides, for *cis*-bidentate platinum complexes the

negative band is reported to be almost absent when saturation is reached, which could explain the results observed for r_i = 1.5.[404]

Finally, it is noteworthy that the 220 nm spectropolarimetric fingerprint shows the same conduct for the three complexes. The general behaviour shows an intensity decrease for the lower r_i, but a trend is not found for higher tested equivalents. Typically, a decrease in the elliptical 220 nm signal is compatible with hydrogen bonding interactions, taking place after minor groove binding.[453] Nonetheless, the structural features of the **Pt-Ls** do not match typical groove binders, which usually are small, planar and torsional-free molecules that bind the minor groove mainly by Van der Waal forces.[451]

In summary, the positive and negative characteristic bands of the *ct*-DNA spectra are maintained, and the observed alterations suggest slight non-covalent binding between the DNA and the complexes.

UV-vis spectroscopy is one of the most convenient techniques to study the binding between drugs and DNA. Using UV-vis, the absorption spectra of the DNA or the drug can be screened, examining shifts and/or intensity variations of the spectral bands.

Modifications in the absorption spectra of the complexes are screened upon the addition of *ct*-DNA to a fixed concentration of **Pt-L2**, **Pt-L6** and **Pt-L10**. The absorption spectra were recorded at 100 µM complex concentration with increasing quantities of *ct*-DNA up to 200 µM, in the typical range for recording the UV-vis spectra of our **Pt-Ls** (from 190 to 600 nm). The results are shown in **Figure 6.3** given after the blank and dilution effect correction.

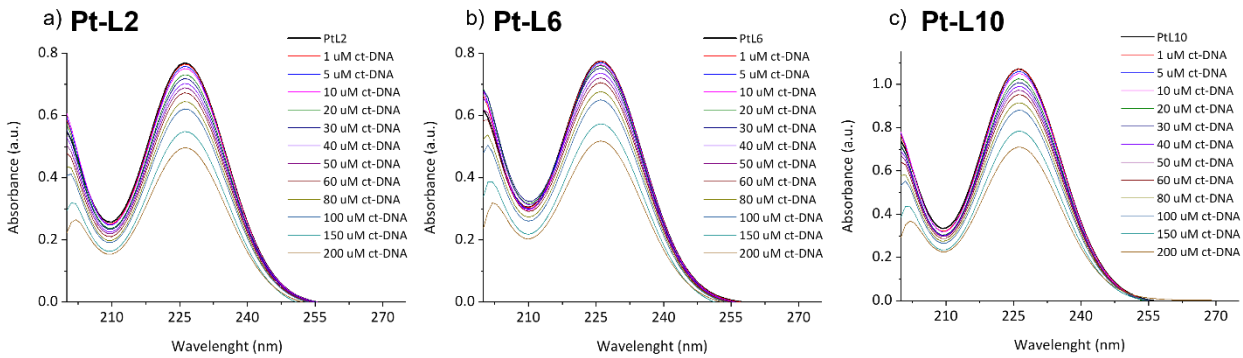

Figure 6.3 UV-Vis at 20 µM of **Pt-L2** (a), **Pt-L6** (b), and **Pt-L10** (c) titrated with *ct*-DNA from 0 to 200 µM of in Tris·HCl 5 mM at pH 7.2. Each spectrum was recorded after 4 minutes of stabilisation time.

Analysing the spectra for the three complexes notable hypochromism is observed. Typically, hypochromic effect accompanied by bathochromic effect evidence intercalative binding, related to the decrease in the electron transition energy due to the stacking interaction

between a usually aromatic drug and the base pair of DNA. Intercalators are commonly planar and aromatic molecules that alter the structural features of DNA and unwind the DNA double helix. Hyperchromic effect should be expected for strong electrostatic interactions since external contact or partial denaturalisation of the DNA helix structure would cause an increase in the UV absorption due to the free DNA bases. It usually happens in the presence of charged cations guided by electrostatic interaction to the DNA phosphate backbone, or ligands that rearrange around the helix to form ordered aggregates and reduced charge repulsion.[451,452] Weaker interactions will only show hyper or hypochromic effects, without shifts in the absorbance bands. These are suitable with modest electrostatic interactions or groove binding interactions. Groove binders do not disrupt significantly the DNA helix structure, because they bind the minor groove of the DNA helix by mainly Van der Waals forces.[453,457–459]

The extent of hypochromicity and the intrinsic binding constant, K_b are associated with the interaction strength, and gatherted in **Table 6.3**. K_b can be determined from the recorded spectra employing the Benesi-Hildebrand, **Equation 6.2**, where A_0 and A are the complex absorbances in absence of DNA, and at any given DNA concentration, and ε_G and $\varepsilon_{G\text{-}H}$ are the extinction coefficients of the complex and the complex-DNA, respectively. K_b is obtained by the ratio between the intercept and the slope of the linear fit: $A_0/(A-A_0)$ *vs* 1/[DNA] (**Figure A72**).[451,457] The data, summarised in **Table 6.3**, derives from an approximated DNA-drug model and thus, they should be compared in orders of magnitude, rather than with the exact numbers.

$$\frac{A_0}{A-A_0} = \frac{\varepsilon_G}{\varepsilon_{H-G}-\varepsilon_G} + \frac{\varepsilon_G}{\varepsilon_{H-G}-\varepsilon_G} \cdot \frac{1}{K[DNA]} \qquad \textbf{Equation 6.2}$$

Table 6.3 Hypochromism and intrinsic binding constant (K_b) for the interaction between **Pt-Ls** and *ct*-DNA. K_b is acquired from the intercept to the slope in the Benesi-Hildebrand equation, after the fitting of the UV-vis data in **Figure 6.3**.

	Pt-L2	**Pt-L6**	**Pt-L10**
Hypochromicity (%) [226 nm]	5.2 (20 µM *ct*-DNA) 36.4 (200 µM *ct*-DNA)	1.3 (20 µM *ct*-DNA) 34.6 (200 µM *ct*-DNA)	4.7 (20 µM *ct*-DNA) 34.6 (200 µM *ct*-DNA)
K_b (M^{-1}); (log K_b)	$1.17 \cdot 10^4$ (4.07)	$5.27 \cdot 10^4$ (4.72)	$3.00 \cdot 10^3$ (3.48)

The K_b values obtained are in the order of 10^3 - 10^4. Strong interactions are established in the order 10^6 – 10^7 and so, the obtained data is in accordance with moderate non-intercalative binding interactions between complexes and *ct*-DNA, which furthermore are similar to those

reported for cisplatin.[354,451,452,457,460] **Pt-L2** bears the greatest non-covalent interaction among the complex family, probably reinforced by the small size of their alkyl chains. Followed by **Pt-L6**, and **Pt-L10**, the latest showing the lowest K_b.

For **Pt-L10**, the binding interaction results obtained by CD and UV-vis generated controversial conclusions: the lowest interaction by both the percentage of hypochromicity decrease and K_b value is seen, although the CD shows the highest modification in the DNA helicity. Hence to further justify the binding between the *ct*-DNA and **Pt-L10**, a competition DNA binding experiment was conducted. Ethidium bromide (EB) is a planar cationic dye that intercalates between bases of the DNA double-helix. The EB-DNA complex shows a 20-fold fluorescence increase with respect to the free dye. Thus, competitive binding assays can be carried by titration with the compound in the study. Therefore, if the molecule displaces EB acting as a quencher the fluorescence will decrease. Strong fluorescence quenching is associated with molecules acting as intercalators. Besides, compounds able to alter the DNA structure may also disrupt substantially the DNA conformation causing lighter quenching.[440,453,457,458,461,462] For competitive binding studies with EB, the DNA concentration is fixed and titrated with increasing concentration of the drug (**Figure 6.4**, a).

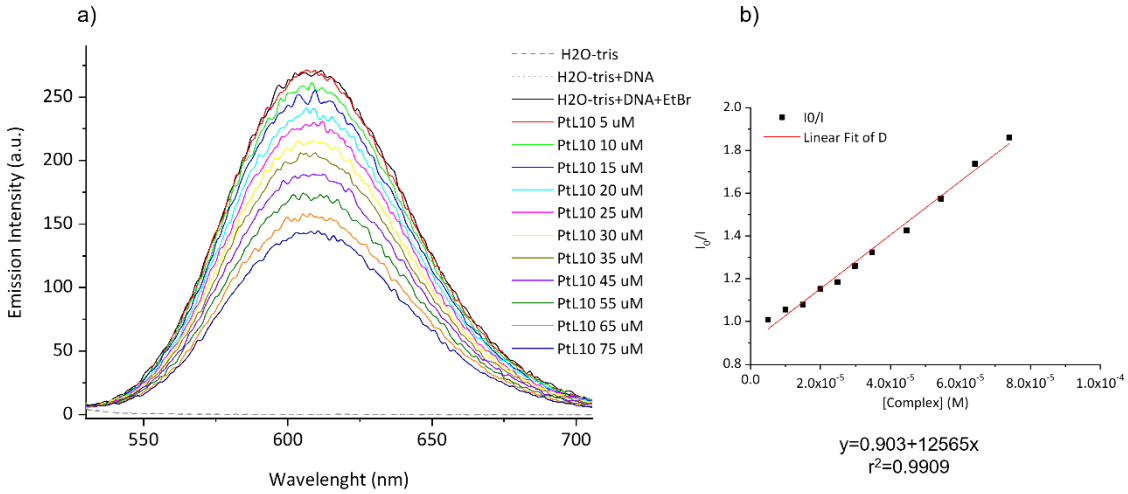

Figure 6.4 Fluorescence emission spectra (a) (λ_{exc} = 514 nm; λ_{em} = 610 nm) of EB bound *ct*-DNA upon the addition of increasing [**Pt-L10**] (from 0 to 70 µM) in a 5 mM Tris·HCl; [EB] = 12.5 µM and [*ct*-DNA] = 2.5 µM. The data has been corrected by the dilution factor. (b) Linear fitting of I_0/I vs complex concentration, where the slope corresponds to K_{sv} accordingly to Stern-Volmer equation (**Equation 6.1**).

The fluorescence spectrum shows fluorescence quenching upon **Pt-L10** addition. **Pt-L10** arises fluorescence quenching (by 47.2 % at 608 nm), suggesting that it can compete with EB for the DNA intercalating sites. Previously, intercalation has been already discarded by the absence of

bathochromic shifts in UV-vis studies. Hence, we propose that electrostatic interactions should be sufficient to substantially modify the DNA conformation, inducing the release of EB.[458]

Additionally, the quenching constant, Stern-Volmer constant (K_{sv}) was calculated from the Stern-Volmer equation (**Equation 6.1**). Where, I_0 and I are the emission intensity in the absence of quencher and when it is submitted to a specific amount of it, respectively and [Q] is the quencher concentration. The K_{sv} is obtained from the slope of the linear fitted plot I_0/I *vs* **Pt-L10** concentration (**Figure 6. 4**, b). The K_{sv} value obtained ($1.26 \cdot 10^4$ M^{-1}) further confirmed the ability of **Pt-L10** to displace EB from the DNA double helix.

The remarks after the CD and UV-vis studies of the interaction between *ct*-DNA and **Pt-Ls** are in agreement with moderate non-covalent binding by electrostatic and/or minor groove binding interactions. Interestingly, UV-vis pointed **Pt-L2** as the complex producing the higher hypochromicity. Also, K_b values showed the highest binding affinity for by **Pt-L6**, in the order of 10^4 M^{-1}, while **Pt-L10** exhibited the lowest affinity, 10^3 M^{-1}. Whereas by CD **Pt-L10** showed higher interaction with *ct*-DNA and their ellipticity modification reassemble to other *cis*-bidentate platinum molecules described in literature. Competitive binding studies agreed with the role of **Pt-L10** as a moderate binder, able to displace EB.

With all, we believe that electrostatic interactions should be the most plausible non-covalent interactions occurring between *ct*-DNA and our complexes. Mainly due to the negatively charged sulfonate groups or after the displacement of the iodide ligands. Likewise, their bulkiness, mainly when bearing **L6** and **L10,** lead us to consider groove binding as less a reasonable interaction. In fact, the distinctive bulkiness of alkyl amines Pt(II) complexes have been lately remarked to present different DNA binding, being coordinated with short groups, as ethyl groups, and electrostatically in the case of butyl analogues.[288]

6.3 In vitro anticancer studies

6.3.1 Alkyl amino sulfonates and Pt(II) alkyl amino sulfonated cytotoxicity assays

In vitro antiproliferative activity of the complexes, **Pt-L2**, **Pt-L6**, and **Pt-L10**, and their corresponding ligands, **L2**, **L6**, and **L10** has been assessed against three immortalised cancer cell lines: HeLa, A2780 and A549. Human adenocarcinoma HeLa cells epithelial cervix; human A2780 cells are from an ovarian adenocarcinoma and A549 adenocarcinoma cells are from a human alveolar basal epithelial cells of cancer lung tissue. These studies were performed in

collaboration with Dr. Julia Lorenzo and Dr. David Montpeyó, from the *Institut de Biotecnologia i de Biomedicina* (IBB) at UAB.

The prominent solubility of the complexes allowed the direct solubilisation in the working medium: MEMα for HeLa cell line, DMEM for A549 cell line, and RPMI for A2780 cell line as detailed in the experimental section. The tested **Pt-Ls** and **Ls** concentrations were 0 - 200 µM and the cell proliferation count was done using the cell viability reagent alamarBlue™. The full protocol can be found in chapter 8. The results shown in **Figure 6.5** were obtained after 72 h of incubation in triplicate with three independent experiments.

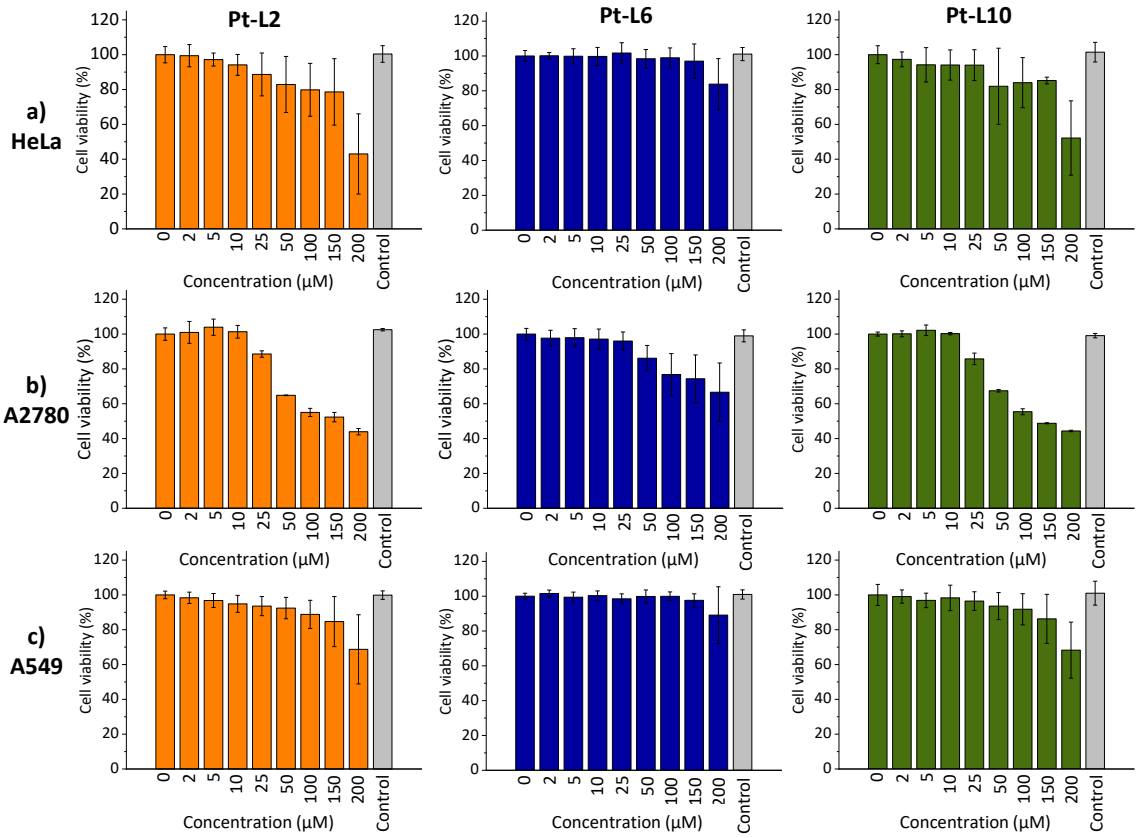

Figure 6.5 Cell viability assays for HeLa (a), A2780 (b) and A549 (c) cell lines treated with **Pt-L2** (left), **Pt-L6** (centre), and **Pt-L10** (right) after 72 h of treatment at different concentrations. The results are an average of three independent experiments conducted in triplicate.

None of the ligands, **L2**, **L6** nor **L10**, exhibited antiproliferative activity against either of the tested cell lines in the tested conditions (**Figure A73**).

Remarkably, the complexes displayed poor cytotoxic activity, but showed distinctive activity against the three cell lines. More specific, the three complexes exhibited lower cell viability percentages for A2780 and HeLa cell lines but were almost negligible for A549 cell line. In

general terms, it is reported that A2780 cell line is more sensitive to cisplatin treatment, while A549 and HeLa cell lines present a higher resistance against it.[463]

Pt-L2 produced superior decreased cell viability reaching a 43% at 200 µM, followed by **Pt-L10** which rendered a 52% at the same concentration. Conversely, **Pt-L6** did not show almost any cytotoxic effect in HeLa cell line. The higher cytotoxicity was observed against A2780 cell line, in which the cell viability diminished in the order **Pt-L2** ~ **Pt-L10** > **Pt-L6**. Peculiarly, the three **Pt-Ls** displayed poor cytotoxicity against A549, showing a cell viability decrease until ~68% at 200 µM with **Pt-L2** and **Pt-L10**, and negligible with **Pt-L6**.

We consider that the distinct cytotoxicity among the three complexes should be driven by their size and molecular weight, and hence its capacity to enter the cell; probably the internalisation of **Pt-L2** is different from the internalisation of **Pt-L10** and **Pt-L6**. Or rather, the mechanism of action by which toxicity is exerted diverts. For instance not the same cytotoxic activity has been reported for self-aggregation complexes, below or above the CAC.[237] However, this is merely an assumption that regrettably could not be further investigated.

6.3.2 Metallosomes cytotoxicity assays

The previous chapter was fully dedicated to the description and understanding of the preparation of **MTL** internalising **Pt-L10.** Diverse structural lipids have been investigated in the preparation of the **MTL**, and this section gathers the results obtained in their preliminary cytotoxicity studies against several cell lines. The antiproliferative activity of the **MTL** was tested in HeLa, A2780 and A549 cell lines to evaluate their toxicity and to be compared with that of the free complex (section 6.3.2.1). Moreover, they were further tested against Huh-7, using a protocol that allows estimating the specific activity of the **MTL**, detailed in section 6.3.2.2. Besides, the implications of the distinct lipid formulation, DOPC, SPC, DMPC or DSPC, are considered hereinafter.

In the previous chapter, it was proven that **MTL** properties do not significantly differ from the pure liposome up to at a molar ratio 100/1 (lipid:**Pt-L10**). Thus, it was the concentration chosen to conduct the cytotoxicity assays that ranged from 1500-200 µM of lipid to 15-2 µM of **Pt-L10**.

6.3.2.1 Metallosomes against HeLa, A2780 and A549 cell lines

Also, in IBB, the four **MTL** formulations were tested against HeLa, A2780 and A549, using the same protocol as in the cytotoxicity assays for **Pt-Ls** and **Ls**. Celll viability was evaluated for 24

and 72 h of treatment and the highest lipid concentrations in the **MTL** were tested as pure liposome (with comparable sizes) as the control for the cytotoxicity of **MTL**.

The results, in **Figures 6.6** to **6.9** gather the cell viability assays for 24 and 72 h of treatment with the following formulation: DOPC:**Pt-L10**, DMPC:**Pt-L10**, SPC:**Pt-L10**, and DSPC:**Pt-L10**.

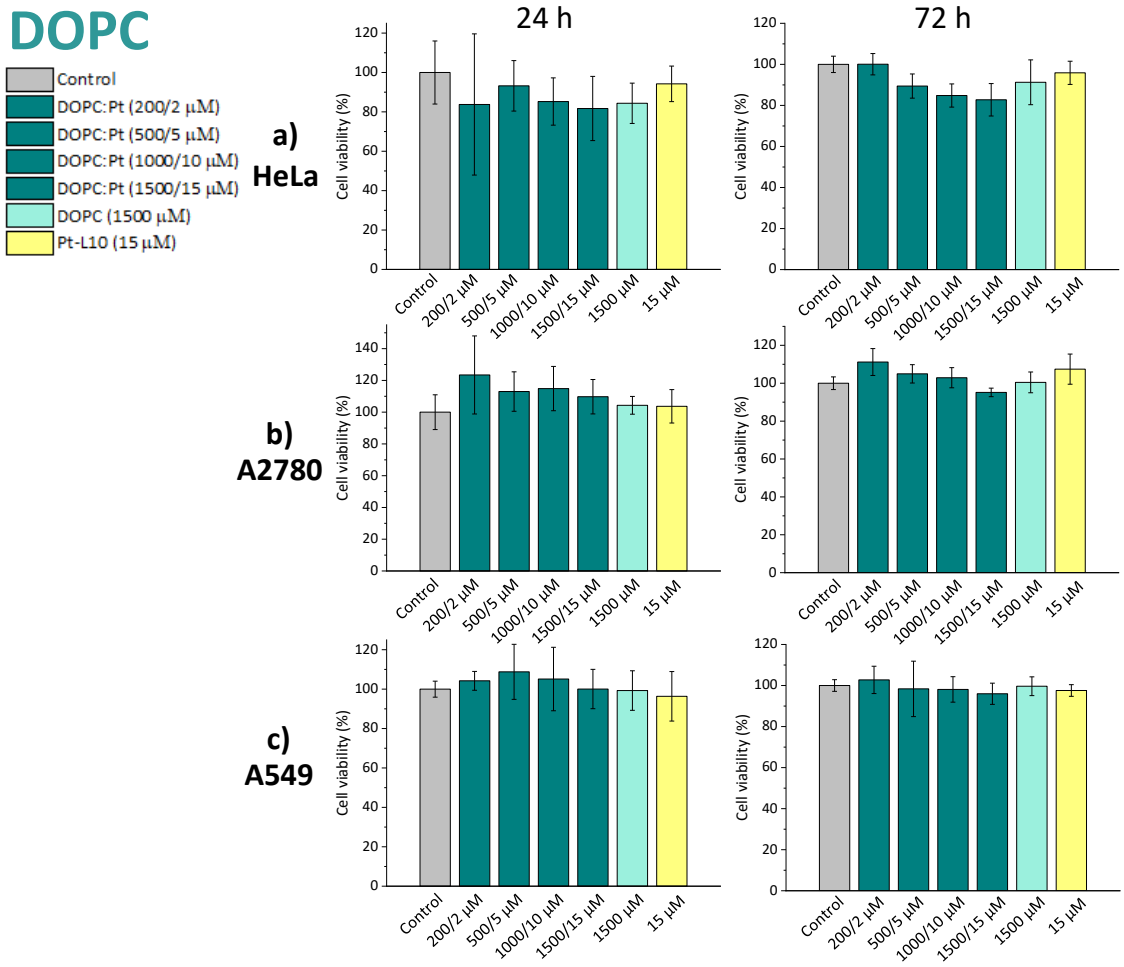

Figure 6.6 Cell viability assays for DOPC **MTL** in HeLa (a), A2780 (b) and A549 (c) cell lines after 24 (left) and 72 h (right) of treatment. Light blue and yellow bars show the cell viability after treatment with pure liposome and **Pt-L10**, respectively, at the maximum experimental concentration. The results are an average of three independent experiments in triplicate.

The assays conducted for DOPC **MTL** (**Figure 6.6**) showed poor cytotoxicity against the three tested cell lines. The toxicity against A2780 and A549 cell lines is negligible and, exclusively, HeLa cell line revealed certain diminished cell viability for 72 h of treatment.

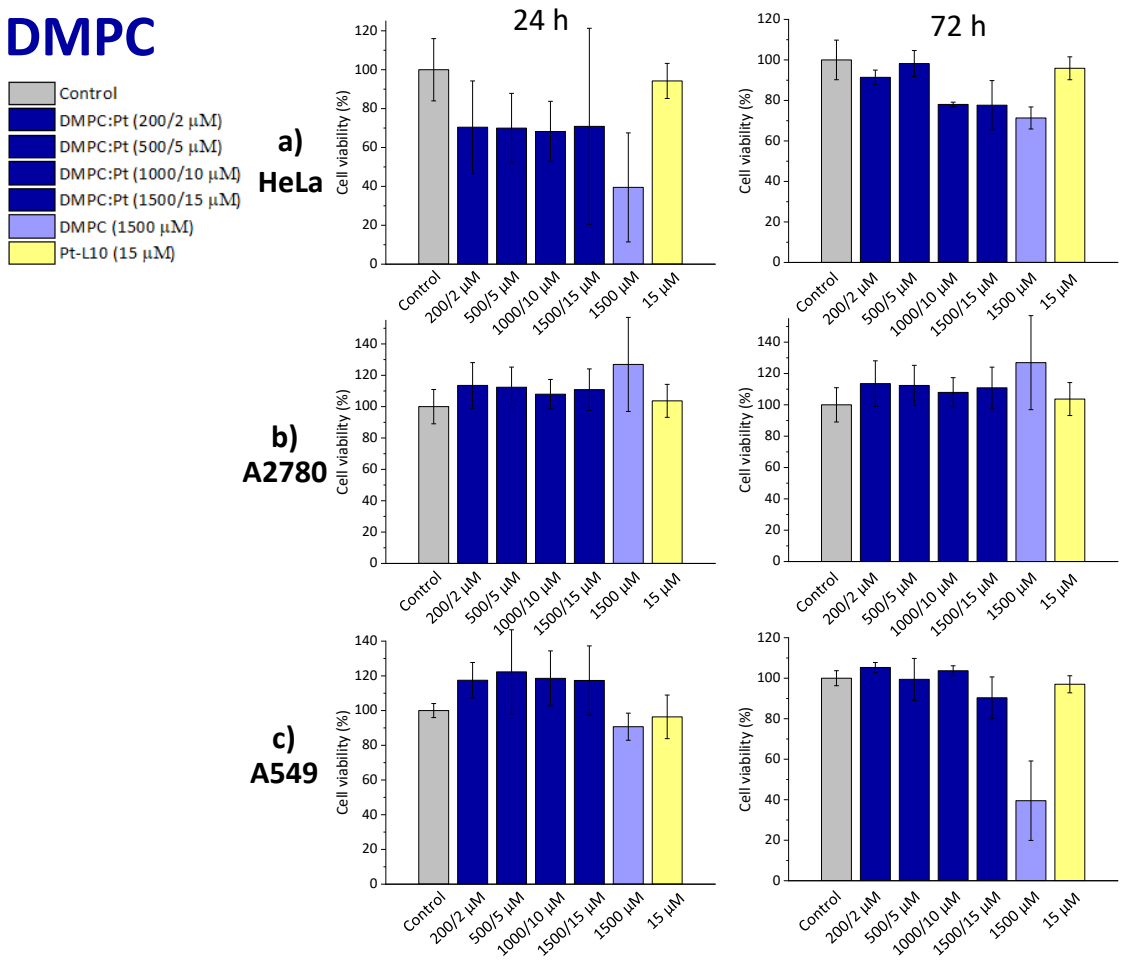

Figure 6.7 Cell viability assays for DMPC **MTL** in HeLa (a), A2780 (b) and A549 (c) cell lines after 24 (left) and 72 h (right) of treatment. Light purple and yellow bars show the cell viability after treatment with pure liposome and **Pt-L10**, respectively, at the maximum experimental concentration. The results are an average of three independent experiments in triplicate.

DMPC **MTL** (**Figure 6.7**) demonstrated no activity against A2780 and A549 cell lines, whose cell viability is maintained. Moderately activity against HeLa cell line is exhibited, which unpredictably seemed greater for 24 h of treatment. Besides, plain DMPC liposomes showed cytotoxicity against HeLa and A549. Remarkable, saturated lipids are reported to usually show low toxicity, but lipids with shorter alkyl chains have higher toxicity attributed, as in the case of DMPC (C14).[464]

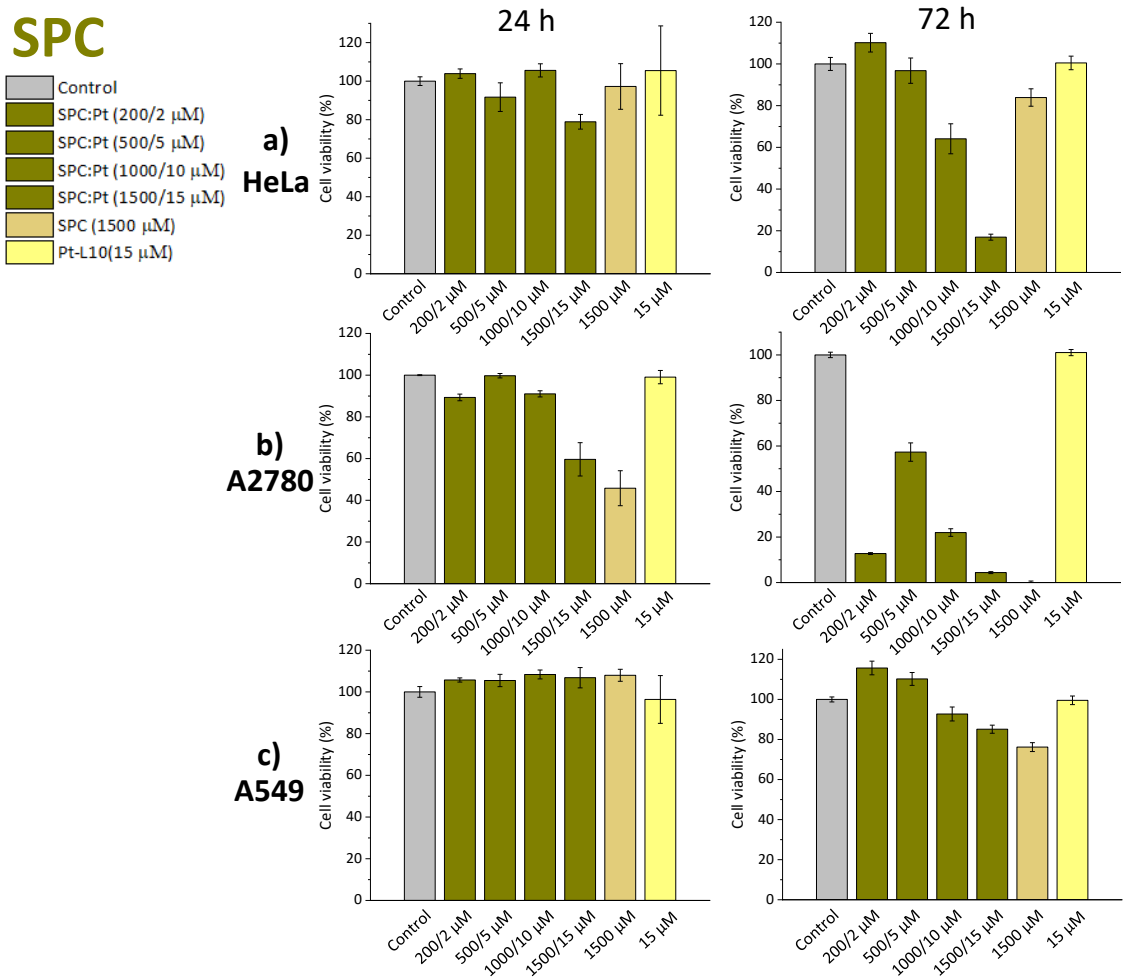

Figure 6.8 Cell viability assays for SPC **MTL** in HeLa (a), A2780 (b) and A549 (c) cell lines after 24 (left) and 72 h (right) of treatment. Dark yellow and yellow bars show the cell viability after treatment with pure liposome and **Pt-L10**, respectively, at the maximum experimental concentration. The results are an average of three independent experiments in triplicate.

The cell viability assays for SPC **MTL** (**Figure 6.8**) revealed greater toxicity after 72 h against the three cell lines. However, the cell viability decrease was highlighted in HeLa and A2780 cell lines. Gratifyingly, the viability after 72 h in A2780 reached almost 0% in 1500/15 SPC:**Pt-L10** molar ratio, and more surprisingly for the pure SPC liposomes (the 200/2 SPC:**Pt-L10** molar ratio has been avoided because it is beyond the reasonable tendency). Nonetheless, it is important to note that SPC is highly used in DDS and the low toxicity of plain SPC liposomes is ratified in several works, with negligible cytotoxicity for defined values up to $1.29 \cdot 10^{8}$ µM, against several cancerous and healthy cell lines.[275,432,465] Consequently, the results obtained for SPC **MTL** are not conclusive, and to obtain clearer information the cell viability assays must be repeated for SPC **MTL**. But, unfortunately, the results are pending to be repeated and could not be included in this thesis.

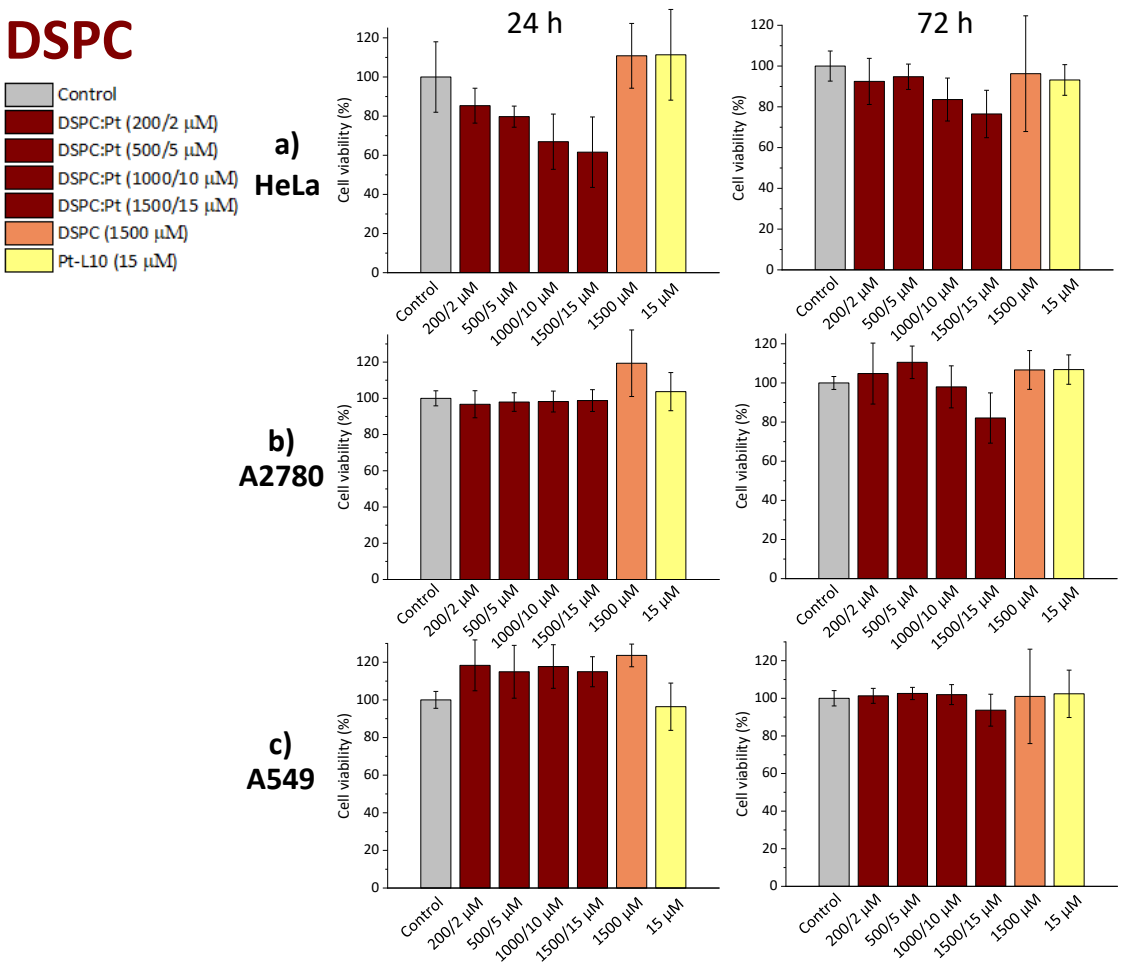

Figure 6.9 Cell viability assays for DSPC **MTL** in HeLa (a), A2780 (b) and A549 (c) cell lines after 24 (left) and 72 h (right) of treatment. Orange and yellow bars show the cell viability after treatment with pure liposome and **Pt-L10**, respectively at the maximum experimental concentration. The results are an average of three independent experiments in triplicate.

The results for DSPC **MTL** (**Figure 6.9**) exhibited poor results against A549 cell lines, displaying 100% cell viability for 24 and 72 h treatment. Against A2780, the cell viability after 72 h slightly decreased for the highest concentration of **MTL**. The greatest cytotoxicity of DSPC **MTL** was observed against HeLa cell line that showed decreased cell viability for 24 and 72 h of treatment. However, it is unusual that cytotoxicity was greater for 24 h of treatment than 72 h. In literature, diminished cytotoxicity after 72 h, compared to 24 h is reported and presumably related to cellular adaptation to the current condition.[466] Nonetheless, further rationalisation of this fact has not been learnt from literature.

Taken together, the results concerning the four formulations of **MTL**, displayed increased cytotoxicity of the **MTL** with respect to their counterpart **Pt-L10**, which did not show cytotoxicity against any of the three cell lines at the tested concentration (15 µM). The results

have been for SPC **MTL**, suggest greater activity against HeLa and A2780 cell lines, and even slightly activity against A549, which remained with negligible cell death in front of the rest of the formulations. DMPC **MTL**, DOPC **MTL** and DSPC **MTL** lack cytotoxic activity against A2780 and A549 cell lines, but certain activity against HeLa cell line is identified.

6.3.2.2 Metallosomes against Huh-7

During the internship carried in Luciani Research group, cytotoxicity assays were conducted in collaboration with Dr. Gina Valentino. The protocol for the cytotoxicity assays, specified in chapter 8, slightly varies from the protocol used at the IBB. The main difference consists in the addition of 10% of serum to the media prior to its use in the experiments conducted in IBB. The serum, serves as a source of hormones and nutrients for cells, allowing the test to be conducted throughout longer than 24 h of treatment. The avoidance of serum is referred as starvation.[467,468] Besides, by avoiding the addition of the serum, the system is simplified because proteins that could kidnap the DDS, the **MTL** in this case, will not be present. Hence, it is an appealing strategy to estimate the specific activity of the **MTL**.

The molar ratio 100/1 (lipid:Pt) was tested against Huh-7, a hepatocyte-derived carcinoma from liver tumour, in DMEM for 6 and 24 h of treatment. All the concentrations of pure liposome and PBS concentration that arises from **MTL** hydration were also tested as controls. The cell count was performed using the cell counting kit-8 (CCK8, based on WST-8 salt). It is distinct from the Presto Blue reagent used for cell counting of the previously presented cell viability experiments conducted in IBB, but it is also based on the metabolic activity of the living cells.

The results, in **Figure 6.10** gathers the cell viability assays at 6 and 24 h of treatment for the four lipid formulations.

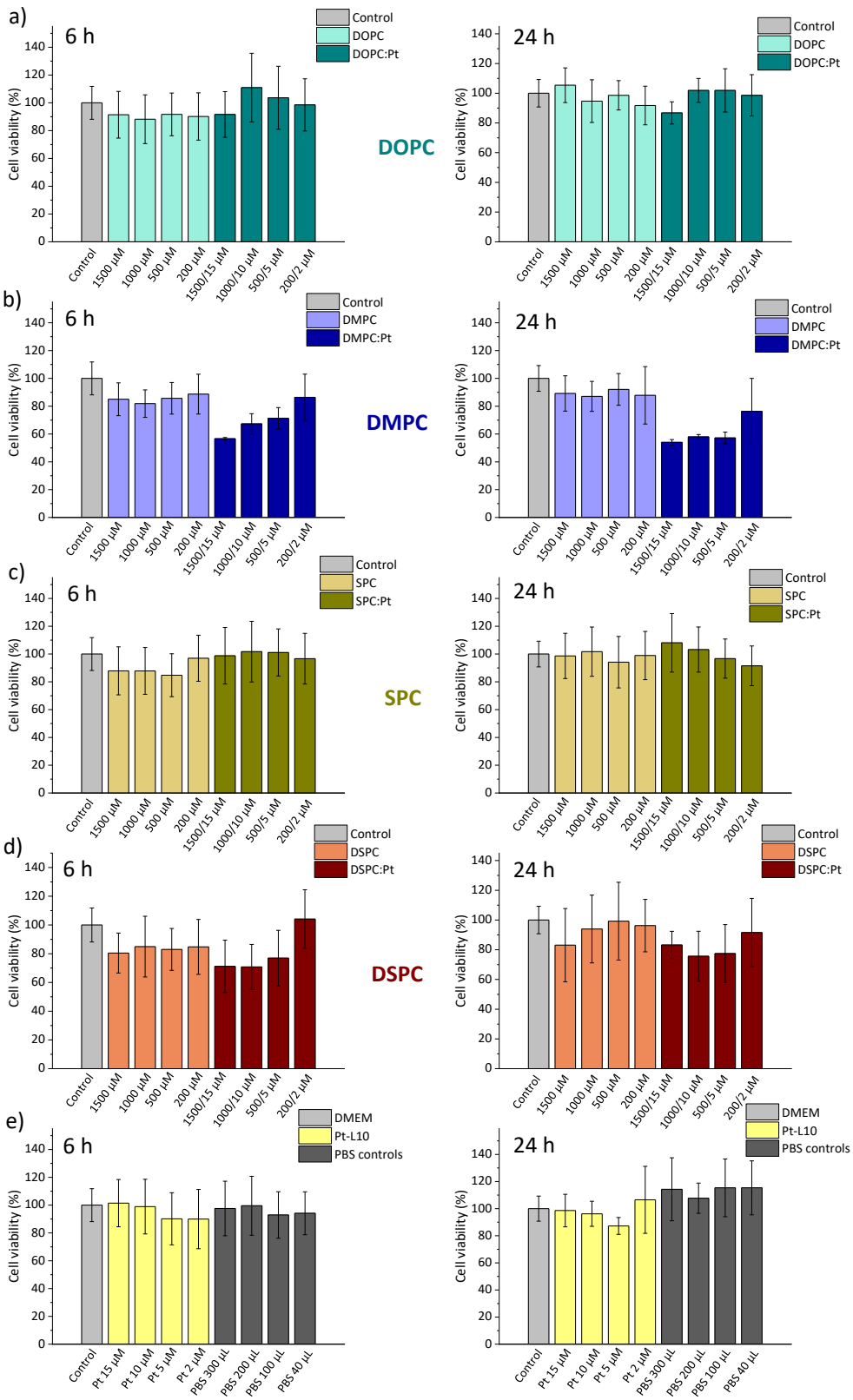

Figure 6.10 Cell viability assays for **MTL** in Huh-7 cell line after 6 (left) and 24 h (right) of treatment for DOPC (a), DMPC (b), SPC (c), DSPC (d) formulations with their respective controls (e). Lighter bars show the plain liposome at the tested concentrations, while the darker bars show the lipid:**Pt-L10** molar ratio. The controls display the cell viability after treatment with **Pt-L10**, referred as Pt, and the corresponding amount of PBS. The results are an average of three independent experiments in triplicate.

At the experimental conditions, no cytotoxicity was exerted by PBS addition and neither by the tested concentrations of **Pt-L10**. Furthermore, SPC **MTL** and DOPC **MTL** showed no cell viability decrease. Diminished cell viability was exhibited for DSPC **MTL** and DMPC **MTL** after 6 h of treatment, being greater for DMPC **MTL**. After 24 h of treatment, the toxicity shown by DSPC **MTL** is similar than for 6 h of treatment. DMPC **MTL** at 24 h displayed increased toxicity, with respect to 6 h of treatment.

The results for the **MTL** cytotoxicity showed higher activity against Huh-7 than the parental **Pt-L10** complex. Respect the toxicity seen against HeLa, A2780 and A549 cell lines at 24 h of treatment, DMPC **MTL** formulation was revealed as the most cytotoxic formulation. Altogether, the general observed trend shows moderate higher activity against Huh-7, with respect to HeLa, A2780 and A549 cell lines. It could be attributed to the absence of serum that would diminish the interaction and further inactivation of the DDS. The experiments have been conducted in two different laboratories with different protocols and due to the elevated costs of the experiments, there was no possibility of reproducing none of them using a unique protocol. Hence, it was not proven if proteins interaction led to lower cytotoxicity, or if the distinct activity was related to the cell line. However, the already discarded covalent interactions with some proteins points that it should not be the main reason. Nonetheless, even the dissimilar protocols, the obtained cell viability results point to comparable trends.

It is worthy of mention that both cell counting assays (AB and WST-8) used in the cell viability experiments rely on the metabolic activity of living cells, which reduces the corresponding dye. It is established that distinct cellular stages of death show differential metabolic activity, and also the reagent may be reduced distinctly. Thus, alterations in the cellular metabolic activity can produce substantial changes in the results.[469,470]

When relating the moderate percentage of platinum release described in the previous chapter, in section 5.2.3.7, it seems to correlate with the modest cytotoxicity shown by the **MTL**. An explanation might be that the **MTL** enter the cell but not distribute the platinum content. It is worth noting that the intracellular pH is 7.2, but it differs between organelles, such as for lysosomes which are considered to be responsible for the release in several DDS and have a pH value of about 4.5.[471–473] Thus, if repeating the release experiment at acidic pH there was increased platinum release, it would mean that the **MTL** is probably not internalising in cells.. Nonetheless, if similar release values were obtained, it could imply both, low **MTL**

internalisation or that the high stability of the **MTL** hinder the release of the platinum complex activity.

6.4 General remarks and future perspectives

The protein interaction study by ESI-MS gratifyingly revealed low to moderate interactions between **Pt-Ls** and HSA, Mb, Cyt c, Tf and Zn_7-MT1. Moreover, the interaction between **Pt-Ls** and **Ls**, and HSA investigated by fluorescence spectroscopy evidenced modest interactions in all the cases, which are greater for the complexes respect their parental ligand.

The interaction with *ct*-DNA, rationalised after CD and UV-vis studies, revealed interactions attributed to non-covalent interactions, which within all, pointed electrostatic interactions as the most plausible.

Cytotoxic assays encompassed the study of the ligands and complexes, as well as the final Pt-**MTL** with the four lipid formulations. The toxicity shown by **Pt-Ls** and **Ls** was higher against two of the tested cell lines, HeLa and A2780 but scarce against A549 at the tested concentrations. Then, when testing the **MTL,** two distinct protocols were followed, mainly differing in the treatment time and the use of serum, present in the assays against Huh-7, and absent in the assays against HeLa, A2780 and A549. The studies evidenced DMPC **MTL** formulations as the most cytotoxic. Comparing both **MTL** cytotoxicity assays, increased toxicity against Huh-7 was observed, respect to HeLa, A2780 and A549.

Interestingly, the **Pt-Ls** exhibited low toxicities against the tested cell lines, but when **Pt-L10** is formulated as **MTL** the toxicity increases, since low concentrations of platinum have demonstrated improved cytotoxicity. The moderate toxicity exerted by the **MTL** can be correlated with the low platinum release appreciated in the previous chapter.

Overall, initial stage cytotoxic assays support the **MTL** strategy because the activity exerted by **MTL** is, without doubt, superior with respect to their homologous complex, **Pt-L10**. Nonetheless, to attain concise conclusions, several assays should be resumed and repeated. Still, we are optimistic about the approach based on mixed vesicles. Although, we consider that the formulation improvement of the **MTL**, for instance, adding cholesterol and/or PEG will improve the pharmacokinetics of the **MTL**. In short, the results obtained in this part of the thesis, we do believe that they show a way forward with promising results.

7. CONCLUSIONS

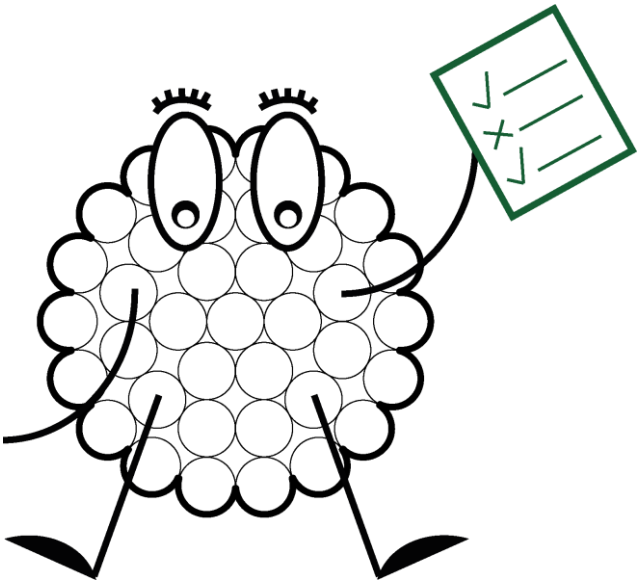

This section reflects and states the main aspects arose during the current work.

- Three alkyl amino sulfonate ligands with 2, 6, and 10 carbon atoms chain length (**L2**, **L6**, and **L10**), have been synthesised and physiochemically characterised. The lack of aggregation has been determined for **L2** and **L6**. Regardless of aggregation has neither been determined for **L10** it has shown amphiphilic behaviour and solubility issues that most probably are related to their specific physicochemical features.

- Three complexes with the general formula *cis*-$[PtI_2(L)_2]$ (**Pt-L2**, **Pt-L6**, and **Pt-L10**) bearing the alkyl amino sulfonate ligands have been synthesised and fully characterised. Supramolecular organisation in water has been revealed for the two longer complexes (**Pt-L6**, and **Pt-L10**) by light scattering and SAXS.

- Regarding its biological characterisation, the complexes showed non-fouling properties in front of the tested proteins (HSA, Mb, Cyt C, Tf, and Zn_7-MT1). In addition, their interaction with *ct*-DNA revealed moderate interactions attributed to non-covalent bindings, most presumably electrostatic. The cell viability assays against HeLa, A2780, and A549 cancerous cell lines showed modest toxicity, which was higher against HeLa and A2780 and scarcer against A549.

- For the preparation of **MTL** with **Pt-L10** the thin film method was employed. For it **Pt-L10** could be added in two distinct stages with comparable platinum internalisation, however, a more homogeneous film was obtained when adding the complex before the film obtention. The preliminary characterisation of the **MTL** evidence that **Pt-L10** influences the vesicles' sizes. Moreover, the **MTL** display great stability when stored at 4 °C.

- The **MTL** can be successfully produced with SPC, DOPC, DSPC, and DMPC as structural phospholipids. After the extrusion of the vesicles, all the formulations show vesicles' sizes ranging from 65 to 160 nm with low PDIs. The platinum internalisation values are significant, and compatible with the presence of the **Pt-L10** in the lipidic bilayer. Likewise, ZP values are consistent with its introduction in the bilayer. Perturbations of

the bilayer differ between lipids: DOPC formulations evidence **Pt-L10** to induce greater modifications in the bilayer. Whereas DSPC, DMPC, and SPC formulations suggest a non-homogenous mixing of the components. All the formulations display extensive stability: up to 8 weeks for DOPC and SPC formulations and over 4 weeks for DMPC and DSPC formulation.

- The **MTL** characterisation unveils that the disturbances caused in the bilayer by **Pt-L10** are marginal up to 100/1 lipid:**Pt-L10** molar ratios. The **MTL** at 100/1 molar ratio were tested against HeLa, A2780, A549, and Huh-7 cell lines showing that the anticancer activity increases with respect to **Pt-L10**. However, the toxicity evidenced by the **MTL** is still moderate. Among them, DMPC formulations are the most cytotoxic. Undistinguishably, the **MTL** moderate toxicity correlates with the low platinum release observed in the release experiment.

To conclude, we highlight the successful preparation and characterisation of Pt(II) containing **MTL**. Although the toxicity of the prepared **MTL** is limited, the initial stage cytotoxic assays support their preparation because the activity exerted is, without doubt, superior to that of the homologous complex, **Pt-L10**. Hence, endorsing their exploration as promising chemotherapeutic DDS.

8. EXPERIMENTAL SECTION

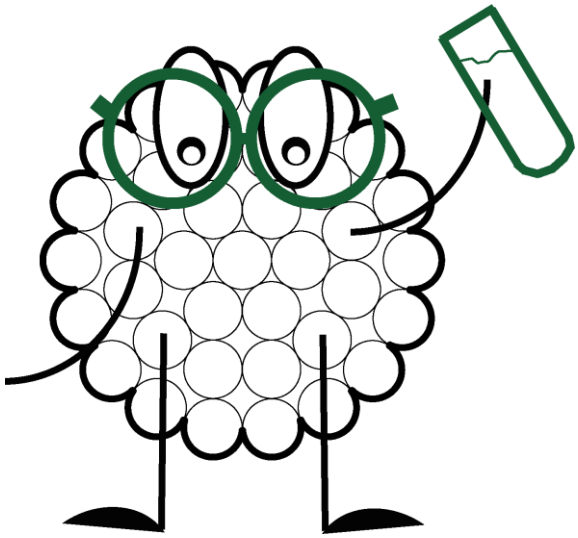

This chapter summarises the instrumentation, methodologies, and experimental procedures employed in this thesis. The vast number of techniques employed allowed the understanding of the chemical structure of the prepared ligands and complexes, and the supramolecular organisation of the final **MTL**. The characterisation techniques and methodologies are described in the first part of the chapter, and a description of the synthetic procedures is found subsequently.

8.1 Chemicals

Chemicals were purchased from Sigma-Aldrich and the solvents from VWR or Thermo Fisher Scientific. The chemicals were commercially available and used as received, except for 1,2-dibromotehane and 1,6-dibromohexane, which were previously distilled. Deuterated solvents were purchased from Eurisotop. Lipids were acquired from Lipoid GmbH. PBS buffer was prepared using ROTI® Fair PBS 7.4 tabs (10 mM phosphate, 0.14 M NaCl and 2.7 mM KCl, pH 7.4).

8.2 Instruments and experimental procedures

8.2.1 Nuclear magnetic resonance spectroscopy (NMR)

Nuclear magnetic resonance (NMR) is a common technique that applies a magnetic field along with radiofrequency pulses to obtain information about the atomic nucleus of a molecule, allowing to obtain information about non-zero nuclear spin of each atom and according to its surrounding. NMR has been registered in *Servei de Ressonància Magnètica* at the UAB using three different equipment ^{1}H-NMR spectra were recorded on Bruker DPX250 (250 MHz), Bruker DPX360 (360 MHz), and Bruker AR430 (400 MHz) spectrometers. Proton chemical shifts (δ) are reported in ppm with the non-deuterated residual solvent as internal reference (CD_3OD, 3.31 ppm, $CDCl_3$ 7.26 ppm and D_2O 4.79 ppm). ^{13}C NMR spectra were recorded with complete proton decoupling on DPX360 (91 MHz), and Bruker AR430 (101 MHz). Carbon chemical shifts are reported in ppm with the non-deuterated residual solvent as internal reference ($CDCl_3$, 77.16 ppm, CD_3OD, 49.00 ppm) All the NMR spectra have been treated using MestReNova v6.0.2-5475 software.

8.2.2 Infrared spectroscopy (FTIR-ATR)

Infrared spectroscopy (IR) measures the wavelength and intensity of the absorption of the infrared wavelength by a sample. IR spectroscopy relies on the absorption between the vibrational and rotational states of functional groups to elucidate the molecular structure

and/or interactions occurring in the sample. Fourier transform infrared attenuated total reflectance (FTIR-ATR) instruments usually focus on the 4000-400 cm^{-1} (mid-IR region), in which are located the fundamental vibrations and the associated rotational-vibrational structure.[474] The spectra were acquired on a Bruker Tensor 27 Spectrophotometer equipped with a Golden Gate Single Refraction Diamond ATR accessory at *Servei d'Anàlisi Química* at the UAB. The solid products were directly located in the diamond Specac Golden Gate and the peaks are reported in cm^{-1}.

8.2.3 UV-Vis spectroscopy (UV-Vis)

Ultraviolet visible spectroscopy (UV-Vis) is a technique based on the absorption of molecules in the visible and ultraviolet wavelength. The recorded absorptions are related to electronic transitions from a ground to a excited states. Electronic absorption spectra were recorded in a UV-Vis 8453, Hewlett-Packard with Diode-array detector, and a measurement range of 190-1100 nm at *Servei d'Anàlisi Química* at the UAB. The spectra of **Ls** and **Pt-Ls** were obtained using 1 cm thick quartz cuvettes, solving the solid products in Milli-Q water.

The interaction between *ct*-DNA and **Pt-Ls** were recorded in the same instrument. Samples were prepared from the corresponding *ct*-DNA sodium salt (Sigma Aldrich) and the concentration was determined from its absorbance at 260 nm (ε = 6600 cm-1). Blank and dilution effects were corrected in all the cases.

The quantification of SPC liposomes for its sedimentation and the lipid quantification by means of Stewart method in Chapter 5 were performed with a Varian UV–Vis Cary 3Bio spectrophotometer (Palo Alto, California, USA) at *Unitat de Biofísica* at the UAB. In this case, the lipid in a liposomal suspension is determined or quantified by UV-Vis absorbance at a given wavelength (usually 280 to 600 nm) and compared with a previously performed calibration pattern "absorbance *vs* lipid concentration". In the case of liposomal suspensions, the absorbance measurement corresponds to an apparent absorbance or turbidity, generated by the presence of suspended vesicles. The measured absorbances depend on several factors such as the lipid concentration or the vesicles' sizes. Hence, this method must be exclusively employed to calculate the concentration of samples that do not endure size modification processes with respect to the original one. In the current thesis, this methodology had been employed (i) in the sedimentation of 3 mM SPC liposomes, which were measured by diluting the samples to 0.6 mM and centrifuging them at 16000 rcf for a specific time, and (ii) when

determining the remaining liposome in each fraction after Sephadex purification attempt. In both cases, the liposomes were measured by UV-Vis at 360 nm and quantified with a previously calibrated pattern.

For the quantification of phospholipid one of the most employed procedures is the Stewart Method, described in Chapter 5.[396] It is an unspecific method to determine the total phospholipid content. The method consists of the formation of a complex between the phospholipid and ammonium ferrothiocyanate that is extracted from chloroform and measured by UV-Vis at 475 nm. Phosphate based buffers do not interact with the ammonium ferrothiocyanate and only one calibration pattern must be conducted in advance. In the procedure, 2 mL of Stewart reagent (of $FeCl_3 \cdot 6H_20$ -0.1 M- and NH_4SCN -0.4 M- in Milli-Q water) and 2 mL of $CHCl_3$ are poured into vials with Teflon caps. Then, the liposomal solution for analyse is added; the total aqueous quantity must not exceed the 5% of the total volume. Subsequently, the vials are vortexed for 30 seconds and the superior aqueous phase is removed and discarded while the chloroformed phase is measured at the absorbance maxima. The results are interpolated with the calibration pattern, prepared following the same procedure.

8.2.4 Circular dichroism (CD)

Circular dichroism (CD) is the preferred technique for the structural characterisation of proteins or biopolymers, such as nucleic acid. CD spectroscopy is a type of light absorption spectroscopy that determines the variation in absorbance of right and left polarised light. It is the perfect tool to investigate DNA conformational variations in solution, since it is possible to identify morphology changes caused by its interaction with other molecules.[399] CD experiments were recorded on a JASCO 715 spectropolarimeter. Measurements were conducted to previously incubated simples (37 °C) during 24 h. The concentration of ct-DNA was set at 50 µM and treated at r_i = 0.25, 005, 0.75, 1 and 1.5, where r_i is [Pt]/[DNA]. Each spectrum was recorded after 4 minutes of stabilisation time and after two accumulation per sample. Temperature was set at 20 °C and scanned in a wavelength range between 200 and 350 nm utilising a 1mm path cuvette, with a speed of 50 nm/min and a data pitch of 2 nm.

8.2.5 Electrospray ionisation mass spectrometry (ESI-MS)

Mass spectroscopy (MS) is based on the characterisation and detection of ionic species in the gas phase after its molecular weight. The molecules of interest are first introduced into the

ionisation source of the mass spectrometer, where they are first ionised to acquire positive or negative charges. Electrospray ionisation (ESI) is a soft ionisation process that uses electrical energy to assist the transfer of ions from solution into the gaseous phase before they are subjected to mass spectrometric analysis. Then, the ions travel through the mass analyser and arrive at different parts of the detector according to their mass/charge (m/z) ratio. The results obtained in the measurements are shown, normally, in a spectrum where the intensity (or abundance) of each species is based on their mass-to-charge ratio (m/z).[475,476]

All the synthesised compounds were characterized by Electrospray ionisation Time-of-Fligh Mass Spectrometry (ESI-TOF MS) in a Micro TOF-Q instrument (Bruker Daltonics GmbH, Bremen, Germany) connected to a Series 1200 HPLC Agilent pump up and controlled by the Compass Software at *Servei d'Anàlisi Química* at the UAB. Sample were analyzed using a running buffer of ammonium acetate (20 mM, pH 7.0). Samples were prepared by solving a small amount of the solid product in Milli-Q water filtered with a 0.22 µm syringe filter and measured in negative or positive ESI mode depending on the necessities.

The interaction between biomolecules and **Pt-Ls** was performed following a previously reported procedure in our group.[443] The protein and complexes were prepared by solving the corresponding amount of protein and complex in ammonium acetate buffer (20 mM, pH 7.0) and incubated at 37 °C for 24 h. The experiments were done in positive mode under the following experimental conditions: 20 µL of the sample was injected at 40 µL/min-; the capillary-counter electrode voltage was set at 4.5 kV; the desolvation temperature was 100 ℃; dry gas at 6L/min. Spectra were collected throughout a *m/z* range from 1000 to 2400.

8.2.6 Inductively coupled plasma optical emission spectrometry (ICP-OES)

The platinum quantification has been attained by Inductively Coupled Plasma Optic Emission Spectrometry and performed at *Servei d'Anàlisi Química* at the UAB. In ICP-OES, the intensity of light emitted from plasma is employed to quantify an element in a sample. To do so, liquid samples are nebulised into an aerosol. Then, they are transported by argon to the plasma that is inductively coupled by radiofrequencies. Due to the high temperatures in the plasma, analytes are ionised, and the emission atomic spectrum is obtained, providing the identity and quantity of an element.[477] Measurements were conducted on an optical emission inductively coupled plasma spectrometer from Perkin-Elmer, Optima 4300DV (Perkin-Elmer, Shelton, CT, USA). Following the protocol at *Servei d'Anàlisi Química*, all the samples were diluted with HCl

(1% v/v) before the injection. Besides, the lipid-containing samples were digested with aqua regia in a microwave with parallel digestion blanks (microwave digestor Milestone, model Ultrawave).

8.2.7 Dynamic light scattering (DLS)

Dynamic Light Scattering (DLS) is a non-destructive technique that offers valuable information about the hydrodynamic size of the particles in solution. The basis of this technique has already been portrayed in section 4.3.2.2. DLS plots can be expressed in volume, number, or intensity. Besides, it provides information about the heterogeneity of the sample based on the measured hydrodynamic diameters, named as Polydispersity index (PDI). The PDI is also attained from DLS instruments.

The **MTL** hydrodynamic diameter and polidisperisty index (PDI) measurement were conducted using the DLS instrument at Bern University, at the Luciani Research Group. They were determined in a Litesizer 500 (Anton Paar, Graz, Austria) equipped with a 175° backscatter angle detector and a semiconductor laser with λ = 658 nm. The liposome formulations were diluted in PBS to a concentration of 100 µM and 1 mL of the diluted dispersion was transferred into disposable semi-micro cuvettes. After equilibrating the sample at 25 °C, the measurement was performed (6 runs with 30 seconds per run). The refractive index was set at 1.33 and the viscosity at 0.89 mPa/s for the solvent. The data was analysed by cumulant method using the software provided by the manufacturer. Furthermore, in section 4.3.2.2, the instrument was employed to seek for a CAC value; for that **Pt-Ls** dilutions were measured, and the intensity of scattered light was registered. The measurements were conducted using two distinct DLS instrument: the Litesizer from Luciani Research Group, as well as the DLS instrument at *Unitat de Biofísica* at UAB, Microtrax Ultrafine Particle Analyser (UPA) 150.

8.2.8 Zeta potential (ZP)

The zeta potential (ZP) is the measurement of the electrical charge at the slipping plane surrounding a colloidal particle. It is also taken as an estimation of the physical stability of a colloidal dispersion. It is considered to present enough repulsive forces between individual particles when the ZP values range from 30 to -30 mV, and thus considered physically stable.[134] The ZP values for the **Pt-Ls** and **MTL** were determined by means of continuously monitored phase-analysis light scattering (cmPALS) in a Litesizer 500 using an Omega cuvette (Anton Paar, Graz, Austria) where a refractive index of 1.33 (for PBS) and a viscosity of 0.89 mPa/s was set

for the solvent. The liposome formulations were diluted in PBS to a concentration of 100 µM and 1 mL. The intensity size distribution of the liposome was unimodal; therefore, the autocorrelation function was analyzed according to the cumulant method by the Kalliope™-software (Anton Paar).

8.2.9 Cryogenic transmission electron microscope (*cryo*-TEM)

Cryogenic transmission electron microscope (*cryo*-TEM) is a type of transmission electron microscopy that allows the direct visualization of vesicles by cooling the samples to cryogenic temperatures. Rapid freezing is critical to avoid the formation of ice crystals and wicking off the aqueous sample before freezing is important to make sure that the sample was not too thick for the electron beam to pass through once converted to a glass.

The used instrument is TEM JEOL 2011 (acceleration voltage: 80-200 kV) with a maximum resolution of 0.18 nm at 200 kV, from *Servei de Microscòpia* at UAB. It is coupled with camera CCD GATAN 895 USC 4000 and it is equipped with a GATAN *cryo*-holder and the detector EDS Oxford Instruments X-max.

A 2 µL aliquot of the sample was added to a Lacey carbon TEM grid, held with a pair of forceps. The grid was loaded onto a preparation chamber, which contained a liquid ethane bath cooled to a temperature between -178°C and -180 °C using an automated liquid nitrogen flow. The solution was quickly wicked off the grid with a piece of filter paper and then plunged into the liquid ethane in one swift motion. The liquid ethane vitrified the vesicles and trapped them in the holes on the TEM grid. Keeping the grid submerged in a liquid nitrogen bath, the frozen grid was loaded into a TEM grid holder cooled with a liquid nitrogen reservoir. The cooled grid holder was then inserted into a JEOL 2011 TEM microscope for imaging. The grids were scanned at low magnification to find regions of low sample thickness where the amorphous water was not too thick and could be positively imaged.

8.2.10 X-ray photospectroscopy (XPS)

The X-ray photoelectron spectroscopy (XPS) is a widely used technique for surface characterisation as it provides quantitative surface elemental composition and chemical state information. The surface of a sample is irradiated by X-ray photons that interact with electrons in the core generating ionised states. As a result, photoelectrons are emitted with a kinetic energy associated with the difference between the irradiated photon energy and the binding

energy. Electrons' orbital energies or binding energies are specific for an atom, which means that direct evidence about the element and its oxidation state can be obtained.[478]

The XPS instrument employed consists of 3 UHV chambers. The analysis chamber is equipped with Analyzer hemispherical Phoibos 150 (SPECS GmbH, Berlin, Germany) at ultra-high vacuum conditions (base pressure $4 \cdot 10^{-10}$ mbar) with mean radius of 150 mm (total energy resolution of 2.9 meV). X-ray source with a monochromatic aluminum Kα (1486.74 eV). The energy resolution as measured by the FWHM of the Ag $3d_{5/2}$ peak for a sputtered silver foil was 0.62 eV. It was measured in the *Institut Català de Nanociència i Nanotecnologia* (ICN2) from UAB.

8.2.11 Fluorescence spectroscopy

Fluorescence spectroscopy allows the determination of the fluorescence of a sample by means of the previous excitation of the electrons that will emit light when relaxing. In this thesis the synthesis compounds are not fluorescence in the visible range of the spectra, however, the technique has been used for recording scattering, or after the addition of a fluorescence probe as hereinafter detailed.

The scattering of **Ls** and **Pt-Ls** was obtained by exciting and recording the emission at a very similar wavelength, to find plausible aggregation of the molecules. The excitation and emission wavelength were set at 500 and 510 nm respectively; slits were set at 15 to assure the best blank signal. The employed instrument was a Perkin Elmer LS 55 50 Hz fluorescence spectrometer using 1 cm quartz cell.

L10 aggregation was also studied using pyranine (HPTS) as a probe to detect the possible presence of aggregation states, using a previously reported procedure.[307] Samples were prepared in PBS buffer. **L10** concentrations were 2, 6, 20, 60, 100, 1000 and 1050 µM and HPTS concentrations were set at 0.56, 5.6 or 88 µM respectively for three independent experiments. Samples were excited at 350 nm and emission was collected from 360 to 650 nm. A blank and negative control were also recorded. These experiments were performed using 1 cm quartz cell in the QuantaMaster™ instrument from the *Unitat de Biofísica* at UAB.

The intrinsic fluorescence of HSA was employed to study the interaction between the biomolecule and **Ls** and **Pt-Ls**. Measurements were performed to solutions of 0.5 µM of HSA and 0.5 µM to 5 µM 1 of each **Ls** or **Pt-Ls** (being 1, 5 or 10 eq.) in PBS buffer, and the corresponding blank solutions. Samples were excited at 285 nm and emission was collected from 300 to 460 nm. Additionally, HSA (0.5 µM) fluorescence quenching occurring after the

addition of $CuCl_2 \cdot H_2O$ (5 µM) was measured as a positive control. The employed instrument was a Perkin Elmer LS 55 50 Hz fluorescence spectrometer using 1 cm quartz cell.

For DNA competitive assays, Ethidium Bromide (EB) was used. In these types of experiments, it is appropriate to fix the DNA concentration and titrate it with the drug; so, the [EB] and [*ct*-DNA] were fixed to 12.5 and 2.5 µM, respectively. The emission spectra with the addition of non-emissive **Pt-L10** (0-65 µM) were then recorded from 520 to 710 nm applying a 520 nm excitation wavelength. The employed instrument was a Perkin Elmer LS 55 50 Hz fluorescence spectrometer using BRAND® polystyrene disposable cuvettes.

8.2.12 Anisotropy fluorescence

The technique used to study the addition of **Pt-L10** into the lipid bilayer was steady-state fluorescence anisotropy spectroscopy (fluorescence anisotropy or anisotropy). The technique was employed to distinguish organisational variations within the lipid bilayer with the addition of 1,6-diphenyl-1,3,5-hexatriene (DPH) probe. Due to its high quantum yield, DPH shows slight variations in the lipid chains organisations. When the probe-containing liposomes are irradiated with UV-light at a fixed wavelength and polarised light level, the probe is excited and then emits light that is partially depolarised, because of the molecular rotations of the probe. This depolarisation is measured as a numerical value of anisotropy (*r*), after Equation. 8.1.

$$r = \frac{G * I_{\parallel} - I_{\perp}}{G * I_{\parallel} + 2I_{\perp}} \qquad \textbf{Equation 8.1}$$

where G is an intrinsic parameter of the spectrometer, and $I_{||}$ and $I_{\perp}$ are the intensities of the emitted light parallel and perpendicular to the plane of excitation, respectively.[418,479]

Following the protocol from Luciani Research Group[479], 10 µg/mL of DPH were solved in THF and stored at −20 °C, protected from light. For the analysis, 1 mL of liposome formulation (100 µM) was mixed with DPH stock solution in a molar ratio 1/330 DPH:lipid. After 30 min of incubation time at 37 °C and 300 rpm, 200 µL was transferred into a black 96-well plate (BRAND, Wertheim, Germany). After two additional shaking steps (orbital, 5 s), fluorescent anisotropy was determined by means of an Infinite 200 Pro F-Plex plate reader (Tecan, Männedorf, Switzerland) equipped with λ_{ex} = 360 ± 35 nm and λ_{em} = 430 ± 20 nm broad-pass filters at 25 and 37 °C. Apparent microviscosity ($\overline{\eta}$) was calculated after anisotropy measurements by **Equation 5.2**.

8.2.13 pH measurements

The determination of pH was conducted using a pH meter that measured the potential along a fine glass membrane separating two solutions with distinct proton concentrations. The pH measurements were conducted in a sensION™+ MM340 from HACH®, previously calibrated with HACH pH buffer solutions.

8.2.14 Conductimetry

The samples' conductivity was measured at 25 °C to analyse conductivity changes along with increasing concentrations of the **Ls** and **Pt-Ls** to relate it with their self-organisation, if happening. The employed instrument was an EC meter GLP 31 with a conductivity cell 50 70, universal with Pt 1000 sensor from Crison instruments, S. A.

8.2.15 Pendant drop method

The pendant drop method analyses optically the profile of a drop hanging from a needle along time and through it, the surface tension is measured. It is based on the Young-Laplace equation that associates the pressure across an interface, its curvature and the interfacial tension.[320] The method was performed in *Institut de Quimica Avançada de Barcelona*, by means of a homemade pendant drop tensiometer previously reported.[313] The solution is placed at the extreme of a straight-cut Teflon tube with 0.8 and 1.58 mm internal and external diameter, respectively. The drop profile was extracted from the images recorded using a web cam (640 x 480 pixels), corrected for spherical aberration, and subtracting the background. The contour of the drop was obtained at the maximum slope of the intensity and fitted to Young-Laplace equation using a self-prepared golden section search algorithm.[480] Temperature was set at 25 °C, to prevent drop evaporation during measurements the atmosphere humidity was saturated. Surface tension measurements for Milli-Q water were in the range of 70 ± 2.0 mN/m, in agreement with published data.[313]

8.2.16 Computational details in Density Functional Theory

To investigate the electronic transitions recorded in the UV-Vis of the complexes, computational methods have been employed to calculate the geometry and the main electronic transitions of **Pt-L10**, which was used as model to understand the occurring transitions observed in the complex family

Theoretical calculations of **Pt-L10** have been performed with Gaussian09 software version D.01.[481] Ground state (GS) geometry optimisation and vertical absorptions from electronically

excited states were computed using Density Functional Theory (DFT) and Time-Dependent Density Functional (TD-DFT), respectively. All of them were calculated using PBE functional[482] with LanL2DZ[483] basis set for Pt, C, H, N, O, S, Na and I atoms. Water solvation effects were incorporated using the polarizable continuum model-Linear Response (PCM-LR). Frequencies of the optimized structure were computed to ensure that geometry corresponds to an energy minimum. The first 180 vertical absorptions from the ground state to the excited states were calculated and only the most probable transitions (higher *f* values) have been selected for the Natural Transition Orbitals (NTOs) analysis. The shift in the theoretical absorption spectra with respect to the experimental is within the range of typical TD-DFT calculations (~0.3 eV) and is produced by computing absorptions as vertical transitions.[484] Simulated UV-vis spectrum was generated from TD-DFT calculation using GaussSum 3.0[485] and then plotted with OriginPro 2019b. Since the understanding and identification of electronic transitions as canonical orbitals is usually intricated, the use of NTOs[486] provides a useful tool to evaluate the predominant contributions of Molecular Orbitals (MOs) on them. NTOs of the selected transitions have been calculated using an isovalue of 0.02.[487]

8.2.17 Small and wide-angle X-ray scattering (SAXS-WAXS)

Small-angle X-ray spectroscopy (SAXS) is a method to obtain structural information on particles system in the nanoscale, such as maximum dimensions, repeating distances, or conformational diversities. For it, the elastic scattering of X-rays when transmitted through the sample is recorded, and so particles analysed by SAXS must present an electron density differing from that of its surrounding. SAXS is a non-destructive technique that only requires a small amount of sample to be measured in a glass or quartz capillary.

As described by Bragg's law, the X-ray diffraction pattern depends on the angle between the incident radiation and the scattered X-rays (θ), and the frequency of the incident radiation (frequency of employed X-ray radiation). Thus, to normalise it to distinct X-ray fonts, the dispersion vector modulus, q value, is defined to standardise the angle and the wavelength.[488]

$$\lambda = \frac{2d}{sin\theta}$$ **Equation 8.2** Bragg's law

$$q = \frac{4sin\theta}{\lambda}$$ **Equation 8.3** Normalisation of θ vs λ

The typical θ angles in SAXS measurement range from 0.1 to 10°. The diffraction intensity at each q value (q is the normalised value of angles with respect to the X-ray wavelengths) is

proportional to the electron density of the sample at each point of space. Hence, samples composed by materials with high atomic number, and so with higher electronic densities, will show higher contrast and lower detection limits. To acquire information from SAXS data, the obtained plot is fitted to theoretical models considering the sample characteristics.[329,489]

In contrast wide-angle X-ray scattering (WAXS) analyses the scattering patterns at high θ angles, which allows the determination of short distances corresponding to the internal structure of the material such as the interatomic or interplanar distances of crystallites.

Initial SAXS measurements of **Pt-L10** solubilised in water at 5 and 10 mM were performed in in *Institut de Quimica Avançada de Barcelona* in a Kratky compact camera of small-angle (Hecus X-ray Systems, Graz) coupled to a Siemens KF 760 (3 KW) generator. Nickel-filtered radiation with a wavelength corresponding to the Cu KR line (1.542 A˚) was used and the collimation system produces a line beam. The linear detector was a PSD-OED50M-Braun, and the temperature controller was a Peltier KPR (AntonPaar, Graz). Samples were introduced amongst two Mylar sheets with a 1 mm distance. The SAXS scattering curves are shown as a function of the scattered vector modulus (q).

For the experiments performed in the NCD-Sweet beamline at Synchrotron ALBA, the detector was located at 2725.36 mm distance, using a radiation wavelength of 0.0099987 nm. All the liquid samples were introduced in a 1 mm diameter capillary. In the synchrotron, the intensity of the X-ray beam can cause damage to the samples, which is usually controlled by applying repetitive short exposures times. The background of the corresponding solution and scans number was subtracted. A linear position detector was employed. It smears the spectra by the deconvolution of the scattered beam with the detector width, which has been considered for model fitting. SAXS experiments were calibrated with silver behenate. The holder was thermostated at 25 °C with a chiller (Accel 250 LC, Thermo Scientific) during all the experiments. For the experiment **Ls** and **Pt-Ls** samples were measured in solid or solved in Milli-Q water, PBS or NaOH solution 10 mM, depending on the necessities. Analysed **MTL** were prepared in PBS.

8.2.18 Differential scanning calorimetry (DSC)

Differential scanning calorimetry (DSC) is a thermoanalytical technique that measures the amount of heat needed to modify the temperature of a sample at a specified heating or cooling rate, in comparison with that of an unfilled crucible.[138] The heat flow associated with lipid

phase transition and interaction of **Pt-L10** with the phospholipid membrane were studied using a DSC 250 (TA Instruments, New Castle, USA) with TRIOS software. Multilamellar liposomes were produced in PBS at 50 mM of lipid and the corresponding concentration of **Pt-L10** for 330/1, 100/1, and 10/1 samples. The weighted amount of each sample (between 15-20 µL) was transferred in a Tzero aluminum pan (TA Instruments, New Castle, USA) and hermetically sealed. A similar PBS volume was used in the reference pan. The heating rate employed was 2 °C/min and N_2 flux was set at 50 mL/min and the scanned temperature ranged varied for each phospholipid. Two to three cycles were performed and the last one was used for the thermal profile evaluation.

8.2.19 Cell viability assays

8.2.19.1 Cell viability assays performed in IBB

Human ovarian carcinoma cell line A2780 (ECACC 93112519) was routinely maintained in Roswell Park Memorial Institute Medium (RPMI 1640, Gibco) supplemented with 10% heat-inactivated Foetal Bovine Serum (FBS), GlutaMAX™ (Gibco) and 1% Antibiotic-Antimycotic (Gibco), in standard growth conditions (37 ºC and 5% CO_2). Human cervix adenocarcinoma cell line HeLa (ATCC CCL-2™) was routinely maintained in Minimum Essential Medium α (MEM α) without nucleosides (Gibco) supplemented with 10% heat-inactivated FBS, GlutaMAX™ (Gibco) and 1% Antibiotic-Antimycotic (Gibco), in standard growth conditions. Human lung carcinoma cell line A549 (86012804) was routinely maintained in Dulbecco's Modified Eagle Medium (DMEM, Gibco) supplemented with 10% heat-inactivated Foetal Bovine Serum (FBS), GlutaMAX™ (Gibco) and 1% Antibiotic-Antimycotic (Gibco), in standard growth conditions (37 ºC and 10% CO_2). Stock solutions for **Ls** and **Pt-Ls** were prepared in Milli-Q water, while **MTL** were used as prepared, correcting the PBS amount in each well.

Cells of each cell line in exponential growth were plated in 96-well plates at a density of $5{\cdot}10^3$, $2{\cdot}10^3$, $3{\cdot}10^3$ cells/well for A2780, HeLa and A549 cell lines, respectively. They were allowed to grow overnight, and after that, cells were treated with different concentrations of each compound, ranging from 2 to 200 µM, during 72 h for **Ls** and **Pt-Ls**. For the **MTL** the concentrations ranged from 200 to 1500 µM of plain liposomes and 2 to 15 µM of **Pt-L10** for 24 and 72 h of treatment. Then, each well was emptied and 100 µL of PrestoBlue reagent (Invitrogen) at a 1:20 dilution in the corresponding medium was added following the standard protocol.[487] After 3 h incubation, fluorescence was measured exciting at 531 nm (emission at

572 nm) using a Victor3 multiwell microplate reader (Perkin Elmer). The relative cell viability (%) for each sample related to the control cells without treatment was calculated. Each sample was tested in triplicates, in two (**Ls**) or three (**Pt-Ls** and **MTL**) independent experiments.

8.2.19.2 Cell viability assays performed in Luciani Research Group

Human hepatocellular carcinoma cell line, Huh-7 cells (RRID: CVCL_0336) were grown at 37 °C in a humidified atmosphere containing 5% CO_2 in DMEM low glucose medium (Carl Roth) supplemented with 1% v/v penicillin/streptomycin mixture (penicillin: 10.000 U/mL, streptomycin: 10.000 µg/mL, Gibco), 2% v/v of L-glutamine (Gibco), and 10% v/v FBS (Merk Millipore). For the cell viability assay medium was serum-free. **MTL** (100/1 – lipid:**Pt-L10** molar ratio) and **Pt-L10** solutions in PBS were diluted in cell medium without FBS at the defined concentration. Cells in exponential growth were plated in 96-well plates at a density of $12.5 \cdot 10^3$ cells/well and let to grow overnight. Cells were treated for 6 and 24 h with defined concentrations of each sample. The cell viability was assayed using the Cell Counting Kit-8 (CCK8; Sigma Aldrich) containing a highly water-soluble tetrazolium salt (WST-8) that upon reduction produces a yellow dye directly proportional to the number of living cells. Before adding the CCK8 solution, cells were washed with PBS. The cells were incubated for the further 2 h at 37 °C, 5% CO_2 with 100 µL/well of CCK8 reagent (90 µL serum-free cell medium + 10 µL CCK8). Absorbance at 450 nm was measured on a Tecan Infinite 200 Pro MNano plate reader (Tecan, Männedorf, Switzerland). The relative cell metabolic activity (%) for each sample related to the control cells without treatment was calculated. The following **Equation 8.4** was used to calculate:

$$Cell\ metabolic\ activity\ (\%) = \left(\frac{OD\ sample}{OD\ control}\right) x\ 100 \qquad \textbf{Equation 8.4}$$

Where “OD sample” refers to the optical density of the cells treated with the substances and “OD control” is the cells exposed only to the serum-free cell medium. Each sample was tested in triplicates, in three independent experiments.

8.2.20 Release study

From the initial lipid to Pt molar ratio of 100/1 (DOPC:**Pt-L10**, DMPC:**Pt-L10**, DSPC:**Pt-L10** and SPC:**Pt-L10**) 500 µL were placed in a pre-swelled dialysis bag closed with two dialysis clamps (Pre-wetted RC Tubing MWCO: 25 kDa, Spectra/Por® 6 Dialysis Membrane, Spectrum Laboratories, Inc.). Then, the dialysis bags were introduced to 100 mL of PBS bath already heated at 37 °C. The sampling was conducted taking 500 µL from the bath at the defined time

and replaced with the same volume of PBS. Samples were taken at time 0, 0.25, 0.5, 1, 3, 6, 10, 25 and 48 h. Finally, the samples were stored in the freezer until analysed by ICP-MS (ICP-MS 7900, Agilent), the samples were diluted with HCl 1 % (v/v) before injection.

The experiment was designed considering that the minimum platinum concentration would be $2.5 \cdot 10^{-4}$ mM in PBS, and if a 50% of the platinum was released the measured platinum concentration, corrected with PBS density, will be 23.8 ppb, suitable for ICP-MS determination.

8.2.21 Data treatment

All the plots and data treatment throughout the thesis have been generated employing OriginPro 2019b software unless specified differently.

8.3 Synthetical procedures and methodologies

8.3.1 Synthesis of alkyl amino sulfonate ligands

The corresponding dibromoalkane (69.62 mmol) and potassium phthalimide (34.82 mmol) were mixed in DMF (80 mL) to react under stirring at room temperature during 18 h. Then, acetone was added to precipitate the KBr, and was removed by filtration. The solution was dried under reduced pressure and the obtained solid or oil was purified by silica gel column chromatography with hexane:AcOEt 10/1 (v/v) to obtain a white solid. The solid (21.25 mmol) and Na_2SO_3 (43.16 mmol) were solved in H_2O:EtOH 3/2 (v/v) (205 mL) and allowed to react with stirring at 95 °C for 20 h. The solution was dried under reduced pressure and the obtained residue was solved in H_2O and washed three times with AcOEt. The aqueous layer was isolated and dried under reduced pressure. HCl (37%, 75 mL) was added to the solid and allowed to react with stirring at 110 °C for 18 h. The obtained solution was diluted with H_2O and dried under reduced pressure to obtain a yellow solid. The solid was washed with acetone to obtain a white solid and finally was recrystallised in H_2O:EtOH 50/50 v/v. The final yield for **L2** was 57%; being 61% after the silica gel column chromatography, 88% after the sulfonation, 117% after the HCl cleavage (due to the presence of salts) and 90% in the purification process. The final yield for **L6** was 46%; being 58% after the silica gel column chromatography, 106% after the sulfonation (due to the presence of salts), 95% after the HCl cleavage and 78% in the purification process. The final yield for **L10** was 28%; being 56% after the silica gel column chromatography, 82% after the sulfonation, 77% after the HCl cleavage and 80% in the purification process.

^{1}H NMR for 2-aminoethanesulfonate (400 MHz, D_2O) δ: 3.44 (t, 2H), 3.27 (t, 2H). ^{13}C NMR (100 MHz, D_2O) δ: 36.48, 53.21. HR-MS (ESI(-), H_2O) for [**L2**]-Na^+ = 124.0071 (theoretical = 124.0073).

^{1}H NMR for 6-aminoethanesulfonate (400 MHz, D_2O) δ: 1.48 (m, 4H), 1.74 (m, 4H), 2.94 (t, 2H), 3.03 (t, 2H). ^{13}C NMR (100 MHz, D_2O) δ: 23.65, 25.00, 26.34, 26.96, 39.99, 50.74. HR-MS (ESI(-), H_2O) for [**L6**]-Na^+ = 180.0691 (theoretical = 180.0699).522

^{1}H NMR for 10-aminodecanesulfonate (400 MHz, D_2O) δ: 1.32-1.42 (m, 14H), 1.74 (m, 2H), 2.61 (t, 2H), 2.91 (t, 2H). ^{13}C NMR (100 MHz, D_2O) δ: 24.32, 26.37, 28.04, 28.55, 28.75, 28.84, 28,92, 31.68, 40.85, 51.47 .HR-MS (ESI(-), H_2O) for [**L10**]-Na^+ = 236.1318 (theoretical = 236.1325).

8.3.2 Synthesis of *cis*-[PtL_2I_2] (L = L2, L6, L10)

K_2PtCl_4 (100 mg, 0.24 mmol) was solved in 2 mL of degassed Milli-Q water and treated with 1 mL degassed solution of 5 eq. of KI (199 mg, 1.2 mmol). The solution was stirred at room temperature under inert atmosphere for 30 min or until a colour change was observed. In a second Schlenk 2 eq. (0.48 mmol) of the corresponding ligand and 2.05 eq. (0.492 0 mmol) of NaOH were solved in 3 ml of degassed water. Then, the K_2PtI_4 solution was added dropwise to the ligand solution. It was stirred at room temperature under inert atmosphere for 6-7 h (until the yellow solution has darkened). Subsequently, the solution was evaporated directly in the line or lyophilised until dryness. At that point, the formation of metallic Pt was visible. The mixtures of solids were solved in hot MeOH and filtered several times to get rid of Pt(0) to finally be dried over reduced pressure. The calculated yields were greater than 100% in **Pt-L2** and **Pt-L6** due to the presence of salts. For **Pt-L10** the calculated yield was 65%; the yellow solid was solved in H_2O and purified through a C18 silica column, eluted with water and MeOH, respectively. The MeOH fraction that contained the final complex was evaporated to obtain a fine yellow solid. C18 silica column purification yield was 41%. In some cases, if organic by-products were observed, further filtration through celite was performed. After getting rid of Pt(0), **Pt-L2** and **Pt-L6** where directly solved in MeOH and filtrated through celite, obtaining a yield after the purification of 70% and 83% for **Pt-L2** and **Pt-L6**, respectively.

^{1}H NMR for *cis*-[Pt(**L2**)$_2$I$_2$] (400 MHz, D_2O) δ: 3.22 (m, 2H), 3.30 (m, 2H). ^{13}C NMR (100 MHz, D_2O) δ: 42.15, 54.45. MS (ESI(-), H_2O) for [**Pt-L2**]$^-$-Na^+ = 719.77 (theoretical = 719.78).

^{1}H NMR for *cis*-[Pt(**L6**)$_2$I$_2$] (400 MHz, D_2O) δ: 1.39 (m, 8H), 1.57-1.68 (m, 8H), 2.86 (m, 8H). ^{13}C NMR (100 MHz, D_2O) δ: 23.86, 25.34, 27.29, 30.36, 46.75, 50.99. HR-MS (ESI(-), H_2O) for [**Pt-L6**]$^-$-Na$^+$ = 831.9011 (theoretical = 831.9034).

^{1}H NMR for *cis*-[Pt(**L10**)$_2$I$_2$] (400 MHz, D_2O) δ: 1.33-1.67 (m, 24H), 1.67-1.74 (m, 8H), 2.91 (m, 4H), 3.00 (m, 4H). ^{13}C NMR (100 MHz, D_2O) δ: 23.86, 25.63, 27.65, 28.11, 28.15, 28.34, 28.38, 30.47, 46.73, 54.05. HR-MS (ESI(-), H_2O) for [**Pt-L10**]$^-$-Na$^+$ = 944.0276 (theoretical = 944.0283).

8.3.3 Liposome preparation

8.3.3.1 Protocol in the study of platinum metallosomes feasibility

Liposomes and MTL were prepared by means of the Thin Lipid Method. Initially, phospholipids were solved in $CHCl_3$/MeOH 2:1 v/v. The appropriate volume of solution is taken and placed in a round bottom flask. For the so-called method B, in which the thin film is prepared as a mixture of **Pt-L10** and the phospholipids, in this step **Pt-L10** in MeOH solution is also added. The homogenous solution is evaporated under vacuum to obtain a thin film and is placed on a desiccator overnight. Following, the film is hydrated: in our case using Milli-Q water for Method B, or **Pt-L10** in Milli-Q water at the desired concentration for Method A. The suspension is vortexed for 30 s and placed in an orbital centrifuge at 1400 rpm, vortexing the solution every 5-10 min during 2 h. With this protocol, mainly MLV are obtained, which can be size and lamellarity reduced and homogenised with complementary techniques.

Manual extrusion was performed at *Unitat de Biofísica*, when needed, to obtain the desired liposome sizes. A membrane with the adequate pore size is located in the manual extruder and using a syringe the dispersion is passed through it at least 6 times. Usually, in the process several membranes, from bigger to smaller pore sizes, must be employed until reaching the final pore size. For phospholipid concentrations greater than 5 mM, the employed method to reduce the size and multilamellarity of the vesicles was sonication. Two cycles of 1 minute sonication at 35% in a Dynatech instrument were employed.

8.3.3.2 Protocol in the improvement of metallosomes formulation

Stock lipid solution were prepared in $CHCl_3$ by weighing the appropriate mass dry lipids and were stored in the freezer under inert gas. The suitable volume of solubilised lipid is taken and added to a vial. At this point, if **MTL** are being produced the needed amount of **Pt-L10**, which has been previously solubilised in MeOH, is added to the vial and both solutions are slightly

mixed. The solvents are removed with inert gas and placed on the desiccator overnight (< 100 mbar). Then, the film is hydrated with the appropriate amount of pre-filtered PBS buffer solution (filtered through a polycarbonate filter of 0.22 µm). The mixture is vortexed for 30 s and put in a water bath for 5 minutes. The temperature of the water bath is 30 ± 5 °C for SPC and DOPC, 35 ± 5 °C for DMPC and 70 ± 5 °C for DSPC. This operation is repeated, and the sample is vortexed at the end. It must be assured that all the film has been completely removed from the walls before proceeding. Subsequently, the solution is transferred to a falcon or Eppendorf tube (depending on the volume) and six freeze-thaw cycles are performed. The solution is freeze using liquid N_2 (~ 1 min) and then placed in a water bath (temperature will be set in accordance with the employed lipid, ~ 5 min). The whole process is repeated six times. Finally, the liposomes are extruded ten times above the phase transition temperature of each lipid in a LIPEX extruder (Evonik, Canada) with 2 polycarbonate membranes of the appropriated pore size (Whatman Nucleopore, Maidstone, UK). The whole process is represented in the next **Scheme 8.1**.

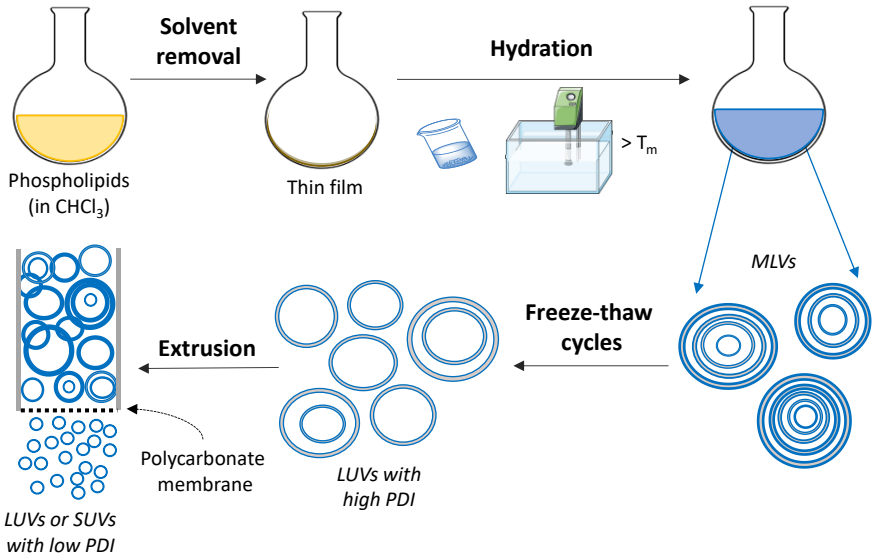

Scheme 8.1 Representation of the method followed for the preparation of MTL.

8.3.4 Size-exclusion chromatography for metallosomes purification

To test the use of Sephadex™ columns as liposomes' purification method liposomes and a **Pt-L10** solution were run through the column independently. For that, 1.5 mM SPC liposomes extruded 5 times at 800 nm, were passed through Sephadex™ G-25 resin (PD-10 column, Cytvia) and collected in several fractions of 1 mL. Each fraction was analysed by UV-vis and its absorption at 470 nm was recorded. As expected for 800 nm size liposomes, they go out

between fractions 3 - 6, with a maximum absorption found at fraction 4 (after the death volume). Then, **Pt-L10** solutions concentrations were 1.3 or 3 mM solutions in Milli-Q water, and after going through the column were also collected in 1 mL fractions. The collected fractions were measured by ICP-OES to ascertain in which fraction **Pt-L10** elutes. It was found that most of the complex flows out in fractions 7 to 12 for 1.3 mM. But for 3 mM **Pt-L10** coeluted with the 800 nm SPC liposomes.

8.3.5 Centrifugation of liposomes

To separate the obtained **MTL** from the supernatant and quantify the non-internalised Pt by ICP, **MTL** were centrifugated at 16800 rcf during 15 min by means of a standard on desk centrifuge. To avoid the remining of smaller vesicles, further on the **MTL** were ultracentrifugated in a SORVALL Discovery M150 SE at 16000 rcf for 1 h, approximately 250 µL ultracentrifugated samples were obtained from a total of 750 µL. Both instruments are from *Unitat de Biofísica* at the UAB.

8.3.6 Breaking liposomes for Pt quantification

For the Pt determination before and after the extrusion process, liposomes were broken following a common method. For it, 25 µL of liposomes were added to 25 µL of 1:1 volume with 10% (w/w) TritonX-100 and stirred for 5 minutes. Then, the solutions were analysed by ICP-MS.

9. BIBLIOGRAPHY

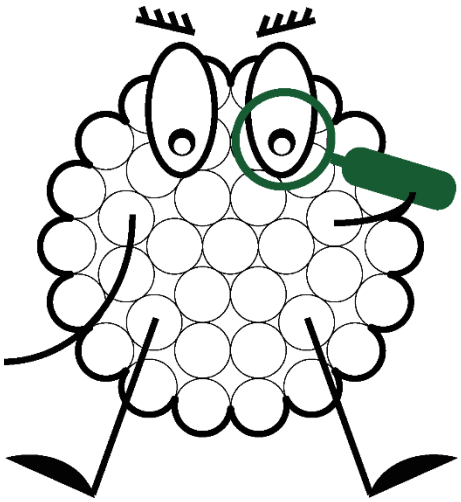

(1) Sung, H.; Ferlay, J.; Siegel, R. L.; Laversanne, M.; Soerjomataram, I.; Jemal, A.; Bray, F. Global Cancer Statistics 2020: GLOBOCAN Estimates of Incidence and Mortality Worldwide for 36 Cancers in 185 Countries. *CA Cancer J. Clin.* **2021**, *71* (3), 209–249. https://doi.org/10.3322/caac.21660.

(2) Bray, F.; Ferlay, J.; Soerjomataram, I.; Siegel, R. L.; Torre, L. A.; Jemal, A. Global Cancer Statistics 2018: GLOBOCAN Estimates of Incidence and Mortality Worldwide for 36 Cancers in 185 Countries. *CA Cancer J. Clin.* **2018**, *68* (6), 394–424. https://doi.org/10.3322/caac.21492.

(3) Cancer Statistics - National Cancer Institute https://www.cancer.gov/about-cancer/understanding/statistics (accessed 2021 -07 -02).

(4) Valastyan, S.; Weinberg, R. A. Tumor Metastasis: Molecular Insights and Evolving Paradigms. *Cell* **2011**, *147* (2), 275–292. https://doi.org/10.1016/j.cell.2011.09.024.

(5) de Bruce, A.; Johnson, Alexander Lewis, J.; Raff, M.; Roberts, K.; Walter, P. *Molecular Biology of the Cell*, 5th ed.; Garland Science, 2007.

(6) Hanahan, D.; Weinberg, R. A. The Hallmarks of Cancer Review. *Cell* **2000**, *100* (7), 57–70.

(7) Hanahan, D.; Weinberg, R. A. Hallmarks of Cancer: The next Generation. *Cell* **2011**, *144* (5), 646–674. https://doi.org/10.1016/j.cell.2011.02.013.

(8) Pavlova, N. N.; Thompson, C. B. The Emerging Hallmarks of Cancer Metabolism. *Cell Metab.* **2016**, *23* (1), 27–47. https://doi.org/10.1016/j.cmet.2015.12.006.

(9) Vander Heiden, M. G.; DeBerardinis, R. J. Understanding the Intersections between Metabolism and Cancer Biology. *Cell* **2017**, *168* (4), 657–669. https://doi.org/10.1016/j.cell.2016.12.039.

(10) Liberti, M. V.; Locasale, J. W. The Warburg Effect: How Does It Benefit Cancer Cells? *Trends Biochem. Sci.* **2016**, *41* (3), 211–218. https://doi.org/10.1016/j.tibs.2015.12.001.

(11) Heiden, M. G. V.; Cantley, L. C.; Thompson, C. B. Understanding the Warburg Effect: The Metabolic Requirements of Cell Proliferation. *Science* **2009**, *324* (5930), 1029–1033. https://doi.org/10.1126/science.1160809.

(12) Chen, X.; Qian, Y.; Wu, S. The Warburg Effect: Evolving Interpretations of an Established Concept. *Free Radic. Biol. Med.* **2015**, *79*, 253–263. https://doi.org/10.1016/j.freeradbiomed.2014.08.027.

(13) Finicle, B. T.; Jayashankar, V.; Edinger, A. L. Nutrient Scavenging in Cancer. *Nat. Rev. Cancer* **2018**, *18* (10), 619–633. https://doi.org/10.1038/s41568-018-0048-x.

(14) Yoshida, G. J. Metabolic Reprogramming: The Emerging Concept and Associated Therapeutic Strategies. *J. Exp. Clin. Cancer Res.* **2015**, *34* (1), 1–10. https://doi.org/10.1186/s13046-015-0221-y.

(15) Spranger, S.; Gajewski, T. F. Impact of Oncogenic Pathways on Evasion of Antitumour Immune Responses. *Nat. Rev. Cancer* **2018**, *18* (3), 139–147. https://doi.org/10.1038/nrc.2017.117.

(16) Carmona-Fontaine, C.; Bucci, V.; Akkari, L.; Deforet, M.; Joyce, J. A.; Xavier, J. B. Emergence of Spatial Structure in the Tumor Microenvironment Due to the Warburg Effect. *PNAS USA* **2013**, *110* (48), 19402–19407. https://doi.org/10.1073/pnas.1311939110.

(17) San-Millán, I.; Brooks, G. A. Reexamining Cancer Metabolism: Lactate Production for Carcinogenesis Could Be the Purpose and Explanation of the Warburg Effect. *Carcinogenesis* **2017**, *38* (2), 119–133. https://doi.org/10.1093/carcin/bgw127.

(18) Devic, S. Warburg Effect - a Consequence or the Cause of Carcinogenesis? *J. Cancer* **2016**, *7* (7), 817–822. https://doi.org/10.7150/jca.14274.

(19) Danhier, P.; Bański, P.; Payen, V. L.; Grasso, D.; Ippolito, L.; Sonveaux, P.; Porporato, P. E. Cancer Metabolism in Space and Time: Beyond the Warburg Effect. *Biochim. Biophys. Acta - Bioenerg.* **2017**, *1858* (8), 556–572. https://doi.org/10.1016/j.bbabio.2017.02.001.

(20) Fidler, I. J. Tumor Heterogeneity and the Biology of Cancer Invasion and Metastasis. *Cancer Res.* **1978**, *38* (9), 2651–2660.

(21) Fidler, I. J. Commentary on "Tumor Heterogeneity and the Biology of Cancer Invasion and Metastasis." *Cancer Res.* **2016**, *76* (12), 3441–3442. https://doi.org/10.1158/0008-5472.CAN-16-1330.

(22) Lambert, A. W.; Pattabiraman, D. R.; Weinberg, R. A. Emerging Biological Principles of Metastasis. *Cell* **2017**, *168* (4), 670–691. https://doi.org/10.1016/j.cell.2016.11.037.

(23) Gupta, G. P.; Massagué, J. Cancer Metastasis: Building a Framework. *Cell* **2006**, *127* (4), 679–695. https://doi.org/10.1016/j.cell.2006.11.001.

(24) The Cell editorial team. Cancer: The Road Ahead. *Cell* **2017**, *168* (4), 545–546. https://doi.org/10.1016/j.cell.2017.01.036.

(25) Jin, K.; Li, T.; van Dam, H.; Zhou, F.; Zhang, L. Molecular Insights into Tumour Metastasis: Tracing the Dominant Events. *J. Pathol.* **2017**, *241* (5), 567–577. https://doi.org/10.1002/path.4871.

(26) Geiger, T. R.; Peeper, D. S. Metastasis Mechanisms. *Biochim. Biophys. Acta* **2009**, *1796* (2), 293–308. https://doi.org/10.1016/j.bbcan.2009.07.006.

(27) Klein, C. A. The Metastasis Cascade. *Science* **2008**, *321*, 1785–1787. https://doi.org/10.1126/science.1164853.

(28) Hosseini, H.; Obradovic, M. M. S.; Hoffmann, M.; Harper, K. L.; Sosa, M. S.; Werner-Klein, M.; Nanduri, L. K.; Werno, C.; Ehrl, C.; Maneck, M.; Patwary, N.; Haunschild, G.; Guzvic, M.; Reimelt, C.; Grauvogl, M.; Eichner, N.; Weber, F.; Hartkopf, A. D.; Taran, F. A.; Brucker, S. Y.; Fehm, T.; Rack, B.; Buchholz, S.; Spang, R.; Meister, G.; Aguirre-Ghiso, J. A.; Klein, C. A. Early Dissemination Seeds Metastasis in Breast Cancer. *Nature* **2016**, *540*, 552–558. https://doi.org/10.1038/nature20785.

(29) Chung, A. S.; Lee, J.; Ferrara, N. Targeting the Tumour Vasculature: Insights from Physiological Angiogenesis. *Nat. Rev. Cancer* **2010**, *10* (7), 505–514. https://doi.org/10.1038/nrc2868.

(30) Magalhães, A.; Dias, S. Angiogenesis – Vessels Recruitment by Tumor Cells. In *Molecular and cell biology of cancer When cells break the rules and hijack their own planet*; Fior, R., Zilhão, R., Eds.; Springer, Cham, 2019; pp 141–157. https://doi.org/10.1007/978-3-030-11812-9_8.

(31) Krock, B. L.; Skuli, N.; Simon, M. C. Hypoxia-Induced Angiogenesis: Good and Evil. *Genes Cancer* **2011**, *2* (12), 1117–1133. https://doi.org/10.1177/1947601911423654.

(32) Kratz, F.; Senter, P. Limits of Conventional Cancer Chemotherapy. In *Drug Delivery in Oncology: From Basic Research to Cancer Therapy*; Kratz, F., Senter, P., Steinhagen, H., Eds.; Wiley-VCH, 2012; pp 1–31. https://doi.org/10.1002/9783527634057.ch1.

(33) DeVita, V. T.; Rosenberg, S. A. Two Hundred Years of Cancer Research. *N. Engl. J. Med.* **2012**, *366* (23), 2207–2214. https://doi.org/10.1056/nejmra1204479.

(34) DeVita, V. T.; Chu, E. A History of Cancer Chemotherapy. *Cancer Res.* **2008**, *68* (21), 8643–8653. https://doi.org/10.1158/0008-5472.CAN-07-6611.

(35) Chabner, B. A. Barnett Rosenberg: In Memoriam (1924–2009). *Cancer Res.* **2010**, *70* (1), 428–429. https://doi.org/10.1158/0008-5472.can-09-4146.

(36) Rosenberg, B.; VanCamp, L.; Trosko, J. E.; Mansour, V. H. Platinum Compounds: A New Class of Potent Antitumour Agents. **1969**, *222*, 385–386. https://doi.org/10.1038/222385a0.

(37) Grimley, E. Discovery and Identification of the First Platinum Anticancer Compound. *Inorganica Chim. Acta* **2019**, *495* (April), 1–5. https://doi.org/10.1016/j.ica.2019.118986.

(38) Browning, R. J.; Reardon, P. J. T.; Parhizkar, M.; Pedley, R. B.; Edirisinghe, M.; Knowles, J. C.; Stride, E. Drug Delivery Strategies for Platinum-Based Chemotherapy. *ACS Nano* **2017**, *11* (9), 8560–8578. https://doi.org/10.1021/acsnano.7b04092.

(39) Johnstone, T. C.; Suntharalingam, K.; Lippard, S. J. The Next Generation of Platinum Drugs: Targeted Pt(II) Agents, Nanoparticle Delivery, and Pt(IV) Prodrugs. *Chem. Rev.* **2016**, *116* (5), 3436–3486. https://doi.org/10.1021/acs.chemrev.5b00597.

(40) Zoroddu, M. A.; Aaseth, J.; Crisponi, G.; Medici, S.; Peana, M.; Nurchi, V. M. The Essential Metals for

Humans: A Brief Overview. *J. Inorg. Biochem.* **2019**, *195*, 120–129. https://doi.org/10.1016/j.jinorgbio.2019.03.013.

(41) Anthony, E. J.; Bolitho, E. M.; Bridgewater, H. E.; Carter, O. W. L.; Donnelly, J. M.; Imberti, C.; Lant, E. C.; Lermyte, F.; Needham, R. J.; Palau, M.; Sadler, P. J.; Shi, H.; Wang, F. X.; Zhang, W. Y.; Zhang, Z. Metallodrugs Are Unique: Opportunities and Challenges of Discovery and Development. *Chem. Sci.* **2020**, *11* (48), 12888–12917. https://doi.org/10.1039/d0sc04082g.

(42) Boros, E.; Dyson, P. J.; Gasser, G. Classification of Metal-Based Drugs According to Their Mechanisms of Action. *Chem* **2020**, *6* (1), 41–60. https://doi.org/10.1016/j.chempr.2019.10.013.

(43) Mjos, K. D.; Orvig, C. Metallodrugs in Medicinal Inorganic Chemistry. *Chem. Rev.* **2014**, *114* (8), 4540–4563. https://doi.org/10.1021/cr400460s.

(44) Fanelli, M.; Formica, M.; Fusi, V.; Giorgi, L.; Micheloni, M.; Paoli, P. New Trends in Platinum and Palladium Complexes as Antineoplastic Agents. *Coord. Chem. Rev.* **2016**, *310*, 41–79. https://doi.org/10.1016/j.ccr.2015.11.004.

(45) Cai, L.; Yu, C.; Ba, L.; Liu, Q.; Qian, Y.; Yang, B.; Gao, C. Anticancer Platinum-Based Complexes with Non-Classical Structures. *Appl. Organomet. Chem.* **2018**, *32* (4), 1–17. https://doi.org/10.1002/aoc.4228.

(46) Walker, E. M.; Walker, S. M. Evolution of Chemotherapy with Platinum Compounds. *Ann. Clin. Lab. Sci.* **1999**, *29* (4), 263–274.

(47) Ghosh, S. Cisplatin: The First Metal Based Anticancer Drug. *Bioorg. Chem.* **2019**, *88*. https://doi.org/10.1016/j.bioorg.2019.102925.

(48) Gately, D. P.; Howell, S. B. Cellular Accumulation of the Anticancer Agent Cisplatin: A Review. *Br. J. Cancer* **1993**, *67* (6), 1171–1176. https://doi.org/10.1038/bjc.1993.221.

(49) Howell, S. B.; Safaei, R.; Larson, C. A.; Sailor, M. J. Copper Transporters and the Cellular Pharmacology of the Platinum-Containing Cancer Drugs. *Mol. Pharmacol.* **2010**, *77* (6), 887–894. https://doi.org/10.1124/mol.109.063172.

(50) Egger, A. E.; Rappel, C.; Jakupec, M. A.; Hartinger, C. G.; Heffeter, P.; Keppler, B. K. Development of an Experimental Protocol for Uptake Studies of Metal Compounds in Adherent Tumor Cells. *J. Anal. At. Spectrom.* **2009**, *24* (1), 51–61. https://doi.org/10.1039/b810481f.

(51) Basu, A.; Krishnamurthy, S. Cellular Responses to Cisplatin-Induced DNA Damage. *J. Nucleic Acids* **2010**, *2010*. https://doi.org/10.4061/2010/201367.

(52) Ishida, S.; Lee, J.; Thiele, D. J.; Herskowitz, I. Uptake of the Anticancer Drug Cisplatin Mediated by the Copper Transporter Ctr1 in Yeast and Mammals. *PNAS* **2002**, *99* (22), 14298–14302. https://doi.org/10.1073/pnas.162491399.

(53) Massai, L.; Pratesi, A.; Gailer, J.; Marzo, T.; Messori, L. The Cisplatin/Serum Albumin System: A Reappraisal. *Inorganica Chim. Acta* **2019**, *495* (April), 1–7. https://doi.org/10.1016/j.ica.2019.118983.

(54) Rottenberg, S.; Disler, C.; Perego, P. The Rediscovery of Platinum-Based Cancer Therapy. *Nat. Rev. Cancer* **2021**, *21* (1), 37–50. https://doi.org/10.1038/s41568-020-00308-y.

(55) Nakano, T.; Morishita, S.; Katafuchi, A.; Matsubara, M.; Horikawa, Y.; Terato, H.; Salem, A. M. H.; Izumi, S.; Pack, S. P.; Makino, K.; Ide, H. Nucleotide Excision Repair and Homologous Recombination Systems Commit Differentially to the Repair of DNA-Protein Crosslinks. *Mol. Cell* **2007**, *28* (1), 147–158. https://doi.org/10.1016/j.molcel.2007.07.029.

(56) Nakano, T.; Katafuchi, A.; Matsubara, M.; Terato, H.; Tsuboi, T.; Masuda, T.; Tatsumoto, T.; Pil Pack, S.; Makino, K.; Croteau, D. L.; Van Houten, B.; Iijima, K.; Tauchi, H.; Ide, H. Homologous Recombination but Not Nucleotide Excision Repair Plays a Pivotal Role in Tolerance of DNA-Protein Cross-Links in Mammalian Cells. *J. Biol. Chem.* **2009**, *284* (40), 27065–27076. https://doi.org/10.1074/jbc.M109.019174.

(57) Wong, D. L.; Stillman, M. J. Capturing Platinum in Cisplatin: Kinetic Reactions with Recombinant Human Apo-Metallothionein 1a. *Metallomics* **2018**, *10* (5), 713–721. https://doi.org/10.1039/c8mt00029h.

(58) Kuo, M. T.; Chen, H. H. W. Role of Glutathione in the Regulation of Cisplatin Resistance in Cancer Chemotherapy. *Met. Based. Drugs* **2010**, *2010*. https://doi.org/10.1155/2010/430939.

(59) Okuno, S.; Sato, H.; Kuriyama-Matsumura, K.; Tamba, M.; Wang, H.; Sohda, S.; Hamada, H.; Yoshikawa, H.; Kondo, T.; Bannai, S. Role of Cystine Transport in Intracellular Glutathione Level and Cisplatin Resistance in Human Ovarian Cancer Cell Lines. *Br. J. Cancer* **2003**, *88* (6), 951–956. https://doi.org/10.1038/sj.bjc.6600786.

(60) Chen, S. H.; Chang, J. Y. New Insights into Mechanisms of Cisplatin Resistance: From Tumor Cell to Microenvironment. *Int. J. Mol. Sci.* **2019**, *20* (17), 1–21. https://doi.org/10.3390/ijms20174136.

(61) Stewart, D. J. Mechanisms of Resistance to Cisplatin and Carboplatin. *Crit. Rev. Oncol. Hematol.* **2007**, *63* (1), 12–31. https://doi.org/10.1016/j.critrevonc.2007.02.001.

(62) Galluzzi, L.; Senovilla, L.; Vitale, I.; Michels, J.; Martins, I.; Kepp, O.; Castedo, M.; Kroemer, G. Molecular Mechanisms of Cisplatin Resistance. *Oncogene* **2012**, *31* (15), 1869–1883. https://doi.org/10.1038/onc.2011.384.

(63) Dilruba, S.; Kalayda, G. V. Platinum-Based Drugs: Past, Present and Future. *Cancer Chemother. Pharmacol.* **2016**, *77*, 1103–1124. https://doi.org/10.1007/s00280-016-2976-z.

(64) Garattini, S. Pharmacokinetics in Cancer Chemotherapy. *Eur. J. Cancer* **2007**, *43* (2), 271–282. https://doi.org/10.1016/j.ejca.2006.10.015.

(65) Ruiz-garcia, A. N. A.; Bermejo, M.; Moss, A.; Casabo, V. G. Pharmacokinetics in Drug Discovery. *J. Pharm. Sci.* **2008**, *97* (2), 654–690. https://doi.org/10.1002/jps.21009.

(66) Liu, R.; Xiao, K.; Juntao Luo, J.; Lam, K. S. Development of Cancer-Targeting Ligands and Ligand-Drug Conjugates. In *Drug Delivery in Oncology: From Basic Research to Cancer Therapy*; Kratz, F., Senter, P., Steinhagen, H., Eds.; Wiley-VCH, 2012; pp 121–168. https://doi.org/10.1002/9783527634057.ch5.

(67) Chu, Y. H.; Sibrian-Vazquez, M.; Escobedo, J. O.; Phillips, A. R.; Dickey, D. T.; Wang, Q.; Ralle, M.; Steyger, P. S.; Strongin, R. M. Systemic Delivery and Biodistribution of Cisplatin in Vivo. *Mol. Pharm.* **2016**, *13* (8), 2677–2682. https://doi.org/10.1021/acs.molpharmaceut.6b00240.

(68) Oun, R.; Moussa, Y. E.; Wheate, N. J. The Side Effects of Platinum-Based Chemotherapy Drugs: A Review for Chemists. *Dalton Trans.* **2018**, *47* (19), 6645–6653. https://doi.org/10.1039/c8dt00838h.

(69) McWhinney, S. R.; Goldberg, R. M.; McLeod, H. L. Platinum Neurotoxicity Pharmacogenetics. *Mol. Cancer Ther.* **2009**, *8* (1), 10–16. https://doi.org/10.1158/1535-7163.MCT-08-0840.

(70) Introduction to Chemotherapy | SEER Training https://training.seer.cancer.gov/treatment/chemotherapy/ (accessed 2021 -07 -01).

(71) Xie, P.; Wang, Y.; Wei, D.; Zhang, L.; Zhang, B.; Xiao, H.; Song, H.; Mao, X. Nanoparticle-Based Drug Delivery Systems with Platinum Drugs for Overcoming Cancer Drug Resistance. *J. Mater. Chem. B* **2021**, *9*, 5173–5194. https://doi.org/10.1039/d1tb00753j.

(72) Jia, C.; Deacon, G. B.; Zhang, Y.; Gao, C. Platinum(IV) Antitumor Complexes and Their Nano-Drug Delivery. *Coord. Chem. Rev.* **2021**, *429*. https://doi.org/10.1016/j.ccr.2020.213640.

(73) Lin, Y. X.; Wang, Y.; An, H. W.; Qi, B.; Wang, J.; Wang, L.; Shi, J.; Mei, L.; Wang, H. Peptide-Based Autophagic Gene and Cisplatin Co-Delivery Systems Enable Improved Chemotherapy Resistance. *Nano Lett.* **2019**, *19* (5), 2968–2978. https://doi.org/10.1021/acs.nanolett.9b00083.

(74) Foulkes, R.; Man, E.; Thind, J.; Yeung, S.; Joy, A.; Hoskins, C. The Regulation of Nanomaterials and Nanomedicines for Clinical Application: Current and Future Perspectives. *Biomater. Sci.* **2020**, *8* (17), 4653–4664. https://doi.org/10.1039/d0bm00558d.

(75) Vega-Vásquez, P.; Mosier, N. S.; Irudayaraj, J. Nanoscale Drug Delivery Systems: From Medicine to Agriculture. *Front. Bioeng. Biotechnol.* **2020**, *8* (February), 1–16. https://doi.org/10.3389/fbioe.2020.00079.

(76) Sung, Y. K.; Kim, S. W. Recent Advances in Polymeric Drug Delivery Systems. *Biomater. Res.* **2020**, *24* (1),

1–12. https://doi.org/10.1186/s40824-020-00190-7.

(77) Bandopadhyay, S.; Manchanda, S.; Chandra, A.; Ali, J.; Deb, P. K. Overview of Different Carrier Systems for Advanced Drug Delivery. In *Drug Delivery Systems*; Tekade, R. K., Ed.; Elsevier Inc., 2019; pp 179–233. https://doi.org/10.1016/B978-0-12-814487-9.00005-3.

(78) Senapati, S.; Mahanta, A. K.; Kumar, S.; Maiti, P. Controlled Drug Delivery Vehicles for Cancer Treatment and Their Performance. *Signal Transduct. Target. Ther.* **2018**, *3* (1), 7. https://doi.org/10.1038/s41392-017-0004-3.

(79) Bertrand, N.; Wu, J.; Xu, X.; Kamaly, N.; Farokhzad, O. C. Cancer Nanotechnology: The Impact of Passive and Active Targeting in the Era of Modern Cancer Biology. *Adv. Drug Deliv. Rev.* **2014**, *66*, 2–25. https://doi.org/10.1016/j.addr.2013.11.009.

(80) Noble, G. T.; Stefanick, J. F.; Ashley, J. D.; Kiziltepe, T.; Bilgicer, B. Ligand-Targeted Liposome Design: Challenges and Fundamental Considerations. *Trends Biotechnol.* **2014**, *32* (1), 32–45. https://doi.org/10.1016/j.tibtech.2013.09.007.

(81) Maeda, H. Enhanced Permeability and Retention Effect in Relation to Tumor Targeting. In *Drug Delivery in Oncology: From Basic Research to Cancer Therapy*; Kratz, F., Senter, P., Steinhagen, H., Eds.; Wiley-VCH Verlag GmbH & Co, 2011; Vol. 1, pp 65–84. https://doi.org/10.1002/9783527634057.ch3.

(82) Cabral, H.; Matsumoto, Y.; Mizuno, K.; Chen, Q.; Murakami, M.; Kimura, M.; Terada, Y.; Kano, M. R.; Miyazono, K.; Uesaka, M.; Nishiyama, N.; Kataoka, K. Accumulation of Sub-100 Nm Polymeric Micelles in Poorly Permeable Tumours Depends on Size. *Nat. Nanotechnol.* **2011**, *6* (12), 815–823. https://doi.org/10.1038/nnano.2011.166.

(83) Farjadian, F.; Ghasemi, A.; Gohari, O.; Roointan, A.; Karimi, M.; Hamblin, M. R. Nanopharmaceuticals and Nanomedicines Currently on the Market: Challenges and Opportunities. *Nanomedicine (Lond).* **2019**, *14* (1), 93–126. https://doi.org/10.2217/nnm-2018-0120.

(84) Barrán-Berdón, A. L.; Pozzi, D.; Caracciolo, G.; Capriotti, A. L.; Caruso, G.; Cavaliere, C.; Riccioli, A.; Palchetti, S.; Laganaì, A. Time Evolution of Nanoparticle-Protein Corona in Human Plasma: Relevance for Targeted Drug Delivery. *Langmuir* **2013**, *29* (21), 6485–6494. https://doi.org/10.1021/la401192x.

(85) Sudimack, J. B. A.; Lee, R. J. Targeted Drug Delivery via the Folate Receptor. *Adv. Drug Deliv. Rev.* **2000**, *41*, 147–162. https://doi.org/10.1016/s0169-409x(99)00062-9.

(86) Akbarian, A.; Ebtekar, M.; Pakravan, N.; Hassan, Z. M. Folate Receptor Alpha Targeted Delivery of Artemether to Breast Cancer Cells with Folate-Decorated Human Serum Albumin Nanoparticles. *Int. J. Biol. Macromol.* **2020**, *152*, 90–101. https://doi.org/10.1016/j.ijbiomac.2020.02.106.

(87) Shegokar, R. Preclinical Testing—Understanding the Basics First. In *Drug Delivery Aspects*; Shegokar, R., Ed.; Elsevier Inc., 2020; pp 19–32. https://doi.org/10.1016/b978-0-12-821222-6.00002-6.

(88) Caracciolo, G. Liposome-Protein Corona in a Physiological Environment: Challenges and Opportunities for Targeted Delivery of Nanomedicines. *Nanomedicine: NMB* **2015**, *11* (3), 543–557. https://doi.org/10.1016/j.nano.2014.11.003.

(89) Ventola, C. L. Progress in Nanomedicine: Approved and Investigational Nanodrugs. *Pharmacol. Ther.* **2017**, *42* (12), 742–755.

(90) Palchetti, S.; Pozzi, D.; Capriotti, A. L.; Barbera, G. La; Chiozzi, R. Z.; Digiacomo, L.; Peruzzi, G.; Caracciolo, G.; Laganà, A. Influence of Dynamic Flow Environment on Nanoparticle-Protein Corona: From Protein Patterns to Uptake in Cancer Cells. *Colloids Surf B Biointerfaces* **2017**, *153*, 263–271. https://doi.org/10.1016/j.colsurfb.2017.02.037.

(91) Foulkes, R.; Man, E.; Thind, J.; Yeung, S.; Joy, A.; Hoskins, C. The Regulation of Nanomaterials and Nanomedicines for Clinical Application: Current and Future Perspectives. *Biomater. Sci.* **2020**, *8* (17), 4653–4664. https://doi.org/10.1039/d0bm00558d.

(92) Martins, J. P.; das Neves, J.; de la Fuente, M.; Celia, C.; Florindo, H.; Günday-Türeli, N.; Popat, A.; Santos, J. L.; Sousa, F.; Schmid, R.; Wolfram, J.; Sarmento, B.; Santos, H. A. The Solid Progress of Nanomedicine. *Drug Deliv. Transl. Res.* **2020**, *10* (3), 726–729. https://doi.org/10.1007/s13346-020-00743-2.

(93) Germain, M.; Caputo, F.; Metcalfe, S.; Tosi, G.; Spring, K.; Åslund, A. K. O.; Pottier, A.; Schiffelers, R.; Ceccaldi, A.; Schmid, R. Delivering the Power of Nanomedicine to Patients Today. *J. Control. Release* **2020**, *326* (July), 164–171. https://doi.org/10.1016/j.jconrel.2020.07.007.

(94) Mitragotri, S.; Anderson, D. G.; Chen, X.; Chow, E. K.; Ho, D.; Kabanov, A. V.; Karp, J. M.; Kataoka, K.; Mirkin, C. A.; Petrosko, S. H.; Shi, J.; Stevens, M. M.; Sun, S.; Teoh, S.; Venkatraman, S. S.; Xia, Y.; Wang, S.; Gu, Z.; Xu, C. Accelerating the Translation of Nanomaterials in Biomedicine. *ACS Nano* **2015**, *9* (7), 6644–6654. https://doi.org/10.1021/acsnano.5b03569.

(95) Zalba, S.; Garrido, M. J. Liposomes, a Promising Strategy for Clinical Application of Platinum Derivatives. *Expert Opin. Drug Deliv.* **2013**, *10* (6), 829–844. https://doi.org/10.1517/17425247.2013.778240.

(96) Odiba, A.; Ukegbu, C.; Anunobi, O.; Chukwunonyelum, I.; Esemonu, J. Making Drugs Safer: Improving Drug Delivery and Reducing the Side Effect of Drugs on the Human Biochemical System. *Nanotechnol. Rev.* **2016**, *5* (2), 183–194. https://doi.org/10.1515/ntrev-2015-0055.

(97) Li, C.; Wang, J.; Wang, Y.; Gao, H.; Wei, G.; Huang, Y.; Yu, H.; Gan, Y.; Wang, Y.; Mei, L.; Chen, H.; Hu, H.; Zhang, Z.; Jin, Y. Recent Progress in Drug Delivery. *Acta Pharm. Sin. B* **2019**, *9* (6), 1145–1162. https://doi.org/10.1016/j.apsb.2019.08.003.

(98) Ivanov, A. I.; Christodoulou, J.; Parkinson, J. A.; Barnham, K. J.; Tucker, A.; Woodrow, J.; Sadler, P. J. Cisplatin Binding Sites on Human Albumin. *J. Biol. Chem.* **1998**, *273* (24), 14721–14730. https://doi.org/10.1074/jbc.273.24.14721.

(99) Chen, H.; He, W.; Guo, Z. An H_2O_2-Responsive Nanocarrier for Dual-Release of Platinum Anticancer Drugs and O_2: Controlled Release and Enhanced Cytotoxicity against Cisplatin Resistant Cancer Cells. *Chem. Commun.* **2014**, *50* (68), 9714–9717. https://doi.org/10.1039/c4cc03385j.

(100) Binauld, S.; Scarano, W.; Stenzel, M. H. PH-Triggered Release of Platinum Drugs Conjugated to Micelles via an Acid-Cleavable Linker. *Macromolecules* **2012**, *45* (17), 6989–6999. https://doi.org/10.1021/ma3012812.

(101) Bangham, A. D.; Horne, R. W. Action of Saponin on Biological Cell Membranes. *Nature* **1962**, *196* (4858), 953–955. https://doi.org/10.1038/196953a0.

(102) Bangham, A. D.; Standish, M. M.; Weissmann, G. The Action of Steroids and Streptolysin S on the Permeability of Phospholipid Structures to Cations. *J. Mol. Biol.* **1965**, *13* (1), 253–259. https://doi.org/10.1016/S0022-2836(65)80094-8.

(103) Bangham, A. D. Physical Structure and Behavior of Lipids and Lipid Enzymes. In *Advances in lipid research*; Paoletti, R., Kritchevsky, D., Eds.; Elsevier, 1963; Vol. 1, pp 65–104. https://doi.org/10.1016/b978-1-4831-9937-5.50008-9.

(104) Bangham, A. D.; Standish, M. M.; Watkins, J. C. Diffusion of Univalent Ions across the Lamellae of Swollen Phospholipids. *J. Mol. Biol.* **1965**, *13* (1), 238–252. https://doi.org/10.1016/S0022-2836(65)80093-6.

(105) Fahy, E.; Subramaniam, S.; Murphy, R. C.; Nishijima, M.; Raetz, C. R. H.; Shimizu, T.; Spener, F.; Van Meer, G.; Wakelam, M. J. O.; Dennis, E. A. Update of the LIPID MAPS Comprehensive Classification System for Lipids. *J. Lipid Res.* **2009**, *50* (SUPPL.), 9–14. https://doi.org/10.1194/jlr.R800095-JLR200.

(106) Harayama, T.; Riezman, H. Understanding the Diversity of Membrane Lipid Composition. *Nat. Rev. Mol. Cell Biol.* **2019**, *19* (5), 281–296. https://doi.org/10.1038/nrm.2017.138.

(107) Drescher, S.; van Hoogevest, P. The Phospholipid Research Center: Current Research in Phospholipids and Their Use in Drug Delivery. *Pharmaceutics* **2020**, *12* (12), 1–36. https://doi.org/10.3390/pharmaceutics12121235.

(108) Shen, H.; Blanco, E.; Godin, B.; Serda, R. E.; Streiff, A. K.; Ferrari, M. Overview on Nanocarriers as Delivery Systems. In *Drug Delivery in Oncology: From Basic Research to Cancer Therapy*; Kratz, F., Senter, P., Steinhagen, H., Eds.; Wiley-VCH, 2011; pp 887–949. https://doi.org/10.1002/9783527634057.ch27.

(109) Sorrenti, A.; Illa, O.; Ortuño, R. M. Amphiphiles in Aqueous Solution: Well beyond a Soap Bubble. *Chem. Soc. Rev.* **2013**, *42* (21), 8200–8219. https://doi.org/10.1039/c3cs60151j.

(110) Pinazo, A.; Pons, R.; Bustelo, M.; Manresa, M. Á.; Morán, C.; Raluy, M.; Pérez, L. Gemini Histidine Based Surfactants: Characterization; Surface Properties and Biological Activity. *J. Mol. Liq.* **2019**, *289*. https://doi.org/10.1016/j.molliq.2019.111156.

(111) Pinazo, A.; Pons, R.; Ana, M.; Farfan, M.; da Silva, A.; Perez, L. Biocompatible Catanionic Vesicles from Arginine-Based Surfactants: A New Strategy to Tune the Antimicrobial Activity and Cytotoxicity of Vesicular Systems. **2020**, *12* (9), 857–881. https://doi.org/10.3390/pharmaceutics12090857.

(112) Guida, V. Thermodynamics and Kinetics of Vesicles Formation Processes. *Adv. Colloid Interface Sci.* **2010**, *161* (1–2), 77–88. https://doi.org/10.1016/j.cis.2009.11.004.

(113) Aulton, M. E.; Taylor, K. M. G. *Aulton's Pharmaceutics : The Design and Manufacture of Medicines*, 4th ed.; Aulton, M. E., Taylor, K. M. G., Eds.; Elsevier Health Sciences, 2013.

(114) Israelachvili, J. N.; Mitchell, D. J.; Ninham, B. W. Theory of Self-Assembly of Hydrocarbon Amphiphiles into Micelles and Bilayers. *J. Chem. Soc. Faraday Trans. 2 Mol. Chem. Phys.* **1976**, *72*, 1525–1568. https://doi.org/10.1039/F29767201525.

(115) Dutt, S.; Siril, P. F.; Remita, S. Swollen Liquid Crystals (SLCs): A Versatile Template for the Synthesis of Nano Structured Materials. *RSC Adv.* **2017**, *7* (10), 5733–5750. https://doi.org/10.1039/c6ra26390a.

(116) Cevc, G.; Richardsen, H. Lipid Vesicles and Membrane Fusion. *Adv. Drug Deliv. Rev.* **1999**, *38* (3), 207–232. https://doi.org/10.1016/S0169-409X(99)00030-7.

(117) Janmey, P. A.; Kinnunen, P. K. J. Biophysical Properties of Lipids and Dynamic Membranes. *Trends Cell Biol.* **2006**, *16* (10), 538–546. https://doi.org/10.1016/j.tcb.2006.08.009.

(118) Fromherz, P. Lipid-Vesicle Structure: Size Control by Edge-Active Agents. *Chem. Phys. Lett.* **1983**, *94* (3), 259–266. https://doi.org/10.1016/0009-2614(83)87083-3.

(119) Huang, C.; Quinn, D.; Sadovsky, Y.; Suresh, S.; Hsia, K. J. Formation and Size Distribution of Self-Assembled Vesicles. *PNAS USA* **2017**, *114* (11), 2910–2915. https://doi.org/10.1073/pnas.1702065114.

(120) Patil, Y. P.; Jadhav, S. Novel Methods for Liposome Preparation. *Chem. Phys. Lipids* **2014**, *177*, 8–18. https://doi.org/10.1016/j.chemphyslip.2013.10.011.

(121) Pattni, B. S.; Chupin, V. V.; Torchilin, V. P. New Developments in Liposomal Drug Delivery. *Chem. Rev.* **2015**, *115* (19), 10938–10966. https://doi.org/10.1021/acs.chemrev.5b00046.

(122) Akbarzadeh, A.; Rezaei-sadabady, R.; Davaran, S.; Joo, S. W.; Zarghami, N. Liposome: Classification , Preparation, and Applications. *Nanoscale Res. Lett.* **2013**, *8* (1), 1–9. https://doi.org/10.1186/1556-276X-8-102.

(123) Vergara-Irigaray, N. *Encyclopedia of Nanotechnology*, 1st ed.; Bhushan, B., Ed.; Springer Netherlands, 2012. https://doi.org/10.1007/978-90-481-9751-4.

(124) Nele, V.; Holme, M. N.; Kauscher, U.; Thomas, M. R.; Doutch, J. J.; Stevens, M. M. Effect of Formulation Method, Lipid Composition, and PEGylation on Vesicle Lamellarity: A Small-Angle Neutron Scattering Study. *Langmuir* **2019**, *35* (18), 6064–6074. https://doi.org/10.1021/acs.langmuir.8b04256.

(125) Frey, L.; Hiller, S.; Riek, R.; Bibow, S. Lipid- and Cholesterol-Mediated Time-Scale-Specific Modulation of the Outer Membrane Protein X Dynamics in Lipid Bilayers. *J. Am. Chem. Soc.* **2018**, *140* (45), 15402–15411. https://doi.org/10.1021/jacs.8b09188.

(126) Li, J.; Wang, X.; Zhang, T.; Wang, C.; Huang, Z.; Luo, X.; Deng, Y. A Review on Phospholipids and Their Main Applications in Drug Delivery Systems. *Asian J. Pharm. Sci.* **2015**, *10* (2), 81–98. https://doi.org/10.1016/j.ajps.2014.09.004.

(127) Has, C.; Sunthar, P. A Comprehensive Review on Recent Preparation Techniques of Liposomes. *J. Liposome Res.* **2020**, *30* (4), 336–365. https://doi.org/10.1080/08982104.2019.1668010.

(128) Trucillo, P.; Campardelli, R.; Reverchon, E. Liposomes: From Bangham to Supercritical Fluids. *Processes* **2020**, *8*, 1–15. https://doi.org/10.3390/pr8091022.

(129) Zangh, H. Thin-Film Hydration Followed by Extrusion Method Fot Liposome Preparation. In *Liposomes.*

Methods in Molecular Biology; D'Souza, Gerard, D. M., Eds.; Springer New York: New York, 2017; pp 17–22. https://doi.org/10.1007/978-1-4939-6591-5_2.

(130) Torchilin, V.; Weissig, V. *Liposomes: A Practical Approach*, 2nd ed.; Torchilin, V., Weissig, V., Eds.; OUP Oxford, 2003.

(131) Gouda, A.; Sakr, O. S.; Nasr, M.; Sammour, O. Ethanol Injection Technique for Liposomes Formulation : An Insight into Development , Influencing Factors , Challenges and Applications. *J. Drug Deliv. Sci. Technol.* **2021**, *61*, 102174. https://doi.org/10.1016/j.jddst.2020.102174.

(132) Filipczak, N.; Pan, J.; Siva, S.; Yalamarty, K.; Torchilin, V. P. Recent Advancements in Liposome Technology. *Adv. Drug Deliv. Rev.* **2020**, *156*, 4–22. https://doi.org/10.1016/j.addr.2020.06.022.

(133) Shah, S.; Dhawan, V.; Holm, R.; Nagarsenker, M. S.; Perrie, Y. Liposomes: Advancements and Innovation in the Manufacturing Process. *Adv. Drug Deliv. Rev.* **2020**, *155*, 102–122. https://doi.org/10.1016/j.addr.2020.07.002.

(134) Bhattacharjee, S. DLS and Zeta Potential - What They Are and What They Are Not? *J. Control. Release* **2016**, *235*, 337–351. https://doi.org/10.1016/j.jconrel.2016.06.017.

(135) Danaei, M.; Dehghankhold, M.; Ataei, S.; Davarani, F. H.; Javanmard, R.; Dokhani, A.; Khorasani, S.; Id, M. R. M. Impact of Particle Size and Polydispersity Index on the Clinical Applications of Lipidic Nanocarrier Systems. *Pharmaceutics* **2018**, *10* (57), 1–17. https://doi.org/10.3390/pharmaceutics10020057.

(136) Gabrielle-Madelmont, C.; Lesieur, S.; Ollivon, M. Characterization of Loaded Liposomes by Size Exclusion Chromatography. *J. Biochem. Biophys. Methods* **2003**, *56*, 189–217. https://doi.org/10.1016/S0165-022X(03)00059-9.

(137) Robson, A.; Dastoor, P. C.; Flynn, J.; Palmer, W.; Martin, A.; Smith, D. W.; Woldu, A.; Hua, S. Advantages and Limitations of Current Imaging Techniques for Characterizing Liposome Morphology. *Front. Pharmacol.* **2018**, *9*, 1–8. https://doi.org/10.3389/fphar.2018.00080.

(138) Demetzos, C. Differential Scanning Calorimetry (DSC): A Tool to Study the Thermal Behavior of Lipid Bilayers and Liposomal Stability. *J. Liposome Res.* **2008**, *18* (3), 159–173. https://doi.org/10.1080/08982100802310261.

(139) Poojari, C.; Wilkosz, N.; Lira, R. B.; Dimova, R.; Jurkiewicz, P.; Petka, R.; Kepczynski, M.; Róg, T. Behavior of the DPH Fluorescence Probe in Membranes Perturbed by Drugs. *Chem. Phys. Lipids* **2019**, *223*, 1–9. https://doi.org/10.1016/j.chemphyslip.2019.104784.

(140) Filipe, H. A. L.; Moreno, M. J.; Loura, L. M. S. The Secret Lives of Fluorescent Membrane Probes as Revealed by Molecular Dynamics Simulations. *Molecules* **2020**, *25* (15), 3424. https://doi.org/10.3390/molecules25153424.

(141) Alavi, M.; Karimi, N.; Safaei, M. Application of Various Types of Liposomes in Drug Delivery Systems. *Adv. Pharm. Bull.* **2017**, *7* (1), 3–9. https://doi.org/10.15171/apb.2017.002.

(142) Demetzos, C. Biophysics and Thermodynamics: The Scientific Building Blocks of Bio-Inspired Drug Delivery Nano Systems. *Am. Assoc. Pharm. Sci.* **2015**, *16* (3), 491–495. https://doi.org/10.1208/s12249-015-0321-1.

(143) Anderson, M.; Omri, A. The Effect of Different Lipid Components on the in Vitro Stability and Release Kinetics of Liposome Formulations. *Drug Deliv.* **2004**, *11* (1), 33–39. https://doi.org/10.1080/10717540490265243.

(144) Tretiakova, D.; Onishchenko, N.; Boldyrev, I.; Mikhalyov, I.; Tuzikov, A.; Bovin, N.; Evtushenko, E.; Vodovozova, E. Influence of Stabilizing Components on the Integrity of Antitumor Liposomes Loaded with Lipophilic Prodrug in the Bilayer. *Colloids Surf B Biointerfaces* **2018**, *166*, 45–53. https://doi.org/10.1016/j.colsurfb.2018.02.061.

(145) Susa, F.; Bucca, G.; Limongi, T.; Cauda, V.; Pisano, R. Enhancing the Preservation of Liposomes: The Role of Cryoprotectants, Lipid Formulations and Freezing Approaches. *Cryobiology* **2021**, *98*, 46–56. https://doi.org/10.1016/j.cryobiol.2020.12.009.

(146) Briuglia, M. L.; Rotella, C.; McFarlane, A.; Lamprou, D. A. Influence of Cholesterol on Liposome Stability and on in Vitro Drug Release. *Drug Deliv. Transl. Res.* **2015**, *5* (3), 231–242. https://doi.org/10.1007/s13346-015-0220-8.

(147) Farzaneh, H.; Ebrahimi Nik, M.; Mashreghi, M.; Saberi, Z.; Jaafari, M. R.; Teymouri, M. A Study on the Role of Cholesterol and Phosphatidylcholine in Various Features of Liposomal Doxorubicin: From Liposomal Preparation to Therapy. *Int. J. Pharm.* **2018**, *551* (1–2), 300–308. https://doi.org/10.1016/j.ijpharm.2018.09.047.

(148) Düzgünes, N.; Nir, S. Mechanisms and Kinetics of Liposome–Cell Interactions. *Adv. Drug Deliv. Rev.* **1999**, *40* (1–2), 3–18. https://doi.org/10.1016/S0169-409X(99)00037-X.

(149) Miller, C. R.; Bondurant, B.; McLean, S. D.; McGovern, K. A.; O'Brien, D. F. Liposome-Cell Interactions in Vitro: Effect of Liposome Surface Charge on the Binding and Endocytosis of Conventional and Sterically Stabilized Liposomes. *Biochemistry* **1998**, *37* (37), 12875–12883. https://doi.org/10.1021/bi980096y.

(150) Senior, J. H.; Trimble, K. R.; Maskiewicz, R. Interaction of Positively-Charged Liposomes with Blood: Implications for Their Application in Vivo. *Biochim. Biophys. Acta - Biomembr.* **1991**, *1070* (1), 173–179. https://doi.org/10.1016/0005-2736(91)90160-A.

(151) Zhao, Z.; Yao, W.; Wang, N.; Liu, C.; Zhou, H.; Chen, H.; Qiao, W. Synthesis and Evaluation of Mono- and Multi-Hydroxyl Low Toxicity PH-Sensitive Cationic Lipids for Drug Delivery. *Eur. J. Pharm. Sci.* **2019**, *133* (March), 69–78. https://doi.org/10.1016/j.ejps.2019.03.018.

(152) Nosova, A. S.; Koloskova, O. O.; Nikonova, A. A.; Simonova, V. A.; Smirnov, V. V.; Kudlay, D.; Khaitov, M. R. Diversity of PEGylation Methods of Liposomes and Their Influence on RNA Delivery. *Med. Chem. Commun.* **2019**, *10* (3), 369–377. https://doi.org/10.1039/c8md00515j.

(153) Mohamed, M.; Abu Lila, A. S.; Shimizu, T.; Alaaeldin, E.; Hussein, A.; Sarhan, H. A.; Szebeni, J.; Ishida, T. PEGylated Liposomes: Immunological Responses. *Sci. Technol. Adv. Mater.* **2019**, *20* (1), 710–724. https://doi.org/10.1080/14686996.2019.1627174.

(154) Sieber, S.; Grossen, P.; Uhl, P.; Detampel, P.; Mier, W.; Witzigmann, D.; Huwyler, J. Zebrafish as a Predictive Screening Model to Assess Macrophage Clearance of Liposomes in Vivo. *Nanomedicine: NMB* **2019**, *17* (2019), 82–93. https://doi.org/10.1016/j.nano.2018.11.017.

(155) Pamunuwa, G.; Karunaratne, V.; Karunaratne, D. N. Effect of Lipid Composition on in Vitro Release and Skin Deposition of Curcumin Encapsulated Liposomes. *J. Nanomater.* **2016**, *2016*. https://doi.org/10.1155/2016/4535790.

(156) Evjen, T. J.; Nilssen, E. A.; Fowler, R. A.; Røgnvaldsson, S.; Brandl, M.; Fossheim, S. L. Lipid Membrane Composition Influences Drug Release from Dioleoylphosphatidylethanolamine-Based Liposomes on Exposure to Ultrasound. *Int. J. Pharm.* **2011**, *406* (1–2), 114–116. https://doi.org/10.1016/j.ijpharm.2010.12.026.

(157) Cipolla, D.; Wu, H.; Gonda, I.; Eastman, S.; Redelmeier, T.; Chan, H. K. Modifying the Release Properties of Liposomes toward Personalized Medicine. *J. Pharm. Sci.* **2014**, *103* (6), 1851–1862. https://doi.org/10.1002/jps.23969.

(158) Hang, Z.; Cooper, M. A.; Ziora, Z. M. Platinum-Based Anticancer Drugs Encapsulated Liposome and Polymeric Micelle Formulation in Clinical Trials. *Biochem. Compd.* **2016**, *4* (1), 1. https://doi.org/10.7243/2052-9341-4-2.

(159) Liu, D.; He, C.; Wang, A. Z.; Lin, W. Application of Liposomal Technologies for Delivery of Platinum Analogs in Oncology. *Int. J. Nanomedicine* **2013**, *8*, 3309–3319. https://doi.org/10.2147/IJN.S38354.

(160) Stathopoulos, G. P.; Boulikas, T. Lipoplatin Formulation Review Article. *J. Drug Deliv.* **2012**, *2012*, 1–10. https://doi.org/10.1155/2012/581363.

(161) White, S. C.; Lorigan, P.; Margison, G. P.; Margison, J. M.; Martin, F.; Thatcher, N.; Anderson, H.; Ranson, M. Phase II Study of SPI-77 (Sterically Stabilised Liposomal Cisplatin) in Advanced Non-Small-Cell Lung Cancer. *Br. J. Cancer* **2006**, *95* (7), 822–828. https://doi.org/10.1038/sj.bjc.6603345.

(162) De Jonge, M. J. A.; Slingerland, M.; Loos, W. J.; Wiemer, E. A. C.; Burger, H.; Mathijssen, R. H. J.; Kroep, J.

R.; Den Hollander, M. A. G.; Van Der Biessen, D.; Lam, M. H.; Verweij, J.; Gelderblom, H. Early Cessation of the Clinical Development of LiPlaCis, a Liposomal Cisplatin Formulation. *Eur. J. Cancer* **2010**, *46* (16), 3016–3021. https://doi.org/10.1016/j.ejca.2010.07.015.

(163) Zisman, N.; Dos Santos, N.; Johnstone, S.; Tsang, A.; Bermudes, D.; Mayer, L.; Tardi, P. Optimizing Liposomal Cisplatin Efficacy through Membrane Composition Manipulations. *Chemother. Res. Pract.* **2011**, *2011*, 1–7. https://doi.org/10.1155/2011/213848.

(164) K. K. Sankhala , A. C. Mita , R. Adinin , L. Wood , M. Beeram , S. BullockN. Yamagata , K. Matsuno , T. Fujisawa, A. P. A Phase I Pharmacokinetic (PK) Study of MBP-426, a Novel Liposome Encapsulated Oxaliplatin. *J. Clin. Oncol.* **2009**, *27* (15), 2535. https://doi.org/10.1200/jco.2009.27.15_suppl.2535.

(165) El-Shafie, S.; Fahmy, S. A.; Ziko, L.; Elzahed, N.; Shoeib, T.; Kakarougkas, A. Encapsulation of Nedaplatin in Novel Pegylated Liposomes Increases Its Cytotoxicity and Genotoxicity against A549 and U2os Human Cancer Cells. *Pharmaceutics* **2020**, *12* (9), 1–18. https://doi.org/10.3390/pharmaceutics12090863.

(166) Zahednezhad, F.; Zakeri-Milani, P.; Shahbazi Mojarrad, J.; Valizadeh, H. The Latest Advances of Cisplatin Liposomal Formulations: Essentials for Preparation and Analysis. *Expert Opin. Drug Deliv.* **2020**, *17* (4), 523–541. https://doi.org/10.1080/17425247.2020.1737672.

(167) Mi, P.; Miyata, K.; Kataoka, K.; Cabral, H. Clinical Translation of Self-Assembled Cancer Nanomedicines. *Adv. Ther.* **2021**, *4* (1), 1–29. https://doi.org/10.1002/adtp.202000159.

(168) Polarz, S.; Landsmann, S.; Klaiber, A. Hybrid Surfactant Systems with Inorganic Constituents. *Angew. Chem. Int. Ed.* **2014**, *53* (4), 946–954. https://doi.org/10.1002/anie.201303159.

(169) Hovland, R.; Aasen, A. J.; Klaveness, J. Preparation and in Vitro Evaluation of GdPCTA-[12] Derivate; a Micellar MRI Contrast Agent. *Org. Biomol. Chem.* **2003**, *1* (4), 644–647. https://doi.org/10.1039/b301944f.

(170) Vaccaro, M.; Accardo, A.; Tesauro, D.; Mangiapia, G.; Löf, D.; Schillén, K.; Söderman, O.; Morelli, G.; Paduano, L. Supramolecular Aggregates of Amphiphilic Gadolinium Complexes as Blood Pool MRI/MRA Contrast Agents: Physicochemical Characterization. *Langmuir* **2006**, *22* (15), 6635–6643. https://doi.org/10.1021/la053500k.

(171) Chen, Y.; Yang, H.; Tang, W.; Cui, X.; Wang, W.; Chen, X.; Yuan, Y.; Hu, A. Attaching Double Chain Cationic Gd(III)-Containing Surfactants on Nanosized Colloids for Highly Efficient MRI Contrast Agents. *J. Mater. Chem. B* **2013**, *1* (40), 5443. https://doi.org/10.1039/c3tb20807a.

(172) Gong, P.; Chen, Z.; Chen, Y.; Wang, W.; Wang, X.; Hu, A. High-Relaxivity MRI Contrast Agents Prepared from Miniemulsion Polymerization Using Gadolinium(III)-Based Metallosurfactants. *Chem. Commun.* **2011**, *47* (14), 4240–4242. https://doi.org/10.1039/c0cc05746k.

(173) Xu, K.; Xu, N.; Zhu, Y.; Zhang, M.; Tang, W.; Ding, Y.; Hu, A. Co-Assembly of Gd(III)-Based Metallosurfactant and Conjugated Polymer Nanoparticles in Organosilica Cross-Linked Block Copolymer Micelles for Highly Efficient MRI and Fluorescent Bimodal Imaging. *Part. Part. Syst. Charact.* **2020**, *37* (4), 1–8. https://doi.org/10.1002/ppsc.202000044.

(174) Wang, R.; Liang, Y.; Schmehl, R. H. Light Induced Exchange Energy Transfer Reactions of Micelle Forming Ru(II) Diimine Complexes. *Inorganica Chim. Acta* **1994**, *225* (1–2), 275–283. https://doi.org/10.1016/0020-1693(94)04058-3.

(175) Terasaki, N.; Akiyama, T.; Yamada, S. Structural Characterization and Photoelectrochemical Properties of the Self-Assembled Monolayers of Tris(2,2'-Bipyridine)Ruthenium(II)-Viologen Linked Compounds Formed on the Gold Surface. *Langmuir* **2002**, *18* (22), 8666–8671. https://doi.org/10.1021/la025936v.

(176) Chu, B. W. K.; Yam, V. W. W. Synthesis, Characterization, Langmuir-Blodgett Film-Forming Properties, and Second-Harmonic-Generation Studies of Ruthenium(II) Complexes with Long Hydrocarbon Chains. *Inorg. Chem.* **2001**, *40* (14), 3324–3329. https://doi.org/10.1021/ic001326b.

(177) Yam, V. W. W.; Li, B.; Zhu, N. Synthesis of Mesoporous Silicates with Controllable Pore Size Using Surfactant Ruthenium(II) Complexes as Templates. *Adv. Mater.* **2002**, *14* (10), 719–722. https://doi.org/10.1002/1521-4095(20020517)14:10<719::AID-ADMA719>3.0.CO;2-5.

(178) do Pim, W. D.; Ribeiro-Santos, T. A.; Jardim, I. S.; de Castro, M. C. M.; Braga, A. H.; do Nascimento, G. M.; Binatti, I.; Stumpf, H. O.; Lorençon, E.; Araujo, M. H.; Pereira, C. L. M. Bistable Copper(II) Metallosurfactant as Molecular Machine for the Preparation of Hybrid Silica-Based Porous Materials. *Mater. Des.* **2018**, *160*, 876–885. https://doi.org/10.1016/j.matdes.2018.10.023.

(179) Berro, Y.; Gueddida, S.; Bouizi, Y.; Bellouard, C.; Bendeif, E. E.; Gansmuller, A.; Celzard, A.; Fierro, V.; Ihiawakrim, D.; Ersen, O.; Kassir, M.; El Haj Hassan, F.; Lebegue, S.; Badawi, M.; Canilho, N.; Pasc, A. Imprinting Isolated Single Iron Atoms onto Mesoporous Silica by Templating with Metallosurfactants. *J. Colloid Interface Sci.* **2020**, *573*, 193–203. https://doi.org/10.1016/j.jcis.2020.03.095.

(180) Dwars, T.; Paetzold, E.; Oehme, G. Reactions in Micellar Systems. *Angew. Chem. Int. Ed.* **2005**, *44*, 7174–7199. https://doi.org/10.1002/anie.200501365.

(181) Hay, R. W.; Govan, N.; Parchment, K. E. A Metallomicelle Catalysed Hydrolysis of a Phosphate Triester, a Phosphonate Diester and O-Isopropyl Methylfluorophosphonate (Sarin). *Inorg. Chem. Commun.* **1998**, *1* (6), 228–231. https://doi.org/10.1016/S1387-7003(09)00062-8.

(182) Bhattacharya, S.; Snehalatha, K.; George, S. K. Synthesis of Some Copper(II) -Chelating (Dialkylamino) Pyridine Amphiphiles and Evaluation of Their Esterolytic Capacities in Cationic Micellar Media. *J. Org. Chem.* **1998**, *3263* (1), 27–35. https://doi.org/10.1021/jo9707996.

(183) Kimura, E.; Hashimoto, H.; Koike, T. Hydrolysis of Lipophilic Esters Catalyzed by a Zinc(II) Complex of a Long Alkyl-Pendant Macrocyclic Tetraamine in Micellar Solution. *J. Am. Chem. Soc.* **1996**, *118* (45), 10963–10970. https://doi.org/10.1021/ja961789+.

(184) Kagalwala, H. N.; Chirdon, D. N.; Mills, I. N.; Budwal, N.; Bernhard, S. Light-Driven Hydrogen Generation from Microemulsions Using Metallosurfactant Catalysts and Oxalic Acid. *Inorg. Chem.* **2017**, *56* (17), 10162–10171. https://doi.org/10.1021/acs.inorgchem.7b00463.

(185) Kaur, N.; Kaur, G.; Bhalla, A.; Dhau, J. S.; Chaudhary, G. R. Metallosurfactant Based Pd-Ni Alloy Nanoparticles as a Proficient Catalyst in the Mizoroki Heck Coupling Reaction. *Green Chem.* **2018**, *20* (7), 1506–1514. https://doi.org/10.1039/c7gc03877a.

(186) Kaur, R.; Mehta, S. K. Self Aggregating Metal Surfactant Complexes: Precursors for Nanostructures. *Coord. Chem. Rev.* **2014**, *262* (1), 37–54. https://doi.org/10.1016/j.ccr.2013.12.014.

(187) Schattschneider, C.; Doniz Kettenmann, S.; Hinojosa, S.; Heinrich, J.; Kulak, N. Biological Activity of Amphiphilic Metal Complexes. *Coord. Chem. Rev.* **2019**, *385*, 191–207. https://doi.org/10.1016/j.ccr.2018.12.007.

(188) Walker, G. W.; Geue, R. J.; Sargeson, A. M.; Behm, C. A. Surface-Active Cobalt Cage Complexes: Synthesis, Surface Chemistry, Biological Activity, and Redox Properties. *Dalton Trans.* **2003**, No. 15, 2992–3001. https://doi.org/10.1039/b302230g.

(189) Kaur, G.; Singh, P.; Mehta, S. K.; Kumar, S.; Dilbaghi, N.; Chaudhary, G. R. A Facile Route for the Synthesis of Co, Ni and Cu Metallic Nanoparticles with Potential Antimicrobial Activity Using Novel Metallosurfactants. *Appl. Surf. Sci.* **2017**, *404*, 254–262. https://doi.org/10.1016/j.apsusc.2017.01.284.

(190) Sharma, N. K.; Singh, M. Multifunctional Supramolecular Ionic Metallosurfactants (SMIMSs) for Antimicrobial, Anticancer and Serum Albumins Binding. *J. Mol. Liq.* **2018**, *263*, 463–471. https://doi.org/10.1016/j.molliq.2018.04.138.

(191) Kumar, R. S.; Arunachalam, S. Synthesis, Micellar Properties, DNA Binding and Antimicrobial Studies of Some Surfactant-Cobalt(III) Complexes. *Biophys. Chem.* **2008**, *136* (2–3), 136–144. https://doi.org/10.1016/j.bpc.2008.05.007.

(192) Dogra, V.; Kaur, G.; Kaur, A.; Kumar, R.; Kumar, S. In Vitro Assessment of Antimicrobial and Genotoxic Effect of Metallosurfactant Based Nickel Hydroxide Nanoparticles against Escherichia Coli and Its Genomic DNA. *Colloids Surf B Biointerfaces* **2018**, *170*, 99–108. https://doi.org/10.1016/j.colsurfb.2018.05.069.

(193) Cuerva, C.; Campo, J. A.; Cano, M.; Lodeiro, C. Multi-Stimuli-Responsive Properties of Aggregation-Enhanced Emission-Active Unsymmetrical PtII Metallomesogens through Self-Assembly. *Chem. Eur. J.* **2019**, *25* (52), 12046–12051. https://doi.org/10.1002/chem.201901763.

(194) Simon, J.; Le Moigne, J.; Markovitsi, D.; Dayantis, J. Annelides. 3. Complexation of Dioxygen in Organized Cobaltous Complex Assemblies. A New Approach to Kinetic Studies in Micellar Phases. *J. Am. Chem. Soc.* **1980**, *102* (24), 7247–7252. https://doi.org/10.1021/ja00544a013.

(195) Bruce, D. W.; Dunmur, D. A.; Maitlis, P. M.; Watkins, J. M.; Tiddy, G. J. T. The Synthesis and Lyotropic Phase Behaviour of Some Aquatetra(Cyano)-Dodecylaminoferrate(II) Complexes. *Liq. Cryst.* **1992**, *11* (1), 127–133. https://doi.org/10.1080/02678299208028976.

(196) Bruce, D. W.; Denby, I. R.; Tiddy, G. J. T.; Watkins, J. M. Synthesis and Properties of Surfactant Complexes of Cobalt(III) and Chromium(III). *J. Mater. Chem.* **1993**, *3* (9), 911–916. https://doi.org/10.1039/jm9930300911.

(197) Neve, F.; Ghedini, M.; De Munno, G.; Levelut, A. M. Ionic Amphiphilic Metallomesogens. *Chem. Mater.* **1995**, *7* (4), 688–693. https://doi.org/10.1021/cm00052a013.

(198) Kumaraguru, N.; Arunachalam, S.; Arumugham, M. N.; Santhakumar, K. Metallosurfactants of Chromium(III) Coordination Complexes. Synthesis, Characterization and Determination of CMC Values. *Transit. Met. Chem.* **2006**, *31*, 62–70. https://doi.org/10.1007/s11243-005-6400-5.

(199) Santhakumar, K.; Kumaraguru, N.; Arunachalam, S.; Arumugham, M. N. Studies on Cobalt(III) Metallosurfactants. Kinetics and Mechanism of Reduction of Cobalt(III) by Iron(II) in Aqueous Acid Medium. *Transit. Met. Chem.* **2007**, *31* (1), 62–70. https://doi.org/10.1007/s11243-005-6356-5.

(200) Santhakumar, K.; Kumaraguru, N.; Arunachalam, S.; Arumugham, M. N. Thermodynamics and Micellar Properties of Some Surface Active Cobalt(III) Metallosurfactants in Nonaqueous Medium. *Int. J. Chem. Kinet.* **2006**, *39* (3), 22–31. https://doi.org/10.1002/kin.

(201) Iida, M.; Baba, C.; Inoue, M.; Yoshida, H.; Taguchi, E.; Furusho, H. Ionic Liquids of Bis(Alkylethylenediamine)Silver(I) Salts and the Formation of Silver(0) Nanoparticles from the Ionic Liquid System. *Chem. Eur. J.* **2008**, *14* (16), 5047–5056. https://doi.org/10.1002/chem.200701764.

(202) Manna, A.; Imae, T.; Iida, M.; Hisamatsu, N. Formation of Silver Nanoparticles from a N-Hexadecylethylenediamine Silver Nitrate Complex. *Langmuir* **2001**, *17* (19), 6000–6004. https://doi.org/10.1021/la010389j.

(203) Er, H.; Asaoka, N.; Hisamatsu, N.; Iida, M.; Imae, T. Effects of Metal-Counterion Interactions on the Percolation in Microemulsions Composed of Bis(N-Octylethylenediamine)Metal(II) Complexes in Water/Benzene and Water/Chloroform Systems. *Colloids Surf. A: Physicochem. Eng. Asp.* **2003**, *221* (1–3), 119–129. https://doi.org/10.1016/S0927-7757(03)00129-8.

(204) Iida, M.; Asayama, K.; Ohkawa, S. The Aggregation of Dichlorobis(N-Hexylethylenediamine)Zinc(II) in Water and Water/Chloroform Mixed Solvents. *Bull. Chem. Soc. Jpn.* **2002**, *75* (3), 521–529. https://doi.org/10.1246/bcsj.75.521.

(205) Ikeda, Y.; Imae, T.; Hao, J. C.; Iida, M.; Kitano, T.; Hisamatsu, N. Structural Characterization of Microemulsions in a Ternary System of Zn(Oct-En)2Cl2 Complex/Benzene/Water. *Langmuir* **2000**, *16* (20), 7618–7623. https://doi.org/10.1021/la000140m.

(206) Iida, M.; Er, H.; Hisamatsu, N.; Tanase, T. Hydrophilic-Hydrophobic Balance of Bis(Octylethylenediamine) Zn(II), Cd(II), and Pd(II) Chlorides in Methanol/Water and Chloroform/Water Systems. *Chem. Lett.* **2000**, *29* (5), 518–519. https://doi.org/10.1246/cl.2000.518.

(207) Iida, M.; Tanase, T.; Asaoka, N.; Nakanishi, A. A Molecular Structure of Bis(N-Octylethylenediamine)Zinc(II) Nitrate in Crystal and the Aggregations in Wet Chloroform and Benzene Solutions. *Chem. Lett.* **1998**, No. 12, 1275–1276. https://doi.org/10.1246/cl.1998.1275.

(208) Iida, M.; Yonezawa, A.; Tanaka, J. A Novel Reverse Micellar System Composed of Bis(Octylethylenediamine)Zinc(II) Chloride in Aqueous Benzene and Chloroform Solutions. *Chem. Lett.* **1997**, No. 7, 663–664. https://doi.org/10.1246/cl.1997.663.

(209) Er, H.; Ohkawa, S.; Iida, M. Aggregation Behavior of Alkylethylenediamine Palladium(II) Complexes in Water and in Water/Organic Solvent Mixtures. *Colloids Surf. A: Physicochem. Eng. Asp.* **2007**, *301* (1–3), 189–198. https://doi.org/10.1016/j.colsurfa.2006.12.053.

(210) Fallis, I. A.; Griffiths, P. C.; Griffiths, P. M.; Hibbs, D. E.; Hursthouse, M. B.; Angie, L. Solid State and Solution Behaviour of Novel Transition Metal Containing Surfactants. *Chem. Commun.* **1998**, *2* (15), 665–666.

(211) Griffiths, P. C.; Fallis, I. A.; Willock, D. J.; Paul, A.; Barrie, C. L.; Griffiths, P. M.; Williams, G. M.; King, S. M.; Heenan, R. K.; Görgl, R. The Structure of Metallomicelles. *Chem. Eur. J.* **2004**, *10* (8), 2022–2028. https://doi.org/10.1002/chem.200305670.

(212) Griffiths, P. C.; Fallis, I. A.; Chuenpratoom, T.; Watanesk, R. Metallosurfactants: Interfaces and Micelles. *Adv. Colloid Interface Sci.* **2006**, *122* (1–3), 107–117. https://doi.org/10.1016/j.cis.2006.06.010.

(213) Menger, F. M.; Gan, L. H.; Johnson, E.; Durst, D. H. Phosphate Ester Hydrolysis Catalyzed by Metallomicelles. *J. Am. Chem. Soc.* **1987**, *109* (9), 2800–2803. https://doi.org/10.1021/ja00243a038.

(214) Polyzos, A.; Hughes, A. B.; Christie, J. R. Catalysis of Aryl Ester Hydrolysis in the Presence of Metallomicelles Containing a Copper(II) Diethylenetriamine Derivative. *Langmuir* **2007**, *23* (4), 1872–1879. https://doi.org/10.1021/la0626454.

(215) Koutsantonis, G. A.; Nealon, G. L.; Buckley, C. E.; Paskevicius, M.; Douce, L.; Harrowfield, J. M.; McDowall, A. W. Wormlike Micelles from a Cage Amine Metallosurfactant. *Langmuir* **2007**, *23* (24), 11986–11990. https://doi.org/10.1021/la701283b.

(216) Bowers, J.; Danks, M. J.; Bruce, D. W.; Heenan, R. K. Surface and Aggregation Behavior of Aqueous Solutions of Ru(II) Metallosurfactants: 1. Micellization of $[Ru(Bipy)_2(Bipy')][Cl]_2$ Complexes. *Langmuir* **2003**, *19* (2), 292–298. https://doi.org/10.1021/la025967q.

(217) Danks, M. J.; Jervis, H. B.; Nowotny, M.; Zhou, W.; Maschmeyer, T. A.; Bruce, D. W. High-Activity Heterogeneous Catalysts Prepared in One Step from the Mesophases of Metallosurfactants. *Catal. Letters* **2002**, *82* (1–2), 95–98. https://doi.org/10.1023/A:1020552427133.

(218) Holbrey, J. D.; Tiddy, G. J. T.; Bruce, D. W. Amphiphilic Terpyridine Complexes of Ruthenium and Rhodium Displaying Lyotropic Mesomorphism. *Dalton Trans.* **1995**, No. 11, 1769–1774. https://doi.org/10.1039/DT9950001769.

(219) Giroud-Godquin, A. -M; Maitlis, P. M. Metallomesogens: Metal Complexes in Organized Fluid Phases. *Angew. Chem. Int. Ed.* **1991**, *30* (4), 375–402. https://doi.org/10.1002/anie.199103751.

(220) Giménez, R.; Lydon, D. P.; Serrano, J. L. Metallomesogens: A Promise or a Fact? *Curr. Opin. Solid State Mater. Sci.* **2002**, *6* (6), 527–535. https://doi.org/10.1016/S1359-0286(03)00009-3.

(221) Yang, X.; Wu, X.; Zhou, D.; Yu, J.; Xie, G.; Bruce, D. W.; Wang, Y. Platinum-Based Metallomesogens Bearing a Pt(4,6-Dfppy)(Acac) Skeleton: Synthesis, Photophysical Properties and Polarised Phosphorescence Application. *Dalton Trans.* **2018**, *47* (38), 13368–13377. https://doi.org/10.1039/c8dt03017k.

(222) Bowers, J.; Danks, M. J.; Bruce, D. W.; Heenan, R. K. Surface and Aggregation Behavior of Aqueous Solutions of Ru(II) Metallosurfactants: 2. Adsorbed Films of $[Ru(Bipy)_2(Bipy')][Cl]_2$ Complexes. *Langmuir* **2003**, *19* (2), 299–305. https://doi.org/10.1021/la025967q.

(223) Bowers, J.; Amos, K. E.; Bruce, D. W.; Heenan, R. K. Surface and Aggregation Behavior of Aqueous Solutions of Ru(II) Metallosurfactants. 3. Effect of Chain Number and Orientation on the Structure of Adsorbed Films of $[Ru(Bipy)_2(Bipy')]Cl_2$ Complexes. *Langmuir* **2005**, *21* (4), 1346–1353. https://doi.org/10.1021/la0478705 CCC:

(224) Bowers, J.; Amos, K. E.; Bruce, D. W.; Heenan, R. K. Surface and Aggregation Behavior of Aqueous Solutions of Ru(II) Metallosurfactants: 4. Effect of Chain Number and Orientation on the Aggregation of $[Ru(Bipy)_2(Bipy')]Cl_2$ Complexes. *Langmuir* **2005**, *21* (13), 5696–5706. https://doi.org/10.1021/la050241q.

(225) Gao, L. H.; Wang, K. Z.; Cai, L.; Zhang, H. X.; Jin, L. P.; Huang, C. H.; Gao, H. J. Studies of Langmuir-Blodgett Films of an Ion Pair Metal Complex Containing Eu(III)-Ru(II) Dual Chromophores. *J. Phys. Chem. B* **2006**, *110* (14), 7402–7408. https://doi.org/10.1021/jp054525v.

(226) Taniguchi, M.; Ueno, N.; Okamoto, K.; Karthaus, O.; Shimomura, M.; Yamagishi, A. Monolayer and Fluorescence Properties of a Chiral Amphiphilic Ruthenium(II) Complex at an Air-Water Interface. *Langmuir* **1999**, *15* (22), 7700–7707. https://doi.org/10.1021/la990145n.

(227) Haga, M. a.; Kato, N.; Monjushiro, H.; Wang, K.; Hossain, M. D. Metal Coordination to Amphiphilic Ru Complexes at the Air-Water Interface. *Supramol. Sci.* **1998**, *5* (3–4), 337–342. https://doi.org/10.1016/S0968-5677(98)00028-5.

(228) Domínguez-Gutiérrez, D.; Surtchev, M.; Eiser, E.; Elsevier, C. J. Ru(II)-Based Metallosurfactant Forming Inverted Aggregates. *Nano Lett.* **2006**, *6* (2), 145–147. https://doi.org/10.1021/nl051944v.

(229) Domínguez-Gutiérrez, D.; De Paoli, G.; Guerrero-Martínez, A.; Ginocchietti, G.; Ebeling, D.; Eiser, E.; De Cola, L.; Elsevier, C. J. Inverted Aggregates of Luminescent Ruthenium Metallosurfactants. *J. Mater. Chem.* **2008**, *18* (24), 2762–2768. https://doi.org/10.1039/b717859j.

(230) Kobayashi, Y.; Muranaka, A.; Kato, K.; Saeki, A.; Tanaka, T.; Uchiyama, M.; Osuka, A.; Aida, T.; Sakurai, T. A Structural Parameter to Link Molecular Geometry to Macroscopic Orientation in Discotic Liquid Crystals: Study of Metalloporphyrin Tapes. *Chem. Commun.* **2021**, *57* (10), 1206–1209. https://doi.org/10.1039/d0cc07241a.

(231) Roldán-Carmona, C.; González-Delgado, A. M.; Guerrero-Martínez, A.; Cola, L. De; Giner-Casares, J. J.; Pérez-Morales, M.; Martín-Romero, M. T.; Camacho, L. Molecular Organization and Effective Energy Transfer in Iridium Metallosurfactant-Porphyrin Assemblies Embedded in Langmuir-Schaefer Films. *Phys. Chem. Chem. Phys.* **2011**, *13* (7), 2834–2841. https://doi.org/10.1039/c0cp01683g.

(232) Gameiro, P.; Maia, A.; Pereira, E.; De Castro, B.; Burgess, J. Bis-(4-Methyl-4′-Pentyl-2,2′-Bipyridyl)(Dicyano)Iron(II): A Versatile Solvatochromic Solvation Probe. *Transit. Met. Chem.* **2000**, *25* (3), 283–286. https://doi.org/10.1023/A:1007045326027.

(233) Gameiro, P.; Pereira, E.; Garcia, P.; Breia, S.; Burgess, J.; De Castro, B. Derivatives of Bis(2,2′-Bipyridyl)Dicyanoiron(II) with Long Alkyl Chains - Versatile Solvatochromic Probes That Form Metalloaggregates in Water-Rich Media. *Eur. J. Inorg. Chem.* **2001**, No. 11, 2755–2761. https://doi.org/10.1002/1099-0682(200111)2001:11<2755::AID-EJIC2755>3.0.CO;2-L.

(234) Garcia, P.; Eaton, P.; Geurts, H. P. M.; Sousa, M.; Gameiro, P.; Feiters, M. C.; Nolte, R. J. M.; Pereira, E.; De Castro, B. AFM and Electron Microscopy Study of the Unusual Aggregation Behavior of Metallosurfactants Based on Iron(II) Complexes with Bipyridine Ligands. *Langmuir* **2007**, *23* (15), 7951–7957. https://doi.org/10.1021/la700560y.

(235) Van Den Brom, C. R.; Wagner, M.; Enkelmann, V.; Landfester, K.; Weiss, C. K. Alkylsulfides of Ag(I) and Au(I) as Metallosurfactants. *Langmuir* **2010**, *26* (20), 15794–15801. https://doi.org/10.1021/la1027543.

(236) Ghirlanda, G.; Scrimin, P.; Kaifer, A. E.; Echegoyen, L. A. Self-Assembled Monolayers of Cu(II) Metallosurfactants on GC and HOPG. *Langmuir* **1996**, *12* (15), 3695–3701. https://doi.org/10.1021/la960052v.

(237) Siewert, B.; van Rixel, V. H. S.; van Rooden, E. J.; Hopkins, S. L.; Moester, M. J. B.; Ariese, F.; Siegler, M. A.; Bonnet, S. Chemical Swarming: Depending on Concentration, an Amphiphilic Ruthenium Polypyridyl Complex Induces Cell Death via Two Different Mechanisms. *Chem. Eur. J.* **2016**, *22* (31), 10960–10968. https://doi.org/10.1002/chem.201600927.

(238) Siewert, B.; Langerman, M.; Hontani, Y.; Kennis, J. T. M.; Van Rixel, V. H. S.; Limburg, B.; Siegler, M. A.; Talens Saez, V.; Kieltyka, R. E.; Bonnet, S. Turning on the Red Phosphorescence of a [Ru(Tpy)(Bpy)(Cl)]Cl Complex by Amide Substitution: Self-Aggregation, Toxicity, and Cellular Localization of an Emissive Ruthenium-Based Amphiphile. *Chem. Commun.* **2017**, *53* (81), 11126–11129. https://doi.org/10.1039/c7cc02989f.

(239) Kumar, R. S.; Arunachalam, S.; Periasamy, V. S.; Preethy, C. P.; Riyasdeen, A.; Akbarsha, M. A. Surfactant-Cobalt(III) Complexes: Synthesis, Critical Micelle Concentration (CMC) Determination, DNA Binding, Antimicrobial and Cytotoxicity Studies. *J. Inorg. Biochem.* **2009**, *103* (1), 117–127. https://doi.org/10.1016/j.jinorgbio.2008.09.010.

(240) Kumar, R. S.; Paul, P.; Riyasdeen, A.; Wagniéres, G.; van den Bergh, H.; Akbarsha, M. A.; Arunachalam, S. Human Serum Albumin Binding and Cytotoxicity Studies of Surfactant-Cobalt(III) Complex Containing 1,10-Phenanthroline Ligand. *Colloids Surf B Biointerfaces* **2011**, *86* (1), 35–44. https://doi.org/10.1016/j.colsurfb.2011.03.012.

(241) Nagaraj, K.; Arunachalam, S. Synthesis, CMC Determination, Nucleic Acid Binding and Cytotoxicity of a Surfactant-Cobalt(III) Complex: Effect of Ionic Liquid Additive. *New J. Chem.* **2014**, *38* (1), 366–375. https://doi.org/10.1039/c3nj00832k.

(242) Riyasdeen, A.; Senthilkumar, R.; Periasamy, V. S.; Preethy, P.; Srinag, S.; Zeeshan, M.; Krishnamurthy, H.; Arunachalamb, S.; Akbarsha, M. A. Antiproliferative and Apoptosis-Induction Studies of a Metallosurfactant in Human Breast Cancer Cell MCF-7. *RSC Adv.* **2014**, *4* (91), 49953–49959. https://doi.org/10.1039/c4ra06702a.

(243) Perera-Bobusch, C.; Hormann, J.; Weise, C.; Wedepohl, S.; Dernedde, J.; Kulak, N. Significantly Enhanced Proteolytic Activity of Cyclen Complexes by Monoalkylation. *Dalton Trans.* **2016**, *45* (26), 10500–10504. https://doi.org/10.1039/c6dt00681g.

(244) Manabe, K.; Mori, Y.; Wakabayashi, T.; Nagayama, S.; Kobayashi, S. Organic Synthesis inside Particles in Water: Lewis Acid - Surfactant-Combined Catalysts for Organic Reactions in Water Using Colloidal Dispersions as Reaction Media. *J. Am. Chem. Soc.* **2000**, *122* (30), 7202–7207. https://doi.org/10.1021/ja001420r.

(245) Peng, Q.; Yang, Y.; Wang, C.; Liao, X.; Yuan, Y. Aqueous Biphasic Hydroformylation of Higher Olefins Catalyzed by Rhodium Complexes with Amphiphilic Ligands of Sulfonated Triphenylphosphine Analog. *Catal. Letters* **2003**, *88* (3–4), 219–225. https://doi.org/10.1023/A:1024078209782.

(246) Ding, H.; Hanson, B. E.; Bartik, T.; Bartik, B. Two-Phase Hydroformylation of Octene-1 with Rhodium Complexes of $P[C_6H_4(CH_2)MC_6H_4\text{-}p\text{-}SO_3Na]_3$ (m =3, 6). Rate and Selectivity Enhancement with Surface-Active Phosphines. *Organometallics* **1994**, *13* (10), 3761–3763. https://doi.org/10.1021/om00022a005.

(247) Fu, H.; Li, M.; Chen, H.; Li, X. Higher Olefin Hydroformylation in Organic/Aqueous Biphasic System Accelerated by Double Long-Chain Cationic Surfactants. *J. Mol. Catal. A Chem.* **2006**, *259* (1–2), 156–160. https://doi.org/10.1016/j.molcata.2006.06.017.

(248) De Wolf, E.; Spek, A. L.; Kuipers, B. W. M.; Philipse, A. P.; Meeldijk, J. D.; Bomans, P. H. H.; Frederik, P. M.; Deelman, B. J.; Van Koten, G. Fluorous Derivatives of $[Rh(COD)(Dppe)]BX_4$ (X=F, Ph): Synthesis, Physical Studies and Application in Catalytic Hydrogenation of 1-Alkenes and 4-Alkynes. *Tetrahedron* **2002**, *58* (20), 3911–3922. https://doi.org/10.1016/S0040-4020(02)00217-X.

(249) Goedheijt, M. S.; Hanson, B. E.; Reek, J. N. H.; Kamer, P. C. J.; Van Leeuwen, P. W. N. M. Accelerated Biphasic Hydroformylation by Vesicle Formation of Amphiphilic Diphosphines. *J. Am. Chem. Soc.* **2000**, *122* (8), 1650–1657. https://doi.org/10.1021/ja9925610.

(250) Sieffert, N.; Wipff, G. Adsorption at the Liquid-Liquid Interface in the Biphasic Rhodium Catalyzed Hydroformylation of Olefins Promoted by Cyclodextrins: A Molecular Dynamics Study. *J. Phys. Chem. B* **2006**, *110* (9), 4125–4134. https://doi.org/10.1021/jp057023q.

(251) Chen, H.; Li, Y.; Chen, J.; Cheng, P.; He, Y. E.; Li, X. Micellar Effect in High Olefin Hydroformylation Catalyzed by Water- Soluble Rhodium Complex. *J. Mol. Catal.* **1999**, *149* (1–2), 1–6. https://doi.org/10.1016/S1381-1169(99)00165-X.

(252) Van Esch, J. H.; Stols, A. L. H.; Nolte, R. J. M. Surfactants Containing Imidazole Ligands. Spontaneous Formation of Vesicles by Addition of Metal Ions. *J. Chem. Soc. Chem. Commun.* **1990**, No. 22, 1658–1660. https://doi.org/10.1039/C39900001658.

(253) Jaeger, D. A.; Peacock, M. F.; Scott Bohle, D. A Surfactant Transition Metal Chelate. *Langmuir* **2003**, *19* (11), 4859–4862. https://doi.org/10.1021/la026894d.

(254) Jaeger, D. A.; Zeng, X.; Wang, Y. A Surfactant Co(III) Chelate Containing Two Tridentate Ligands. *Colloids Surf. A: Physicochem. Eng. Asp.* **2006**, *289* (1–3), 158–162. https://doi.org/10.1016/j.colsurfa.2006.04.025.

(255) Jaeger, D. A.; Jose, R.; Mendoza, A.; Apkarian, R. P. Surfactant Transition Metal Chelates. *Colloids Surf. A: Physicochem. Eng. Asp.* **2007**, *302* (1–3), 186–196. https://doi.org/10.1016/j.colsurfa.2007.02.021.

(256) Santhakumar, K.; Kumaraguru, N.; Arumugham, M. N.; Arunachalam, S. Metallomicelles of Co(III) Coordination Complexes - Synthesis, Characterization and Determination of CMC Values. *Polyhedron*

2006, *25* (7), 1507–1513. https://doi.org/10.1016/j.poly.2005.08.054.

(257) Garg, P.; Kaur, G.; Chaudhary, G. R.; Gawali, S. L.; Hassan, P. A. Fabrication of Metalosomes (Metal Containing Cationic Liposomes) Using Single Chain Surfactants as a Precursor: Via Formation of Inorganic Organic Hybrids. *Phys. Chem. Chem. Phys.* **2017**, *19* (37), 25764–25773. https://doi.org/10.1039/c7cp02908j.

(258) Scrimin, P.; Tecilla, P.; Tonellato, U.; Vendrame, T. Aggregate Structure and Ligand Location Strongly Influence Copper(II) Binding Ability of Cationic Metallosurfactants. *J. Org. Chem.* **1989**, *54*, 5988–5991. https://doi.org/10.1021/jo00286a037.

(259) Wagay, T. A.; Ismail, K. Assessment of the Aggregation and Adsorption Behavior of Newly Synthesized and Their Interaction with Bovine Serum Albumin. *New J. Chem.* **2020**, *44*, 15018–15030. https://doi.org/10.1039/d0nj02169e.

(260) Valls, E.; Solsona, A.; Suades, J.; Mathieu, R.; Comelles, F.; López-Iglesias, C. Synthesis and Characterization of New Amphiphilic Phosphines and Palladium Metallosurfactants. *Organometallics* **2002**, *21* (12), 2473–2480. https://doi.org/10.1021/om020067q.

(261) Condom, M.; Suades, J. One Step Synthesis of a New Asymmetric Water-Soluble Phosphine. *Inorg. Chem. Commun.* **2005**, *8* (4), 355–357. https://doi.org/10.1016/j.inoche.2005.01.015.

(262) Menger, F. M.; Keiper, J. S. Gemini Surfactants. *Angew. Chem. Int. Ed.* **2000**, *39* (11), 1906–1920. https://doi.org/10.1533/9781845698614.151.

(263) Solsona, A.; Suades, J.; Mathieu, R. Hydridorhodium(I) Complexes with Amphiphilic Polyether Phosphines. NMR Study and Biphasic Hydroformylation of 1-Octene. *J. Organomet. Chem.* **2003**, *669* (1–2), 172–181. https://doi.org/10.1016/S0022-328X(03)00040-8.

(264) Sharma, N. K.; Singh, M.; Bhattarai, A. Hydrophobic Study of Increasing Alkyl Chain Length of Platinum Surfactant Complexes: Synthesis, Characterization, Micellization, Thermodynamics, Thermogravimetrics and Surface Morphology. *RSC Adv.* **2016**, *6* (93), 90607–90623. https://doi.org/10.1039/c6ra20330b.

(265) Sharma, N. K.; Singh, M. New Class of Platinum Based Metallosurfactant: Synthesis, Micellization, Surface, Thermal Modelling and in Vitro Biological Properties. *J. Mol. Liq.* **2018**, *268*, 55–65. https://doi.org/10.1016/j.molliq.2018.07.041.

(266) Parera, E.; Comelles, F.; Barnadas, R.; Suades, J. New Surfactant Phosphine Ligands and Platinum(II) Metallosurfactants. Influence of Metal Coordination on the Critical Micelle Concentration and Aggregation Properties. *Langmuir* **2010**, *26* (2), 743–751. https://doi.org/10.1021/la902459f.

(267) Aydogan, N.; Abbott, N. L. Comparison of the Surface Activity and Bulk Aggregation of Ferrocenyl Surfactants with Cationic and Anionic Headgroups. *Langmuir* **2001**, *17* (19), 5703–5706. https://doi.org/10.1021/la010178e.

(268) Kakizawa, Y.; Sakai, H.; Yamaguchi, A.; Kondo, Y.; Yoshino, N.; Abe, M. Electrochemical Control of Vesicle Formation with a Double-Tailed Cationic Surfactant Bearing Ferrocenyl Moieties. *Langmuir* **2001**, *2001* (17), 8044–8048. https://doi.org/10.1021/la010772o.

(269) Kakizawa, Y.; Sakai, H.; Nishiyama, K.; Abe, M.; Shoji, H.; Kondo, Y.; Yoshino, N. Solution Properties of Double-Tailed Cationic Surfactants Having Ferrocenyl Groups in Their Hydrophobic Moieties. *Langmuir* **1996**, *12* (4), 921–924. https://doi.org/10.1021/la950600p.

(270) Parera, E.; Comelles, F.; Suades, J. Formation of Vesicles with an Organometallic Amphiphile Bilayer by Supramolecular Arrangement of Metal Carbonyl Metallosurfactants. *Chem. Commun.* **2011**, *47*, 4460–4462. https://doi.org/10.1039/c0cc05493c.

(271) Parera, E.; Marín-García, M.; Pons, R.; Comelles, F.; Suades, J.; Barnadas-Rodríguez, R. Supramolecular Arrangement of Molybdenum Carbonyl Metallosurfactants with CO-Releasing Properties. *Organometallics* **2016**, *35* (4), 484–493. https://doi.org/10.1021/acs.organomet.5b00917.

(272) Wang, J.; Wang, A. Z.; Lv, P.; Tao, W.; Liu, G. Advancing the Pharmaceutical Potential of Bioinorganic Hybrid Lipid-Based Assemblies. *Adv. Sci.* **2018**, *5* (9). https://doi.org/10.1002/advs.201800564.

(273) Hainfeld, J. F.; Furuya, F. R.; Powell, R. D. Metallosomes. *J. Struct. Biol.* **1999**, *127* (2), 152–160. https://doi.org/10.1006/jsbi.1999.4145.

(274) Marín-García, M.; Benseny-Cases, N.; Camacho, M.; Perrie, Y.; Suades, J.; Barnadas-Rodríguez, R. Metallosomes for Biomedical Applications by Mixing Molybdenum Carbonyl Metallosurfactants and Phospholipids. *Dalton Trans.* **2018**, *47* (40), 14293–14303. https://doi.org/10.1039/c8dt01584h.

(275) Marín-García, M.; Benseny-Cases, N.; Camacho, M.; Suades, J.; Barnadas-Rodríguez, R. Low-Toxicity Metallosomes for Biomedical Applications by Self-Assembly of Organometallic Metallosurfactants and Phospholipids. *Chem. Commun.* **2017**, *53* (60), 8455–8458. https://doi.org/10.1039/c7cc04945e.

(276) Sakla, R.; Jose, D. A. Vesicles Functionalized with a CO-Releasing Molecule for Light- Induced CO Delivery. *Appl. Mater. Interfaces* **2018**, *10*, 14214–14220. https://doi.org/10.1021/acsami.8b03310.

(277) Gruber, B.; Stadlbauer, S.; Woinaroschy, K.; König, B. Luminescent Vesicular Receptors for the Recognition of Biologically Important Phosphate Species. *Org. Biomol. Chem.* **2010**, *8* (16), 3704–3714. https://doi.org/10.1039/c004916f.

(278) Gruber, B.; Kataev, E.; Aschenbrenner, J.; Stadlbauer, S.; König, B. Vesicles and Micelles from Amphiphilic Zinc(II)-Cyclen Complexes as Highly Potent Promoters of Hydrolytic DNA Cleavage. *J. Am. Chem. Soc.* **2011**, *133* (51), 20704–20707. https://doi.org/10.1021/ja209247w.

(279) Aryal, S.; Hu, C. M. J.; Zhang, L. Synthesis of Ptsome: A Platinum-Based Liposome-like Nanostructure. *Chem. Commun.* **2012**, *48* (20), 2630–2632. https://doi.org/10.1039/c2cc18176b.

(280) Borràs, J.; Mesa, V.; Barnadas-Rodríguez, R.; Suades, J. Direct Synthesis of Rhenium and Technetium-99m Metallosurfactants by a Transmetallation Reaction of Lipophilic Groups: Potential Applications in the Radiolabeling of Liposomes. *Langmuir* **2020**, *36*, 1993–2002. https://doi.org/10.1021/acs.langmuir.9b03231.

(281) Askes, S. H. C.; Bahreman, A.; Bonnet, S. Activation of a Photodissociative Ruthenium Complex by Triplet-Triplet Annihilation Upconversion in Liposomes. *Angew. Chem. Int. Ed.* **2014**, *53* (4), 1029–1033. https://doi.org/10.1002/anie.201309389.

(282) Côte, A. P.; Shimizu, G. K. H. The Supramolecular Chemistry of the Sulfonate Group in Extended Solids. *Coord. Chem. Rev.* **2003**, *245*, 49–64. https://doi.org/10.1016/S0010-8545(03)00033-X.

(283) Di, L.; Kerns, E. H. Solubility. In *Drug-Like Properties*; Elsevier Inc., 2016; pp 61–93. https://doi.org/10.1016/B978-0-12-801076-1.00007-1.

(284) Lambert, I. H.; Kristensen, D. M.; Holm, J. B.; Mortensen, O. H. Physiological Role of Taurine – from Organism to Organelle. *Acta Physiol.* **2015**, *213* (1), 191–212. https://doi.org/10.1111/apha.12365.

(285) Schaffer, S.; Kim, H. W. Effects and Mechanisms of Taurine as a Therapeutic Agent. *Biomol. Ther.* **2018**, *26* (3), 225–241. https://doi.org/10.4062/biomolther.2017.251.

(286) Kosswig, K. Sulfonic Acids, Aliphatic. In *ULLMANN'S Encyclopedia of Industrial Chemistry*; Wiley-VCH, 2000; pp 1–4. https://doi.org/10.1002/14356007.a25_503.

(287) Arnold J. Gordon, R. A. F. *The Chemist's Companion: A Handbook of Practical Data, Techniques, and References*, 6th ed.; Wiley-VCH: New York, 1972.

(288) Rahiminezhad, A.; Eslami Moghadam, M.; Divsalar, A.; Mesbah, A. W. In Vitro Activity, Stability, and Lipophilicity Changes of Cisplatin through Substitution of Different Amine Ligands. *J. Iran. Chem. Soc.* **2022**, *19* (2). https://doi.org/10.1007/s13738-022-02491-1.

(289) Shreve, R. N.; Burtsfield, D. R. Amination in Liquid Ammonia. *Ind. Eng. Chem.* **1941**, *33* (1), 218–221. https://doi.org/10.1021/ie50374a016.

(290) Gibson, M. S.; Bradshaw, R. W. The Gabriel Synthesis of Primary Amines. *Angew. Chem. Int. Ed.* **1968**, *7* (12), 919–930. https://doi.org/10.1002/anie.196809191.

(291) Wedgwood, J. L.; Hunter, A. P.; Kresinski, R. A.; Platt, A. W. G.; Stein, B. K. Water Soluble Platinum(II) and Palladium(II) Complexes of Alkyl Sulfonated Phosphines. *Inorganica Chim. Acta* **1999**, *290*, 189–196.

https://doi.org/10.1016/S0020-1693(99)00140-1.

(292) Deng, H.; Liu, X.; Xie, J.; Yin, R.; Huang, N.; Gu, Y.; Zhao, J. Quantitative and Site-Directed Chemical Modification of Hypocrellins toward Direct Drug Delivery and Effective Photodynamic Activity. *J. Med. Chem.* **2012**, *55*, 1910–1919. https://doi.org/10.1021/jm2017368.

(293) Steckel, A.; Schlosser, G. An Organic Chemist's Guide to Electrospray Mass Spectrometric Structure Elucidation. *Molecules* **2019**, *24* (3), 1–11. https://doi.org/10.3390/molecules24030611.

(294) Weber, R.; Levsen, K.; Louter, G. J.; Henk Boerboom, A. J.; Haverkamp, J. Direct Mixture Analysis of Surfactants by Combined Field Desorption/Collisionally Activated Dissociation Mass Spectrometry with Simultaneous Ion Detection. *Anal. Chem.* **1982**, *54* (9), 1458–1466. https://doi.org/10.1021/ac00246a005.

(295) Lyon, P. A.; Stebbings, W. L.; Crow, F. W.; Tomer, K. B.; Lippstreu, D. L.; Gross, M. L. Analysis of Anionic Surfactants by Mass Spectrometry/Mass Spectrometry with Fast Atom Bombardment. *Anal. Chem.* **1984**, *56* (1), 8–13. https://doi.org/10.1021/ac00265a004.

(296) Siuzdak, G.; Bothner, B. Gas-Phase Micelles. *Angew. Chem. Int. Ed.* **1995**, *34* (18), 2053–2055. https://doi.org/10.1002/anie.199520531.

(297) Bongiorno, D.; Ceraulo, L.; Ruggirello, A.; Liveri, V. T.; Basso, E.; Seraglia, R.; Traldi, P. Surfactant Self-Assembling in Gas Phase: Electrospray Ionization- and Matrix-Assisted Laser Desorption/Ionization-Mass Spectrometry of Singly Charged AOT Clusters. *J. Mass Spectrom.* **2005**, *40* (12), 1618–1625. https://doi.org/10.1002/jms.965.

(298) Ceraulo, L.; Giorgi, G.; Liveri, V. T.; Bongiorno, D.; Indelicato, S.; Gaudio, F. Di; Indelicato, S. Mass Spectrometry of Surfactant Aggregates. *Eur. J. Mass Spectrom.* **2011**, *17* (6), 525–541. https://doi.org/10.1255/ejms.1158.

(299) Fujimori, K. The Infrared Spectra of Alkane-1-Sulfonates. *Bull. Chem. Soc. Jpn.* **1959**, *32* (8), 850–852. https://doi.org/10.1246/bcsj.32.850.

(300) Zundel, G. Hydration Structure and Intermolecular Interaction in Polyelectrolytes. *Angew. Chem. Int. Ed.* **1969**, *8* (7), 499–509. https://doi.org/10.1002/anie.196904991.

(301) ACS Division of Organic Chemistry. Hans Reich's Collection. Bordwell pKa Table https://organicchemistrydata.org/hansreich/resources/pka/ (accessed 2021 -10 -05).

(302) Heacock, R. A.; Marion, L. The Infrared Spectra of Secondary Amines. *Can. J. Chem.* **1956**, *34*, 1782–1795. https://doi.org/10.1139/v56-231.

(303) Barnadas-Rodríguez, R.; Estelrich, J. Photophysical Changes of Pyranine Induced by Surfactants: Evidence of Premicellar Aggregates. *J. Phys. Chem. B* **2009**, *113* (7), 1972–1982. https://doi.org/10.1021/jp806808u.

(304) Barnadas-Rodríguez, R. Effect and Mechanism of Association of 8-Hydroxy-1,3,6-Pyrenetrisulfonic Acid to Chitosan: Physicochemical Properties of the Complex. *Macromol. Chem. Phys.* **2013**, *214* (1), 99–106. https://doi.org/10.1002/macp.201200266.

(305) Penfold, J.; Thomas, R. K.; Zhang, X. L.; Taylor, D. J. F. Nature of Amine - Surfactant Interactions at the Air - Solution Interface. *Langmuir* **2009**, *25* (7), 3972–3980. https://doi.org/10.1021/la8024843.

(306) Caron, G.; Ermondi, G.; Scherrer, R. A. Lipophilicity, Polarity, and Hydrophobicity. In *Comprehensive Medicinal Chemistry II*; Taylor, J. B., Triggle, D. J., Eds.; Elsevier, 2007; pp 425–452. https://doi.org/10.1016/B0-08-045044-X/00135-8.

(307) Barnadas-Rodríguez, R.; Cladera, J. Steroidal Surfactants: Detection of Premicellar Aggregation, Secondary Aggregation Changes in Micelles, and Hosting of a Highly Charged Negative Substance. *Langmuir* **2015**, *31* (33), 8980–8988. https://doi.org/10.1021/acs.langmuir.5b01352.

(308) (HSDB), H. S. D. B. PubChem Annotation Record for Ethylamine https://pubchem.ncbi.nlm.nih.gov/source/hsdb/803 (accessed 2021 -10 -05).

(309) (HSDB), H. S. D. B. PubChem Annotation Record for 1-Hexylamine https://pubchem.ncbi.nlm.nih.gov/source/hsdb/8444. (accessed 2021 -10 -05).

(310) (HSDB), H. S. D. B. PubChem Annotation Record for Decylamine https://pubchem.ncbi.nlm.nih.gov/source/hsdb/7324 (accessed 2021 -10 -05).

(311) Considerations, G.; Good, E.; Izawa, S. Hydrogen Ion Buffers. *Methods Enzymol.* **1972**, *24*, 53–68. https://doi.org/10.1016/0076-6879(72)24054-X.

(312) Long, R. D.; Jr, N. P. H.; Chhatre, S. A.; Timofeeva, T. V; Yakovenko, A. A.; Dei, D. K.; Mensah, E. A. Comparison of Zwitterionic N -Alkylaminomethane- Sulfonic Acids to Related Compounds in the Good Buffer Series. *Beilstein J. Org. Chem.* **2010**, *7* (31), 1–7. https://doi.org/10.3762/bjoc.6.31.

(313) Mezei, A.; Pérez, L.; Pinazo, A.; Comelles, F.; Infante, M. R.; Pons, R. Self Assembly of PH-Sensitive Cationic Lysine Based Surfactants. *Langmuir* **2012**, *28* (49), 16761–16771. https://doi.org/10.1021/la304117f.

(314) Ràfols, C.; Subirats, X.; Rubio, J.; Rosés, M.; Bosch, E. Lipophilicity of Amphoteric and Zwitterionic Compounds: A Comparative Study of Determination Methods. *Talanta* **2017**, *162* (June 2016), 293–299. https://doi.org/10.1016/j.talanta.2016.10.038.

(315) Shao, Q.; Jiang, S. Molecular Understanding and Design of Zwitterionic Materials. *Adv. Mater.* **2015**, *27* (1), 15–26. https://doi.org/10.1002/adma.201404059.

(316) Anastasiadis, S. H.; Chen, J. K.; Koberstein, J. T.; Siegel, A. F.; Sohn, J. E.; Emerson, J. A. The Determination of Interfacial Tension by Video Image Processing of Pendant Fluid Drops. *J. Colloid Interface Sci.* **1987**, *119* (1), 55–66. https://doi.org/10.1016/0021-9797(87)90244-X.

(317) Li, P. X.; Li, Z. X.; Shen, H. H.; Thomas, R. K.; Penfold, J.; Lu, J. R. Application of the Gibbs Equation to the Adsorption of Nonionic Surfactants and Polymers at the Air-Water Interface: Comparison with Surface Excesses Determined Directly Using Neutron Reflectivity. *Langmuir* **2013**, *29* (30), 9324–9334. https://doi.org/10.1021/la4018344.

(318) Xu, H.; Li, P. X.; Ma, K.; Thomas, R. K.; Penfold, J.; Lu, J. R. Limitations in the Application of the Gibbs Equation to Anionic Surfactants at the Air/Water Surface: Sodium Dodecylsulfate and Sodium Dodecylmonooxyethylenesulfate above and below the CMC. *Langmuir* **2013**, *29* (30), 9335–9351. https://doi.org/10.1021/la401835d.

(319) Li, P. X.; Thomas, R. K.; Penfold, J. Limitations in the Use of Surface Tension and the Gibbs Equation to Determine Surface Excesses of Cationic Surfactants. *Langmuir* **2014**, *30* (23), 6739–6747. https://doi.org/10.1021/la501287v.

(320) Berry, J. D.; Neeson, M. J.; Dagastine, R. R.; Chan, D. Y. C.; Tabor, R. F. Measurement of Surface and Interfacial Tension Using Pendant Drop Tensiometry. *J. Colloid Interface Sci.* **2015**, *454*, 226–237. https://doi.org/10.1016/j.jcis.2015.05.012.

(321) Beattie, J. K.; Djerdjev, A. M.; Gray-Weale, A.; Kallay, N.; Lützenkirchen, J.; Preočanin, T.; Selmani, A. PH and the Surface Tension of Water. *J. Colloid Interface Sci.* **2014**, *422*, 54–57. https://doi.org/10.1016/j.jcis.2014.02.003.

(322) Eastoe, J.; Dalton, J. S. Dynamic Surface Tension and Adsorption Mechanisms of Surfactants at the Air-Water Interface. *Adv. Colloid Interface Sci.* **2000**, *85* (2), 103–144. https://doi.org/10.1016/S0001-8686(99)00017-2.

(323) Fuguet, E.; Ràfols, C.; Rosés, M.; Bosch, E. Critical Micelle Concentration of Surfactants in Aqueous Buffered and Unbuffered Systems. *Anal. Chim. Acta* **2005**, *548* (1–2), 95–100. https://doi.org/10.1016/j.aca.2005.05.069.

(324) Cipollone, M.; De Maria, P.; Fontana, A.; Frascari, S.; Gobbi, L.; Spinelli, D.; Tinti, M. Formation of Micelles and Liposomes from Carnitine Amphiphiles. *Eur. J. Med. Chem.* **2000**, *35* (10), 903–911. https://doi.org/10.1016/S0223-5234(00)01168-5.

(325) Papović, S.; Gadžurić, S.; Bešter-Rogač, M.; Vraneš, M. Effect of the Alkyl Chain Length on the Electrical Conductivity of Six (Imidazolium-Based Ionic Liquids+γ-Butyrolactone) Binary Mixtures. *J. Chem. Thermodynamics* **2016**, *102*, 367–377. https://doi.org/10.1016/j.jct.2016.07.039.

(326) Hanabusa, H.; Takeoka, Y.; Rikukawa, M.; Yoshizawa-Fujita, M. Effect of Alkyl Chain Length in Anions on the Physicochemical Properties of Cellulose-Dissolving Protic Ionic Liquids. *Aust. J. Chem.* **2019**, *72* (2), 55–60. https://doi.org/10.1071/CH18170.

(327) Bijma, K.; Engberts, J. B. F. N. Effect of Counterions on Properties of Micelles Formed by Alkylpyridinium Surfactants. 1. Conductometry and ^{1}H-NMR Chemical Shifts. *Langmuir* **1997**, *13* (18), 4843–4849. https://doi.org/10.1021/la970171q.

(328) Matsuoka, K.; Moroi, Y. Micelle Formation of Sodium Deoxycholate and Sodium Ursodeoxycholate (Part 1). *Biochim. Biophys. Acta - Mol. Cell Biol. Lipids* **2002**, *1580* (2–3), 189–199. https://doi.org/10.1016/S1388-1981(01)00203-7.

(329) Schnablegger, H.; Singh, Y. *The SAXS Guide: Getting Acquainted with the Principles*, 4th ed.; Anton Paar GmbH, 2013.

(330) Cleare, M. J.; Hoeschele, J. D. Studies on the Antitumor Activity of Group VIII Transition Metal Complexes. Part I. Platinum (II) Complexes. *Bioinorg. Chem.* **1973**, *2* (3), 187–210. https://doi.org/10.1016/S0006-3061(00)80249-5.

(331) Thuéry, P.; Atoini, Y.; Harrowfield, J. The Sulfonate Group as a Ligand: A Fine Balance between Hydrogen Bonding and Metal Ion Coordination in Uranyl Ion Complexes. *Dalton Trans.* **2019**, *48* (24), 8756–8772. https://doi.org/10.1039/c9dt01024f.

(332) Wilson, J. J.; Lippard, S. J. Synthetic Methods for the Preparation of Platinum Anticancer Complexes. *Chem. Rev.* **2014**, *114* (8), 4470–4495. https://doi.org/10.1021/cr4004314.

(333) Pantoja, E.; Álvarez-Valdés, A.; Pérez, J. M.; Navarro-Ranninger, C.; Reedijk, J. Synthesis and Characterization of New Cis-[$PtCl_2$(Isopropylamine)(Amine')] Compounds: Cytotoxic Activity and Reactions with 5'-GMP Compared with Their Trans-Platinum Isomers. *Inorganica Chim. Acta* **2002**, *339*, 525–531. https://doi.org/10.1016/S0020-1693(02)01050-2.

(334) Talman, E. G.; Bru, W.; Reedijk, J.; Spek, A. L.; Veldman, N. Crystal and Molecular Structures of Asymmetric Cis - and Trans -Platinum (II / IV) Compounds and Their Reactions with DNA Fragments. *Inorg. Chem.* **1997**, *1669* (6), 854–861.

(335) Marzo, T.; Pillozzi, S.; Hrabina, O.; Kasparkova, J.; Brabec, V.; Arcangeli, A.; Bartoli, G.; Severi, M.; Lunghi, A.; Totti, F.; Gabbiani, C.; Messori, L. Cis-Pt $I_2(NH3)_2$: A Reappraisal. *Dalton Trans.* **2015**, *44*, 14896–14905. https://doi.org/10.1039/c5dt01196e.

(336) Messori, L.; Casini, A.; Gabbiani, C.; Michelucci, E.; Cubo, L.; Ríos-Luci, C.; Padrón, J. M.; Navarro-Ranninger, C.; Quiroga, A. G. Cytotoxic Profile and Peculiar Reactivity with Biomolecules of a Novel "Rule-Breaker" Iodidoplatinum(II) Complex. *ACS Med. Chem. Lett.* **2010**, *1* (8), 381–385. https://doi.org/10.1021/ml100081e.

(337) Souchard, J.; Wimmer, F. L.; Ha, T. T. B.; Johnson, N. P. A Rapid Method for the Synthesis of Water-Soluble Platinum(II) Amine And. *Dalton Trans.* **1990**, 307–310. https://doi.org/10.1039/DT9900000307.

(338) Kumar, S.; Sujeet, S.; Chatterjee, K.; Bhattarai, A. The Effect of Methanol on the Micellar Properties of Dodecyltrimethylammonium Bromide (DTAB) in Aqueous Medium at Different Temperatures. *J. Surfactants Deterg.* **2016**, *19* (1), 201–207. https://doi.org/10.1007/s11743-015-1755-x.

(339) Sparks, R. B.; Elder, J. H. A Simple and Rapid Procedure for the Purification of Plasmid DNA Using Reverse-Phase Cl 8 Silica Beads. *Anal. Biochem.* **1983**, *348*, 345–348. https://doi.org/10.1016/0003-2697(83)90694-2.

(340) Fairclough, M.; Matthews, J.; Mcmahon, A.; Brown, C. A.; Barnett, E.; Jones, A. A Highly Reproducible Method for the Measurement of [6- O -Methyl- 11 C] Diprenorphine and Its Radio-Metabolites Based on Solid-Phase Extraction and Radio-High-Pressure Liquid Chromatography. *J. Label. Compd. Radiopharm.* **2021**, *64*, 30–39. https://doi.org/10.1002/jlcr.3886.

(341) Liu, X.; Schneider, G.; Huhmer, A.; Kuster, B. Trimodal Mixed Mode Chromatography That Enables Efficient Offline Two-Dimensional Peptide Fractionation for Proteome Analysis. *Anal. Chem.* **2017**, *89*, 8884–8891. https://doi.org/10.1021/acs.analchem.7b01356.

(342) Bo, G.; Prefot, P.; Jung, S.; Selzer, S.; Mitra, V.; Britton, D.; Kuhn, K.; Pike, I.; Thompson, A. H. Low-PH Solid-Phase Amino Labeling of Complex Peptide Digests with TMTs Improves Peptide Identi Fi Cation Rates for Multiplexed Global Phosphopeptide Analysis. *J. Proteome Res.* **2015**, *14*, 2500–2510. https://doi.org/10.1021/acs.jproteome.5b00072.

(343) Kelly, A. E.; Ou, H. D.; Withers, R.; Dötsch, V. Low-Conductivity Buffers for High-Sensitivity NMR Measurements. *J. Am. Chem. Soc.* **2002**, *124* (40), 12013–12019. https://doi.org/10.1021/ja026121b.

(344) Lanucara, F.; Holman, S. W.; Gray, C. J.; Eyers, C. E. The Power of Ion Mobility-Mass Spectrometry for Structural Characterization and the Study of Conformational Dynamics. *Nat. Chem.* **2014**, *6*, 281–294. https://doi.org/10.1038/nchem.1889.

(345) Mallis, C. S.; Saha, M. L.; Stang, P. J.; Russell, D. H. Topological Characterization of Coordination-Driven Self-Assembly Complexes: Applications of Ion Mobility-Mass Spectrometry. *J. Am. Soc. Mass Spectrom.* **2019**, *30*, 1654–1662. https://doi.org/10.1007/s13361-019-02276-6.

(346) Rochon, F. D.; Buculei, V. Multinuclear NMR Study and Crystal Structures of Complexes of the Types Cis- and Trans-Pt(Amine)$_2$I$_2$. *Inorganica Chim. Acta* **2004**, *357* (8), 2218–2230. https://doi.org/10.1016/j.ica.2003.10.039.

(347) Region, C.; Allen, A. D. Platinum (II) Complexes: Infrared Spectra in the 300-800 Cm-1 Region. *Can. J. Chem.* **1964**, *42* (11), 1–4. https://doi.org/10.1139/v64-238.

(348) Wang, Y.; Liu, Q.; Qiu, L.; Wang, T.; Yuan, H.; Lin, J.; Luo, S. Molecular Structure, IR Spectra, and Chemical Reactivity of Cisplatin and Transplatin: DFT Studies, Basis Set Effect and Solvent Effect. *Spectrochim. Acta - Part A Mol. Biomol. Spectrosc.* **2015**, *150*, 902–908. https://doi.org/10.1016/j.saa.2015.06.027.

(349) Barbieri, A.; Accorsi, G.; Armaroli, N. Luminescent Complexes beyond the Platinum Group: The D10 Avenue. *Chem. Commun.* **2008**, No. 19, 2185–2193. https://doi.org/10.1039/b716650h.

(350) Messori, L.; Cubo, L.; Gabbiani, C.; Amparo, A.; Michelucci, E.; Pieraccini, G.; Carla, R.; Leo, L. G.; Padro, J. M.; Navarro-ranninger, C. Reactivity and Biological Properties of a Series of Cytotoxic PtI$_2$(Amine)$_2$ Complexes, Either Cis or Trans Configured. *Inorg. Chem.* **2012**, *51*, 1717–1726. https://doi.org/10.1021/ic202036c.

(351) Elding, L. I.; Olsson, L. F. Electronic Absorption Spectra of Square-Planar Chloro-Aqua and Bromo-Aqua Complexes of Palladium(II) and Platinum(II). *J. Phys. Chem.* **1978**, *82* (1), 69–74. https://doi.org/0022-3654/78/2082-0069$01 .OO/O 0.

(352) Marzo, T.; Bartoli, G.; Gabbiani, C.; Pescitelli, G.; Severi, M.; Pillozzi, S.; Michelucci, E.; Fiorini, B.; Quiroga, G.; Messori, L.; Ado, A. A. Cisplatin and Its Dibromido Analogue : A Comparison of Chemical and Biological Profiles. *Biometals* **2016**, *29*, 535–542. https://doi.org/10.1007/s10534-016-9934-4.

(353) Smedley, S. B.; Zimudzi, T. J.; Chang, Y.; Bae, C.; Hickner, M. A. Spectroscopic Characterization of Sulfonate Charge Density in Ion-Containing Polymers. *J. Phys. Chem. B* **2017**, *121* (51), 11504–11510. https://doi.org/10.1021/acs.jpcb.7b06904.

(354) Mitra, I.; Mukherjee, S.; B, V. P. R.; Dasgupta, S.; K, J. C. B.; Mukherjee, S.; Linert, W.; Moi, S. C. Benzimidazole Based Pt(II) Complexes with Better Normal Cell Viability than Cisplatin: Synthesis, Substitution Behavior, Cytotoxicity, DNA Binding and DFT Study. *RSC Adv.* **2016**, *6*, 76600–76613. https://doi.org/10.1039/c6ra17788c.

(355) Sánchez-Férez, F.; Rius-Bartra, J. M.; Calvet, T.; Font-Bardia, M.; Pons, J. Steric and Electronic Effects on the Structure and Photophysical Properties of Hg(II) Complexes. *Inorg. Chem.* **2021**, *60* (6), 3851–3870. https://doi.org/10.1021/acs.inorgchem.0c03640.

(356) Feng, R.; Yu, X.; Autschbach, J. Spin-Orbit Natural Transition Orbitals and Spin-Forbidden Transitions. *J. Chem. Theory Comput.* **2021**, *17* (12), 7531–7544. https://doi.org/10.1021/acs.jctc.1c00776.

(357) Moulder, J. F.; Stickle, W. F.; Sobol, P. E.; Bomben, K. D. *Handbook of X-Ray Photoelectron Spectroscopy*; Chastain, J., Ed.; Perkin-Elmer Corporation, 1993.

(358) Hofman, S. *Auger-and X-Ray Phhotoelectron Spectrosocpy in Materials Science*; Ertl G., Luth H., M. D. L., Ed.; Springer Berlin Heidelberg, 2013. https://doi.org/10.1007/978-3-642-27381-0.

(359) Beatty, M. E. S.; Chen, H.; Labrador, N. Y.; Lee, B. J.; Esposito, D. V. Structure-Property Relationships Describing the Buried Interface between Silicon Oxide Overlayers and Electrocatalytic Platinum Thin Films. *J. Mater. Chem. A* **2018**, *6* (44), 22287–22300. https://doi.org/10.1039/C8TA06969G.

(360) Biesinger, M. XPS Reference Pages http://www.xpsfitting.com/search/label/Iodine (accessed 2021 -01 - 22).

(361) Graf, N.; Yegen, E.; Gross, T.; Lippitz, A.; Weigel, W.; Krakert, S.; Terfort, A.; Unger, W. E. S. XPS and NEXAFS Studies of Aliphatic and Aromatic Amine Species on Functionalized Surfaces. *Surf. Sci.* **2009**, *603* (18), 2849–2860. https://doi.org/10.1016/j.susc.2009.07.029.

(362) Truica-Marasescu, F.; Wertheimer, M. R. Nitrogen-Rich Plasma-Polymer Films for Biomedical Applications. *Plasma Process. Polym.* **2008**, *5* (1), 44–57. https://doi.org/10.1002/ppap.200700077.

(363) Ederer, J.; Janoš, P.; Ecorchard, P.; Tolasz, J.; Štengl, V.; Beneš, H.; Perchacz, M.; Pop-Georgievski, O. Determination of Amino Groups on Functionalized Graphene Oxide for Polyurethane Nanomaterials: XPS Quantitation vs. Functional Speciation. *RSC Adv.* **2017**, *7* (21), 12464–12473. https://doi.org/10.1039/c6ra28745j.

(364) Yoshida, T. An X-Ray Photoelectron Spectroscopic Study of Dioxime Metal Complexes. *Bull. Chem. Soc. Jpn.* **1978**, *51*, 3257–3260. https://doi.org/10.1246/bcsj.51.3257.

(365) Zakharova, I. A.; Salyn, J. V.; Tatjanenko, L. V.; Mashkovsky, Y. S.; Ponticelli, G. Inhibitory Activity of Palladium(II) and Platinum(II) Complexes with Isoxazole and Its Derivatives. *J. Inorg. Biochem.* **1981**, *15* (1), 89–92. https://doi.org/10.1016/S0162-0134(00)80138-5.

(366) Battistoni, C.; Giuliani, A. M.; Paparazzo, E.; Tarli, F. Platinum Complexes of the Methyl Esters of Dithiocarbazic Acid and 3-Phenyldithiocarbazic Acid. *J. Chem. Soc. Dalt. Trans.* **1984**, No. 7, 1293–1299. https://doi.org/10.1039/DT9840001293.

(367) Contour, J. P.; Mouvier, G.; Hoogewys, M.; Leclere, C. X-Ray Photoelectron Spectroscopy and Electron Microscopy of PtRh Gauzes Used for Catalytic Oxidation of Ammonia. *J. Catal.* **1977**, *48*, 217–228. https://doi.org/10.1016/0021-9517(77)90093-8.

(368) Clark, D. T.; Adams, D. B.; Briggs, D. X-Ray Photoelectron Studies of Platinum and Palladium Complexes; Observation of the Trans-Influence and Distinction between Terminal and Bridging Chlorine. *J. Chem. Soc. D Chem. Commun.* **1971**, No. 12, 602–604. https://doi.org/10.1039/C29710000602.

(369) Inglezakis, V. J.; Satayeva, A.; Yagofarova, A.; Tauanov, Z.; Meiramkulova, K.; Farrando-Pérez, J.; Bear, J. C. Surface Interactions and Mechanisms Study on the Removal of Iodide from Water by Use of Natural Zeolite-Based Silver Nanocomposites. *Nanomaterials* **2020**, *10* (6). https://doi.org/10.3390/nano10061156.

(370) Matin, M. A.; Lee, E.; Kim, H.; Yoon, W. S.; Kwon, Y. U. Rational Syntheses of Core-Shell Fe@(PtRu) Nanoparticle Electrocatalysts for the Methanol Oxidation Reaction with Complete Suppression of CO-Poisoning and Highly Enhanced Activity. *J. Mater. Chem. A* **2015**, *3* (33), 17154–17164. https://doi.org/10.1039/c5ta03809j.

(371) Dang, D.; Zou, H.; Xiong, Z.; Hou, S.; Shu, T.; Nan, H.; Zeng, X.; Zeng, J.; Liao, S. High-Performance, Ultralow Platinum Membrane Electrode Assembly Fabricated by In Situ Deposition of a Pt Shell Layer on Carbon-Supported Pd Nanoparticles in the Catalyst Layer Using a Facile Pulse Electrodeposition Approach. *ACS Catal.* **2015**, *5* (7), 4318–4324. https://doi.org/10.1021/acscatal.5b00030.

(372) Vinayan, B. P.; Ramaprabhu, S. Platinum-TM (TM = Fe, Co) Alloy Nanoparticles Dispersed Nitrogen Doped (Reduced Graphene Oxide-Multiwalled Carbon Nanotube) Hybrid Structure Cathode Electrocatalysts for High Performance PEMFC Applications. *Nanoscale* **2013**, *5* (11), 5109–5118. https://doi.org/10.1039/c3nr00585b.

(373) Riggs, W. M. X-Ray Photoelectron Spectrometry of Platinum Compounds. *Anal. Chem.* **1972**, *44* (4), 830–832. https://doi.org/10.1021/ac60312a041.

(374) Boschloo, G.; Hagfeldt, A. Characteristics of the Iodide / Triiodide Redox Mediator in Dye-Sensitized Solar Cells. *Acc. Chem. Res.* **2009**, *42* (11), 1819–1826. https://doi.org/10.1021/ar900138m.

(375) Bard, J. A.; Parsons, R.; Jordan, J. *Standard Potentials in Aqueous Solution*, 1st ed.; Bard, J. A., Parsons, R., Jordan, J., Eds.; Dekker, M.: New York, 1985.

(376) Swift, E. H.; Butler, E. A. *Quantitative Measurements and Chemical Equilibria*, 1st ed.; Swift, E. H., Butler, E. A., Eds.; W. H. Freeman: San Francisco, 1972.

(377) Falke, S.; Betzel, C. Dynamic Light Scattering (DLS): Principles, Perspectives, Applications to Biological Samples. In *Radiation in Bioanalysis*; Pereira A., Tavares P., L.-V. P., Ed.; Springer International Publishing, 2019; Vol. 8, pp 173–193. https://doi.org/10.1007/978-3-030-28247-9.

(378) Topel, Ö.; Çakir, B. A.; Budama, L.; Hoda, N. Determination of Critical Micelle Concentration of Polybutadiene-Block- Poly(Ethyleneoxide) Diblock Copolymer by Fluorescence Spectroscopy and Dynamic Light Scattering. *J. Mol. Liq.* **2013**, *177*, 40–43. https://doi.org/10.1016/j.molliq.2012.10.013.

(379) Nagai, A.; Nagai, Y.; Qu, H.; Zhang, S. Dynamic Behaviors of Lipid-like Self-Assembling Peptide A 6D and A 6K Nanotubes. *J. Nanosci. Nanotechnol.* **2007**, *7* (7), 2246–2252. https://doi.org/10.1166/jnn.2007.647.

(380) Benjamin Chu. Laser Light Scattering. *Annu. Rev. Phys. Chem.* **1970**, *21*, 145–174. https://doi.org/10.1146/annurev.pc.21.100170.001045.

(381) Danino, D. Cryo-TEM of Soft Molecular Assemblies. *Curr. Opin. Colloid Interface Sci.* **2012**, *17* (6), 316–329. https://doi.org/10.1016/j.cocis.2012.10.003.

(382) Dobro, M. J.; Melanson, L. A.; Jensen, G. J.; Mcdowall, A. W. Plunge Freezing for Electron Cryomicroscopy. In *Methods in Enzymology*; J.Jensen, G., Ed.; Elsevier Masson SAS, 2010; Vol. 481, pp 63–82. https://doi.org/10.1016/S0076-6879(10)81003-1.

(383) Newbury, D. E.; Ritchie, N. W. M. Is Scanning Electron Microscopy/Energy Dispersive X-Ray Spectrometry (SEM/EDS) Quantitative? *Scanning* **2013**, *35* (3), 141–168. https://doi.org/10.1002/sca.21041.

(384) Newbury, D. E.; Ritchie, N. W. M. Performing Elemental Microanalysis with High Accuracy and High Precision by Scanning Electron Microscopy/Silicon Drift Detector Energy-Dispersive X-Ray Spectrometry (SEM/SDD-EDS). *J. Mater. Sci.* **2014**, *50* (2), 493–518. https://doi.org/10.1007/s10853-014-8685-2.

(385) Harada, Y.; Ikuhara, Y. The Latest Analytical Electron Microscope and Its Application to Ceramics. In *Handbook of Advanced Ceramics: Materials, Applications, Processing, and Properties: Second Edition*; Somiya, S., Ed.; Elsevier Inc., 2013; pp 3–21. https://doi.org/10.1016/B978-0-12-385469-8.00001-0.

(386) Wolfgong, W. J. Chemical Analysis Techniques for Failure Analysis: Part 1, Common Instrumental Methods. In *Handbook of Materials Failure Analysis with Case Studies from the Aerospace and Automotive Industries*; Makhlouf, A. S. H., Aliofkhazraei, M., Eds.; Elsevier Ltd., 2016; pp 279–307. https://doi.org/10.1016/B978-0-12-800950-5.00014-4.

(387) Pabisch, S.; Feichtenschlager, B.; Kickelbick, G.; Peterlik, H. Effect of Interparticle Interactions on Size Determination of Zirconia and Silica Based Systems – A Comparison of SAXS , DLS , BET , XRD and TEM. *Chem. Phys. Lett.* **2012**, *521*, 91–97. https://doi.org/10.1016/j.cplett.2011.11.049.

(388) Fissan, H.; Ristig, S.; Kaminski, H. Comparison of Different Characterization Methods for Nanoparticle Dispersions before and after Aerosolization. *Anal. Methods* **2014**, *6*, 7324–7334. https://doi.org/10.1039/c4ay01203h.

(389) Tomaszewska, E.; Soliwoda, K.; Kadziola, K.; Tkacz-szczesna, B.; Celichowski, G.; Cichomski, M.; Szmaja, W.; Grobelny, J. Detection Limits of DLS and UV-Vis Spectroscopy in Characterization of Polydisperse Nanoparticles Colloids. *J. Nanomater.* **2013**, *2013*. https://doi.org/10.1155/2013/313081.

(390) Griffiths, P. C.; Fallis, I. A.; Tatchell, T.; Bushby, L.; Beeby, A. Aqueous Solutions of Transition Metal Containing Micelles. *Adv. Colloid Interface Sci.* **2008**, *144*, 13–23. https://doi.org/10.1016/j.cis.2008.08.001.

(391) Menger, F. M.; Shi, L.; Rizvi, S. A. A. Re-Evaluating the Gibbs Analysis of Surface Tension at the Air / Water Interface. *J. Am. Chem. Soc.* **2009**, *131* (30), 10380–10381. https://doi.org/10.1021/ja9044289.

(392) Miller, S. E.; House, D. A. The Hydrolysis Products of Cis-Dichlorodiammineplatinum(II) 2. The Kinetics of Formation and Anation of the Cis-Diamminedi(Aqua)Platinum(II) Cation. *Inorganica Chim. Acta* **1989**, *166*

(2), 189–197. https://doi.org/10.1016/S0020-1693(00)80810-5.

(393) Eloy, J. O.; Claro de Souza, M.; Petrilli, R.; Barcellos, J. P. A.; Lee, R. J.; Marchetti, J. M. Liposomes as Carriers of Hydrophilic Small Molecule Drugs: Strategies to Enhance Encapsulation and Delivery. *Colloids Surf B Biointerfaces* **2014**, *123*, 345–363. https://doi.org/10.1016/j.colsurfb.2014.09.029.

(394) *Liposomes Methods and Protocols, Volume 1: Pharmaceutical Nanocarriers*, 1st ed.; Weissig, V., Ed.; Springer Protocols, 2010; Vol. 1. https://doi.org/10.1007/978-1-60327-360-2.

(395) Bozzuto, G.; Molinari, A. Liposomes as Nanomedical Devices. *Int. J. Nanomedicine* **2015**, *10*, 975. https://doi.org/10.2147/IJN.S68861.

(396) Stewart, J. C. M. Colorimetric Determination of Phospholipids with Ammonium Ferrothiocyanate. *Anal. Biochem.* **1980**, *104* (1), 10–14. https://doi.org/10.1016/0003-2697(80)90269-9.

(397) Guimar, D.; Cavaco-paulo, A.; Nogueira, E. Design of Liposomes as Drug Delivery System for Therapeutic Applications. *Int. J. Pharm.* **2021**, *601*. https://doi.org/10.1016/j.ijpharm.2021.120571.

(398) Anderson, M.; Omri, A. The Effect of Different Lipid Components on the In Vitro Stability and Release Kinetics of Liposome Formulations. *Drug Deliv.* **2004**, *11*, 33–39. https://doi.org/10.1080/10717540490265243.

(399) Bagher, M.; Ahmadi, S.; Dadkhah, M.; Akbar, A.; Niazi, A.; Bahaoddini, A.; Youse, R. Anticancer Activity Assessment of Two Novel Binuclear Platinum (II) Complexes. *J. Photochem. Photobiol. B Biol.* **2016**, *161*, 345–354. https://doi.org/10.1016/j.jphotobiol.2016.05.025.

(400) Koynova, R.; Caffrey, M. Phases and Phase Transitions of the Phosphatidylcholines. *Biochim. Biophys. Acta - Rev. Biomembr.* **1998**, *1376* (1), 91–145. https://doi.org/10.1016/S0304-4157(98)00006-9.

(401) McMullen, T. P.; Vilchèze, C.; McElhaney, R. N.; Bittman, R. Differential Scanning Calorimetric Study of the Effect of Sterol Side Chain Length and Structure on Dipalmitoylphosphatidylcholine Thermotropic Phase Behavior. *Biophys. J.* **1995**, *69* (1), 169–176. https://doi.org/10.1016/S0006-3495(95)79887-3.

(402) Rahnfeld, L.; Thamm, J.; Steiniger, F.; Hoogevest, P. Van; Luciani, P. Study on the in Situ Aggregation of Liposomes with Negatively Charged Phospholipids for Use as Injectable Depot Formulation. *Colloids Surf B Biointerfaces* **2018**, *168*, 10–17. https://doi.org/10.1016/j.colsurfb.2018.02.023.

(403) Colletier, J.; Chaize, B.; Winterhalter, M.; Fournier, D. Protein Encapsulation in Liposomes : Efficiency Depends on Interactions between Protein and Phospholipid Bilayer . *BMC Biotechnol.* **2002**, *8*, 1–8. https://doi.org/10.1186/1472-6750-2-9.

(404) Macquet, J.-P.; Butour, J.-L. A Circular Dichroism Study of DNA - Platinum Complexes. *Eur. J. Biochem.* **1978**, *83*, 375–387. https://doi.org/10.1111/j.1432-1033.1978.tb12103.x.

(405) Vakili-Ghartavol, R.; Rezayat, S. M.; Faridi-Majidi, R.; Sadri, K.; Jaafari, M. R. Optimization of Docetaxel Loading Conditions in Liposomes: Proposing Potential Products for Metastatic Breast Carcinoma Chemotherapy. *Sci. Rep.* **2020**, *10* (1), 1–14. https://doi.org/10.1038/s41598-020-62501-1.

(406) Shein, S. A.; Kuznetsov, I. I.; Abakumova, T. O.; Chelushkin, P. S.; Melnikov, P. A.; Korchagina, A. A.; Bychkov, D. A.; Seregina, I. F.; Bolshov, M. A.; Kabanov, A. V.; Chekhonin, V. P.; Nukolova, N. V. VEGF- and VEGFR2-Targeted Liposomes for Cisplatin Delivery to Glioma Cells. *Mol. Pharm.* **2016**, *13* (11), 3712–3723. https://doi.org/10.1021/acs.molpharmaceut.6b00519.

(407) Abuzar, S.; Park, E. J.; Seo, Y.; Lee, J.; Baik, S. H.; Hwang, S. Preparation and Evaluation of Intraperitoneal Liposomal Depot for Colorectal Cancer Treatment. *Pharmaceutics* **2020**, *12*, 1–17. https://doi.org/10.3390/pharmaceutics12080736.

(408) Bang, K.; Na, Y.; Huh, H. W.; Hwang, S.; Kim, M.; Kim, M.; Lee, H.-K.; Cho, C.-W. The Delivery Strategy of Paclitaxel Nanostructured Lipid Carrier Coated with Platelet Membrane. *Cancers* **2019**, *11* (807), 1–16. https://doi.org/10.3390/cancers11060807.

(409) Andersson, M.; Hammarström, L.; Edwards, K. Effect of Bilayer Phase Transitions on Vesicle Structure and Its Influence on the Kinetics of Viologen Reduction. *J. Phys. Chem.* **1995**, *99* (39), 14531–14538. https://doi.org/10.1021/j100039a047.

(410) Reviakine, I.; Gallego, M.; Johannsmann, D.; Tellechea, E. Adsorbed Liposome Deformation Studied with Quartz Crystal Microbalance. *J. Chem. Phys.* **2012**, *136* (8). https://doi.org/10.1063/1.3687351.

(411) Ickenstein, L. M.; Arfvidsson, M. C.; Needham, D.; Mayer, L. D.; Edwards, K. Disc Formation in Cholesterol-Free Liposomes during Phase Transition. *Biochim. Biophys. Acta - Biomembr.* **2003**, *1614* (2), 135–138. https://doi.org/10.1016/S0005-2736(03)00196-2.

(412) Ickenstein, L. M.; Sandström, M. C.; Mayer, L. D.; Edwards, K. Effects of Phospholipid Hydrolysis on the Aggregate Structure in DPPC/DSPE-PEG2000 Liposome Preparations after Gel to Liquid Crystalline Phase Transition. *Biochim. Biophys. Acta - Biomembr.* **2006**, *1758* (2), 171–180. https://doi.org/10.1016/j.bbamem.2006.02.016.

(413) Awad, D.; Bartok, M.; Mostaghimi, F.; Schrader, I.; Sudumbrekar, N.; Schaffran, T.; Jenne, C.; Eriksson, J.; Winterhalter, M.; Fritz, J.; Edwards, K.; Gabel, D. Halogenated Dodecaborate Clusters as Agents to Trigger Release of Liposomal Contents. *Chempluschem* **2015**, *80* (4), 656–664. https://doi.org/10.1002/cplu.201402286.

(414) Dao, T. P. T.; Fernandes, F.; Er-Rafik, M.; Salva, R.; Schmutz, M.; Brûlet, A.; Prieto, M.; Sandre, O.; Le Meins, J. F. Phase Separation and Nanodomain Formation in Hybrid Polymer/Lipid Vesicles. *ACS Macro Lett.* **2015**, *4* (2), 182–186. https://doi.org/10.1021/mz500748f.

(415) Awad, D.; Damian, L.; Winterhalter, M.; Karlsson, G.; Edwards, K.; Gabel, D. Interaction of $Na_2B_{12}H_{11}SH$ with Dimyristoyl Phosphatidylcholine Liposomes. *Chem. Phys. Lipids* **2009**, *157* (2), 78–85. https://doi.org/10.1016/j.chemphyslip.2008.11.006.

(416) Gabel, D.; Awad, D.; Schaffran, T.; Radovan, D.; Dărăban, D.; Damian, L.; Winterhalter, M.; Karlsson, G.; Edwards, K. The Anionic Boron Cluster $(B_{12}H_{11}SH)_2$- as a Means to Trigger Release of Liposome Contents. *ChemMedChem* **2007**, *2* (1), 51–53. https://doi.org/10.1002/cmdc.200600227.

(417) Pandey, B. N.; Mishra, K. P. Radiation Induced Oxidative Damage Modification by Cholesterol in Liposomal Membrane. *Radiat. Phys. Chem.* **1999**, *54* (5), 481–489. https://doi.org/10.1016/S0969-806X(98)00297-7.

(418) Rantamäki, A. H.; Chen, W.; Hyväri, P.; Helminen, J.; Partl, G.; King, A. W. T.; Wiedmer, S. K. Interactions of Ionic Liquids and Spirocyclic Compounds with Liposome Model Membranes. A Steady-State Fluorescence Anisotropy Study. *Sci. Rep.* **2019**, *9* (1), 1–12. https://doi.org/10.1038/s41598-019-53893-w.

(419) Aleandri, S.; Bonicelli, M. G.; Bordi, F.; Casciardi, S.; Diociaiuti, M.; Giansanti, L.; Leonelli, F.; Mancini, G.; Perrone, G.; Sennato, S. How Stereochemistry Affects the Physicochemical Features of Gemini Surfactant Based Cationic Liposomes. *Soft Matter* **2012**, *8* (21), 5904–5915. https://doi.org/10.1039/c2sm25193k.

(420) Koirala, S.; Roy, B.; Guha, P.; Bhattarai, R.; Sapkota, M.; Nahak, P.; Karmakar, G.; Mandal, A. K.; Kumar, A.; Panda, A. K. Effect of Double Tailed Cationic Surfactants on the Physicochemical Behavior of Hybrid Vesicles. *RSC Adv.* **2016**, *6* (17), 13786–13796. https://doi.org/10.1039/c5ra17774j.

(421) Chen, J.; Cheng, D.; Li, J.; Wang, Y.; Guo, J. X.; Chen, Z. P.; Cai, B. C.; Yang, T. Influence of Lipid Composition on the Phase Transition Temperature of Liposomes Composed of Both DPPC and HSPC. *Drug Dev. Ind. Pharm.* **2013**, *39* (2), 197–204. https://doi.org/10.3109/03639045.2012.668912.

(422) Moreno, M. M.; Garidel, P.; Suwalsky, M.; Howe, J.; Brandenburg, K. The Membrane-Activity of Ibuprofen, Diclofenac, and Naproxen: A Physico-Chemical Study with Lecithin Phospholipids. *Biochim. Biophys. Acta - Biomembr.* **2009**, *1788* (6), 1296–1303. https://doi.org/10.1016/j.bbamem.2009.01.016.

(423) Kuntsche, J.; Freisleben, I.; Steiniger, F.; Fahr, A. Temoporfin-Loaded Liposomes: Physicochemical Characterization. *Eur. J. Pharm. Sci.* **2010**, *40* (4), 305–315. https://doi.org/10.1016/j.ejps.2010.04.005.

(424) Ali, S.; Minchey, S.; Janoff, A.; Mayhew, E. A Differential Scanning Calorimetry Study of Phosphocholines Mixed with Paclitaxel and Its Bromoacylated Taxanes. *Biophys. J.* **2000**, *78* (1), 246–256. https://doi.org/10.1016/S0006-3495(00)76588-X.

(425) Ruso, J. M.; Besada, L.; Martínez-Landeira, P.; Seoane, L.; Prieto, G.; Sarmiento, F. Interactions between Liposomes and Cations in Aqueous Solution. *J. Liposome Res.* **2003**, *13* (2), 131–145.

https://doi.org/10.1081/LPR-120020316.

(426) Wolfram, J.; Suri, K.; Yang, Y.; Shen, J.; Celia, C.; Fresta, M.; Zhao, Y.; Shen, H.; Ferrari, M. Shrinkage of Pegylated and Non-Pegylated Liposomes in Serum. *Colloids Surf B Biointerfaces* **2014**, *114*, 294–300. https://doi.org/10.1016/j.colsurfb.2013.10.009.

(427) Yang, X.; Yu, Y.; Huang, X.; Chen, Q.; Wu, H.; Wang, R.; Qi, R. Delivery of Platinum (II) Drugs with Bulky Ligands in Trans -Geometry for Overcoming Cisplatin Drug Resistance. *Mater. Sci. Eng. C* **2019**, *96*, 96–104. https://doi.org/10.1016/j.msec.2018.10.092.

(428) Modi, S.; Anderson, B. D. Determination of Drug Release Kinetics from Nanoparticles: Overcoming Pitfalls of the Dynamic Dialysis Method. *Mol. Pharm.* **2013**, *10*, 3076–3089. https://doi.org/10.1021/mp400154a.

(429) Wallace, S. J.; Li, J.; Nation, R. L.; Boyd, B. J. Drug Release from Nanomedicines: Selection of Appropiate Encapsulation and Release Methodology. *Drug Deliv. Transl. Res.* **2013**, *2* (4), 284–292. https://doi.org/10.1007/s13346-012-0064-4.Drug.

(430) Rice, J. R.; Gerberich, J. L.; Nowotnik, D. P.; Howell, S. B. Preclinical Efficacy and Pharmacokinetics of AP5346, a Novel Diaminocyclohexane-Platinum Tumor-Targeting Drug Delivery System. *Clin. Cancer Res.* **2006**, *12* (7 I), 2248–2254. https://doi.org/10.1158/1078-0432.CCR-05-2169.

(431) Pei, X.; Zhu, Z.; Gan, Z.; Chen, J.; Zhang, X.; Cheng, X.; Wan, Q.; Wang, J. PEGylated Nano-Graphene Oxide as a Nanocarrier for Delivering Mixed Anticancer Drugs to Improve Anticancer Activity. *Sci. Rep.* **2020**, *10* (1), 1–15. https://doi.org/10.1038/s41598-020-59624-w.

(432) Mahmud, M.; Piwoni, A.; Filiczak, N.; Janicka, M.; Gubernator, J. Long-Circulating Curcumin-Loaded Liposome Formulations with High Incorporation Efficiency , Stability and Anticancer Activity towards Pancreatic Adenocarcinoma Cell Lines In Vitro. *PLoS One* **2016**, *11* (12). https://doi.org/10.1371/journal.pone.0167787.

(433) Miao, Y.; Zhao, X.; Qiu, Y.; Liu, Z.; Yang, W.; Jia, X. Metal − Organic Framework-Assisted Nanoplatform with Hydrogen Peroxide / Glutathione Dual-Sensitive On-Demand Drug Release for Targeting Tumors and Their Microenvironment. *ACS Appl. Bio Mater.* **2019**, *2*, 895–905. https://doi.org/10.1021/acsabm.8b00741.

(434) Dai, Y.; Su, J.; Wu, K.; Ma, W.; Wang, B.; Li, M.; Sun, P.; Shen, Q.; Wang, Q.; Fan, Q. Multifunctional Thermosensitive Liposomes Based on Natural Phase-Change Material: Near-Infrared Light-Triggered Drug Release and Multimodal Imaging-Guided Cancer Combination Therapy. *ACS Appl. Mater. Interfaces* **2019**, *11*, 10540–10553. https://doi.org/10.1021/acsami.8b22748.

(435) Talló, K.; Pons, R.; López, O.; Bosch, M.; Bosch, M.; Cocera, M. Preparation and Characterization of a Supramolecular Hydrogel Made of Phospholipids and Oleic Acid with a High Water Content. *J. Mater. Chem. B* **2020**, *8* (1), 161–167. https://doi.org/10.1039/c9tb01599j.

(436) Vergara, D.; López, O.; Bustamante, M.; Shene, C. An in Vitro Digestion Study of Encapsulated Lactoferrin in Rapeseed Phospholipid–Based Liposomes. *Food Chem.* **2020**, *321* (March), 126717. https://doi.org/10.1016/j.foodchem.2020.126717.

(437) Protas, A. V.; Popova, E. A.; Mikolaichuk, O. V.; Porozov, Y. B.; Mehtiev, A. R.; Ott, I.; Alekseev, G. V.; Kasyanenko, N. A.; Trifonov, R. E. Synthesis, DNA and BSA Binding of Pd(II) and Pt(II) Complexes Featuring Tetrazolylacetic Acids and Their Esters. *Inorganica Chim. Acta* **2018**, *473*, 133–144. https://doi.org/10.1016/j.ica.2017.12.040.

(438) Nikolaou, M.; Pavlopoulou, A.; Georgakilas, A. G.; Kyrodimos, E. The Challenge of Drug Resistance in Cancer Treatment : A Current Overview. *Clin. Exp. Metastasis* **2018**, *35* (4), 309–318. https://doi.org/10.1007/s10585-018-9903-0.

(439) Yamasaki, K.; Chuang, V. T. G.; Maruyama, T.; Otagiri, M. Albumin-Drug Interaction and Its Clinical Implication. *Biochim. Biophys. Acta - Gen. Subj.* **2013**, *1830* (12), 5435–5443. https://doi.org/10.1016/j.bbagen.2013.05.005.

(440) Samper, K. G.; Rodríguez, V.; Ortega-Carrasco, E.; Atrian, S.; Maréchal, J. D.; Cutillas, N.; Zamora, A.; de Haro, C.; Capdevila, M.; Ruiz, J.; Palacios, Ò. Understanding the Interaction of an Antitumoral Platinum (II) 7-Azaindolate Complex with Proteins and DNA. *Biometals* **2014**, *27*, 1159–1177.

https://doi.org/10.1007/s10534-014-9780-1.

(441) Knipp, M.; Karotki, A. V; Chesnov, S.; Natile, G.; Sadler, P. J.; Brabec, V.; Vas, M. Reaction of Zn7 Metallothionein with Cis - and Trans - [Pt(N-Donor)$_2$Cl$_2$] Anticancer Complexes : Trans -Pt II Complexes Retain Their N-Donor Ligands. *J. Med. Chem.* **2007**, *50*, 4075–4086. https://doi.org/10.1021/jm070271l.

(442) Hagrman, D.; Goodisman, J.; Dabrowiak, J. C.; Souid, A. Kinetic Study on the Reaction of Cisplatin with Metallothionein. *Drug Metab. Dispos.* **2003**, *31* (7), 916–923. https://doi.org/10.1124/dmd.31.7.916.

(443) Samper, K. G.; Vicente, C.; Rodríguez, V.; Atrian, S.; Cuitillas, N.; Capdevila, M.; Palacios, Ò. Studying the Interactions of a Platinum (II) 9-Aminoacridine Complex with Proteins and Oligonucleotides by ESI-TOF MS. *Dalton Trans.* **2012**, *41*, 300–306. https://doi.org/10.1039/c1dt11506e.

(444) Shoeib, T.; Sharp, B. L. Monomeric Cisplatin Complexes with Glutathione : Coordination Modes and Binding Affinities. *Inorganica Chim. Acta* **2013**, *405*, 258–264. https://doi.org/10.1016/j.ica.2013.06.006.

(445) Topală, T.; Bodoki, A.; Oprean, L.; Oprean, R. Bovine Serum Albumin Interactions with Metal Complexes. *Clujul Med.* **2014**, *87* (4), 5. https://doi.org/10.15386/cjmed-357.

(446) Chen, S.; Zheng, J.; Li, L.; Jiang, S. Strong Resistance of Phosphorylcholine Self-Assembled Monolayers to Protein Adsorption : Insights into Nonfouling Properties of Zwitterionic Materials. *J. Am. Chem. Soc.* **2005**, No. 17, 14473–14478. https://doi.org/10.1021/ja054169u.

(447) Divsalar, A.; Bagheri, M. J.; Saboury, A. A.; Mansoori-Torshizi, H.; Amani, M. Investigation on the Interaction of Newly Designed Anticancer Pd(II) Complexes with Different Aliphatic Tails and Human Serum Albumin. *J. Phys. Chem. B* **2009**, *113* (42), 14035–14042. https://doi.org/10.1021/jp904822n.

(448) Hemmateenejad, B.; Yousefinejad, S. Interaction Study of Human Serum Albumin and ZnS Nanoparticles Using Fluorescence Spectrometry. *J. Mol. Struct.* **2013**, *1037*, 317–322. https://doi.org/10.1016/j.molstruc.2013.01.009.

(449) Liu, H.; Shi, X.; Xu, M.; Li, Z.; Huang, L.; Bai, D.; Zeng, Z. Transition Metal Complexes of 2, 6-Di ((Phenazonyl-4-Imino) Methyl)-4-Methylphenol: Structure and Biological Evaluation. *Eur. J. Med. Chem.* **2011**, *46* (5), 1638–1647. https://doi.org/10.1016/j.ejmech.2011.02.012.

(450) Wani, T. A.; AlRabiah, H.; Bakheit, A. H.; Kalam, M. A.; Zargar, S. Study of Binding Interaction of Rivaroxaban with Bovine Serum Albumin Using Multi-Spectroscopic and Molecular Docking Approach. *Chem. Cent. J.* **2017**, *11* (1), 1–9. https://doi.org/10.1186/s13065-017-0366-1.

(451) Sirajuddin, M.; Ali, S.; Badshah, A. Drug – DNA Interactions and Their Study by UV – Visible , Fluorescence Spectroscopies and Cyclic Voltametry. *J. Photochem. Photobiol. B Biol.* **2013**, *124*, 1–19. https://doi.org/10.1016/j.jphotobiol.2013.03.013.

(452) Shahabadi, N.; Mohammadi, S.; Alizadeh, R. DNA Interaction Studies of a New Platinum (II) Complex Containing Different Aromatic Dinitrogen Ligands. *Bioinorg. Chem. Appl.* **2011**, *2011*. https://doi.org/10.1155/2011/429241.

(453) Kellett, A.; Molphy, Z.; Slator, C.; McKee, V.; Farrell, N. P. Molecular Methods for Assessment of Non-Covalent Metallodrug-DNA Interactions. *Chem. Soc. Rev.* **2019**, *48* (4), 971–988. https://doi.org/10.1039/c8cs00157j.

(454) Akimenko, N.; Cheltsov, P.; Balcarová, Z.; Kleinwächter, V.; Yevdokimov, Y. A Study of Interactions of Platinum (II) Compounds with DNA by Means of CD Spectra of Solutions and Liquid Crystalline Microphases of DNA. *Gen. Physiol. Biophys.* **1985**, *4*, 597–608.

(455) Roy, S.; Westmaas, J. A.; Hagen, K. D.; Wezel, G. P. Van; Reedijk, J. Platinum (II) Compounds with Chelating Ligands Based on Pyridine and Pyrimidine : DNA and Protein Binding Studies. *J. Inorg. Biochem.* **2009**, *103* (9), 1288–1297. https://doi.org/10.1016/j.jinorgbio.2009.07.003.

(456) Serebryanskaya, T. V.; Yung, T.; Bogdanov, A. A.; Shchebet, A.; Johnsen, S. A.; Lyakhov, A. S.; Ivashkevich, L. S.; Ibrahimava, Z. A.; Garbuzenco, T. S.; Kolesnikova, T. S.; Melnova, N. I.; Gaponik, P. N.; Ivashkevich, O. A. Synthesis, Characterization, and Biological Evaluation of New Tetrazole-Based Platinum(II) and Palladium(II) Chlorido Complexes - Potent Cisplatin Analogues and Their Trans Isomers. *J. Inorg. Biochem.* **2013**, *120*, 44–53. https://doi.org/10.1016/j.jinorgbio.2012.12.001.

(457) Peña, Q.; Lorenzo, J.; Sciortino, G.; Rodríguez-calado, S.; Maréchal, J.; Bayón, P.; Simaan, A. J.; Iranzo, O.; Capdevila, M. Studying the Reactivity of " Old " Cu (II) Complexes for " Novel " Anticancer Purposes. *J. Inorg. Biochem.* **2019**, *195*, 51–60. https://doi.org/10.1016/j.jinorgbio.2019.03.011.

(458) Brissos, R. F.; Torrents, E.; Mariana dos Santos Mellos, F.; Carvalho Pires, W.; de Paula Silveira-Lacerda, E.; Caballero, A. B.; Cuabet, A.; Massera, C.; Roubeau, O.; Teat, S. J.; Gamez, P. Highly Cytotoxic DNA-Interacting Copper(II) Coordination Compounds. *Metallomics* **2014**, *6*, 1853–1868. https://doi.org/10.1039/C4MT00152D.

(459) Suntharalingam, K.; Mendoza, O.; Duarte, A. A.; Mann, D. J.; Vilar, R. A Platinum Complex That Binds Non-Covalently to DNA and Induces Cell Death via a Different Mechanism than Cisplatin. *Metallomics* **2013**, *5*, 514–523. https://doi.org/10.1039/c3mt20252f.

(460) Arjmand, F.; Sayeed, F.; Muddassir, M. Synthesis of New Chiral Heterocyclic Schiff Base Modulated Cu(II)/Zn(II) Complexes : Their Comparative Binding Studies with CT-DNA , Mononucleotides and Cleavage Activity. *J. Photochem. Photobiol. B Biol.* **2011**, *103* (2), 166–179. https://doi.org/10.1016/j.jphotobiol.2011.03.001.

(461) Morgan, A. R.; Lee, J. S.; Pulleyblank, D. E.; Murray, N. L.; Evans, D. H. Ethidium Fluorescence Assays. Part 1. Physicochemical Studies. *Nucleic Acids Res.* **1979**, *7* (3), 547–569. https://doi.org/10.1093/nar/7.3.547.

(462) Raj Kumar, R.; Mohamed Subarkhan, M. K.; Ramesh, R. Synthesis and Structure of Nickel(II) Thiocarboxamide Complexes: Effect of Ligand Substitutions on DNA/Protein Binding, Antioxidant and Cytotoxicity. *RSC Adv.* **2015**, *5* (58), 46760–46773. https://doi.org/10.1039/C5RA06112A.

(463) Genomics of Drug Sensitivity in Cancer. https://www.cancerrxgene.org/compound/Cisplatin/1005/overview/ic50? (accessed February 2022).

(464) Smistad, G.; Jacobsen, J.; Sande, S. A. Multivariate Toxicity Screening of Liposomal Formulations on a Human Buccal Cell Line. *Int. J. Pharm.* **2007**, *330* (1–2), 14–22. https://doi.org/10.1016/j.ijpharm.2006.08.044.

(465) Sotto, A. Di; Paolicelli, P.; Nardoni, M.; Abete, L.; Garzoli, S.; Giacomo, S. Di; Mazzanti, G.; Casadei, M. A.; Petralito, S. SPC Liposomes as Possible Delivery Systems for Improving Bioavailability of the Natural Sesquiterpene β -Caryophyllene : Lamellarity and Drug-Loading as Key Features for a Rational Drug Delivery Design. *Pharmaceutics* **2018**, *10*, 274–291. https://doi.org/10.3390/pharmaceutics10040274.

(466) Ashraf, H.; Taherian, A.; Kerdar, A. N. Evaluation of Cytotoxicity of Two Root Canal Filling Materials by MTT Assay. *Aust. Endod. J.* **2010**, *36*, 24–28. https://doi.org/10.1111/j.1747-4477.2009.00173.x.

(467) Sato, G. H. The Role of Serum in Cell Culture. In *Biochemical Actions of Hormones*; Litwak, G., Ed.; Academic Press, INC., 1975; pp 391–396. https://doi.org/10.1016/b978-0-12-452803-1.50018-5.

(468) Heger, J. I.; Froehlich, K.; Pastuschek, J.; Schmidt, A.; Baer, C.; Mrowka, R.; Backsch, C.; Schleußner, E.; Markert, U. R.; Schmidt, A. Human Serum Alters Cell Culture Behavior and Improves Spheroid Formation in Comparison to Fetal Bovine Serum. *Exp. Cell Res.* **2018**, *365* (1), 57–65. https://doi.org/10.1016/j.yexcr.2018.02.017.

(469) Boncler, M.; Rózalski, M.; Krajewska, U.; Podswdek, A.; Watala, C. Comparison of PrestoBlue and MTT Assays of Cellular Viability in the Assessment of Anti-Proliferative Effects of Plant Extracts on Human Endothelial Cells. *J. Pharmacol. Toxicol. Methods* **2014**, *69* (1), 9–16. https://doi.org/10.1016/j.vascn.2013.09.003.

(470) Braissant, O.; Astasov-Frauenhoffer, M.; Waltimo, T.; Bonkat, G. A Review of Methods to Determine Viability, Vitality, and Metabolic Rates in Microbiology. *Front. Microbiol.* **2020**, *11* (2), 1–25. https://doi.org/10.3389/fmicb.2020.547458.

(471) Persi, E.; Duran-frigola, M.; Damaghi, M.; Roush, W. R.; Aloy, P.; Cleveland, J. L.; Gillies, R. J.; Ruppin, E. Systems Analysis of Intracellular PH Vulnerabilities for Cancer Therapy. *Nat. Commun.* **2018**, *9*. https://doi.org/10.1038/s41467-018-05261-x.

(472) Asokan, A.; Moo, J. C. Exploitation of Intracellular PH Gradients in the Cellular Delivery of Macromolecules. *J. Pharm. Sci.* **2002**, *91* (4), 903–913. https://doi.org/10.1002/jps.10095.

(473) Zhao, X.; Yao, Y.; Tian, K.; Zhou, T.; Jia, X.; Li, J.; Liu, P. Leakage-Free DOX / PEGylated Chitosan Micelles Fabricated via Facile One-Step Assembly for Tumor Intracellular PH-Triggered Release. *Eur. J. Pharm. Biopharm.* **2016**, *108*, 91–99. https://doi.org/10.1016/j.ejpb.2016.08.018.

(474) Ghosh, S. N. IR Spectroscopy. In *Handbook of Analytical Techniques in Concrete Science and Technology*; Ramachandran, V. S., Beaudoin, J. J., Eds.; William Andrew Publishing: New York, 2001. https://doi.org/10.1016/B978-081551437-4.50008-4.

(475) Ho, C. S Lam, C. W. Chan, M. H. Cheung, R. C. Law, L. K. Lit, L. C. Ng, K. F., Suen, M. W. Tai, H. L. Electrospray Ionisation Mass Spectrometry: Principles and Clinical Applications. *Clin. Biochem. Rev.* **2003**, *24* (1), 3–12.

(476) Banerjee, S.; Mazumdar, S. Electrospray Ionization Mass Spectrometry: A Technique to Access the Information beyond the Molecular Weight of the Analyte. *Int. J. Anal. Chem.* **2012**, *2012*, 1–40. https://doi.org/10.1155/2012/282574.

(477) Olesik, J. W. Elemental Analysis Using ICP-OES and ICP/MS. *Anal. Chem.* **1991**, *63* (1), 12A-21A. https://doi.org/10.1021/ac00001a711.

(478) Fraxedas, J.; Vollmer, A.; Koch, N.; de Caro, D.; Jacob, K.; Faulmann, C.; Valade, L. Characterization of Charge States in Conducting Organic Nanoparticles by X-Ray Photoemission Spectroscopy. *Materials (Basel).* **2021**, *14* (8), 1–13. https://doi.org/10.3390/ma14082058.

(479) Weber, F.; Ivan, D. C.; Proulx, S. T.; Locatelli, G.; Aleandri, S.; Luciani, P. Beyond Trial and Error: A Systematic Development of Liposomes Targeting Primary Macrophages. *Adv. NanoBiomed Res.* **2021**, *1* (3), 2000098. https://doi.org/10.1002/anbr.202000098.

(480) Pinazo, A.; Angelet, M.; Pons, R.; Lozano, M.; Infante, M. R.; Pérez, L. Lysine-Bisglycidol Conjugates as Novel Lysine Cationic Surfactants. *Langmuir* **2009**, *25* (14), 7803–7814. https://doi.org/10.1021/la901675p.

(481) Frisch, M. J.; Trucks, G. W.; Schlegel, H. B.; Scuseria, G. E. .; Robb, M. A.; Cheeseman, J. R.; Scalmani, G.; Barone, V.; Mennucci B.; Petersson, G. A.; Nakatsuji, H.; Caricato, M.; Li, X.; Hratchian, H. P.; Izmaylov, A. F.; Bloino, J.; Zheng, G.; Sonnen, D. J. Gaussian 09 W. Wallingford, UK 2016.

(482) Perdew, J. P.; Burke, K.; Ernzerhof, M. Generalized Gradient Approximation Made Simple. *Phys. Rev. Lett.* **1996**, *77* (18), 3865–3868. https://doi.org/10.1103/PhysRevLett.77.3865.

(483) Wadt, W. R.; Hay, P. J. Ab Initio Effective Core Potentials for Molecular Calculations. Potentials for Main Group Elements Na to Bi. *J. Chem. Phys.* **1985**, *82* (1), 284–298. https://doi.org/10.1063/1.448800.

(484) Adamo, C.; Jacquemin, D. The Calculations of Excited-State Properties with Time-Dependent Density Functional Theory. *Chem. Soc. Rev.* **2013**, *42* (3), 845–856. https://doi.org/10.1039/C2CS35394F.

(485) O'Boyle, N. M.; Tenderholt, A. L.; Langer, K. M. A Library for Package-Independent Computational Chemistry Algorithms. *J. Comput. Chem.* **2008**, *29* (5), 839–845. https://doi.org/10.1002/jcc.20823.

(486) Martin, R. L. Natural Transition Orbitals. *J. Chem. Phys.* **2003**, *118* (11), 4775–4777. https://doi.org/10.1063/1.1558471.

(487) Lu, T.; Chen, F. Multiwfn: A Multifunctional Wavefunction Analyzer. *J. Comput. Chem.* **2012**, *33* (5), 580–592. https://doi.org/10.1002/jcc.22885.

(488) Suryanarayana, C.; Grant Norton, M. *X-Ray Diffraction: A Practical Approach*; Springer: Boston, MA, 1998; Vol. 36. https://doi.org/10.1007/978-1-4899-0148-4.

(489) Kikhney, A. G.; Svergun, D. I. A Practical Guide to Small Angle X-Ray Scattering (SAXS) of Flexible and Intrinsically Disordered Proteins. *FEBS Lett.* **2015**, *589* (19), 2570–2577. https://doi.org/10.1016/j.febslet.2015.08.027.

10. ANNEX

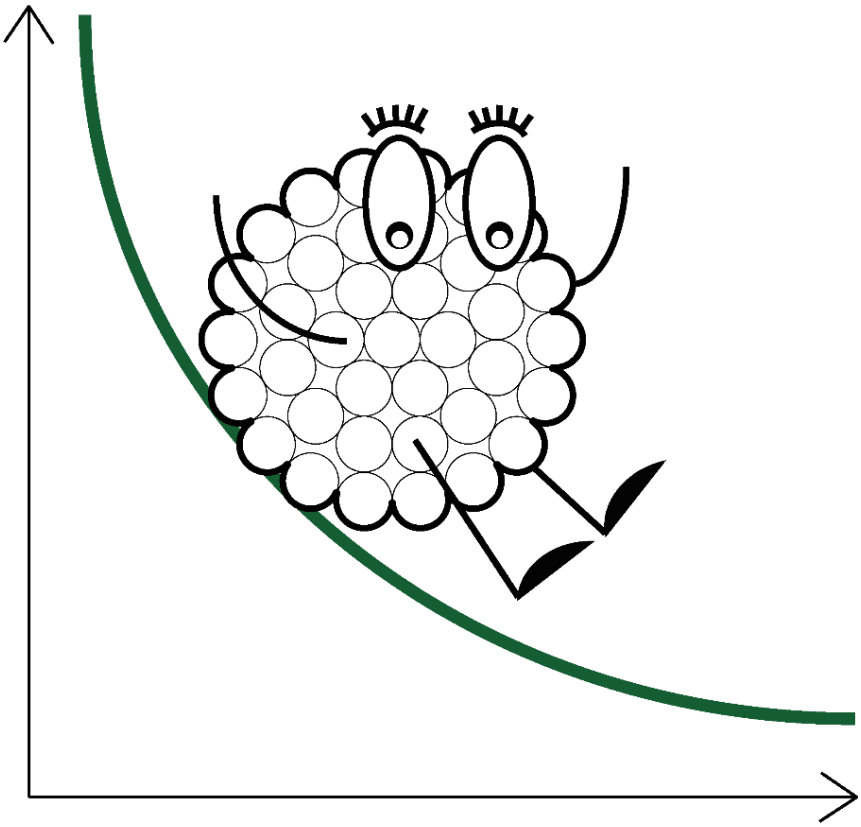

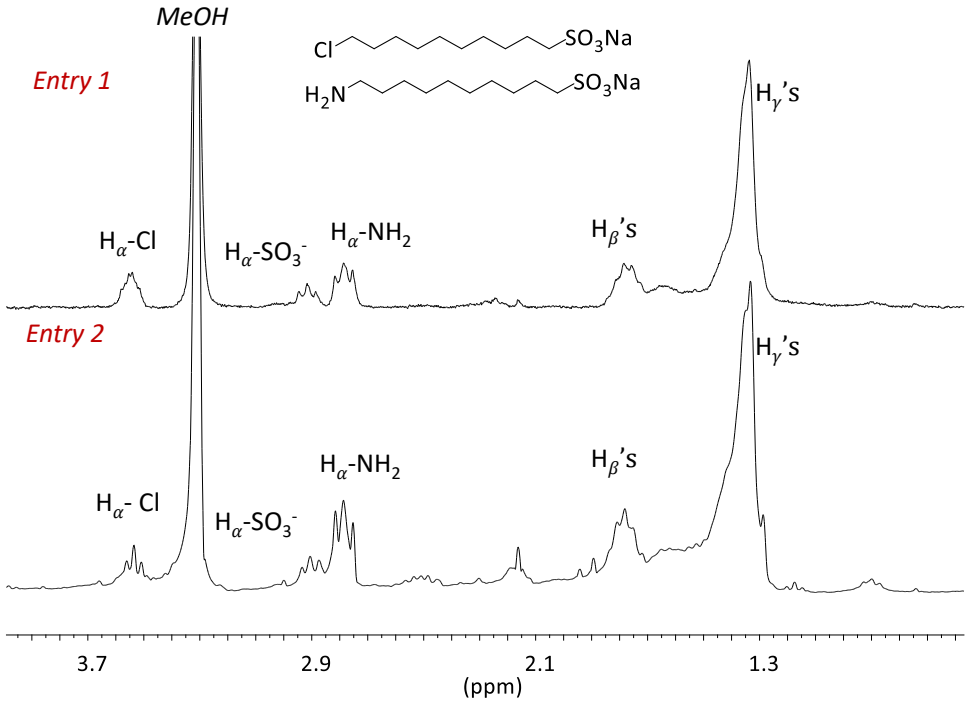

Figure A1 ^{1}H-NMR (360 MHz) spectra after reaction with NH_3 in H_2O under reflux (above, **Table 3.1**, entry **1**) and in autoclave (below, entry **2**). Solvent: methanol-d4.

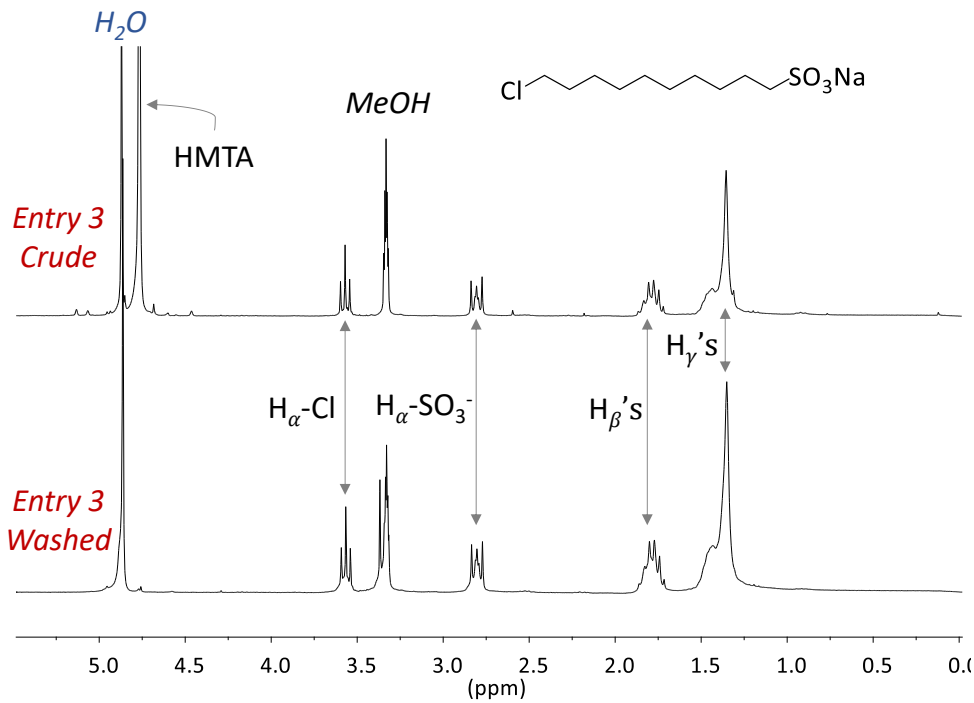

Figure A2 ^{1}H-NMR (360 MHz) spectra after *Delépine* reaction in entry **3**, **Table 3.1**. Above, the crude reaction and below after DCM wash, where **HS** was recovered. Solvent: methanol-d_4.

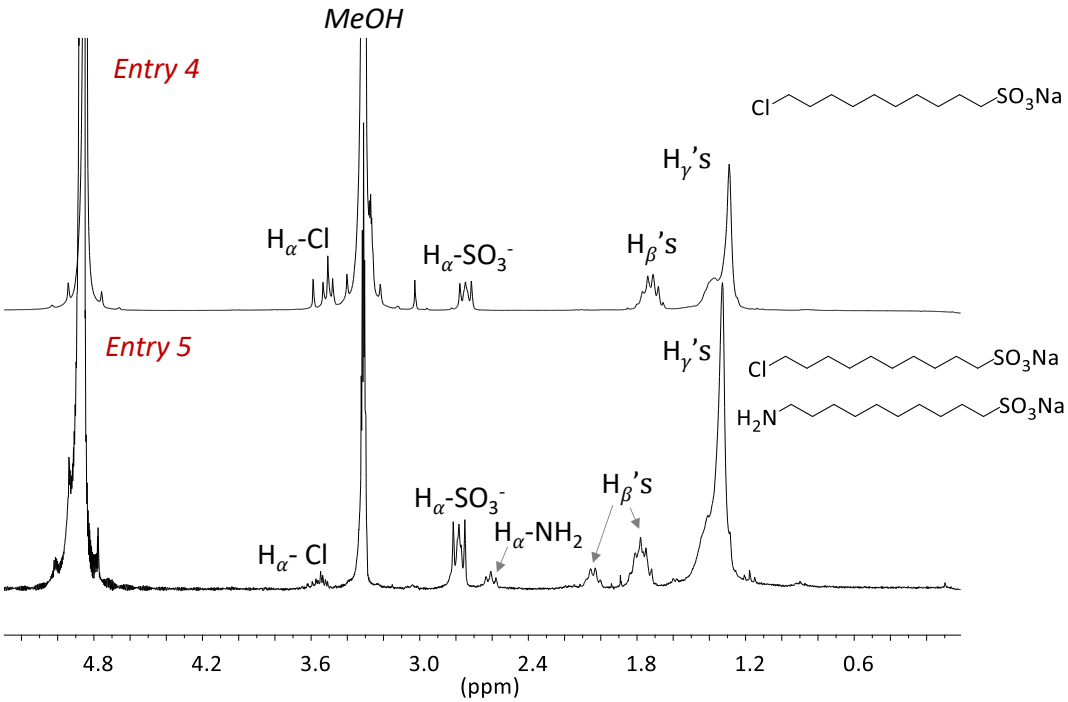

Figure A3 ^{1}H-NMR (360 MHz) spectra of entry **4** in which no amination occurred, and entry **5** (**Table 3.1**) where a mixture of products is observed. Solvent: methanol-d_4.

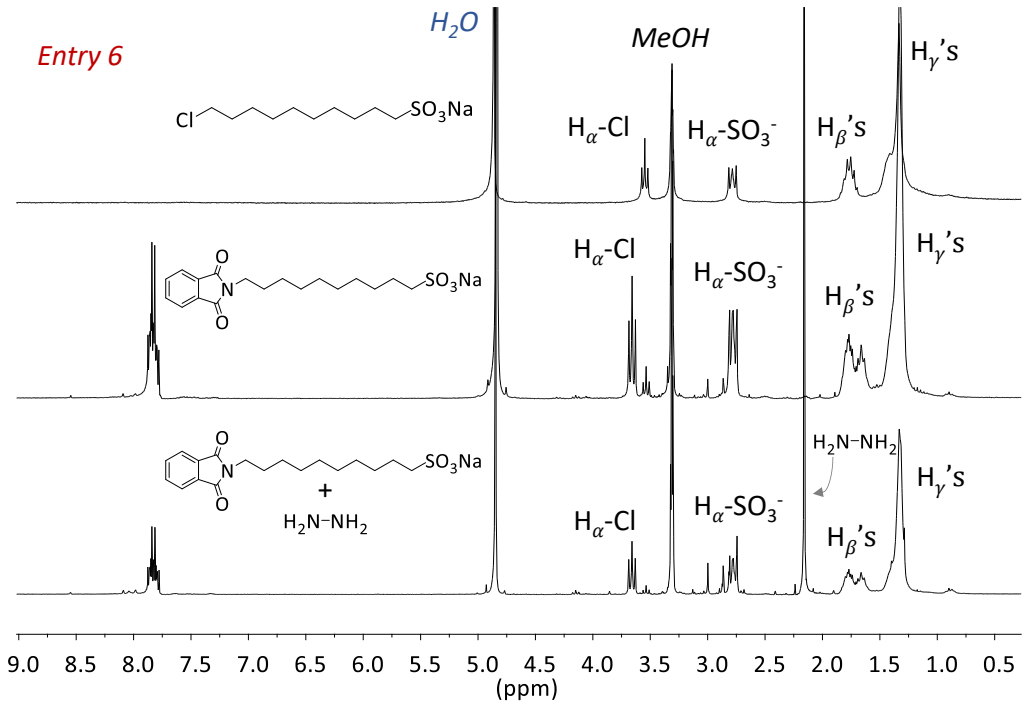

Figure A4 ^{1}H-NMR (360 MHz) of entry **6** (**Table 3.1**) in which **HS** (top) reacted with potassium phthalimide (middle) and failed cleavage using hydrazine (bottom). Solvent: methanol-d_4.

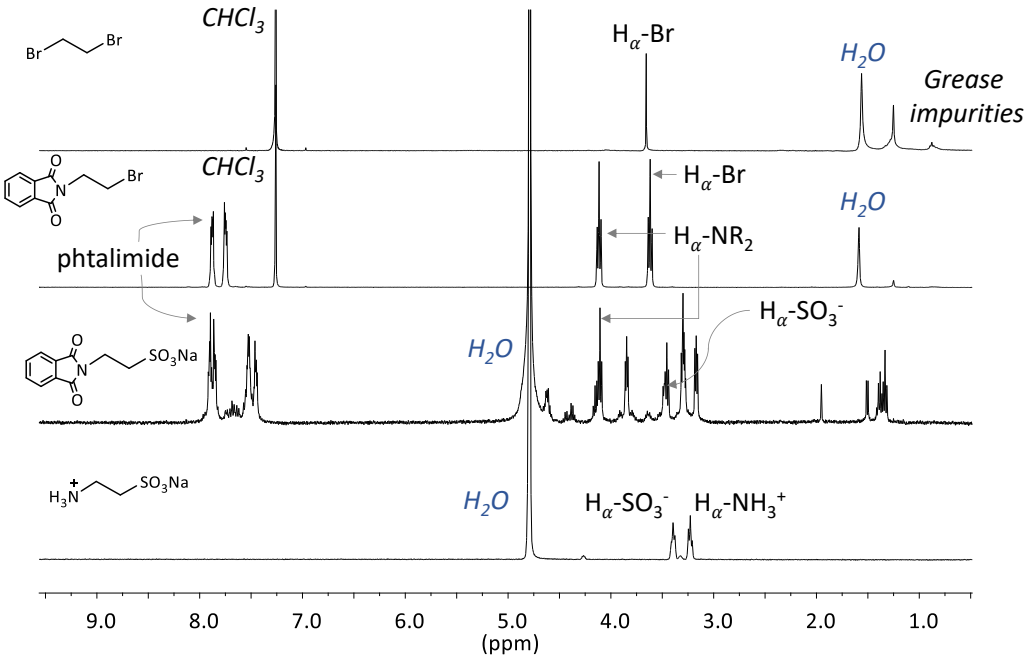

Figure A5 ^{1}H-NMR (360 MHz) spectra of steps on the **L2** synthesis reaction. Solvent: Chloroform-*d₁* for the first and second spectra, and water-*d₂* for the third and fourth.

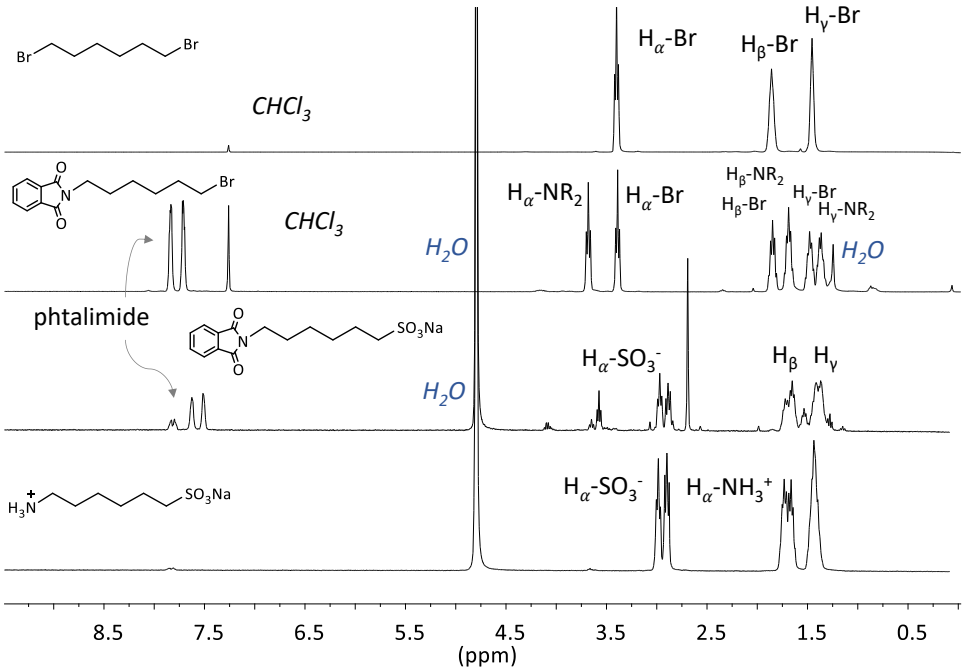

Figure A6 ^{1}H-NMR (360 MHz) spectra of steps on the **L6** synthesis reaction. Solvent: Chloroform-*d₁* for the first and second spectra, and water-*d₂* for the third and fourth.

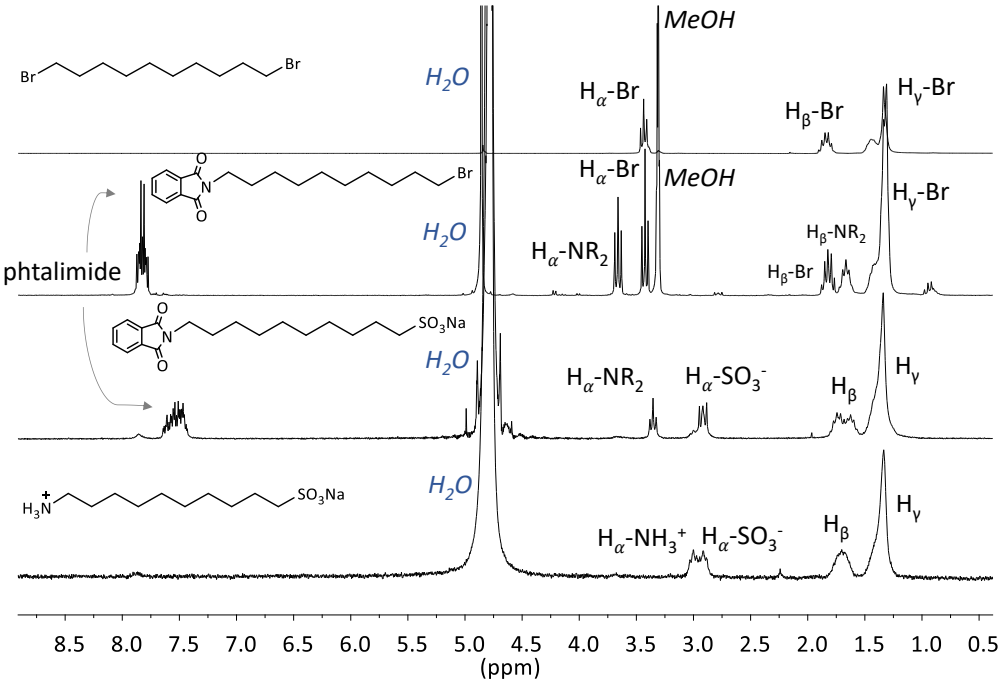

Figure A7 ^{1}H-NMR (360 MHz) spectra of steps on the **L10** synthesis reaction. Solvent: methanol-d_4 for the first and second spectra, and water-d_2 for the third and fourth.

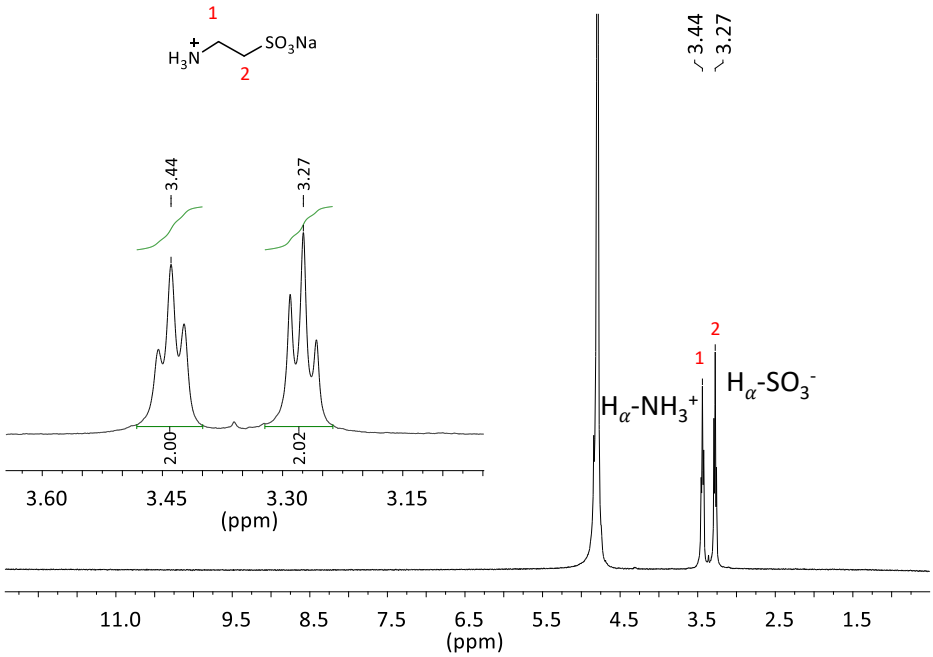

Figure A8 ^{1}H-NMR (400 MHz) spectrum of compound **L2**. Solvent: water-d_2.

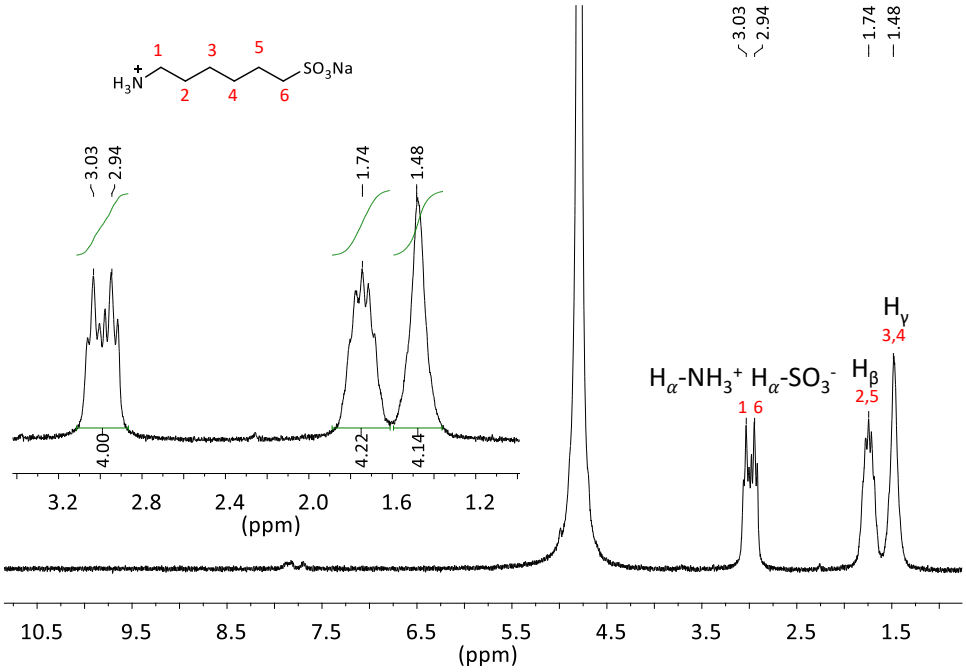

Figure A9 ^{1}H-NMR (400 MHz) spectrum of compound **L6**. Solvent: water-d_2.

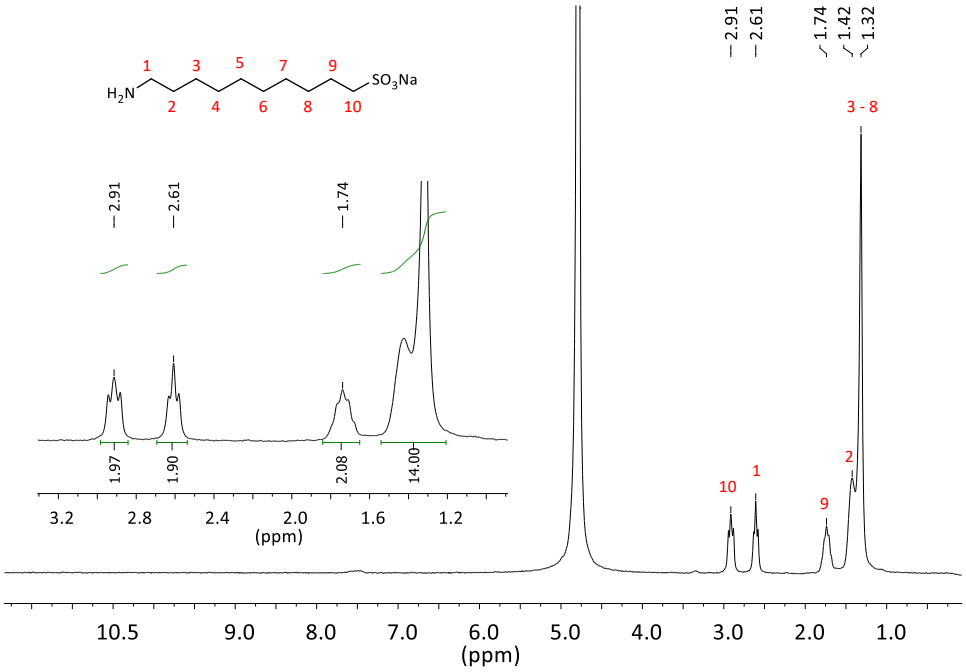

Figure A10 ^{1}H-NMR (400 MHz) spectrum of basic compound **L10**. Solvent: water-d_2.

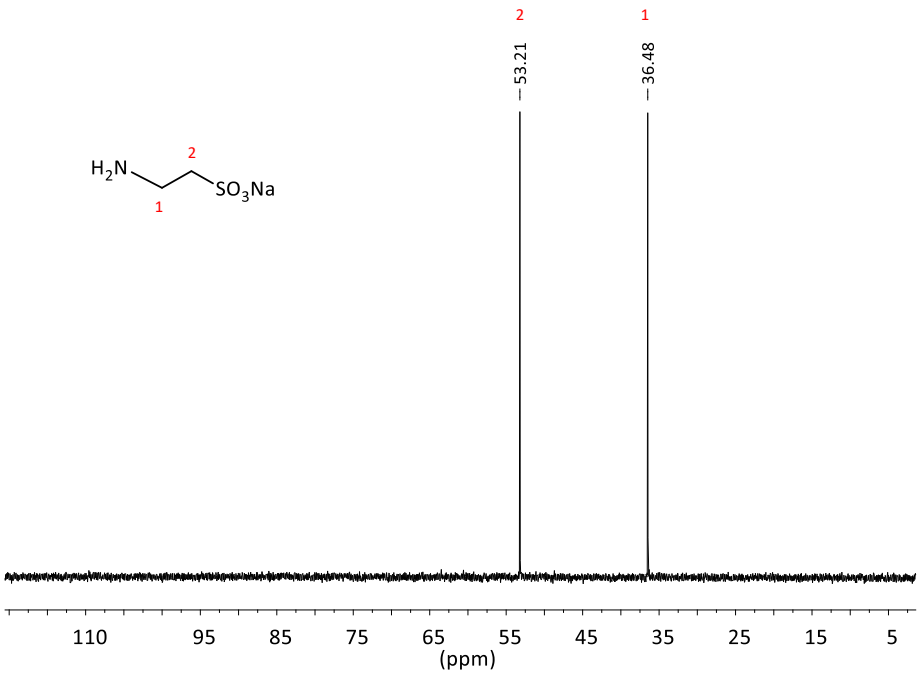

Figure A11 ^{13}C-NMR (90 MHz) spectrum of basic compound **L2**. Solvent: water-d_2.

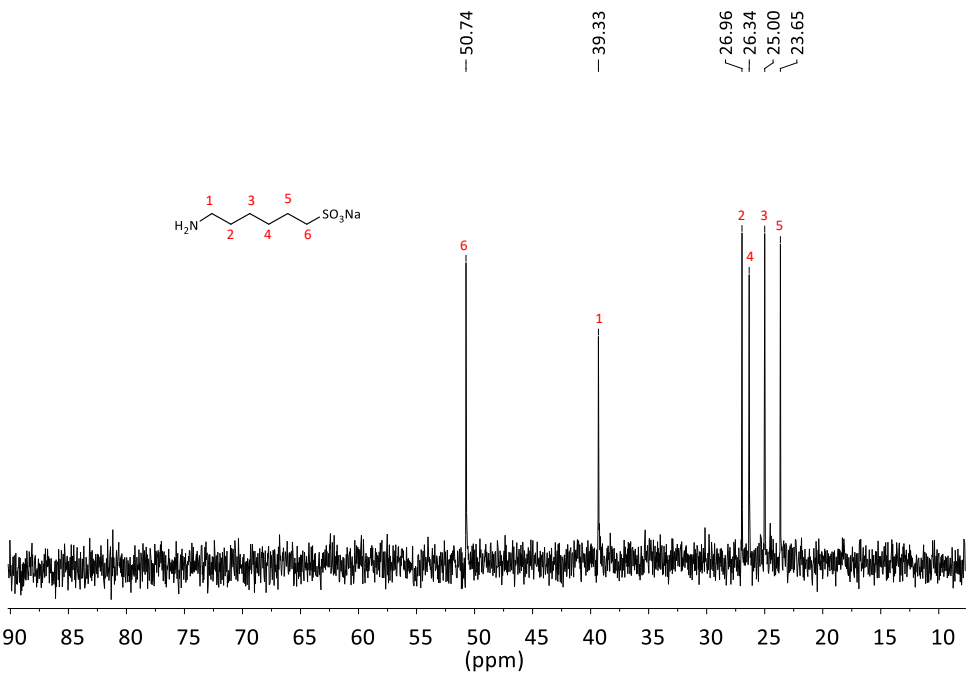

Figure A12 ^{13}C-NMR (90 MHz) spectrum of basic compound **L6**. Solvent: water-d_2.

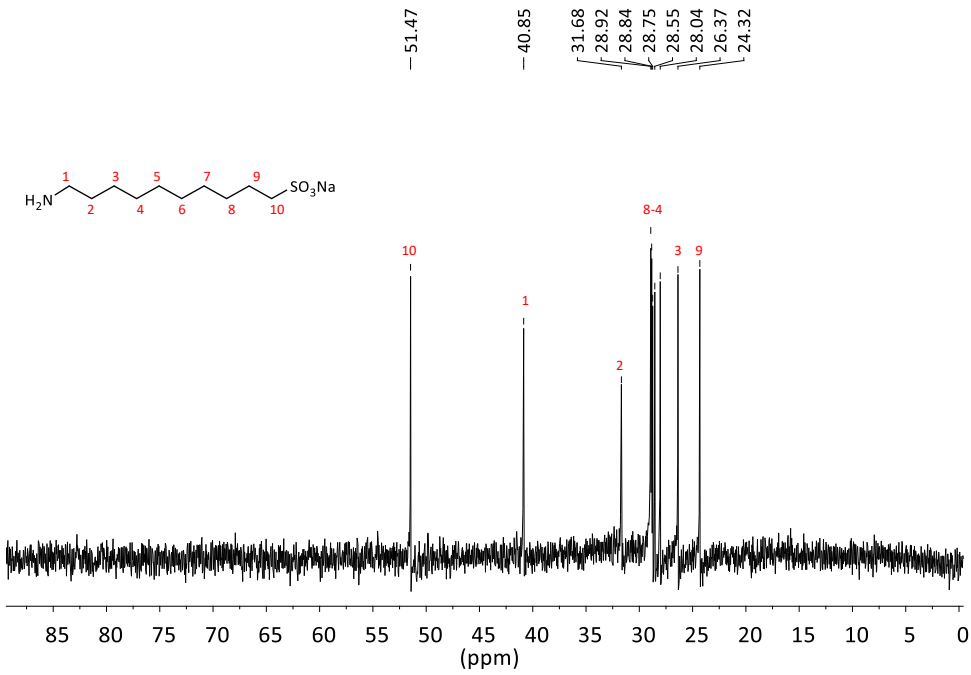

Figure A13 ^{13}C-NMR (90 MHz) spectrum of basic compound **L10**. Solvent: water-d_2.

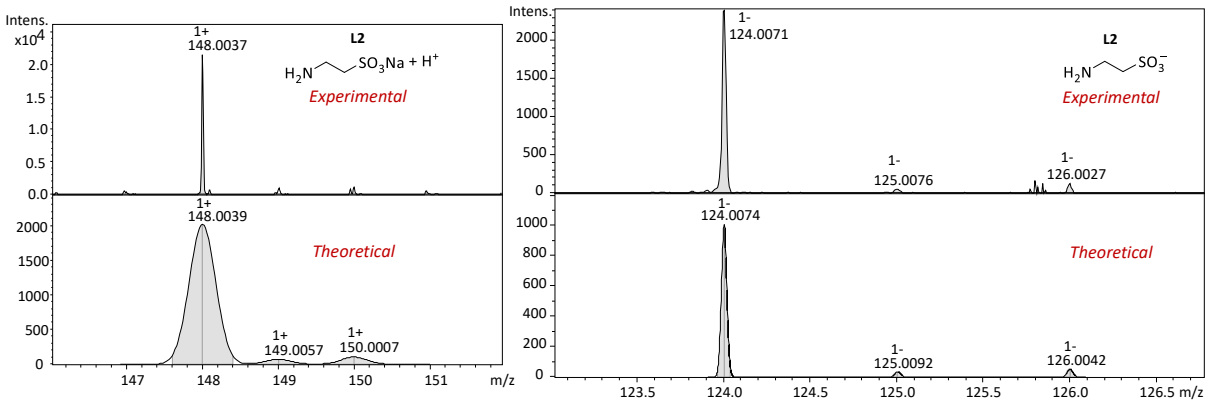

Figure A14 Positive ESI-MS spectrum (left) of compound **L2**+H$^+$ experimental (top) and theoretical (down) and negative ESI-HR-MS spectrum (right) of compound **L2**-Na$^+$ experimental (top) and theoretical (down).

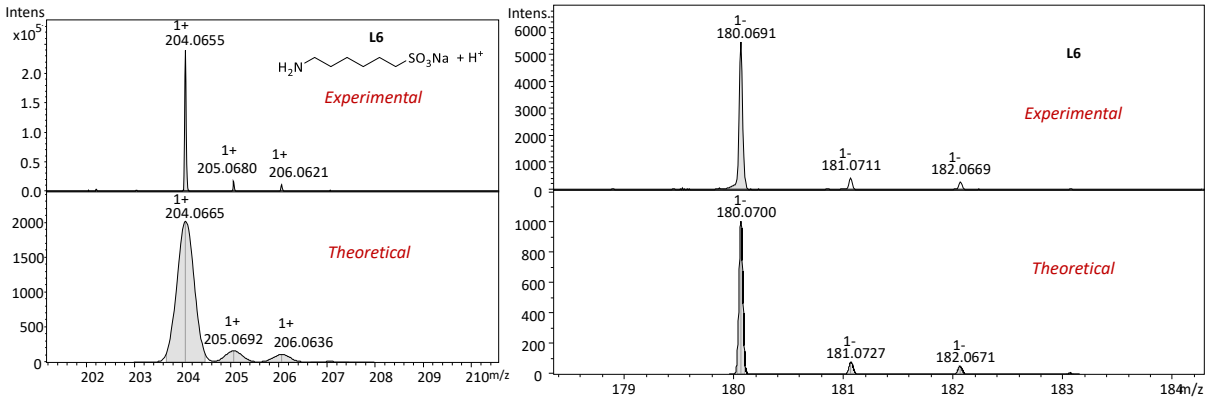

Figure A15 Positive ESI-MS spectrum (left) of compound **L6**+H$^+$ experimental (top) and theoretical (down) and negative ESI-HR-MS spectrum (right) of compound **L6**-Na$^+$ experimental (top) and theoretical (down).

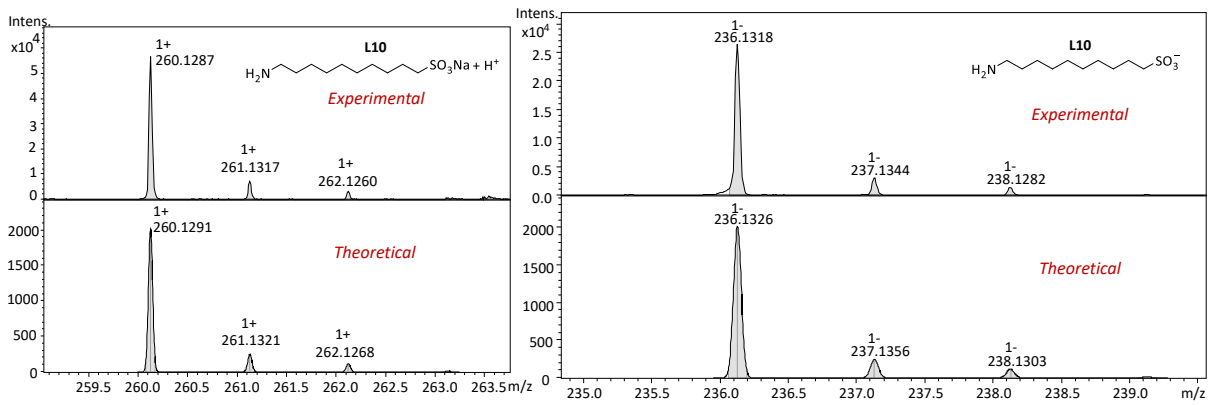

Figure A16 Positive ESI-MS spectrum (left) of compound **L10**+H⁺ experimental (top) and theoretical (down) and negative ESI-HR-MS spectrum (right) of compound **L10**-Na⁺ experimental (top) and theoretical (down).

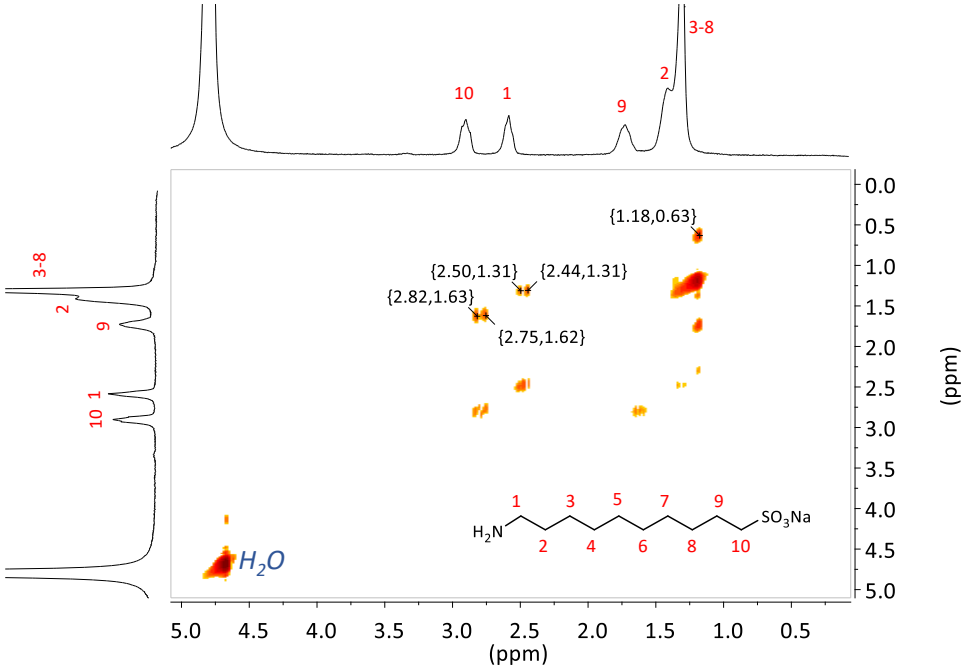

Figure A17 COSY (360 MHz) spectrum of compound **L10**. Solvent: water-d_2.

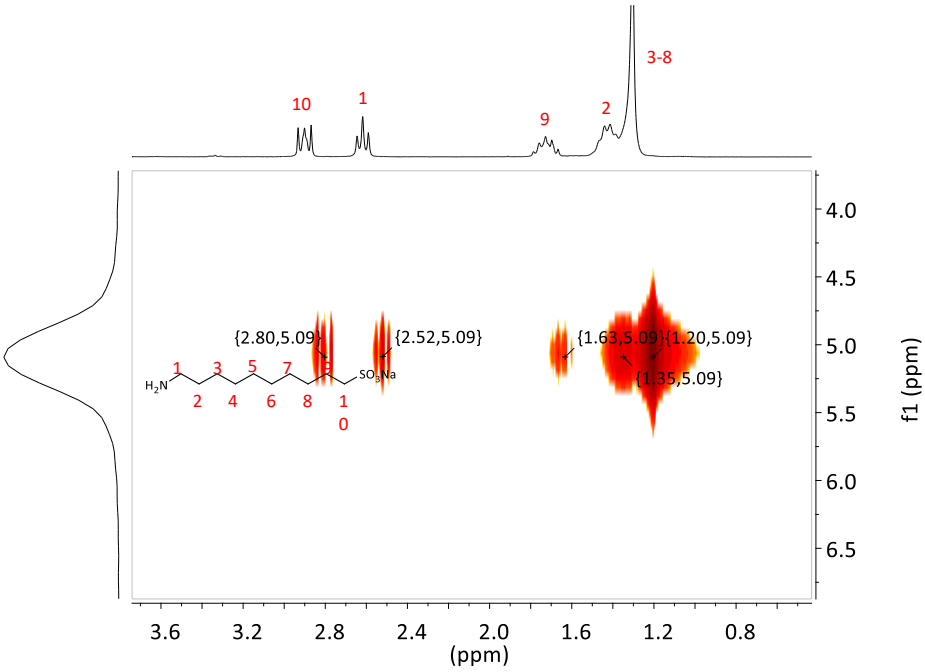

Figure A18 DOSY (360 MHz) spectrum of compound **L10**. Solvent: water-d2.

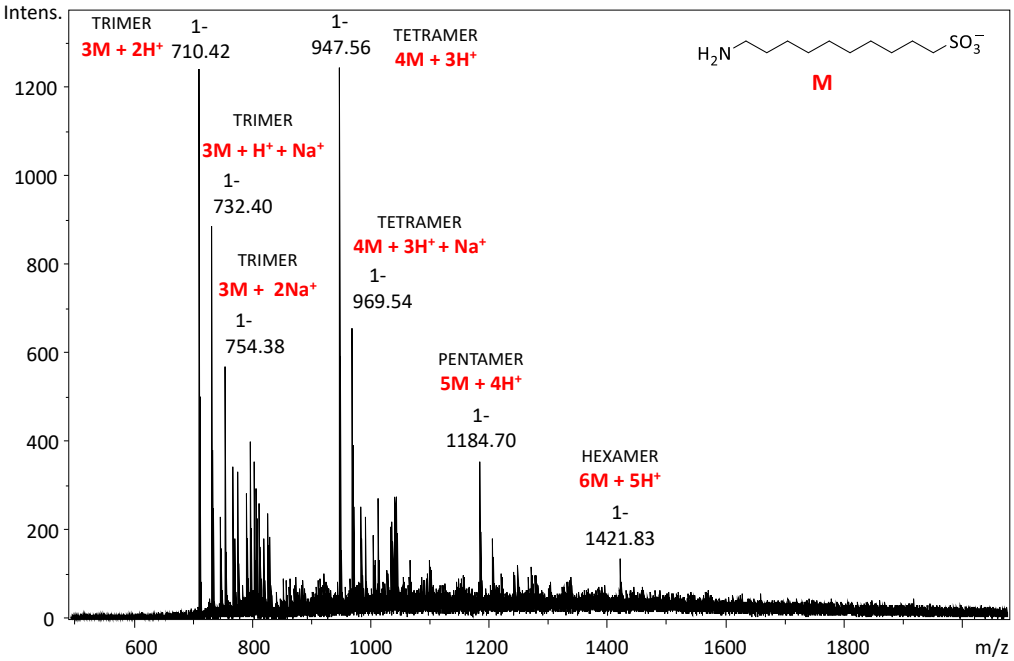

Figure A19 Negative ESI-MS showing association of up to six molecules of **L10**.

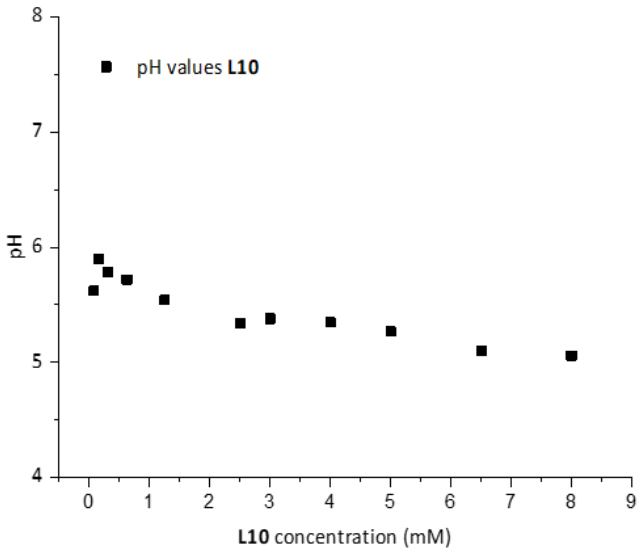

Figure A20 Measured pH values for several concentrations of recrystallised **L10** in Mili-Q water.

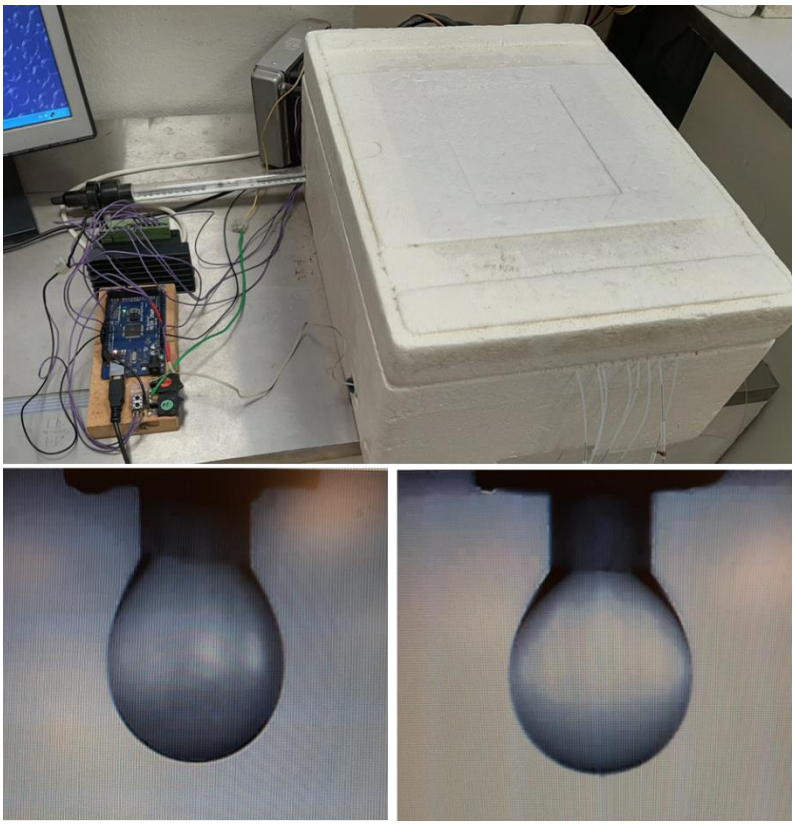

Figure A21 Device used to measure surface tension through pendant drop (top) and photographs of two hanging droplets (down).

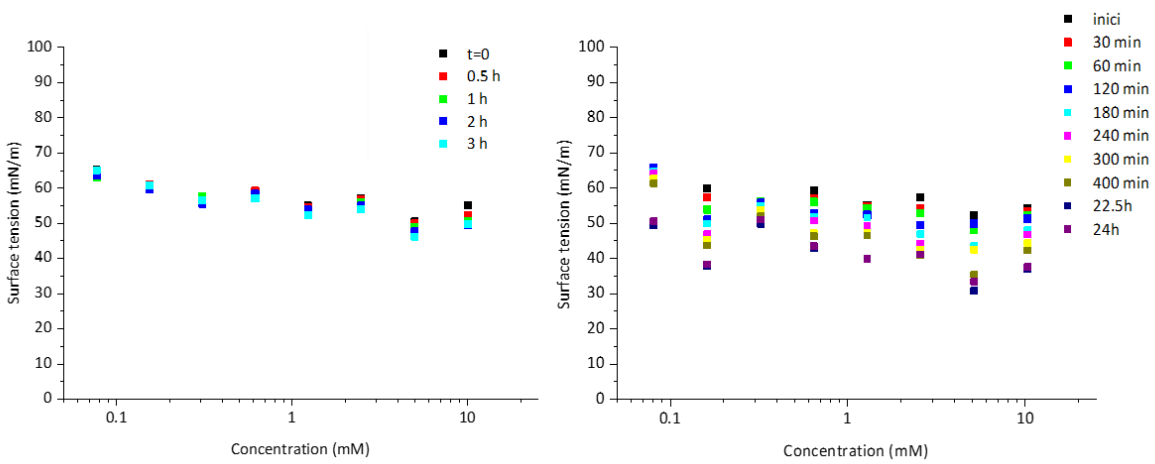

Figure A22 Surface tension vs concentration of **L10** in water (left) and PBS (right) measured by pendant drop method along time.

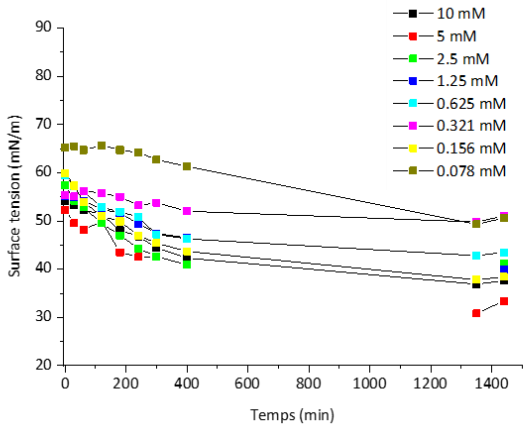

Figure A23 Surface tension vs time of **L10** in PBS at several concentrations measured by pendant drop method.

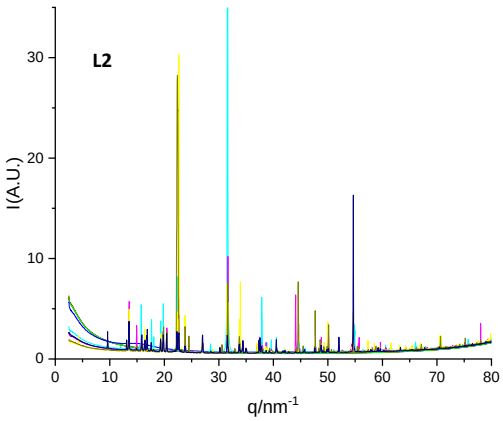

Figure A24 WAXS intensity as function of dispersion vector modulus q for solid **L2**.

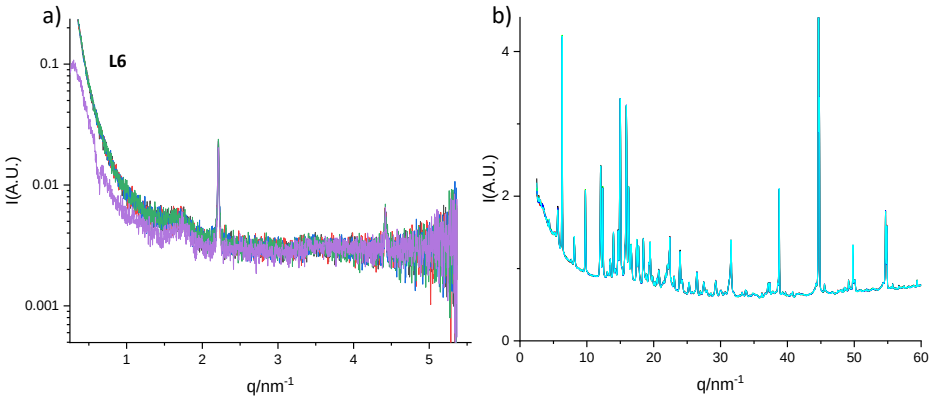

Figure A25 SAXS (a) and WAXS (b) intensity as function of dispersion vector modulus q for solid **L6**.

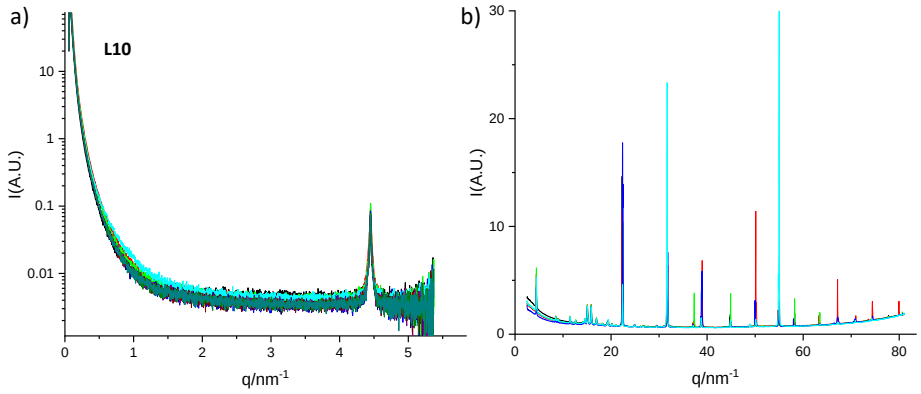

Figure A26 SAXS (a) and WAXS (b) SAXS intensity as function of dispersion vector modulus q for solid **L10**.

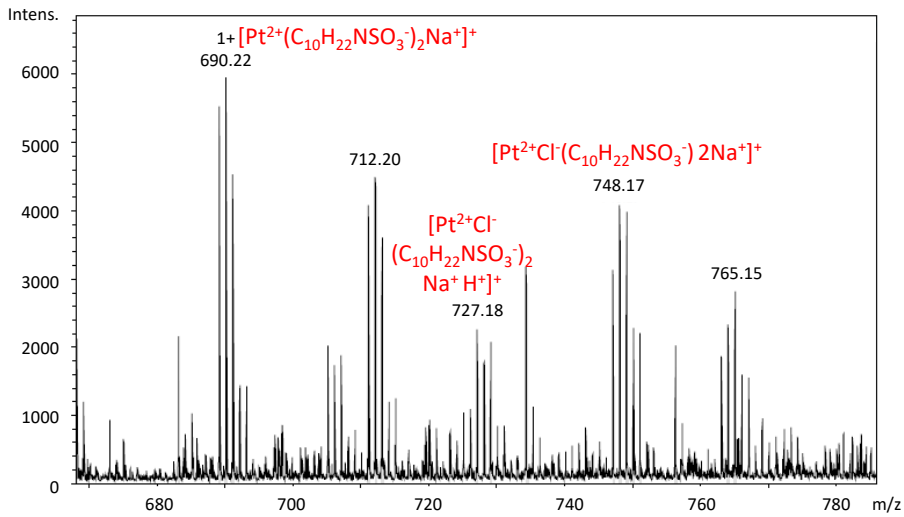

Figure A27 Positive mode ESI-MS spectrum of an attempt of $Pt(Cl_2)(C_{10}H_{22}NSO_3Na)_2$ synthesis from K_2PtCl_4.

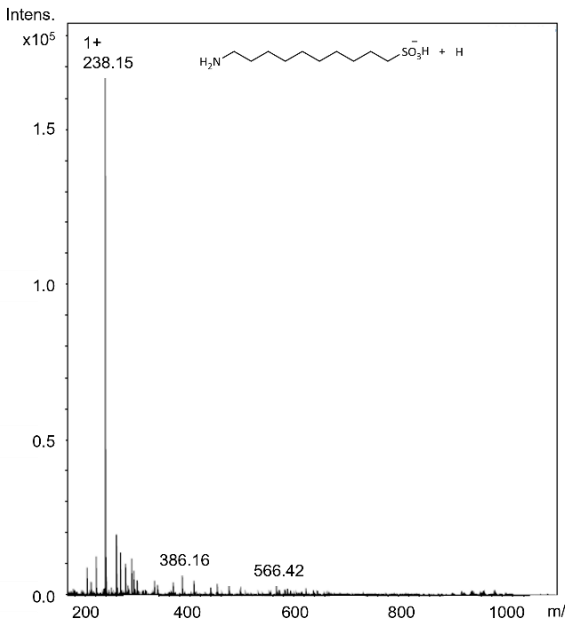

Figure A28 Positive mode ESI-MS spectrum of an attempt of $Pt(Cl_2)(C_{10}H_{22}NSO_3Na)_2$ synthesis from $PtCl_2$.

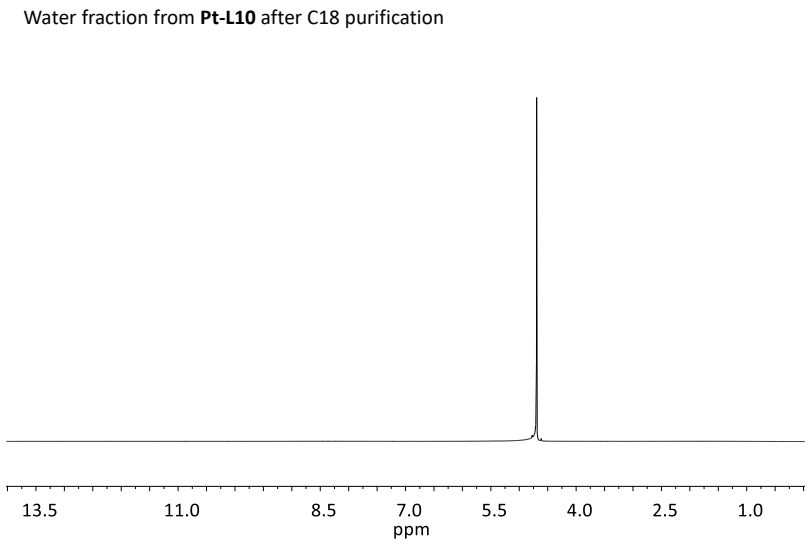

Figure A29 ^{1}H-NMR (250 MHz) spectra of the lyophilised water fraction from reverse phase silica purification of **Pt-L10** solved in water-*d*$_2$.

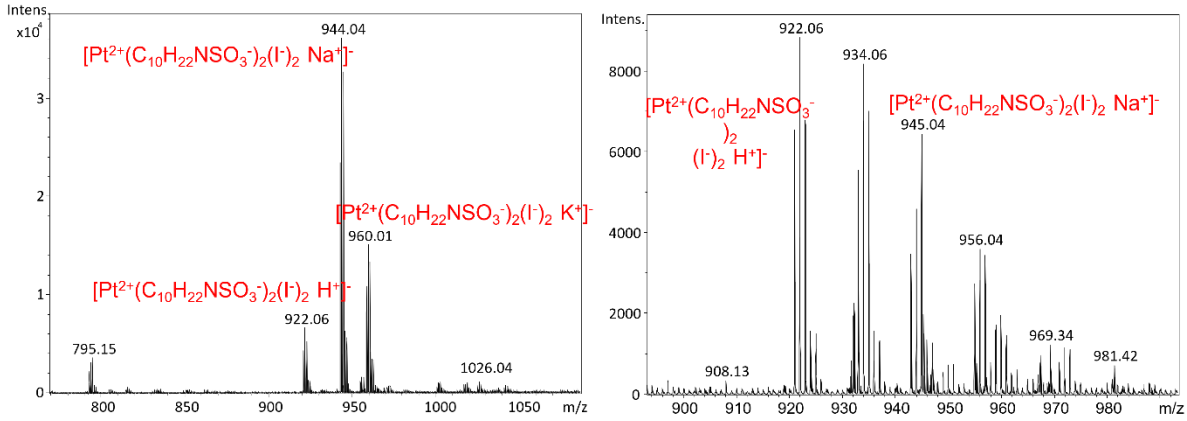

Figure A30 Negative ESI-MS spectrum of **Pt-L10** before and after purification.

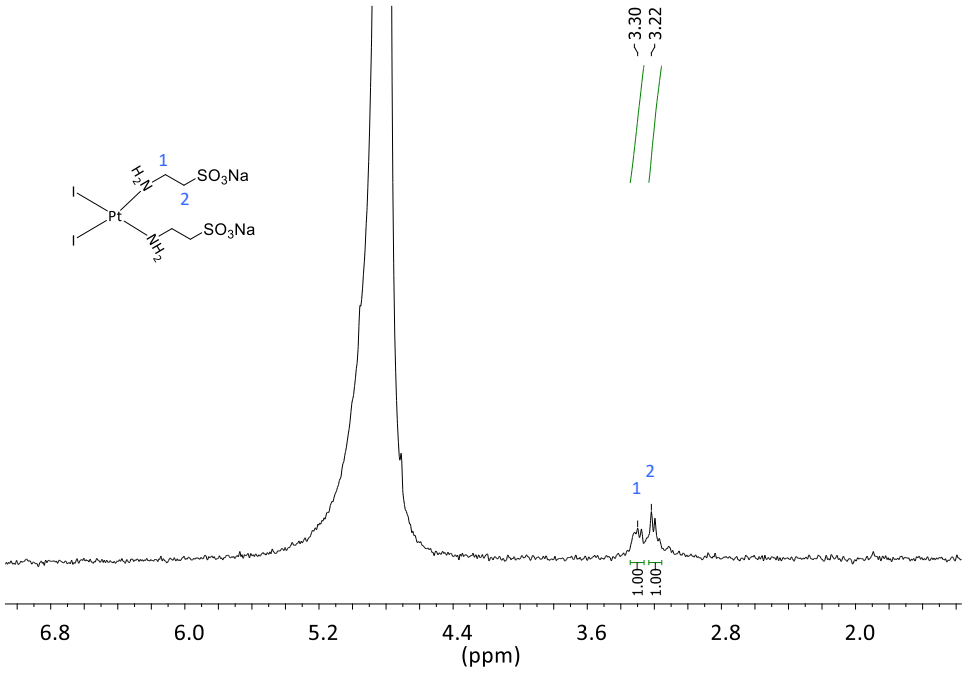

Figure A31 ^{1}H-NMR (mHz) spectra of **Pt-L2** in water-d_2.

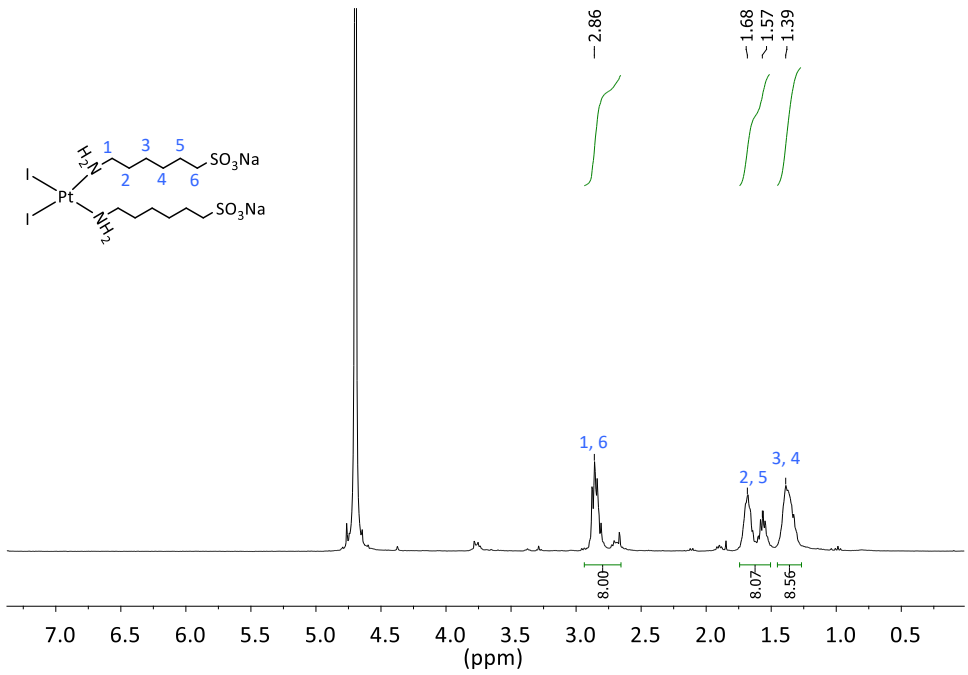

Figure A32 ^{1}H-NMR (400 mHz) spectra of **Pt-L6** in water-d_2.

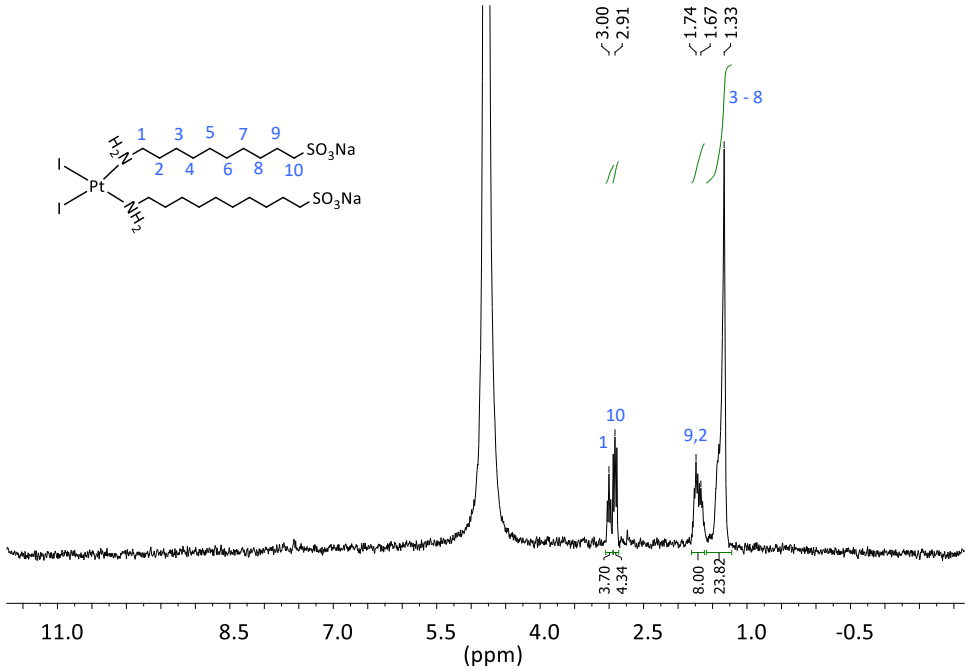

Figure A33 ^{1}H-NMR (400 mHz) spectra of **Pt-L10** in water-d_2.

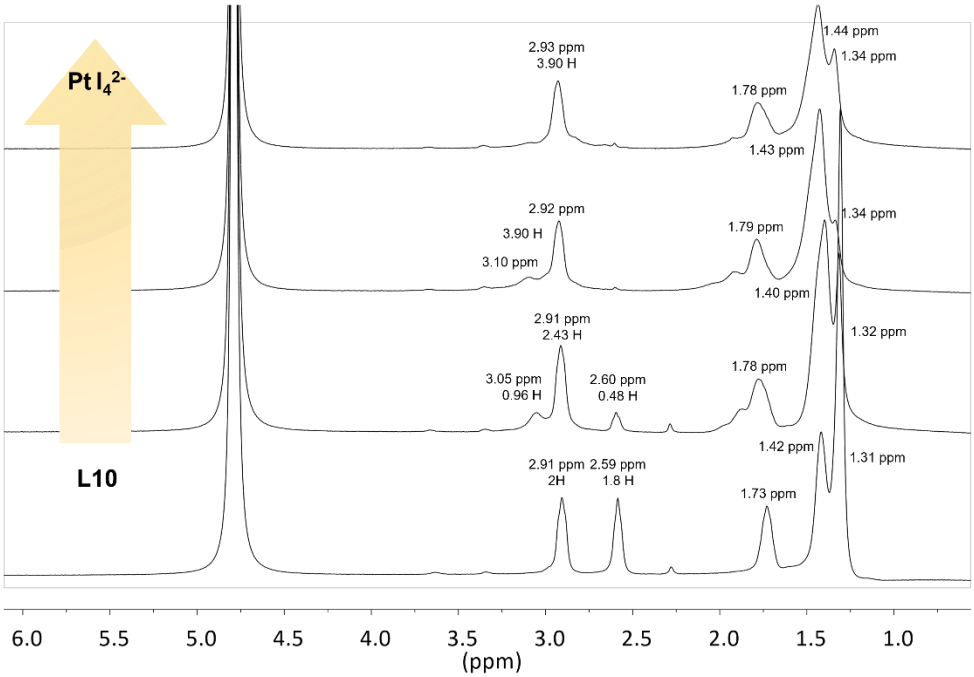

Figure A34 Piled up ^{1}H-NMR spectra of the *in-situ* reaction between $[PtI_4]^{2-}$ and basified **L10**, with the intention of understanding the evolution of the coordination rection focusing on the Hα-NH_2 signal which vanishes after the addition of increasing amount of $[PtI_4]^{2-}$. All the spectra recorded at 250 mHz in water-d_2.

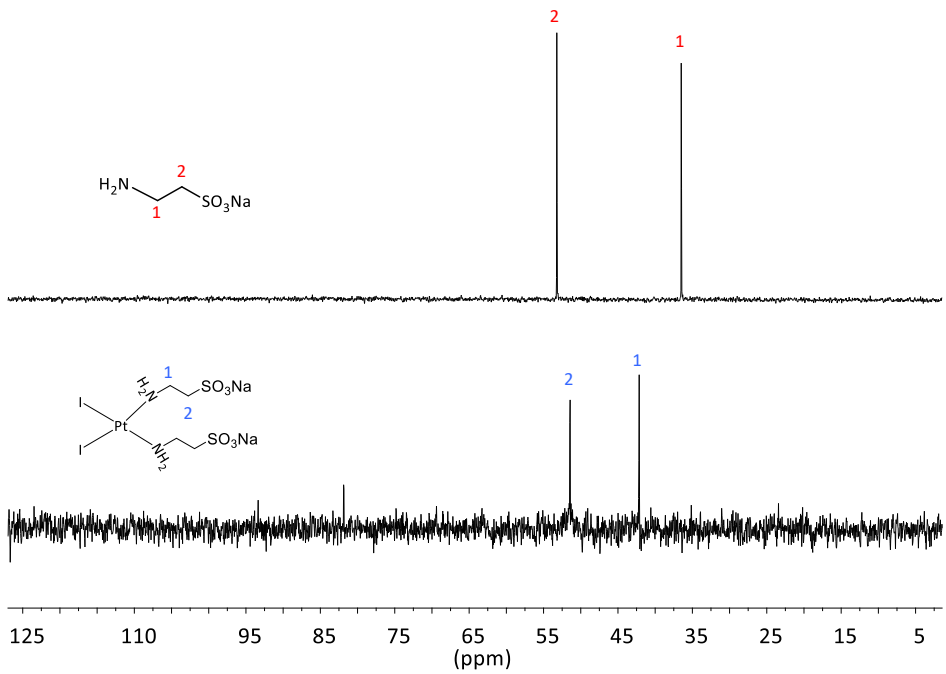

Figure A35 ^{13}C-NMR (100 mHz) spectra of **L2** (top) and **Pt-L2** (bottom) in *d*-D2O.

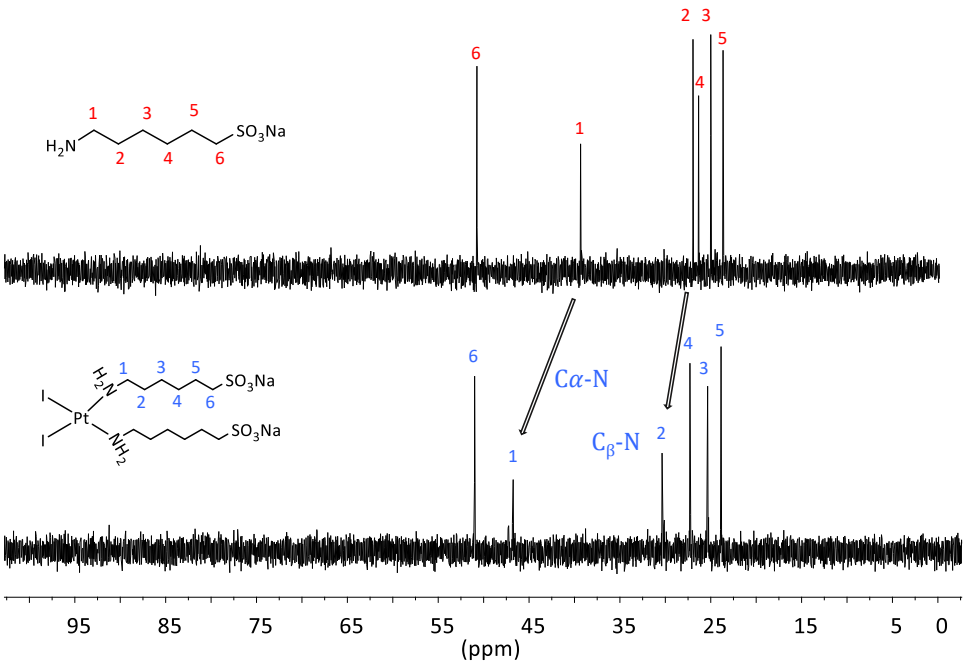

Figure A36 ^{13}C-NMR (100 mHz) spectra of **L6** (top) and **Pt-L6** (bottom) in *d*-D2O.

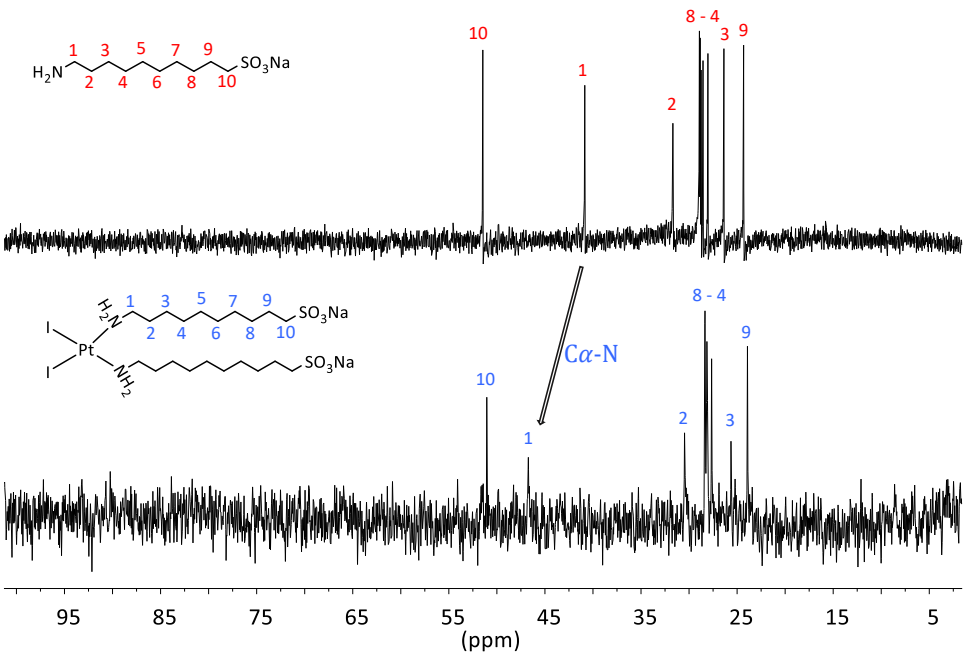

Figure A37 ^{13}C-NMR (100 mHz) spectra of **L10** (top) and **Pt-L10** (bottom) in *d*-D2O.

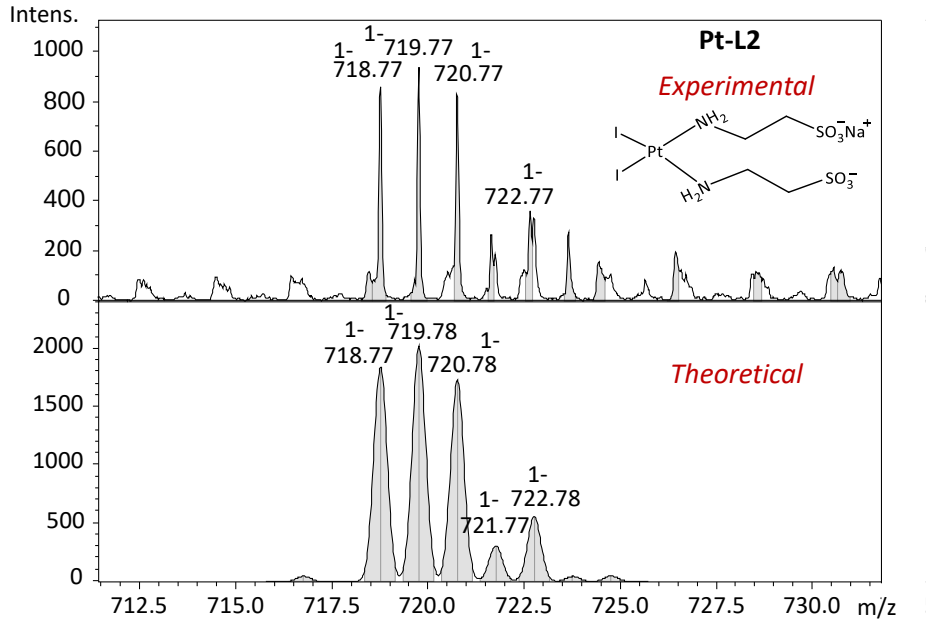

Figure A38 Experimental (top) and theoretical (down) negative ESI-MS spectrum of **Pt-L2**.

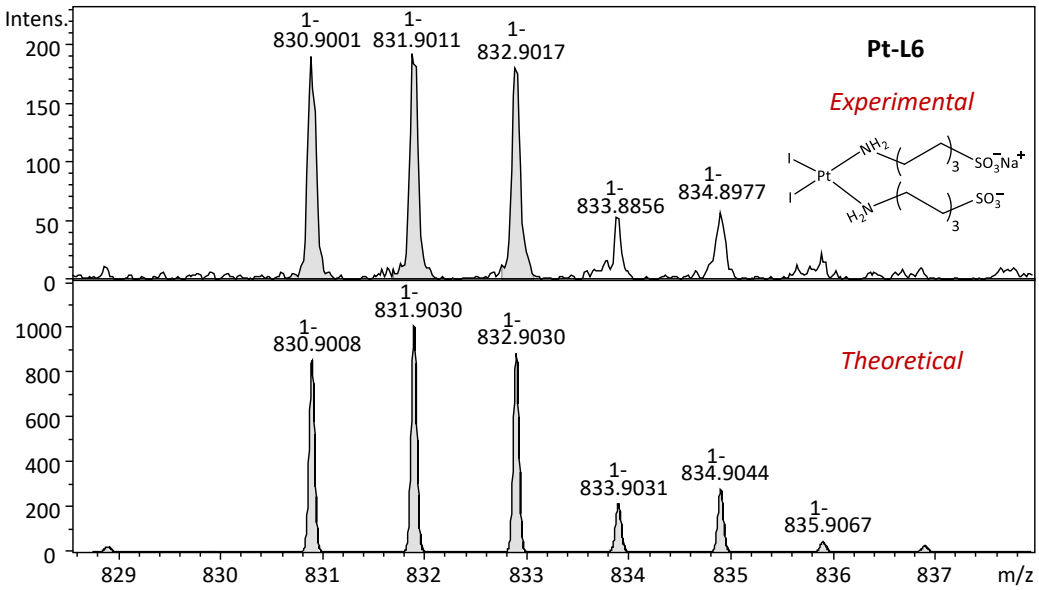

Figure A39 Experimental (top) and theoretical (down) negative ESI-HR-MS spectrum of **Pt-L6**.

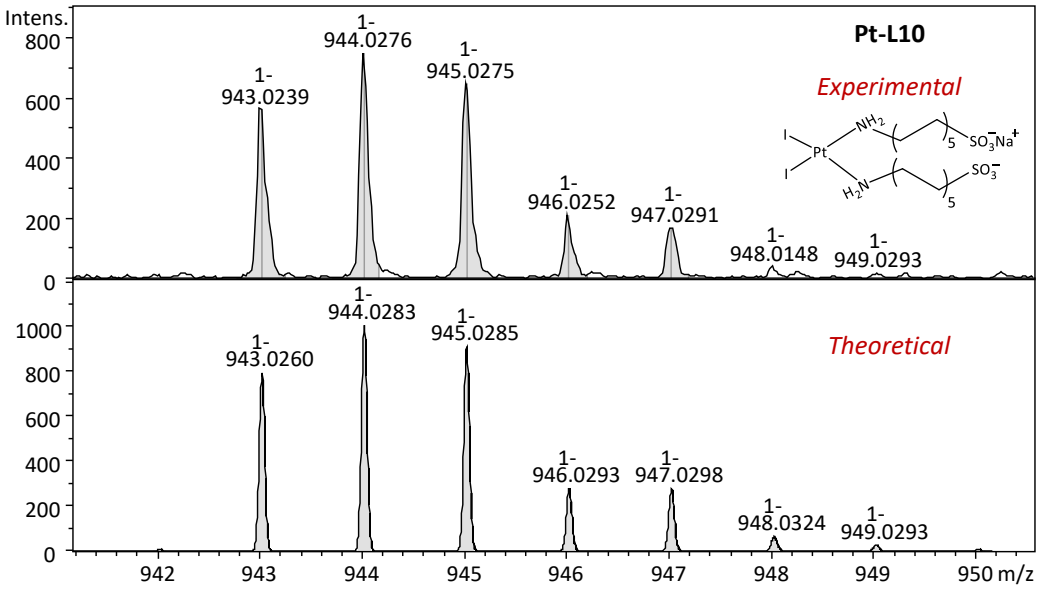

Figure A40 Experimental (top) and theoretical (down) negative ESI-HR-MS spectrum of **Pt-L10**.

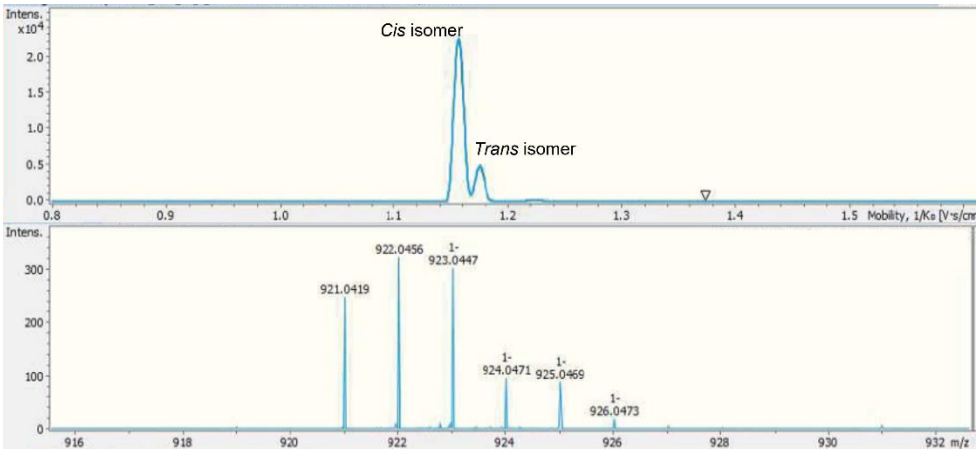

Figure A41 IM MS for **Pt-L10** + H^+ specie without Na^+ as sulphonate counterions as a tool to determine the presence and proportion of cis and trans isomer of the complex.

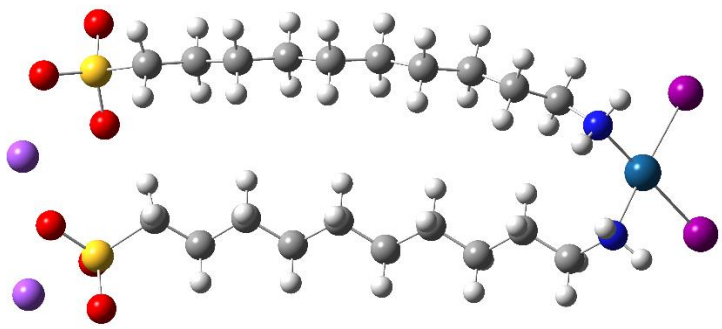

Figure A42 Geometry optimisation of **Pt-L10** by DFT using PBE and LanL2dz base solvated in water.

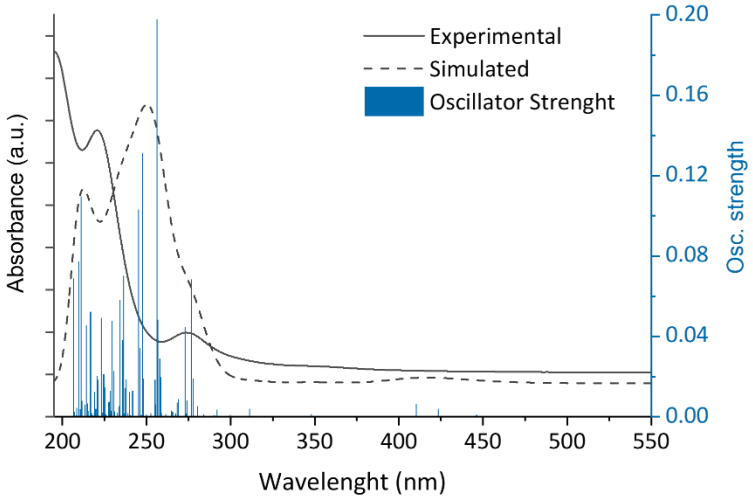

Figure A43 Experimental (solid line) and simulated (dashed line) UV-vis spectra of **Pt-L10.**

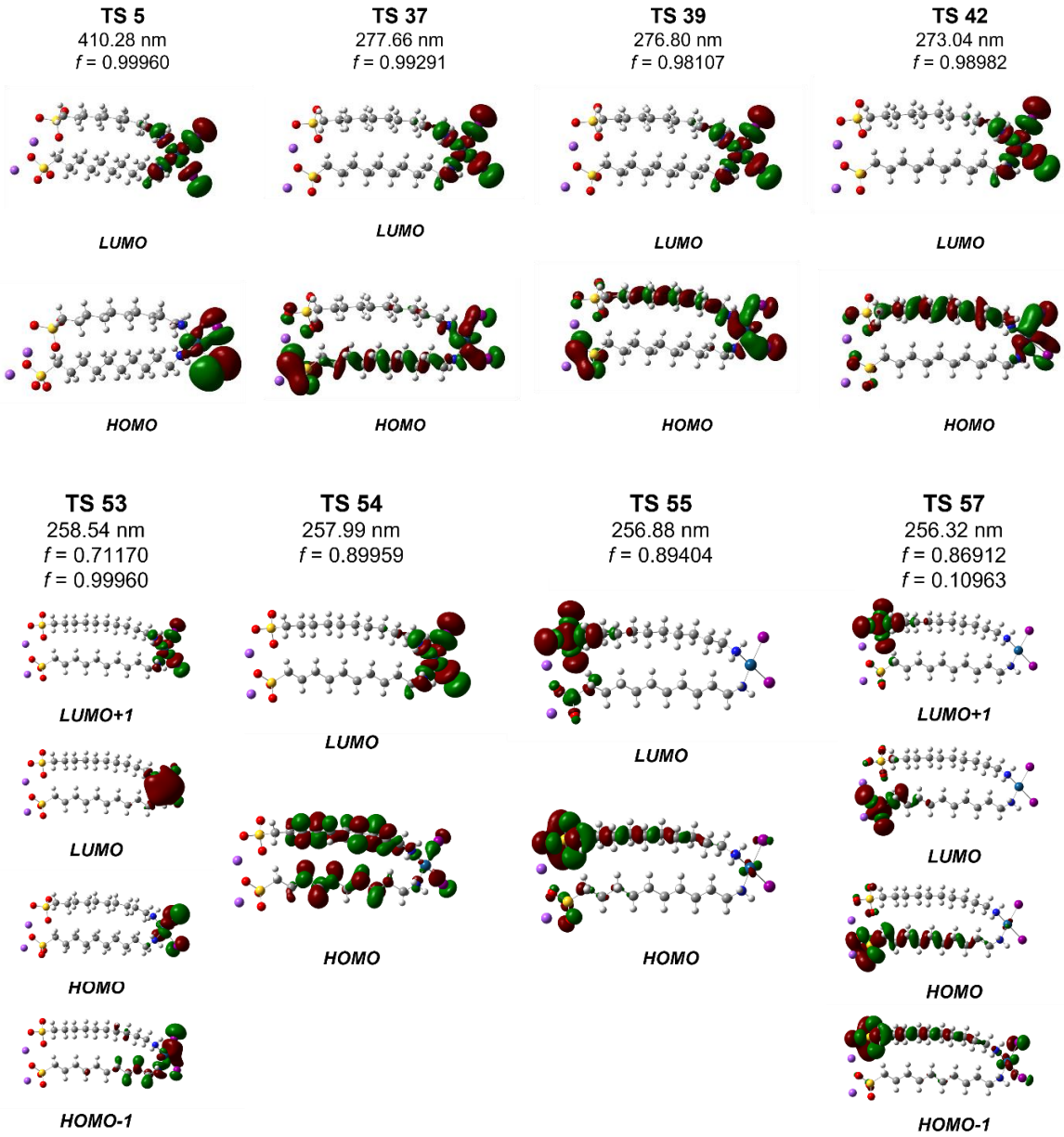

TS 60
255.1 nm
f = 0.57356
f = 0.40957

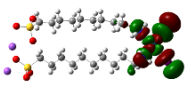

LUMO+1

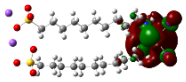

LUMO

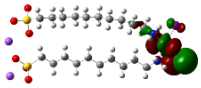

HOMO

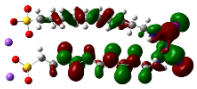

HOMO-1

TS 64
248.21 nm
f = 0.85085

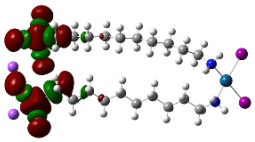

LUMO

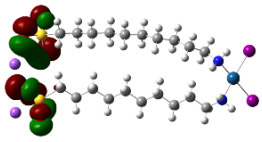

HOMO

TS 65
247.60 nm
f = 0.49681
f = 0.40448

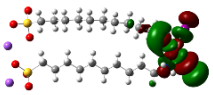

LUMO+1

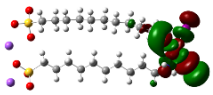

LUMO

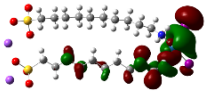

HOMO

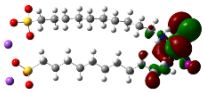

HOMO-1

TS 70
245.39 nm
f = 0.49824
f = 0.41631

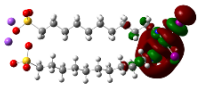

LUMO+1

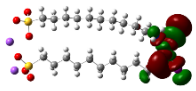

LUMO

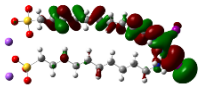

HOMO

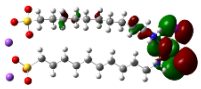

HOMO-1

TS 89
234.33 nm
f = 0.94653

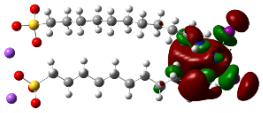

LUMO

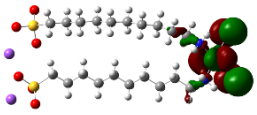

HOMO

TS 98
229.40 nm
f = 0.72021
f = 0.13382

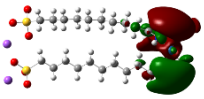

LUMO+1

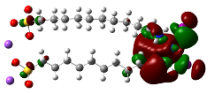

LUMO

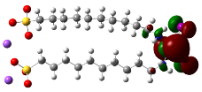

HOMO

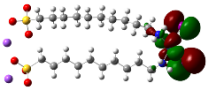

HOMO-1

TS 119
223.23 nm
f = 0.44942
f = 0.29479
f = 0.18598

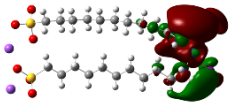

LUMO+2

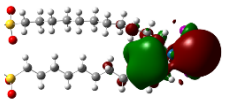

LUMO+1

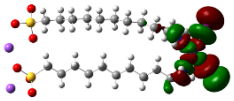

LUMO

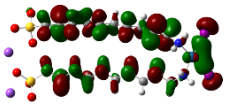

HOMC

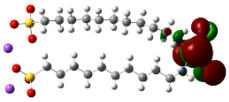

HOMO-2

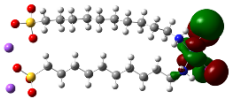

HOMO+1

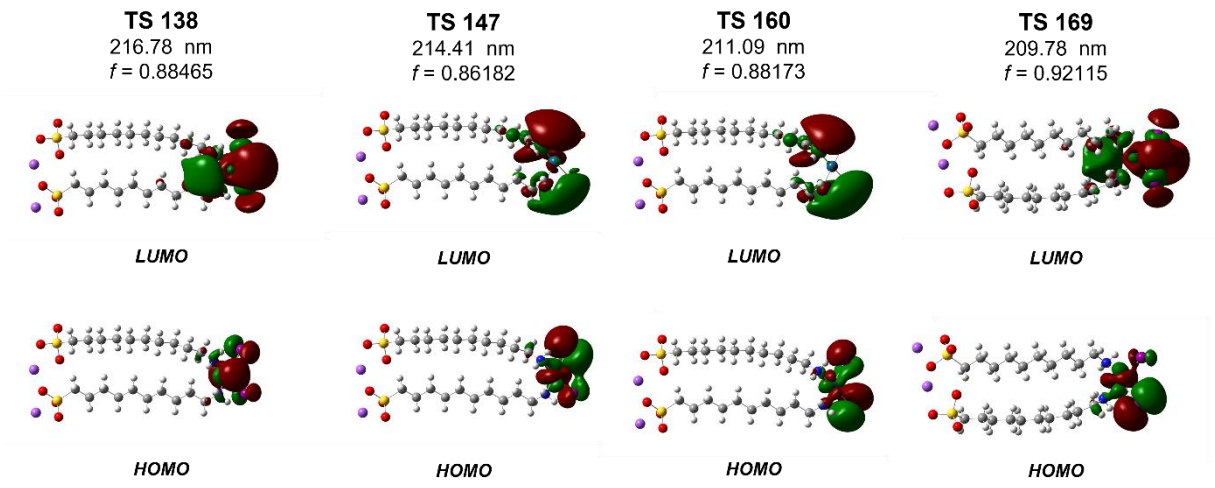

Figure A44 Molecular orbitals representation of the calculated electronic transition states for **Pt-L10**. Each TS indicates the resultant associated absorption band and the oscillator strength value (*f*). Representations obtained using Gaussian 09W and GaussView 6.0.16.

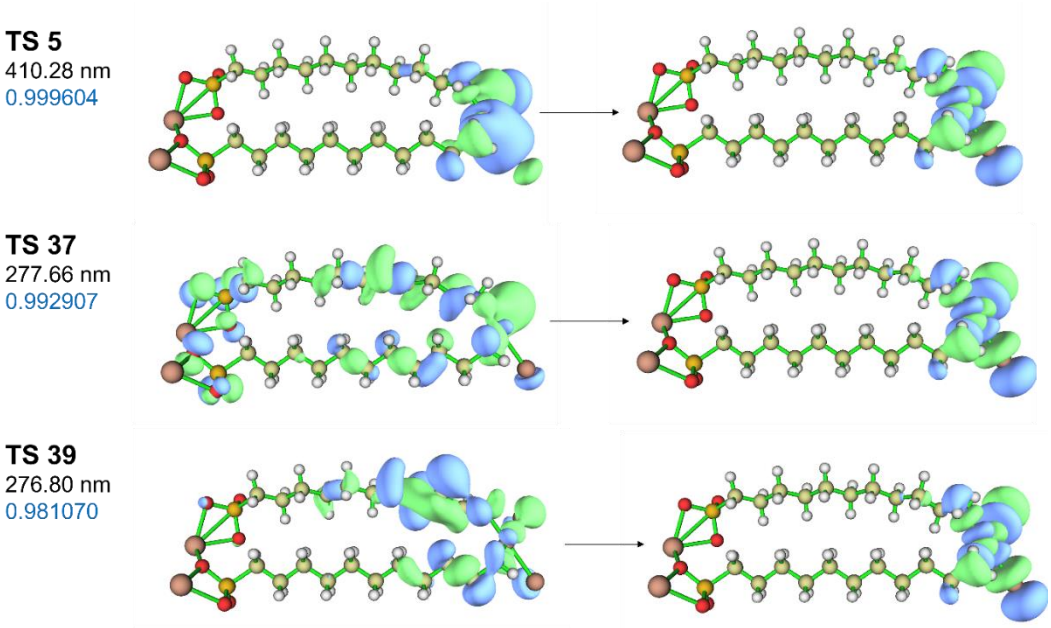

TS 42
273.04 nm
0.989829

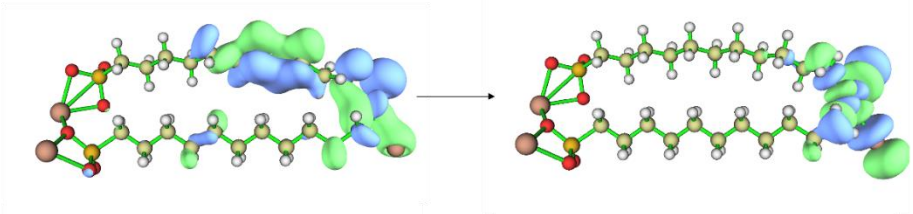

TS 53
258.54 nm
0.711694

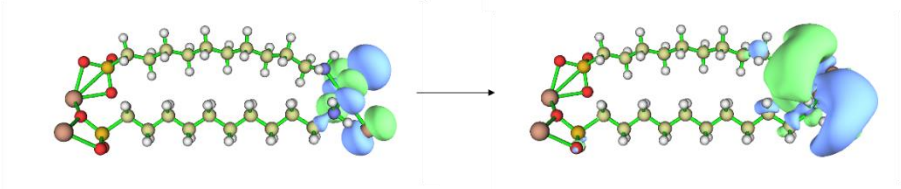

TS 54
257.99 nm
0.899596

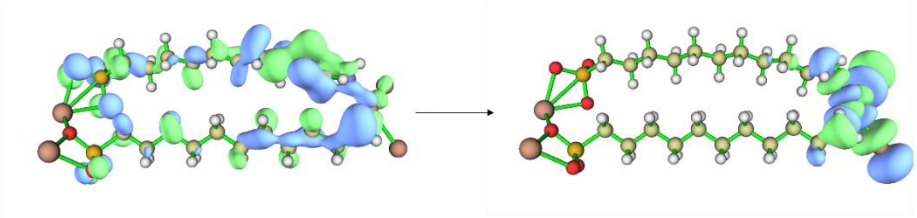

TS 55
256.88 nm
0.894034

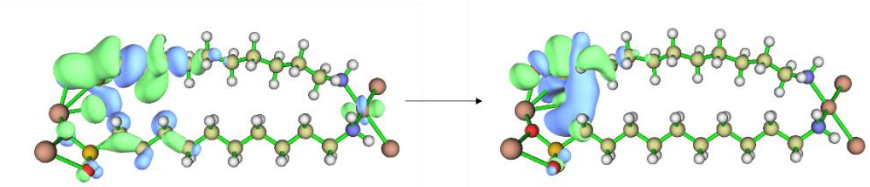

TS 57
256.32 nm
0.869119

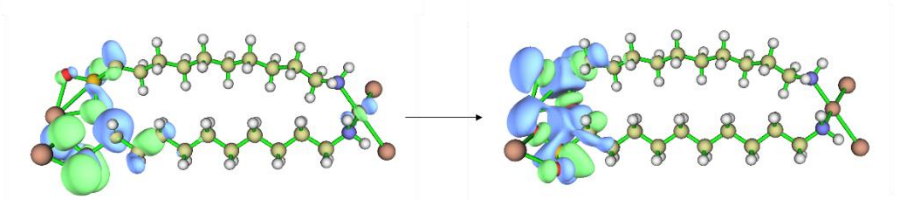

TS 60
255.1 nm
0.583556

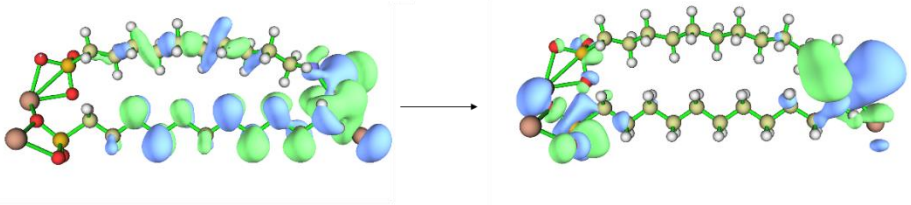

TS 64
248.2 nm
0.850865

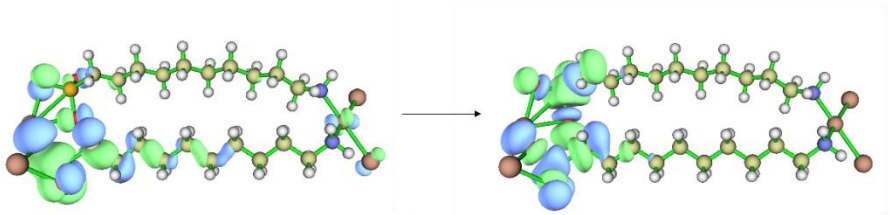

TS 65
247.60 nm
0.496809

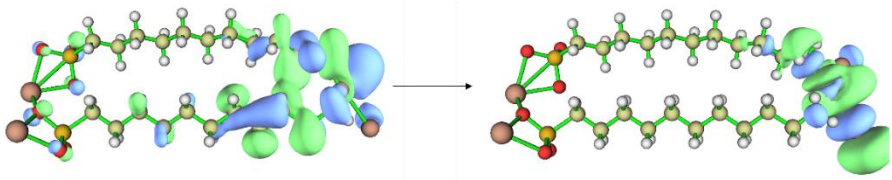

TS 70
245.39 nm
0.498230

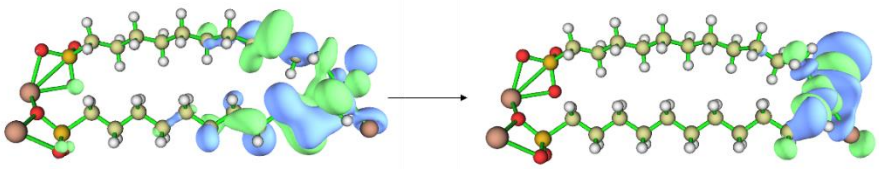

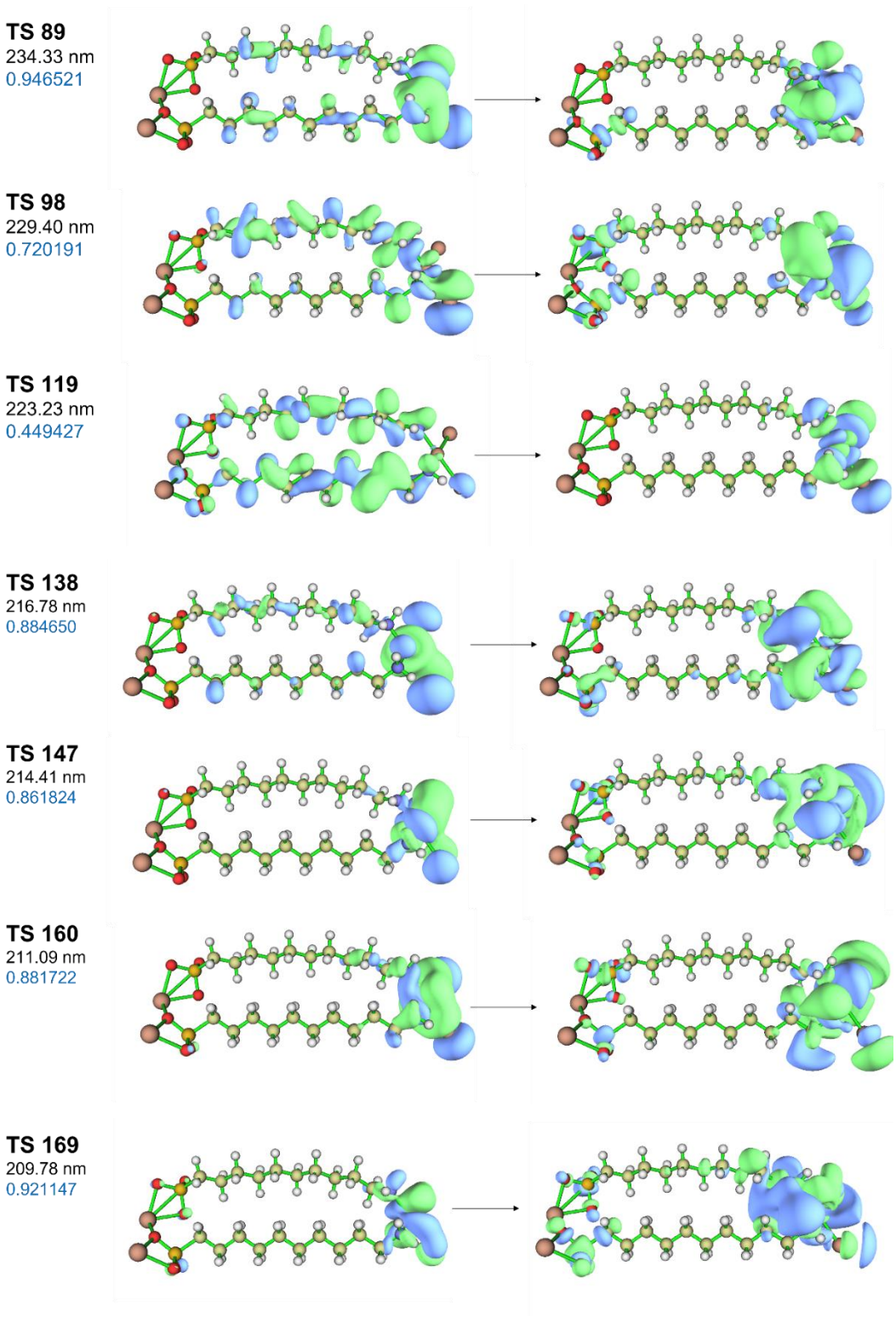

Figure A45 NTOs representation for the calculated TS and their corresponding computed absorption of **Pt-L10**. The NTO eigenvalue are indicated in blue. Representations obtained using Multiwfn 3.7.

Table A1 EDS results from **Pt-L10** *cryo*-TEM micrography at 1500 µM in MiliQ water.

Element	Peak	Area	k	Abs	Weight%	Weight%	Atomic%
	Area	Sigma	factor	Corrn.		Sigma	

Na K	523	140	1.191	1.000	0.62	0.17	3.73
S K	1249	162	0.959	1.000	1.19	0.15	5.14
K K	1995	126	0.970	1.000	1.93	0.12	6.81
I L	22462	318	1.912	1.000	42.85	0.53	46.57
Pt L	20024	333	2.673	1.000	53.41	0.54	37.76
Totals					100.00		

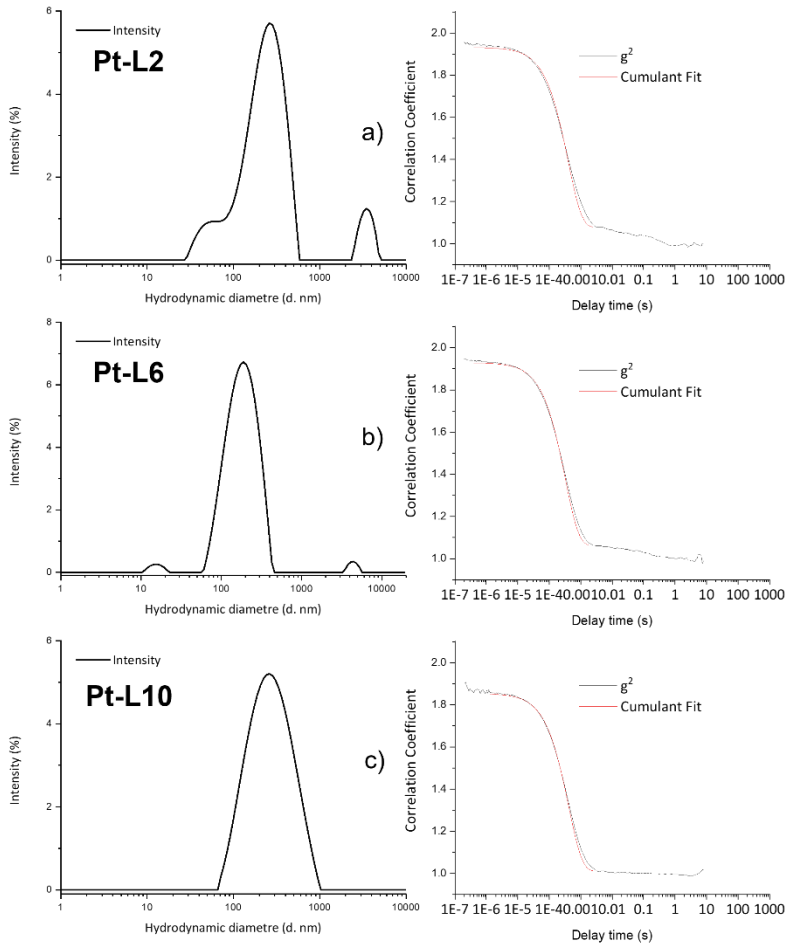

Figure A46 DLS representation of **Pt-L2** (a), **Pt-L6** (b), and **Pt-L10** (c) by intensity, and the associated correlation function (right).

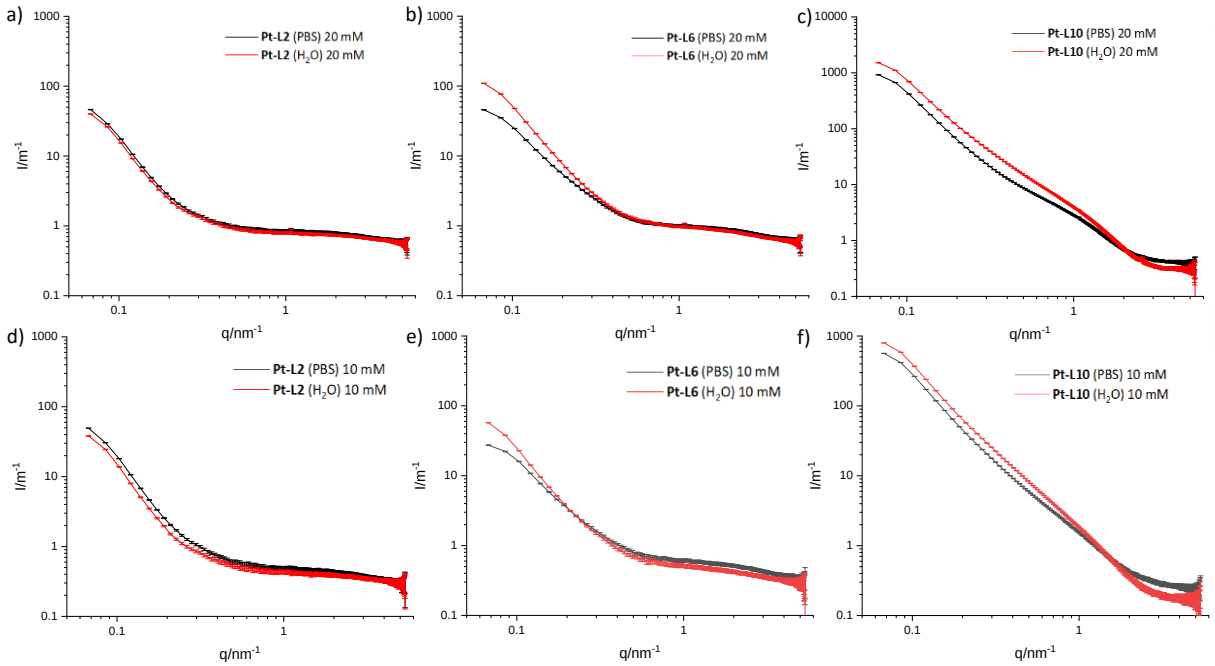

Figure A47 SAXS intensity as function of dispersion vector modulus q for **Pt-L2**, **Pt-L6**, and **Pt-L10** at 20 mM (a), (b), and (c) and 10 mM (d), (e), and (f), respectively.

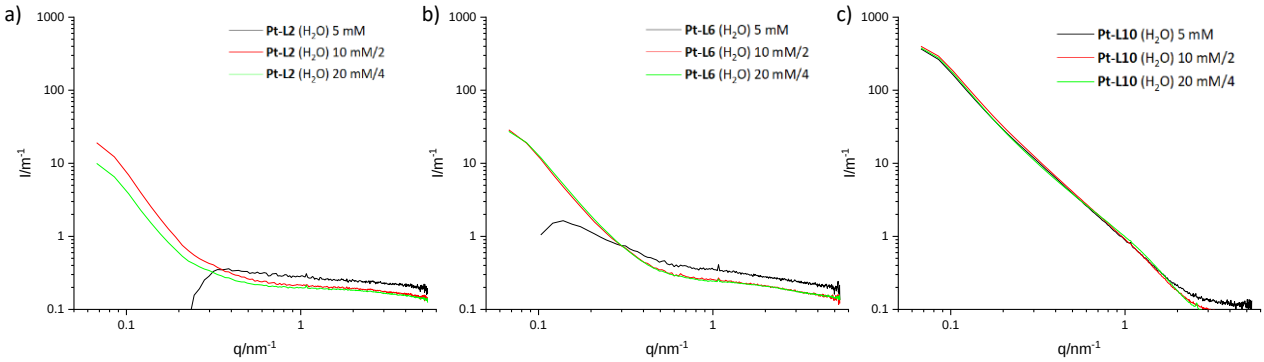

Figure A48 SAXS intensity as function of dispersion vector modulus q for **Pt-L2** (a), **Pt-L6** (b), and **Pt-L10** (c) escalated to 5 mM concentration.

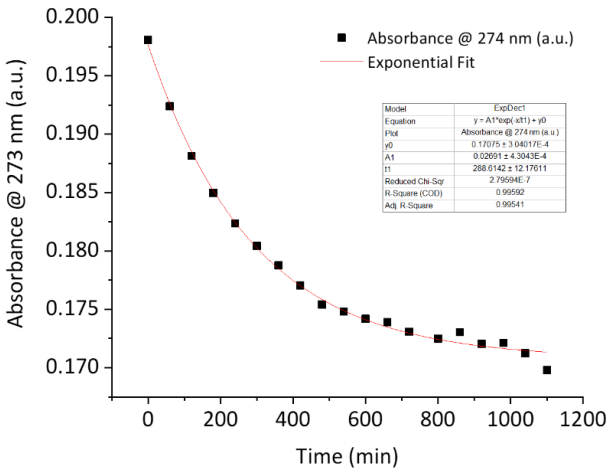

Figure A49 Experimental values for the evolution of the maxima absorbance of **Pt-L10** as function of time (black squares) and the fitted theoretical curve (red line) for the hydrolysis reaction using a single exponential function to obtain k_{obs} and $t_{½}$.

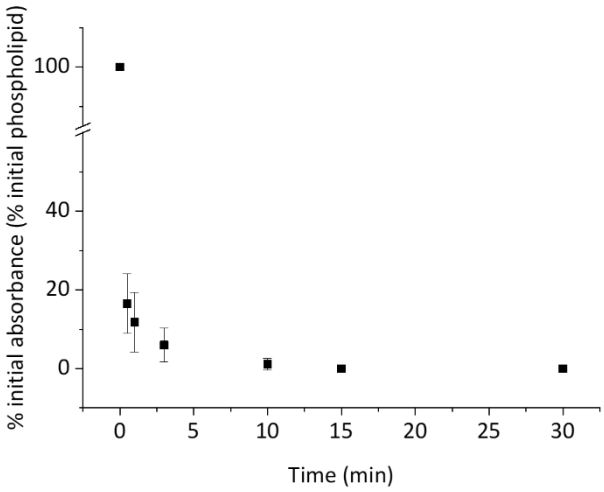

Figure A50 Phospholipid present in the supernatant respect the initial phospholipid percentage over centrifugation times. The mean and standard deviations are the result of two independent experiments with non-extruded SPC liposomes at 3 mM concentration.

Method A

300/50 SPC:**Pt-L10**

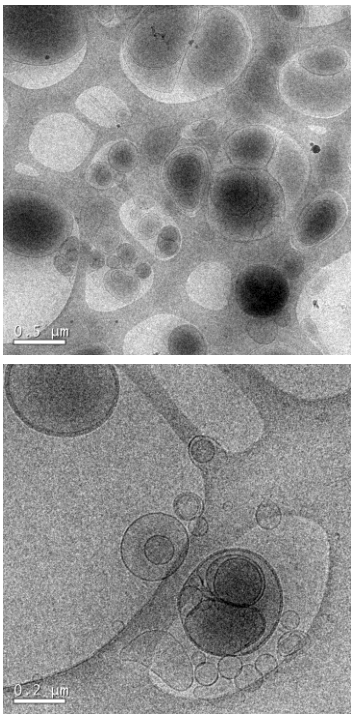

300/100 SPC:**Pt-L10**

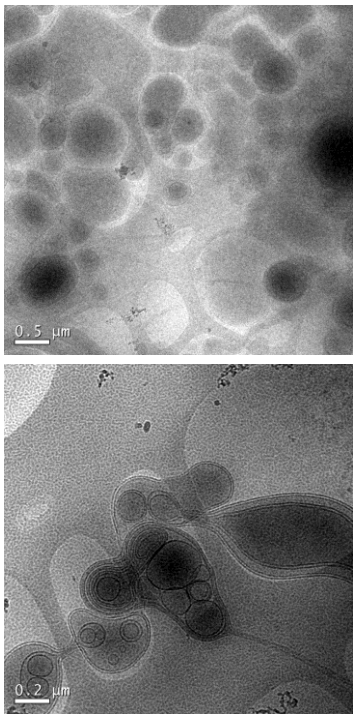

Method B

300/25 SPC:**Pt-L10**

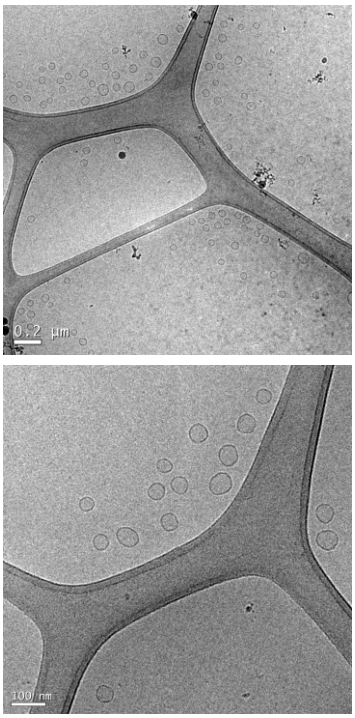

300/25 SPC:**Pt-L10**

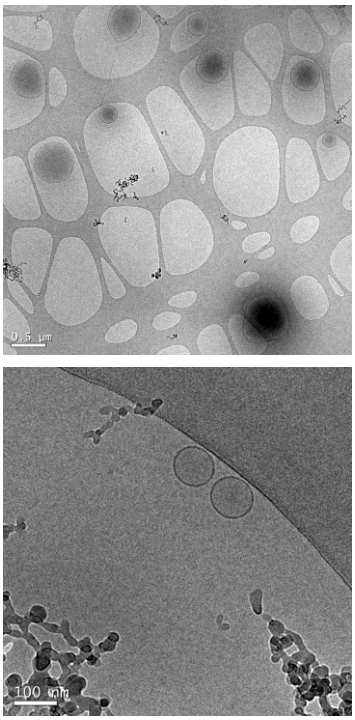

300/25 SPC:**Pt-L10**

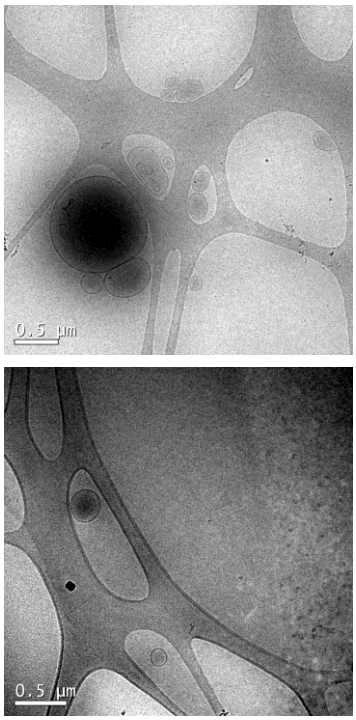

300/50 SPC:**Pt-L10**

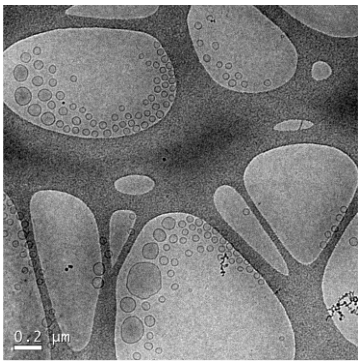

300/50 SPC:**Pt-L10**

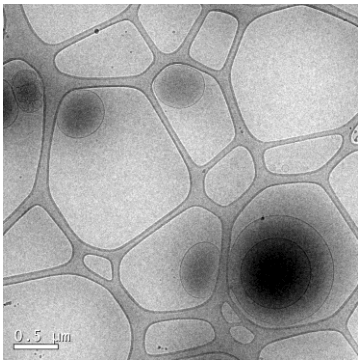

300/50 SPC:**Pt-L10**

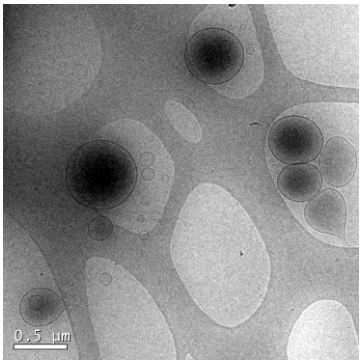

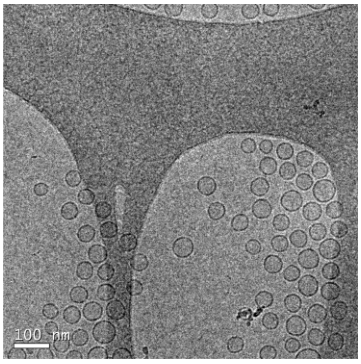

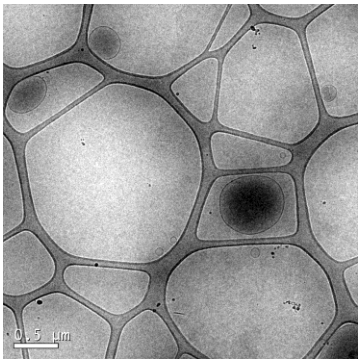

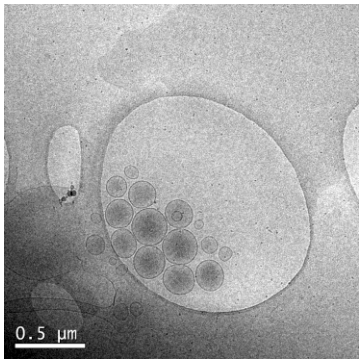

300/75 SPC:**Pt-L10**

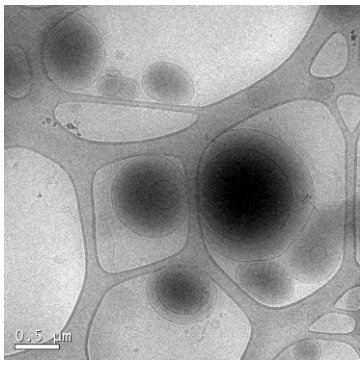

300/75 SPC:**Pt-L10**

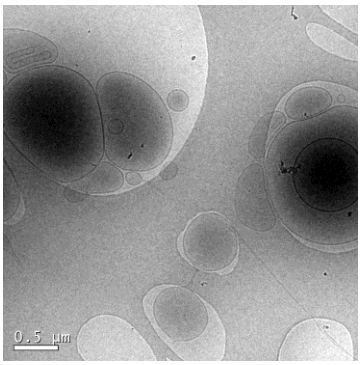

300/75 SPC:**Pt-L10**

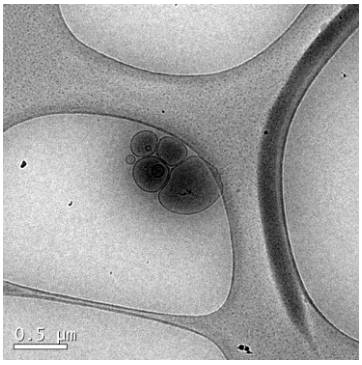

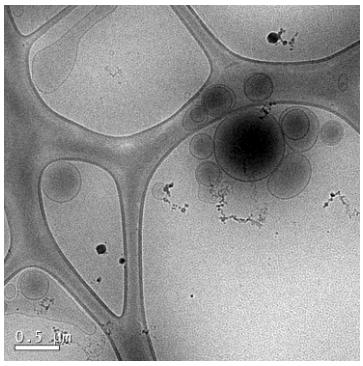

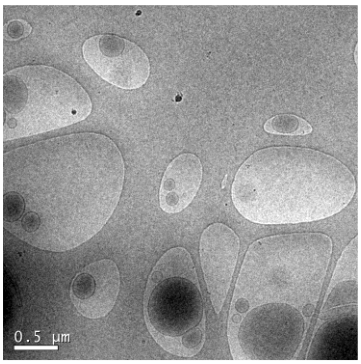

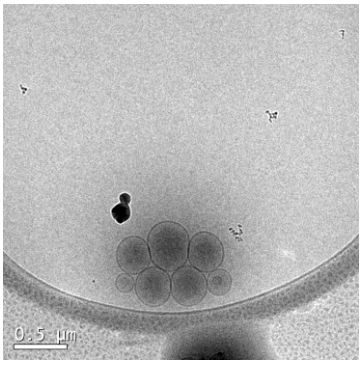

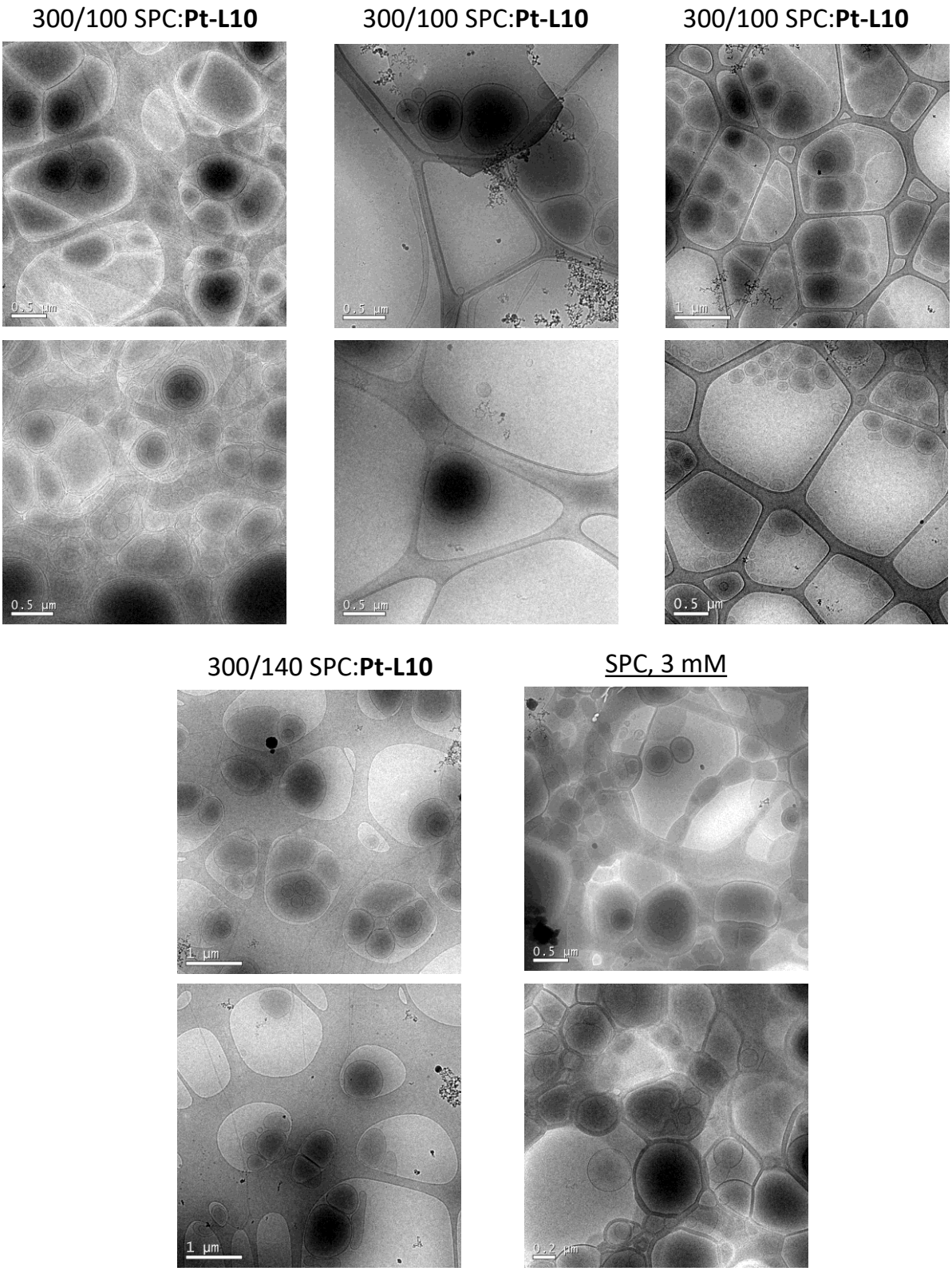

Figure A51 *Cryo*-TEM micrographs for several **MTL** preparation at distinct molar ratios, with method A and method B. The last two micrographs correspond to plain SPC at 3 mM prepared alike as reference.

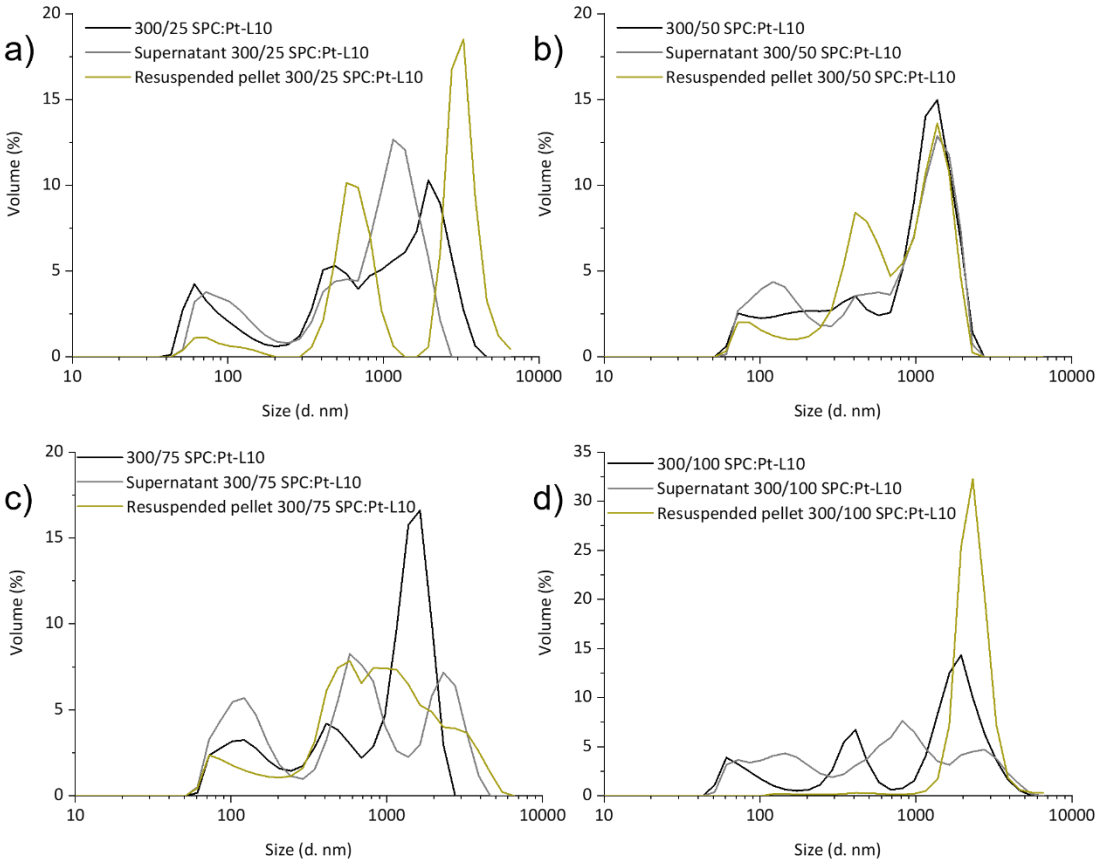

Figure A52 DLS graphs from raw **MTL**, supernatant and resuspended pellet at several SPC:**Pt-L10** molar ratios: (a) 300/25, (b) 300/50, (c) 300/75, and (d) 300/100.

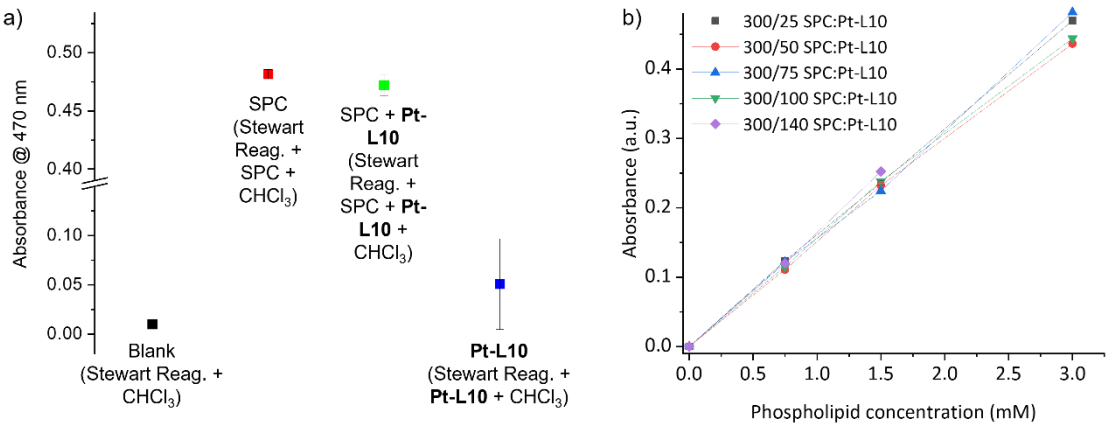

Figure A53 (a) Blank for Stewart method with **Pt-L10** (blue square) and (b) calibration pattern for several **MTL** molar ratios.

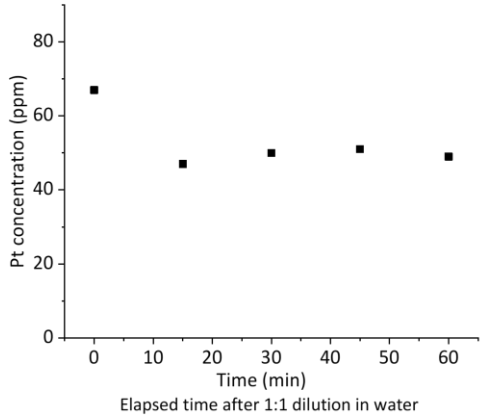

Figure A54 Platinum concentration of **MTL** (300:140 SPC/**PtL10** molar ratio) measured by ICP-OES upon 1:1 dilution over 1 h.

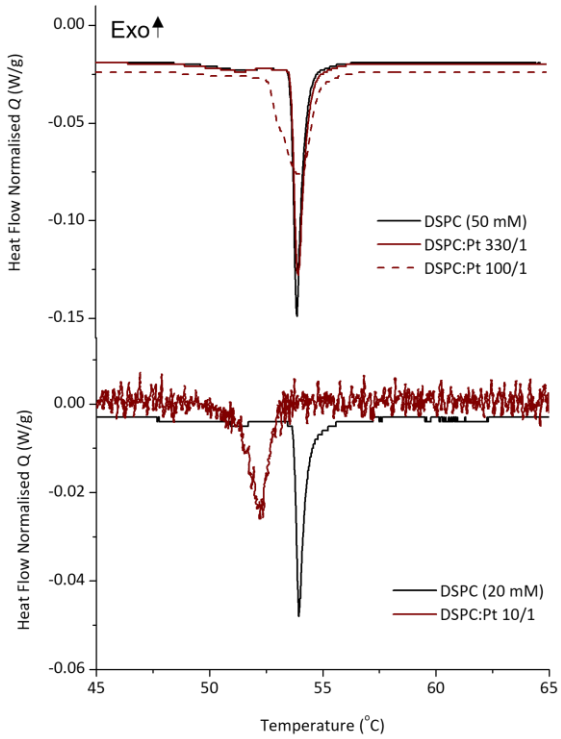

Figure A55 DSC thermograms for DSPC formulations obtained using a ramp of 2 °C/min.

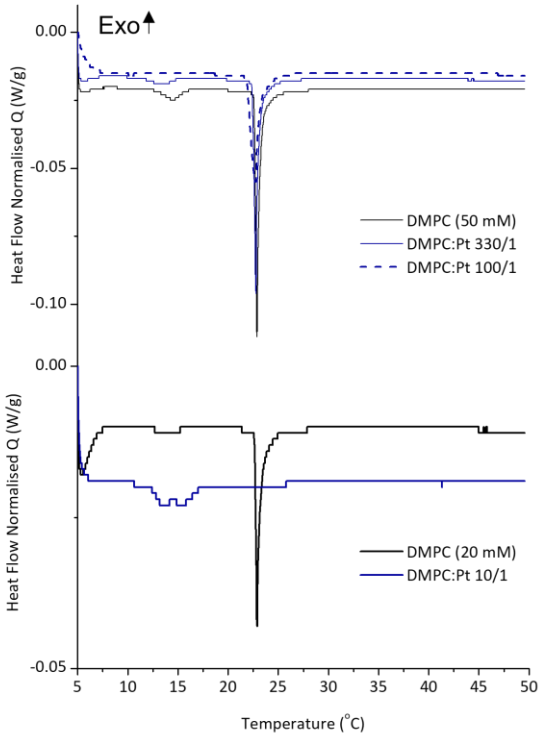

Figure A56 DSC thermograms for DMPC formulations obtained using a ramp of 2 °C/min.

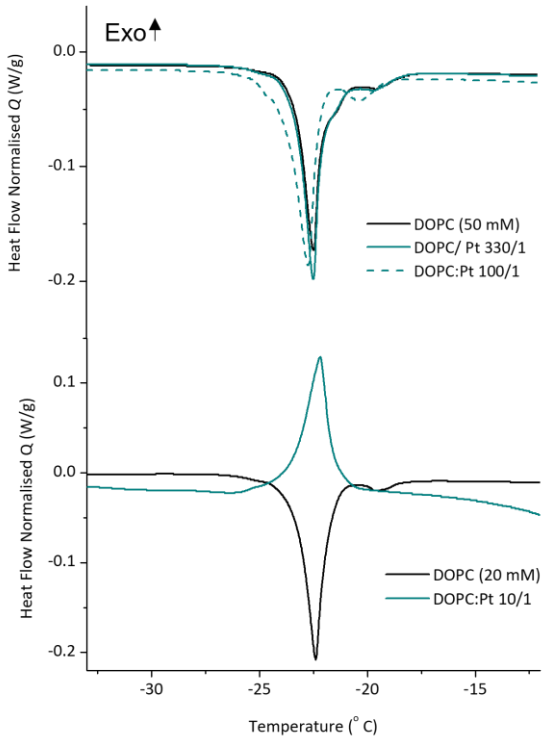

Figure A57 DSC thermograms for DOPC formulations obtained using a ramp of 2 °C/min.

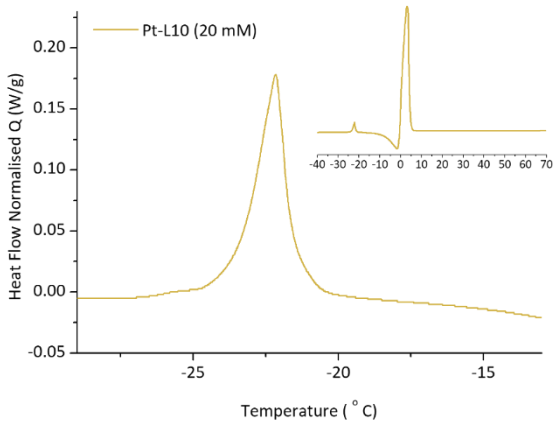

Figure A58 DSC thermogram of **Pt-L10** obtained using a ramp of 2 °C/min. The onset T was -22.55 °C, the Peak T -22.16 °C. The insert shows the whole DSC measured range.

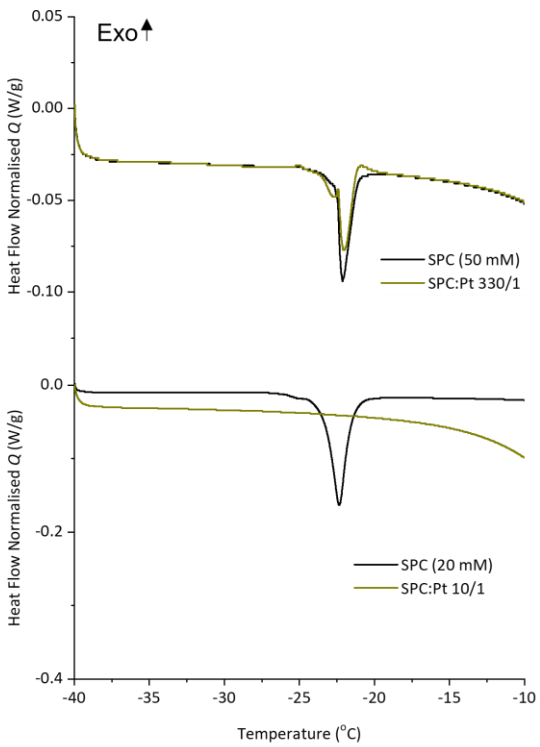

Figure A59 DSC thermograms for SPC formulations obtained using a ramp of 2 °C/min.

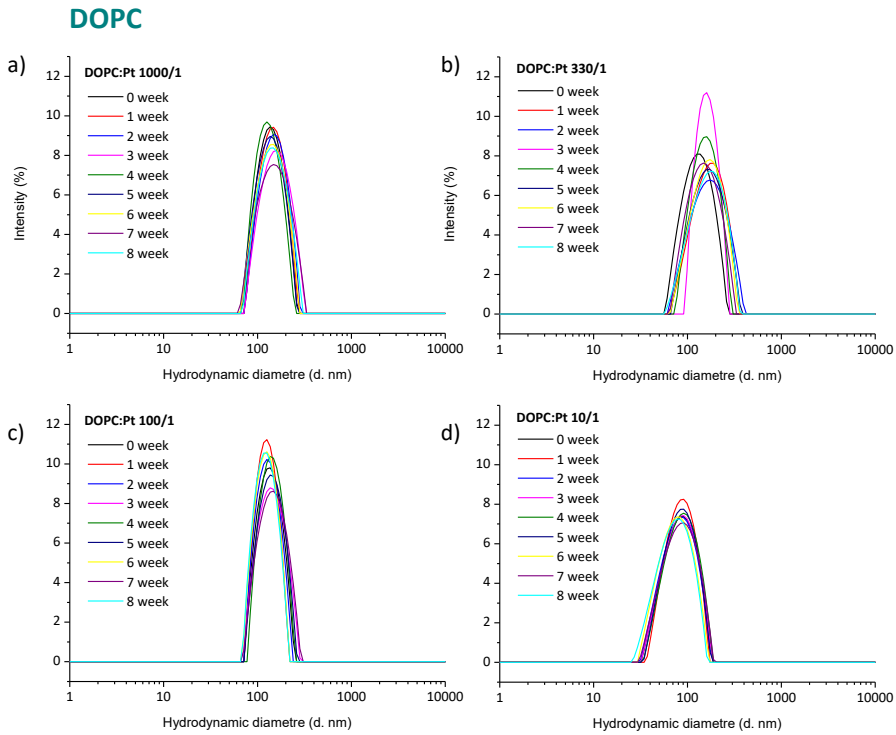

Figure A60 DLS graphs showing the hydrodynamic diameter of the DOPC formulated **MTL** for 1000/1 (a), 330/1 (b), 100/1 (c) and 10/1 (d) lipid:**Pt-L10** molar ratio to disclose the formulations' stability.

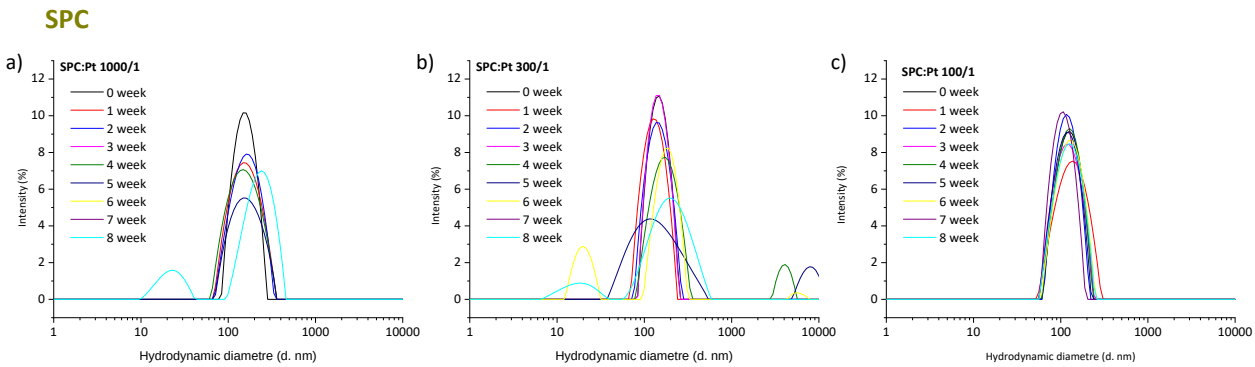

Figure A61 DLS graphs showing the hydrodynamic diameter of the SPC formulated **MTL** for 1000/1 (a), 330/1 (b), and 100/1 (c) lipid:**Pt-L10** molar ratio to disclose the formulations' stability.

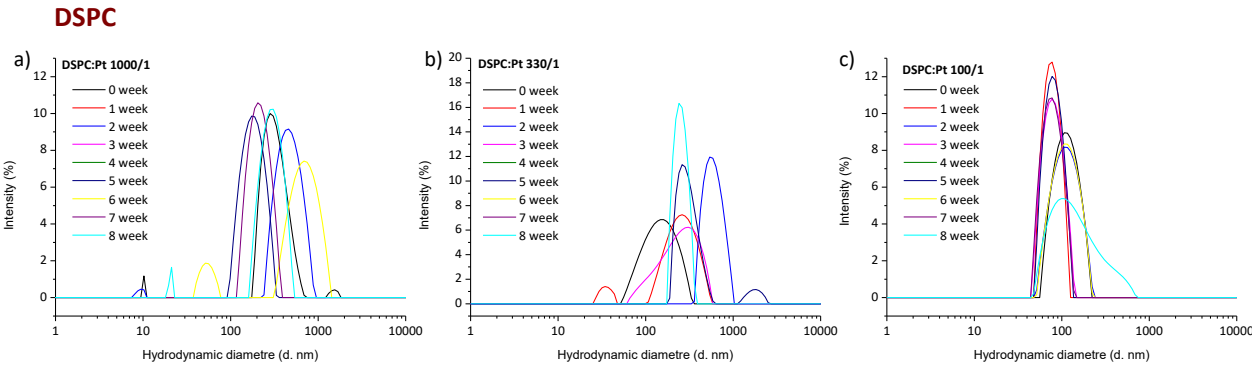

Figure A62 DLS graphs showing the hydrodynamic diameter of the formulated **MTL** for 1000/1 (a), 330/1 (b), and 100/1 (c) lipid:**Pt-L10** molar ratio to disclose the stability of the formulations.

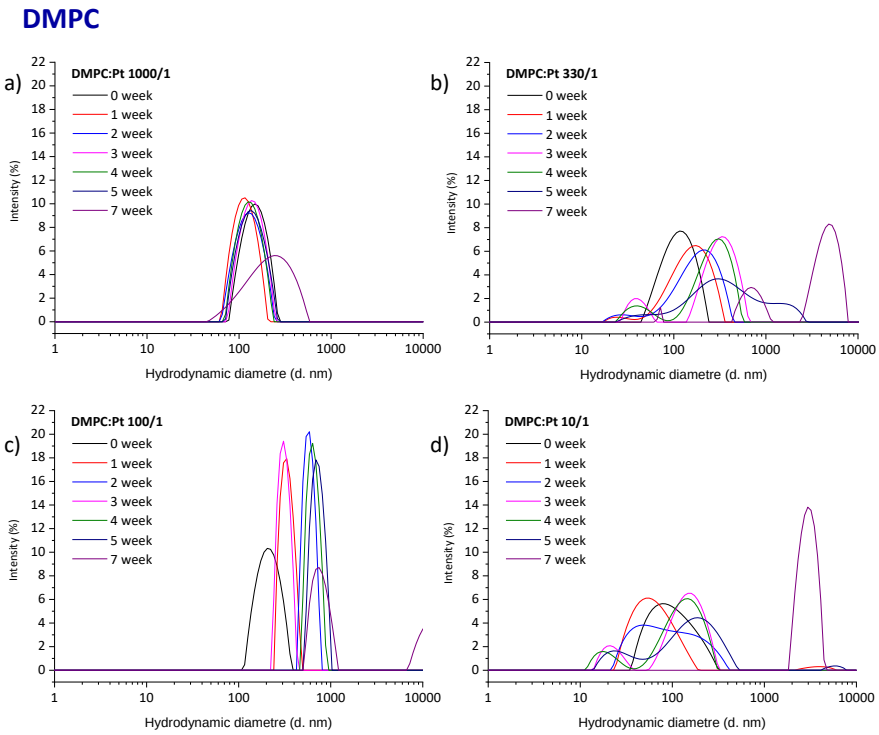

Figure A63 DLS graphs showing the hydrodynamic diameter of the DMPC formulated **MTL** for 1000/1 (a), 330/1 (b), 100/1 (c) and 10/1 (d) lipid:**Pt-L10** molar ratio to disclose the formulations' stability.

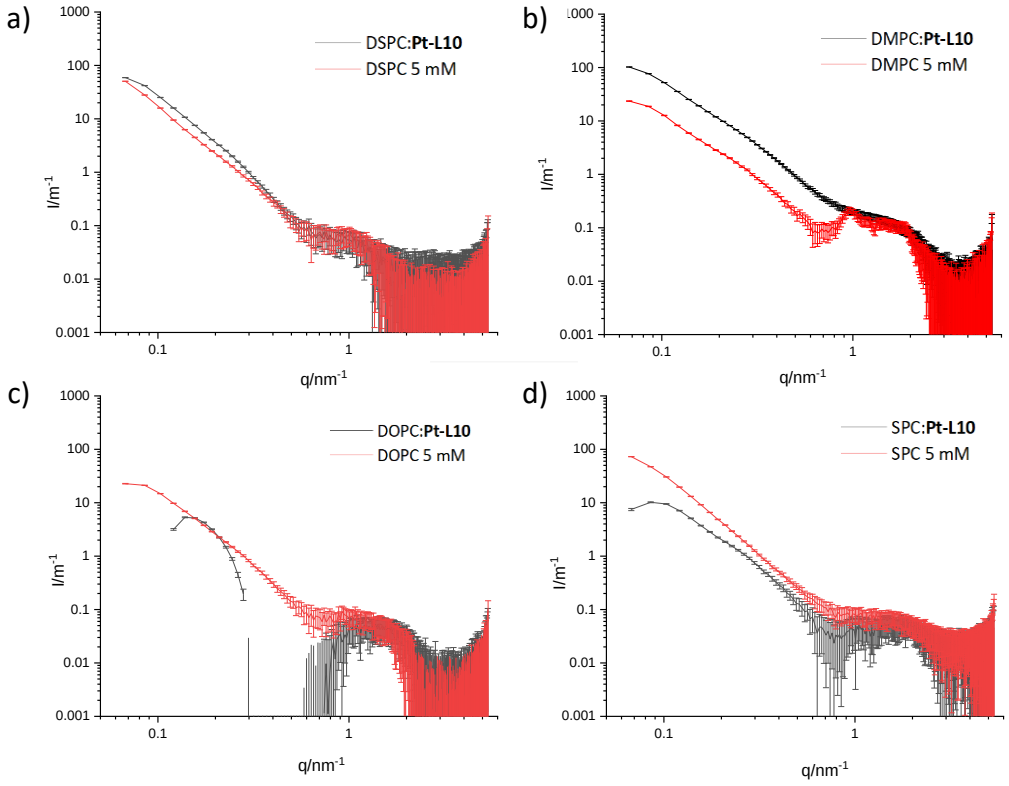

Figure A64 SAXS intensity as function of dispersion vector modulus q for 5 mM plain liposomes and **MTL** (phospholipid:**Pt-L10** molar ratio 100/1) prepared in PBS and after sonication for DSPC (a), DMPC (b), DOPC (c), and SPC (d).

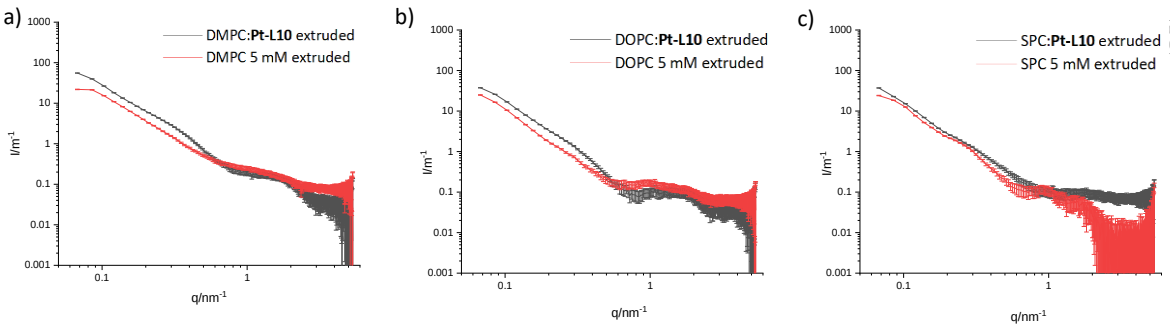

Figure A65 SAXS intensity as function of dispersion vector modulus q for 5 mM plain liposomes and **MTL** (phospholipid:**Pt-L10** molar ratio 100/1) prepared in PBS and after extrusion at 400 nm for DSPC (a), DMPC (b), DOPC (c), and SPC (d).

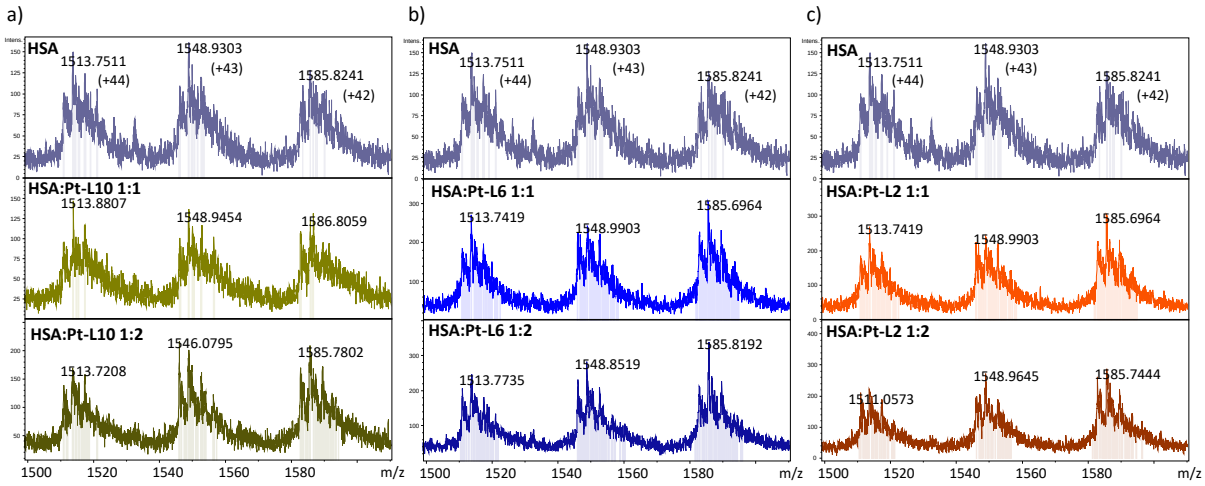

Figure A66 Mass spectra recorded after incubation (24 h at 37 °C) of **Pt-L2** (a), **Pt-L6** (b) and **Pt-L10** (c) with albumin (HSA) at 1:1 (middle) and 1:2 (bottom) Protein:Pt molar ratio. Top spectrum corresponds to HSA as reference.

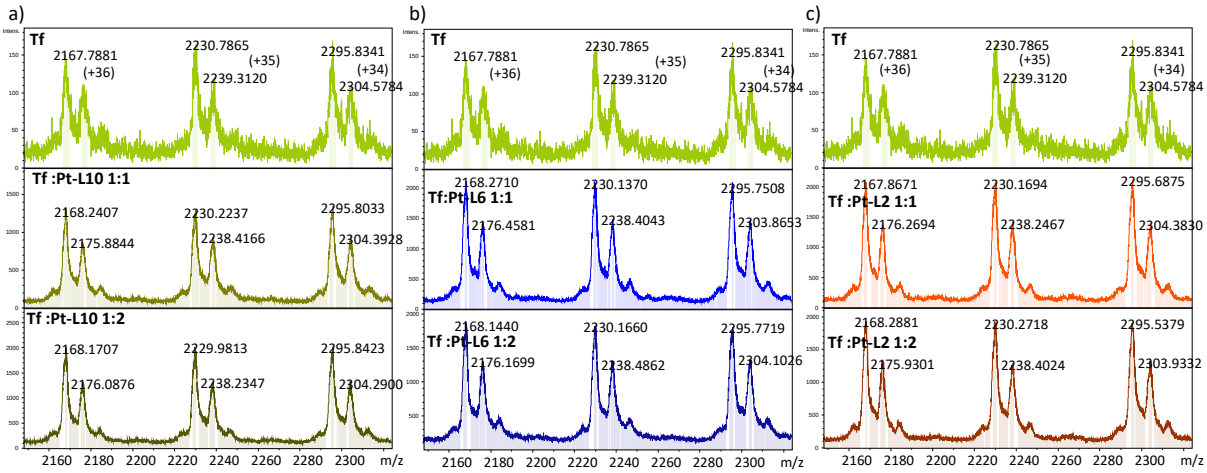

Figure A67 Mass spectra recorded after incubation (24 h at 37 °C) of **Pt-L2** (a), **Pt-L6** (b) and **Pt-L10** (c) with transferrin (Tf) at 1:1 (middle) and 1:2 (bottom) Protein:Pt molar ratio. Top spectrum corresponds to Tf as reference.

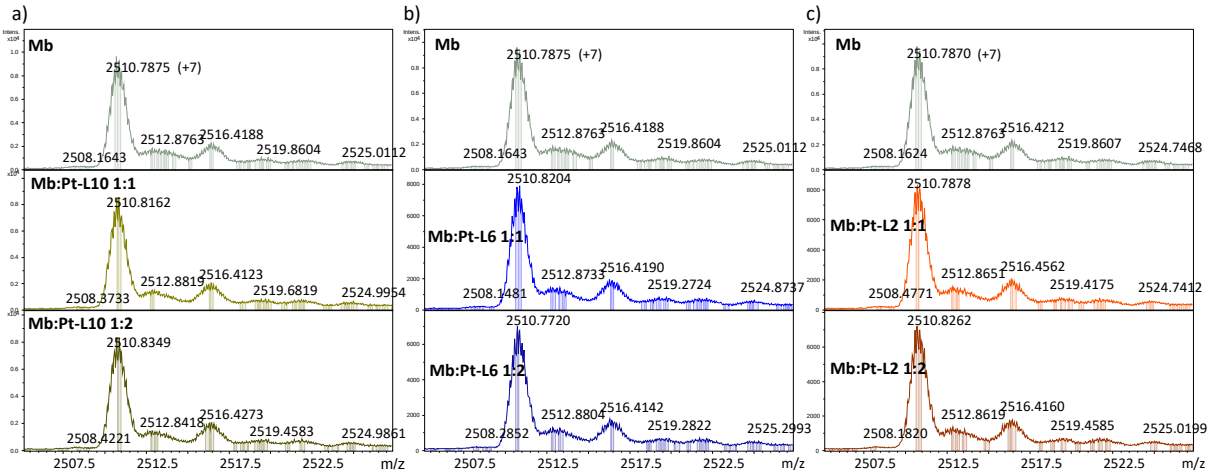

Figure A68 Mass spectra recorded after incubation (24 h at 37 °C) of **Pt-L2** (a), **Pt-L6** (b) and **Pt-L10** (c) with myoglobin (Mb) at 1:1 (middle) and 1:2 (bottom) Protein:Pt molar ratio. Top spectrum corresponds to Mb as reference.

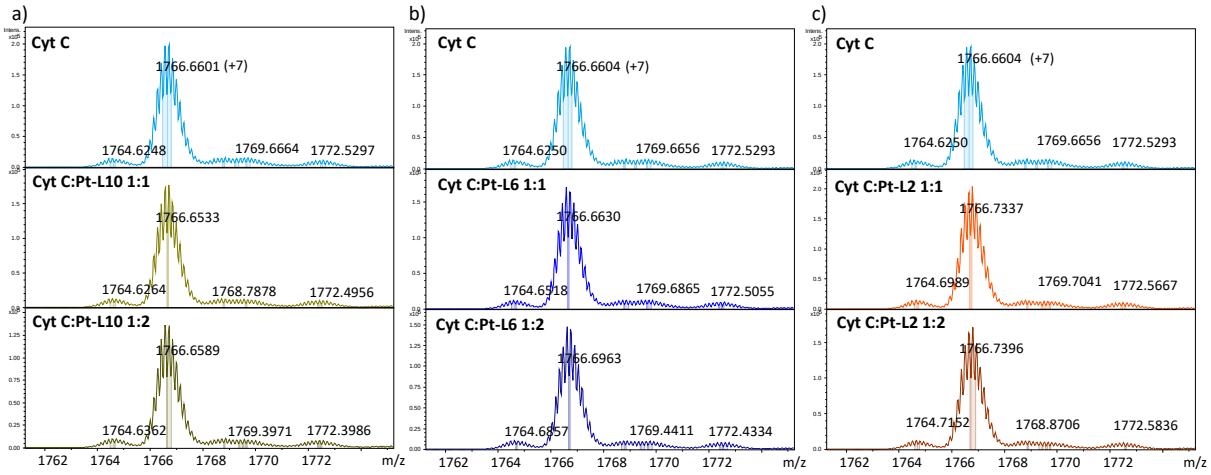

Figure A69 Mass spectra recorded after incubation (24 h at 37 °C) of **Pt-L2** (a), **Pt-L6** (b) and **Pt-L10** (c) with cytochrome C (Cyt C) at 1:1 (middle) and 1:2 (bottom) Protein:Pt molar ratio. Top spectrum corresponds to Cyt C as reference.

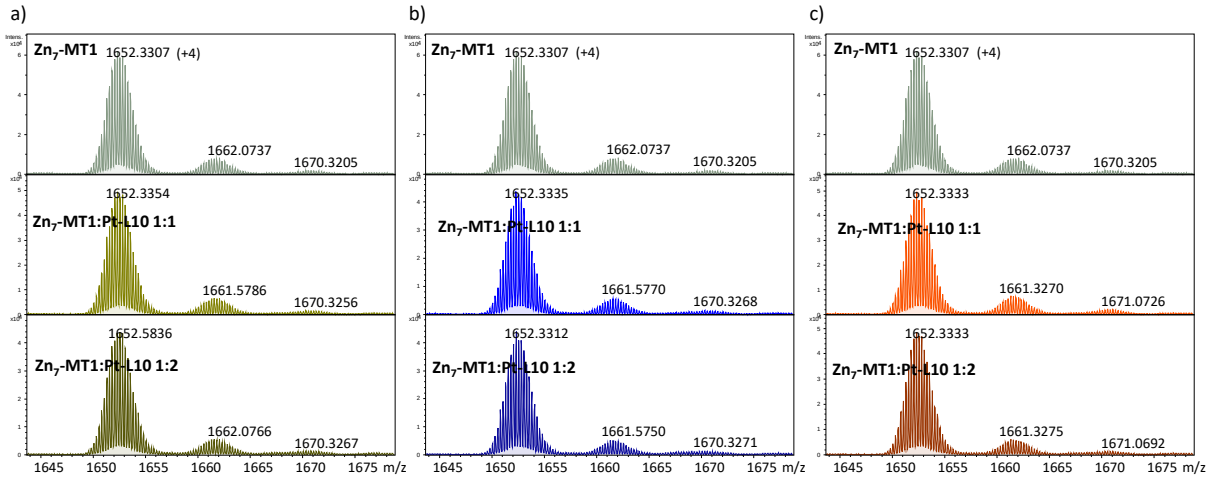

Figure A70 Mass spectra recorded after incubation (24 h at 37 °C) of **Pt-L2** (a), **Pt-L6** (b) and **Pt-L10** (c) with Zn_7-MT1 at 1:1 (middle) and 1:2 (bottom) Protein:Pt molar ratio. Top spectrum corresponds to Zn_7-MT1 as reference.

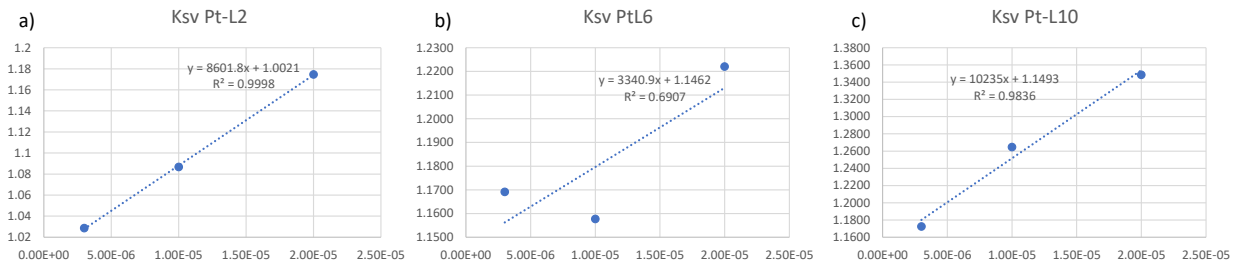

Figure A71 *K*sv calculation by plotting F_0/F vs quencher concentration for **Pt-L2** (a), **Pt-L6** (b), and **Pt-L10** (c).

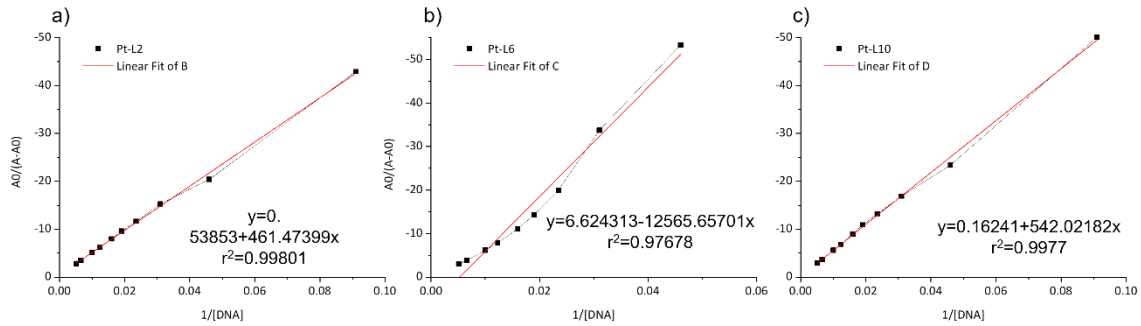

Figure A72 Determination of K_b for **Pt-L2** (a), **Pt-L6** (b) and **Pt-L10** (c): plot for $A_0/(A-A_0)$ *vs* 1/[DNA], where K_b corresponds to the ratio between the intercept and the slope according to Benesi-Hildebrand equation (Equation 6.2).

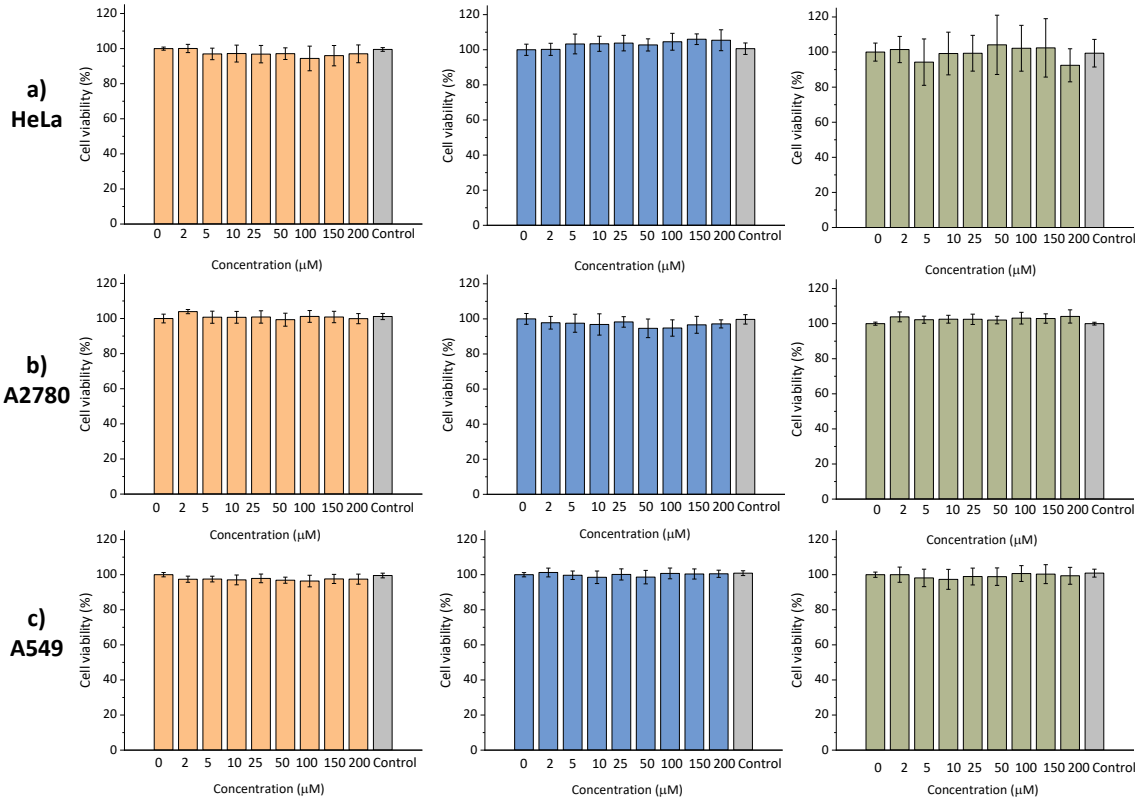

Figure A73 Cell viability assays for HeLa (a), A2780 (b) and A549 (c) cell lines treated with **L2** (left), **L6** (centre), and **L10** (right) after 72 h of treatment at different concentrations. The results are an average of three independent experiments conducted in triplicate.